Synthesis of Fly Ash Supported and Non Supported Metal and Metal Oxide Nanoparticles: Characterization and Catalytic Applications

A Thesis

Submitted to

University of Kota, Kota

for the Award of the Degree of

Doctor of Philosophy

in Chemistry
(Faculty of Science)

Submitted by

RENU HADA

Under the Joint Supervision of

Dr. Vijay Devra
J.D.B. Girls P.G. College, Kota

Prof. Ashu Rani
Department of Pure and Applied Chemistry
University of Kota, Kota

2015

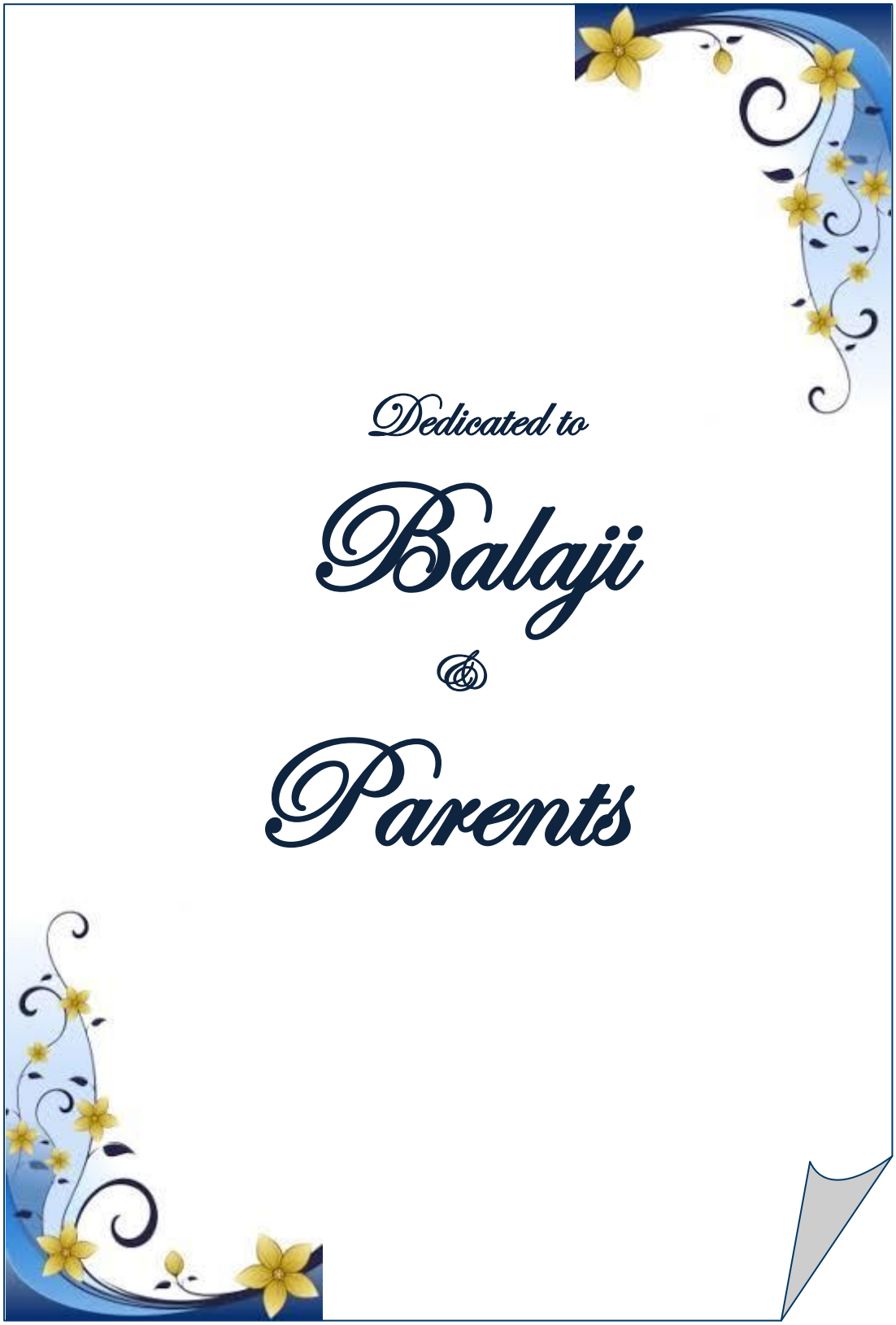
Dedicated to
Balaji
&
Parents

Date:.....

Certificate

It is to certify that,

(i) The thesis entitled **"*Synthesis of Fly Ash Supported and Non Supported Metal and Metal Oxide Nanoparticles: Characterization and Catalytic Applications"*** submitted by ***Renu Hada*** is an original piece of research work carried out by the candidate under my supervision.

(ii) Literary presentation is satisfactory and the thesis is in a suitable form for publication.

(iii) Work evidence the capacity of the candidate for critical examination and independent judgment.

(iv) Fulfills the requirement of the ordinance relating to the Ph. D. degree of the university.

(v) Candidate has put in at least 200 days of attendance every year.

Dr. Vijay Devra
Lecturer,
J.D.B. Girls P.G. College, Kota

Prof. Ashu Rani
Head,
Department of Pure and Applied Chemistry,
University of Kota, Kota

A WORD OF GRATITUDE

It is a great pleasure to convey my deep gratitude to ***Prof. Ashu Rani****, Head, Department of Pure and Applied Chemistry, University of Kota, Kota for providing me unflinching encouragement, advice, guidance and support in various ways. I am very much impressed with her devotion, dedication, sincerity, and modesty. Her generous help, indispensable co-operation, constructive criticism and intellectual guidance made this work possible. She has been not only on inspiring mentor but also gained my respect for her affectionate and kind behaviour. I am sincerely grateful to god for giving me an opportunity to work with such an excellent mentor. I am indebted to her more than she knows.*

Renu Hada

ACKNOWLEDGEMENTS

This thesis is the end of my journey in obtaining my Ph.D. The work presented in this thesis could not have been accomplished without the help of several individuals including my well wishers, my friends and colleagues. At the end of my thesis, it is a pleasant task to express my thanks to all those who contributed in many ways to the success of this study and made it an unforgettable experience for me.

*First and foremost I would like to bow down my head in front of "**Parmeshwer**" continuous source of inspiration, most beneficent and merciful for making this task reaches its completion.*

*I am extremely indebted to my Research Supervisors, **Dr. Vijay Devra**, J.B.D. Govt. Girls College, Kota, and **Prof. Ashu Rani**, University of Kota, Kota, for giving me an opportunity to do research in the field of nanotechnology and waste management under their supervision and strong leadership. I am also extremely grateful to them for their never ending enthusiasm, continuous flow of suggestions, excellent time management and constant encouragement throughout the course of this investigation.*

*I express my sincere thanks to **Dr. S.S. Amritphale**, Chief Scientist, Analytical Chemistry Discipline, AMPRI, CSIR, Bhopal for his fruitful suggestions and constant encouragement throughout my research work.*

*I am grateful to **Sh. Onkar Singh**, Vice Chancellor and **Prof. Madhusudan Sharma**, earlier Vice Chancellor, Univ. of Kota, **Prof. H. S. Meena,** Principal, JDB Girls College, Kota, for providing necessary facilities.*

*I would like to thank to **Dr. Uma Sharma** and **Dr. Naveen Mittal** Department of Chemistry, JDB Girls College, Kota, **Dr. Arun Kumar**, Department of Mathematics, Govt. College, Kota, faculty members of department of pure and applied chemistry, Univ. of Kota. Kota, **Dr. Niloo Chauhan, Dr. Bhawani Singh**, **Dr. Shweta Vyas**, **Dr. Sushil Sharma, Mr. Ankit Sharma**, **Dr. Shweta Saxena** and **Dr. Bhartiya Sharma** and nonteaching staff of Univ. of Kota, Kota and JDB Girls College, Kota, for immediate help and timely cooperation.*

*I wish to express my sincere thanks to **DST-FIST**, New Delhi, **UGC-DAE** Consortium for Scientific Research, Indore, **IIT Madras**, Chennai, **University of Delhi**, New Delhi, **Chandigarh University**, Chandigarh, **University of Pune**, Pune for providing instrumentation facilities for sample analysis and also to **UGC** and **Fly Ash Mission project** for fellowship and financial support..*

*I would like to thank my intimate friends **Dr. Nayma**, **Ekta**, **Dr. Mudita**, **Madhvi**, **Dr. Ruchika**, **Dr. Vishwajeet**, **Dr. Sanjay**, **Dr. Giriraj**, and **Dr. Jeeshan** whom I must thank for providing me an atmosphere of love, support and constant encouragement in the process of my research.*

*My sincere thanks are extended to my other friends, colleagues, seniors and lab mates **Dr. Deepti**, **Dr. Anita**, **Dr. Shefali**, **Mrs. Shanu, Sakshi**, **Stuti, Khushboo**, **Niharika, Priyanka**, **Hari Om**, **Rajesh**, **Shikha, Ankita, Kiran Desai** and **Beerendra** for their all time support.*

*Words won't be enough to thank my parents, **Sh. Lakhapat Singh Hada** and **Smt. Gulab Hada** for being the best teachers of my life, showing interest in my likes and dislikes from my childhood and motivating me towards this successful academic career. I am truly grateful for their endless sacrifices, unconditional support, undying love, encouragement, blessings and prayers, which made tougher times look easier and are acts that could not be thanked by mere words. I am deeply thankful to my uncle and aunti **Sh. Gajendra Singh Hada** and **Smt. Sheela Hada,** elder brother and bhabi **Mr. Shivendra Singh-Kirti Hada**, didi's and jijosa's **Damyanti-Yadunath Singh, Tarkeshwari-Pratap Singh**,and **Preeti-Yuvraj Singh**, younger sister and jawaisa **Neha-Himmat Singh** for their support, love and blessings. **Vishvendra, Rananjay, Aaradhya, Aviraj** and **Hridayaraj** for bringing happiness in our home and life.*

Renu Hada

Contents

Introduction

Abstract

This chapter includes the catalytic applications of metal nanoparticles, metal oxide nanoparticles and limitations of using non supported metal/metal oxide nanoparticles for catalytic applications. The chapter also describes different materials used as support for catalytic applications of metal/metal oxide nanoparticles as well as importance and objectives of the present research work.

Metal/metal oxides, in particular **Ag, Cu, Pd, Pt, SiO_2, TiO_2, Al_2O_3, NiO** and **Fe_2O_3** [1] at present occupy the first position in terms of economic importance within the range of inorganic nanoparticles. Although **Pd**, **Pt**, **SiO_2** and **Fe_2O_3** nanoparticles have a commercial history spanning half a century or more [1], Major application fields of metal/metal oxide nanoparticles are electronics, pharmacy/medicine, cosmetics as well as chemistry and catalysis. In the field of catalysis the biggest market volume can be assigned to porous catalysts support for car exhaust catalysts. Nanoporous **Al_2O_3**, **SiO_2** and carbon serve as supporting material for metal/metal oxide catalysts, which finely dispersed on to the substrate. Nowadays nanoparticles also find increasing applications as catalysts in polymer electrolyte membrane (PEM) fuel cells and hydrogen reformers. Due to size effects as well as structure/function relationships, metal/metal oxide nanoparticles account for such excellent catalytic activity in so many reactions that the nanoparticle catalysts gained tremendous attention of various research groups [2,3].

Nanoparticles can also be used as catalysts in homogeneous systems or alternatively they can be loaded onto a heterogeneous support such as **SiO_2**, **Al_2O_3**, other oxides, activated **C** and fly ash etc. [4] Metal/metal oxide nanoparticles have a higher surface area with increased catalytic activity due to availability of more reactive sites. These catalysts play two different roles in catalytic processes: (i) they can be the site of catalysis or (ii) they can act as a support for catalytic processes [5]. Such nanoparticles are typically used under mild conditions to prevent decomposition of the nanoparticles at extreme conditions [6] during use in catalytic reactions.

A brief review on non supported and supported metal/metal oxide nanoparticles have been presented in this chapter. Some important support materials widely applied for synthesis of different catalysts are described in brief in the chapter to shed some light on the need and importance of using supported metal/metal oxide nanoparticles for catalysis.

1.1 Metal Nanoparticles as Catalyst

Metal nanoparticle catalysts are selective, efficient, and recyclable can now be applied to a lot of reactions i.e. hydrogenation, oxidation, coupling and hydrosilation etc. in both homo and heterogeneous systems [7–13]. Mainly according to the catalytic behavior, the frequently encountered metals in catalysis are devided into six categories which are described as follows.

1.1.1 Ti, Zr, Nb, Mn, V, Cr, Mo and W as Nanocatalyst

These are cost effective catalysts exhibit weak hydrogenation ability and sometimes can be used in hydrogenation reactions. **Ti, Zr, Nb** and **Mn** nanoparticles have been prepared in THF by $K[BEt_3H]$ reduction from metal halide precursors [14]. Colloidal **Ti** nanoparticles are very efficient catalysts for the hydrogenation of **Ti** and **Zr** sponges, **Ni** hydride battery alloy [15] as well as for catalyzing McMurry coupling reaction of various aromatic compounds viz. benzophenone, benzaldehyde and acetophenone. (**Figure 1.1**) [16]. Compared to the metallic state, the oxides of these early transition metals are generally paid more attention as they can effectively catalyze many useful reactions in traditional heterogeneous catalysis [17].

Figure 1. 1 TEM photograph of nano Ti at 38 K [18]**.**

1.1.2 Fe, Co and Ni as Nanocatalyst

Fe, Co and **Ni** are abundant and cost effective elements, and are widely used in oxidation reactions in industry. The catalysts are currently applied in reactions including hydrogenation, hydrosilation, oxidation and C–C coupling reactions. **Ni** nanoparticles have been synthesized via in situ reduction using silane [19], solvothermal reduction [20] decomposition in ionic liquids (IL) [21], and electrochemical method [22] etc. which exhibit excellent activity and selectivity for hydrogenation of nitrobenzene and cyclohexene [20,21], hydrosililation, [3+2] cycloaddition reaction between methylenecyclopropane and methyl acrylate [22] and oxidation etc. **Fe** nanoparticles (**Figure 1.2**) are active catalysts in the hydrogenolysis of naphthyl bibenzyl methane [23] and F–T reactions in glycerol etc [24]. **Fe** nanoparticles prepared by reverse microemulsion can catalyze the oxidation of cyclooctane with acceptable activity under mild conditions in quasi-homogenous mode [25].

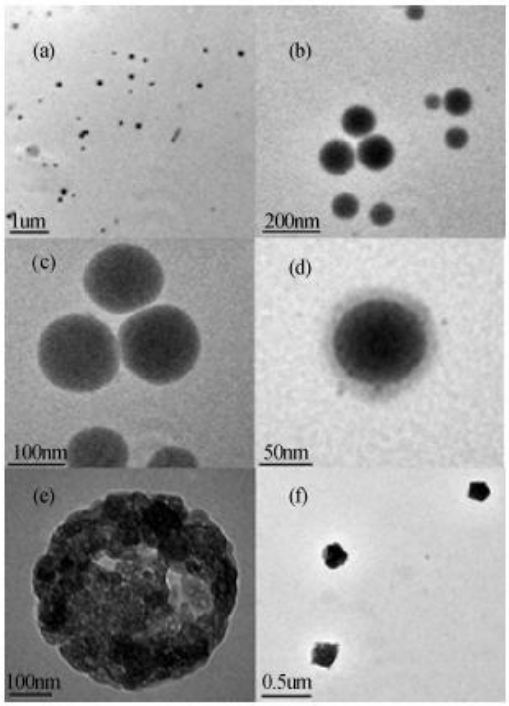

Figure 1. 2 TEM images of Fe ultrafine particles (a), (b), (c), (d) Fe particles before demulsification; (e), (f) Fe nanoparticles after demulsification [26]**.**

Co nanoparticles have been examined for their catalytic property in the selective hydrogenation of α,β-unsaturated aldehydes [27], Fischer–Tropsch (F–T) reaction in IL and squalane [28], oxidation of cyclohexane [29] etc.

1.1.3 Cu, Ag and Au as Nanocatalyst

These noble metals are usually used for redox reactions. Nanoparticles of **Cu, Ag** and **Au** have been synthesized by reduction using various reducing agents viz. trialkylaluminum [30], $NaBH_4$ [31], H_2 [32] and amino acids in plant extracts (glycine max) [33] etc. **Cu** nanoparticles are remarkably active catalysts in homogeneous [34] and quasi-homogeneous phase [30] for methanol synthesis, they can catalyze synthesis of methyl formate (MF) without presence of any base. Whereas at industrial scale, synthesis of MF is catalyzed by a strong base such as CH_3ONa which is highly efficient but obviously not green [31]. **Ag** nanoparticles are mainly used in oxidation/dehydrogenation reactions. **Ag** catalyzed epoxidation reaction is well known and widely applied in ethylene oxide production. Soluble **Ag** nanoparticles in ethanol/water mixture are superior catalysts relative to a conventional heterogeneous **Ag** catalyst [35]. **Au** and **Ag** nanoparticles (**Figure 1.3 a** and **b**) can also effectively catalyzed decomposition of $NaBH_4$, a potential H

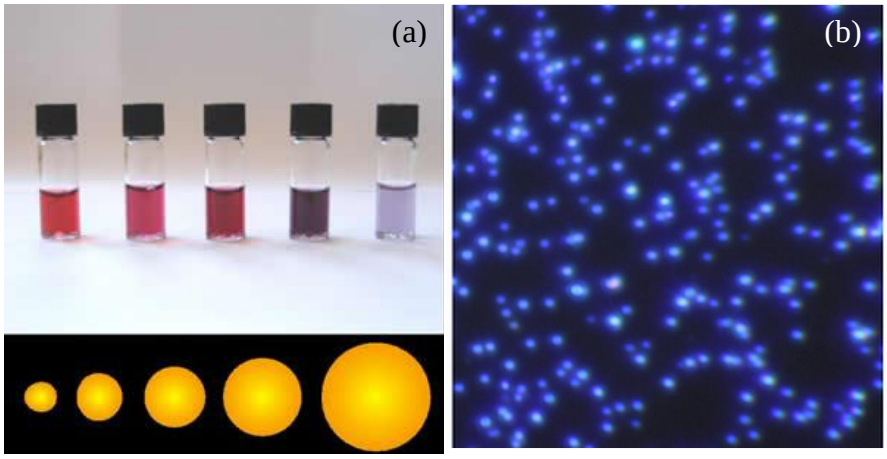

Figure 1. 3 **a) Diameter of Au nanoparticles determines the wavelengths of light absorbed. The colors in this diagram illustrate this effect** [36]**, b) Dark field microscopy image of 60 nm Ag nanoparticles** [37]**.**

(hydrogen) storage material, into H_2 and $NaBO_2$ [38,39]. **Au** nanoparticles are found to be highly active catalysts for the hydrogenation of substituted aldehydes, giving high conversions and chemoselectivities for a wide variety of substrates. **Au** is usually viewed as an inert metal, but surprisingly it has been found that **Au** nanoparticles less than 3–5 nm in diameter are catalytically active for several chemical reactions [40], specially oxidation reactions. Current applications of **Au** nanoparticles include oxidation of carbon monoxide into carbon dioxide and glucose into gluconic acid [41].

1.1.4 Ru, Rh, Pt and Ir as Nanocatalyst

These metals are typical catalysts with excellent hydrogenation ability. For the hydrogenation of C-C bonds, the activity of their metal nanoparticles usually follows the trend of **Rh>Ru>Pt>Ir**. This trend is similar to that observed in traditional heterogeneous catalysis. The hydrogenation of C-C bonds using these soluble nanoparticles is comparatively easy and there are numerous studies reported earlier [42]. **Rh** and **Ru** are the most active metals towards benzene hydrogenation. [43], [44]. While **Ir**, **Pt** and **Ru** exhibit excellent activity for hydrogenation of C-O bonds,. **Ir** nanoparticles have been used for the hydrogenation of acetones [45], **Pt** is more active and **Ru** generally exhibits better selectivity. It has been found that for the reduction of cinnamaldehyde, the addition of some metal ions such as $\mathbf{Fe^{3+}}$, $\mathbf{Co^{2+}}$ and $\mathbf{Ni^{2+}}$ can greatly enhance the selectivity of the aimed unsaturated alcohol product, which may be due to the induction effect of these ions that can activate C-O bonds [46]. **Ru** nanoparticle can catalyze the hydrogenation of glucose to sorbitol, direct hydrogenolysis of cellubiose into polyols [47]. Furthermore, it has been found that unsupported **Ru** nanoparticle catalyst is more active than conventional catalysts for Fischer–Tropsch synthesis in water [48]. **Ru** nanoparticle can also be utilized in oxidation reactions and under water/cyclooctene biphasic conditions, cyclohexane can be converted into cyclooctanone and cyclooctanol under mild conditions [49]. **Ru** and **Pt** nanoparticles are very active for NO reduction similar to CO reduction [50,51]. **Pt** nanoparticles (**Figure 1.4**) are efficient catalyst for hydrosilylation reaction [52]. Soluble **Pt** nanoparticle has been displayed good performance in the oxidation of both activated and non-activated alcohols including a wide range of

aromatic alcohols, allylic alcohols, alicyclic alcohols, and primary and secondary aliphatic alcohols in water under aerobic conditions without using any bases [53].

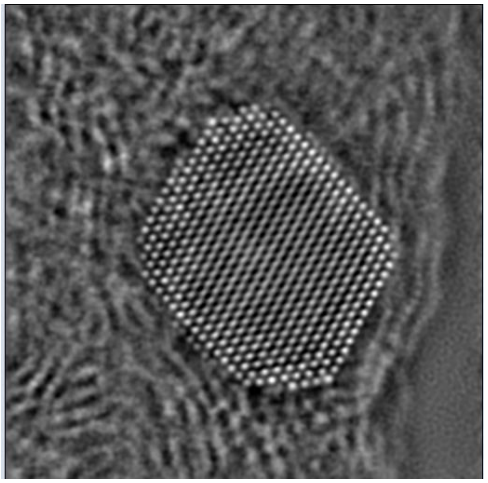

Figure 1. 4 TEM image of a 5 nm Pt nanoparticles [54]**.**

1.1.5 Pd as Nanocatalyst

Pd has shown excellent catalytic activity toward hydrogenation/ dehydrogenation reactions and for many C–C coupling reactions. The most intriguing aspect of **Pd** nanoparticles (**Figure 1.5**) in hydrogenation reactions is its unique selectivity for catalyze the hydrogenation of alkynes and diene compounds into alkenes. PVP stabilized **Pd** nanoparticle can catalyze the production of cyclopentene and cyclooctene from cyclopenta-1,3-diene and cycloocta-1,5-diene, respectively [55]. The dehydroaromatization of limonene to p-cymene under hydrogen atmosphere comprises a relatively complex series of reactions. A biphasic dehydroaromatization of limonene into p-cymene has been carried out using soluble **Pd** nanoparticle catalysts in aqueous solution in the presence of hydrogen under severe conditions (>150 °C) [56]. Tetraalkylammonium bromide protected **Pd** nanoparticles have been used to catalyze the Heck and Suzuki cross coupling reactions [57], [58]. Dendrimer protected **Pd** nanoparticle has catalyzed Suzuki reactions [59]. **Pd** nanoparticle can be used to catalyzed Stille, Sonogashira and Hiyama reactions [59]. It is interesting to note that a common

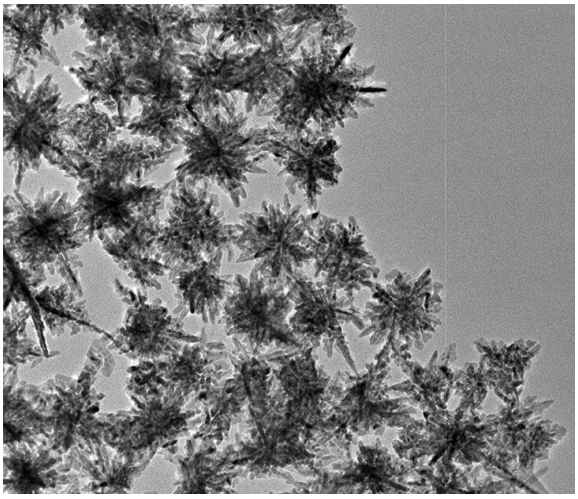

Figure 1. 5 TEM photograph of highly-branched Pd nanoparticles for hydrogenation reactions [60]**.**

drawback with these **Pd** nanoparticles is that they are only active for reactive substrates like benzyl bromide and benzyl iodide. For the more economically attractive and more challenging benzyl chloride substrate, successful examples are extremely rare.

1.1.6 Bimetals as Nanocatalyst

Bimetallic nanoparticles can be prepared using co-reduction of mixed ions, successive reduction, reduction of double complexes and electrochemical approaches etc. [61–64]. **Cu-Zn** nanoparticles are highly active in methanol synthesis whereas **Cu** nanoparticles alone are completely inactive [34]. **Pd-Ag** have been used for the tandem reductive amination between nitroarenes and aldehydes (selectivity > 93%). [65]. Bimetallic **Pt-Au** nanocatalysts have been prepared by block copolymer template, offer superior activity for the oxidation of methanol and can operate with increased electrocatalytic stability and resistance to poisoning than conventionally used single metal **Pt**. The activity of **Pt**-rich core–shell **Pt-Au** nanocatalysts for the electrocatalytic oxidation of methanol was approximately 2-4-fold that of a current **Pt** benchmark catalyst, only 28% less

than that of the **Pt-Ru** bimetallic benchmark catalyst, and show more tolerance to carbonaceous poisoning than **Pt** based catalyst [66].

1.2 Metal Oxide Nanoparticles as Catalyst

Metal oxides are used in a wide variety of technologically important catalytic processes. For example, they are used in selective oxidation, selective reduction and dehydrogenation. A brief review on metal oxide nanocatalyst is given as follows.

1.2.1 Nano Al_2O_3

Nano-**Al_2O_3** with small size, large surface area shows high catalytic activity and widely used as industrial catalyst for petroleum refining, petrochemical and automotive exhaust purification (**Figure 1.6**). Nano-sized porous **γ-Al_2O_3** has been successfully synthesized via precipitation method under ultrasonic vibration mixing for dehydration of methanol to dimethyl ether (DME) [67].

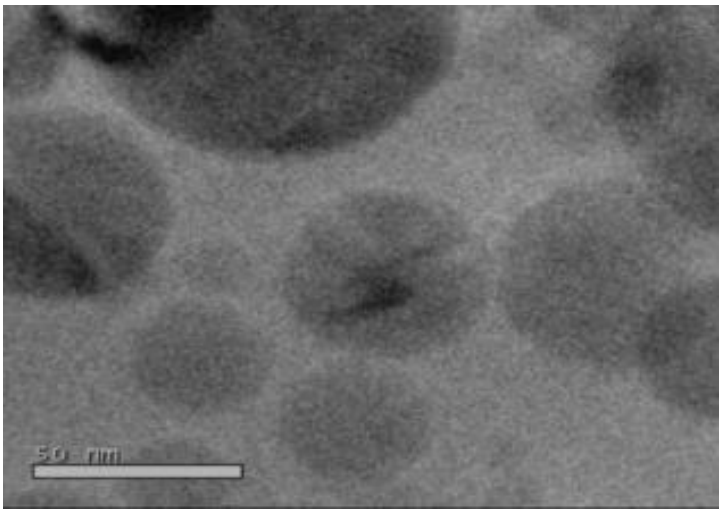

Figure 1. 6 TEM images of spherical nano Al_2O_3 [68]**.**

Mesoporous **Al_2O_3** has been synthesized with triblock copolymers for carbon disulfide hydrolysis with both weak acid sites as well as weak-medium

basic sites on its surface, which exhibited much higher catalytic activity than conventional bulk **γ-Al_2O_3** [69].

Novel nanostructured **Al_2O_3** is currently used as an active phase in the field of catalysis directly coated with other materials [68]. Carbon covered reusable **Al_2O_3** is used as catalyst after electrochemical deposition of **Ag** [70].

1.2.2 Nano MgO and CaO

The catalysts of **CaO** and **MgO** nanoparticles have been demonstrated on a variety of organic reactions like isomerization of alkenes, hydrogenation of alkenes, addition of amines to dienes, aldol condensation of acetone and biodiesel production [71–73] etc. Reusable **MgO** nanoparticles have been prepared by various synthetic techniques viz. an improved sol–gel [74], microemulsion [75] microwave assisted sol-gel [76], and sonochemical [77] techniques, for catalyzing various organic reactions i.e. aza-Michael reaction for addition of amines to a series of α,β-unsaturated carbonyl compounds and nitro olefins [74], Claisen-Schmidt condensation reaction [75], synthesis of Hantzsch 1,4-dihydropyridines from the reaction of aromatic aldehydes, ethyl acetoacetate, and ammonium acetate as shown in **Figure 1.7** [76], synthesis of polyhydroquinoline derivatives from the reaction of dimedone, benzaldehyde, ethyl acetoacetate and ammonium acetate under solvent-free conditions [77] respectively.

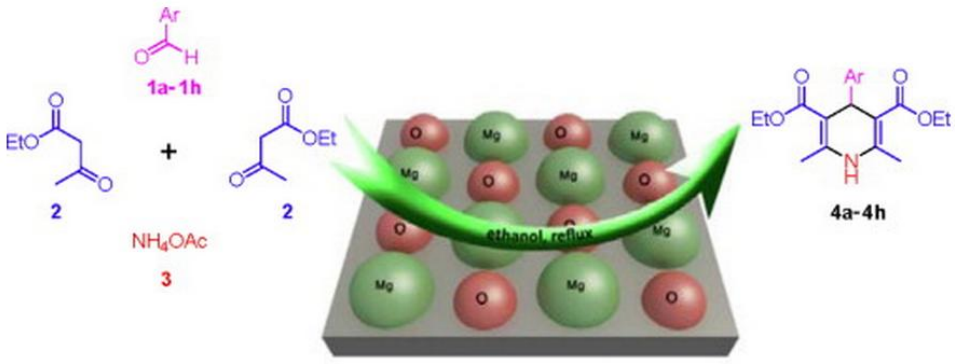

Figure 1. 7 Synthesis of Hantzsch 1,4-dihydropyridines over MgO nanoparticles [76]**.**

CaO nanoparticles have been prepared using thermal-decomposition, co-precipitation, sol-gel and microemulsion method etc [78–81]. which showed excellent catalytic activity for one-pot three-component condensation of aldehydes, thiols and malononitrile [78], decomposition reactions of 2-chloroethyl phenyl sulfide (2-CEPS) as a sulfurous pollutant [79]. **CaO** and **MgO** have also been successfully used as catalyst in transesterification reaction for production of biodiesel using vegetable oils with some advantages, like no soap generation, easer of removing from reaction media and reusability [80,81].

1.2.3 Nano ZrO_2

ZrO_2 is one of the most studied ceramic material widely used as a promising catalyst and catalyst support because of its high thermal stability, amphoteric nature, and redox properties [82]. Sulfated **ZrO_2** nanoparticles have been widely investigated as useful catalyst for various organic reactions. Sulfated **ZrO_2** nanoparticles have been prepared using different methods such as microemulsion route [83], co-precipitation [84], sol gel and hydrothermal treatment [85] etc., being used as catalyst in various reactions like isomerization of n-butane [83], esterification of acetic acid with n-butanol [84], solvent-free synthesis of xanthenediones under microwave irradiation [85], condensation of o-phenylenediamine and arylaldehydes into 2-substituted benzimidazoles [86], dehydration of fructose to 5-hydroxymethylfurfural (HMF) in DMSO [87], electrophilic substitution reaction of indole with various aldehydes and the esterification of long-chain free fatty acids [88] etc. Tetragonal **ZrO_2** nanoparticles have been synthesized by the non-hydrolytic thermal decomposition of zirconyl chloride octahydrate and sol-gel route for Knoevenagel condensation [89] and condensation of various 1,2-diamine and 1,2-dicarbonyl compounds for the synthesis of heterocyclic compounds respectively [90].

1.2.4 Nano TiO_2

Nano **TiO_2** is widely used as photocatalyst for purification of waste water in advanced oxidation process in which nano **TiO_2** generates hydroxyl radicals photocatalytically, these radical are highly reactive and attacks on organic impurities [91] as shown in **Figure 1.8**. A series of activated **TiO_2** (**Figure 1.9**)

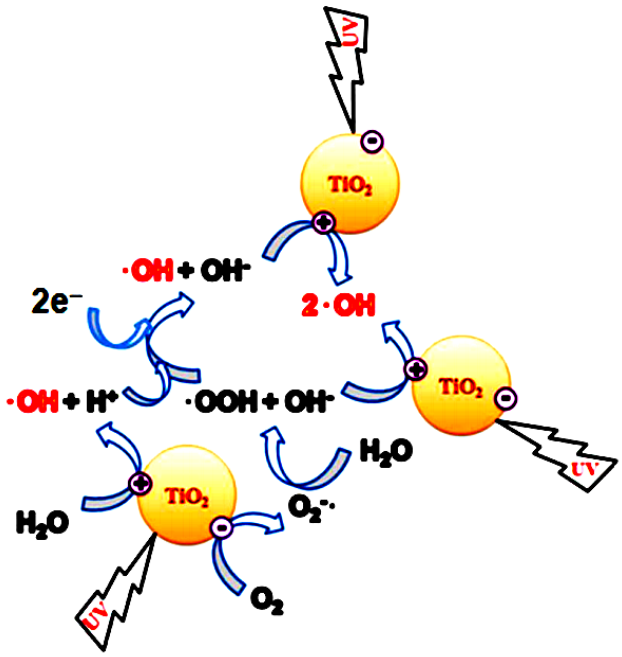

Figure 1. 8 **Photocatalytic generation of hydroxyl radicals on TiO_2 nanoparticles** [91]**.**

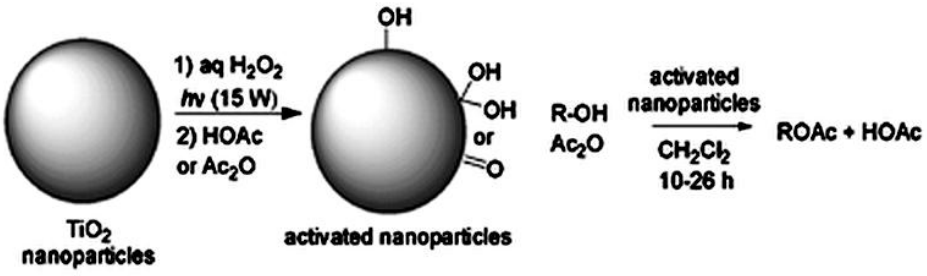

Figure 1. 9 **Oxidative, photo-activated TiO_2 nanoparticles in the catalytic acetylation of primary alcohols** [92]**.**

particles bearing surface peroxo **TiO_2** species have been synthesized by treating **TiO_2** of varying particle sizes from nano to micro scales with three different oxidants (O_2, TBHP and aqueous H_2O_2) under irradiation conditions. The resultant, heterogeneous catalysts have been tested for photo-catalytic acetylation of 2-phenylethanol by acetic anhydride in 8 different solvents. The best scenario involves the use of 32 nm grade of **TiO_2** nanoparticles and aqueous H_2O_2 for pre-activation and the use of CH_2Cl_2 as the reaction solvent.The 2-phenethyl acetate product can be completely formed in 10 h and isolated in essential quantitative yield. It was also found that catalysts derived from **TiO_2** nanoparticles are superior to those from **ZrO_2**, **Y_2O_3** and **WO_3** nanoparticles by using the oxidative, photo-activation protocol [92]. **TiO_2** nanoparticles have been synthesized via sol-gel [93], microemulsion and hydrothermal [94] methods etc., and widely used for synthesis of 2,3-disubstituted dihydroquinazolin-4(1H)-one [95], photocatalytic degradation of chlorophenols namely, 2-chlorophenol (2-CP), 2,4-dichlorophenol (2,4-DCP) and 2,4,6-trichlorophenol (2,4,6T-CP) [93], degradation of Congo Red dye in aqueous solutions under visible irradiation [94].

1.2.5 Nano SiO_2

Successful use of silica gel has been reported as a solid reaction medium for three synthetically useful organic transformations aromatic nitration, Wittig-type olefination, and Morita-Baylis-Hillman reaction, in which no organic solvents are required [96–98]. **SiO_2** nanoparticles has also been used as a high efficient catalyst for various reaction like one-pot synthesis of 3-oxo-3-phenylpropanamid derivatives from isocyanides, phenyl acetaldehyde and secondary amines at room temperature [99], in the bis-Michael addition of active methylene compounds to conjugated alkenes at room temperature [100]. Heterogeneous lewis base mesoporous **SiO_2** nanoparticles catalyst with an immobilized 4-dimethylaminopyridine functionality (DMAP-MSN) have been synthesized for catalyzing several nucleophilic reactions, such as acylation, silylation, and Baylis-Hillman reactions [101]. Sulfonic acid-functionalized mesoporous **SiO_2** nanoparticles (SAMSNs) have been used for green synthesis of dicoumarols by reaction of different aldehydes with 4-hydroxycoumarin in aqueous media [102]. Ligand linked **SiO_2** nanoparticles have been synthesized by reaction of a

synthesized hydroxy functionalized phosphine $Cy_2P(CH_2)_{10}OH$ with Cl_2**Ru**$(PPh_3)_2$([double bond, length as m-dash]CH–Ph) for ring-opening metathesis polymerization [103].

1.2.6 Nano CuO

CuO is widely used in the field of catalysis, superconductors, ceramics as a kind of important inorganic materials. **CuO** nanoparticles have been synthesized using chemical deposition [104], hydrolysis [105], sol-gel, microemulsion route and using microwave [106] etc. **CuO** nanoparticles have shown excellent catalytic activity in oxidation of cyclohexene to 2-cyclohexene-1-one by *t*-butyl hydrogen peroxide (TBHP) in acetonitrile [107], photocatalytic degradation of Rhodamine-B [108] (**Figure 1.10**), oxidative degradation of Rhodamine-B in presence of H_2O_2 [109], thermal decomposition of ammonium perchlorate [110], electrocatalytic oxidation of acetylcholine (ACh) [111], decomposition of ammonium perchlorate [104], ligand free C-S cross-coupling reactions of malononitrile-CS_2 adduct with various aryl halides [105], synthesis of xanthenes in solvent free conditions [106].

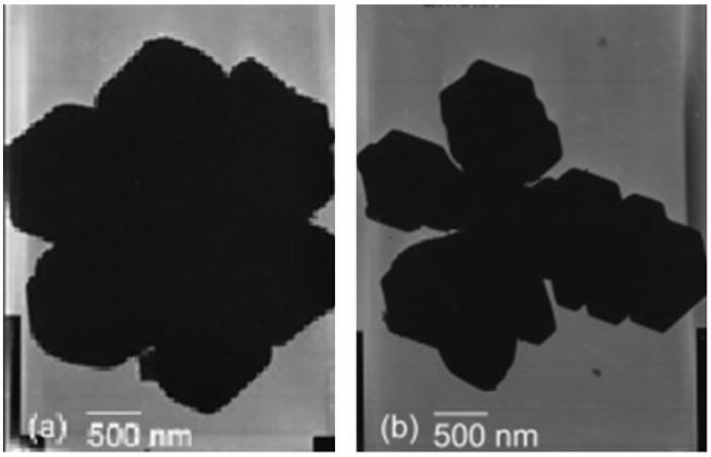

Figure 1. 10 TEM micrographs of the CuO nanoflowers prepared at 140 ◦C for 24 h [112]**.**

1.2.7 Nano ZnO

Nano **ZnO** can be synthesized into a variety of morphologies including nanowires, nanorods, tetrapods, nanobelts, nanoflowers and nanoparticles etc. [113] [114] i.e. wurtzite **ZnO** structures with special morphologies such as nanowires, dandelion-like, peanut-like, nanospheres and microspheres have been fabricated via electrospinning and calcination (**Figure 1.11**). Nano **ZnO** is used in various catalytic processes such as in pretreatment step to remove H_2S from natural gas following hydrogenation of sulfur compounds prior to a methane reformer [114], photocatalytic degradation of methylene blue [115], conversion of isobutanol into isobutene and iso-butyraldehyde [116] and in synthesis of pyranopyrazole derivatives [117] etc.

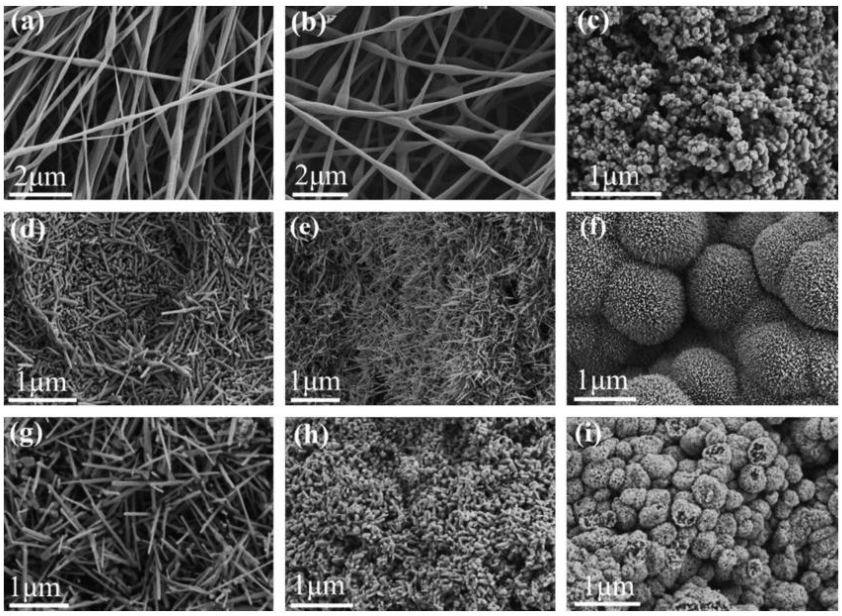

Figure 1. 11 FESEM images of ZnO nanofibres prepared by electospuning with different amount of Zn acetate used as Zn precursor from 0.2-0.8 g [115]**.**

1.2.8 Nano NiO, MoO_3 and CoO

Nano-sized **NiO** is a good catalyst in the process of decomposition, synthesis, transformation of organics such as gasoline hydrogenation cracking,

hydrocarbon conversion and heavy oil hydrogenation. **NiO** has been used as catalyst to remove CH_4, N_2, cyanide, organic dyes, helping to dissolve NO_X [118], for the synthesis of novel spiro and condensed indole derivatives by Knoevenagel condensation followed by Michael addition [119]. Ultrasmall, crystalline, and dispersible **NiO** nanoparticles have been prepared for electrochemical water oxidation using a solvothermal reaction in tert-butanol providing great potential for the preparation of novel composite materials applicable in the field of photo electrochemical water splitting [120].

MoO_3 Nanoparticles have been synthesized via thermal, microwave, precipitation and sonochemical method etc. (**Figure 1.12**) and used as an efficient catalyst for various organic transformations such as aromatization of 1,4-dihydropyridines [121], benzylation of various arenes [122] and ozonation to degrade azo dye in aqueous environment [123] etc.

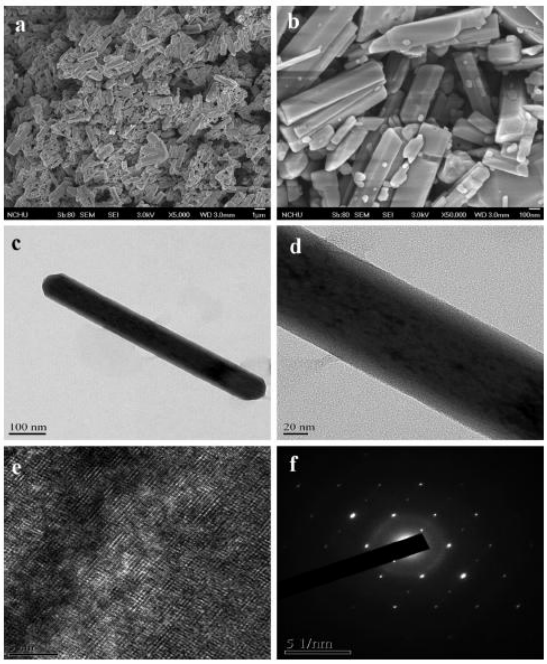

Figure 1. 12 (a) and (b) SEM images, (c) and (d) TEM images, (e) HR-TEM image, and (f) SAED patterns of the MoO_3 nanoparticles synthesized in sonochemical method [123]**.**

CoO nanoparticles are widely used to catalyze various reactions such as for water oxidation in artificial photosynthesis system [124], decomposition of H_2O_2 [125] electrocatalytic evolution of oxygen gas [126] and electrocatalytic detection of Nitrobenzene [127], for direct utilization of solar energy for fuel production without production of electricity [128], oxidation reaction of cyclohexane under mild conditions [129]. **CoO** nanoparticles have been prepared using different methods by reacting $\mathbf{Co(NO_3)_2}$ with oxalic acid, co-precipitating $\mathbf{Co(NO_3)_2}$ with sodium carbonate, using sodium dodecyl sulphate as organic surfactant and thermal decomposition of hydrothermally synthesized Co hydroxide (**Figure 1.13)** [124–127,129] etc.

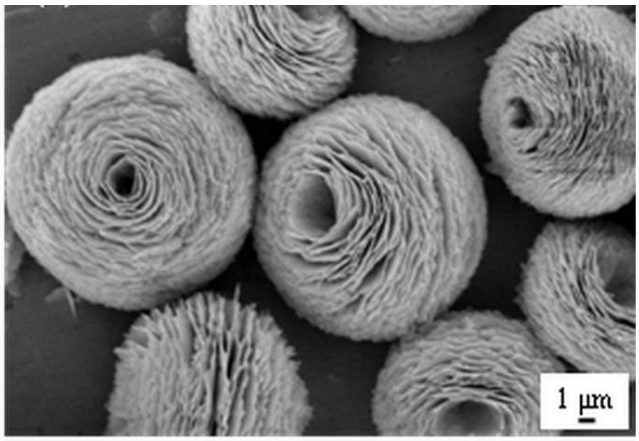

Figure 1. 13 CoO flowers (with nanosheet) obtained by thermal decomposition of hydrothermally synthesized Co hydroxide flowers in air at 400 °C [130]**.**

1.3 Limitations of using Non Supported Metal/Metal Oxide Nanoparticles for Catalytic Applications

Due to size effects as well as structure-function relationship, metal nanoparticles account for excellent catalytic activity in numerous reactions that the nanoparticle catalysts are attracting marvelous interest [131]. However, such nanoparticles having very active surface atoms, can often lead to kinetic liability with respect to inter-particle aggregation to their bulk forms, which undoubtedly

are apt to decrease catalytic activity. This problem has been approached by a variety of methods: The addition of additive stabilizers or supporting the nanoparticle on solid materials. As quasi-homogeneous catalysts, additive-stabilized nanoparticle catalysts show high catalytic activity, but their difficult separation from reaction system for reuse limits their practical applications at larger scale. Solid-supported nanoparticle catalysts allow easy recycling as they work heterogeneously and are easily separated from reaction system by simple filtration.

1.4 Different Materials used as Support for Catalytic Applications of Metal/Metal Oxide Nanoparticles

The catalyst supports can improve specific properties such as mechanical strength, distribution, stability, catalytic activity and selectivity of catalysts. An early purpose of the support was to obtain a solid granular material coated with catalytic component, providing a hard and stable structure to withstand disintegration under gas or liquid flows. Another purpose to load catalytic metal/metal oxide nanomaterials on supports is to dilute them in a larger volume to prevent agglomeration. To overcome the limitations of non-supported nanoparticles as catalyst an alternative way adopted is synthesis of supported nanomaterials. The nature of catalyst support is one of the critical parameters, which determines the catalytic activity. So far, different kinds of materials have been tested as supports, e.g., active supports, such as $\mathbf{TiO_2}$ [132], $\mathbf{Fe_2O_3}$ [133] etc. and passive (inert) supports such as $\mathbf{Mg(OH)_2}$ [134], $\mathbf{Al_2O_3}$ [135], $\mathbf{SiO_2}$ [136], mesoporous materials [137,138], activated carbon (**AC**) [139], and zeolites [140]. Some important support materials are described as follows.

1.4.1 Traditional Carbon Materials as Support

There are several allotropes of carbon of which the best known are graphite, diamond, and amorphous carbon (carbon black and activated carbon). The major catalytic use of graphitic carbon, charcoal and carbon black is to support metals. In addition, charcoals are sometimes used to support compounds such as sulfides and halides. Graphite is used to support metals, but the most

important feature of graphite is its ability to form intercalates, which are the catalysts for some hydrogenation [141], dehydrogenation [142], isomerization [141], alkylation [141], hydrodealkylation [143], polymerization [143] and ammonia formation reactions [144] etc. For charcoal and carbon black-supported metals with various industrial uses, the methods of manufacture can be divided into three broad groups based on the catalytic metal loaded: wet impregnation, hydrolysis impregnation and chemical vapor deposition (CVD) [145].

For degradation of refractory organic pollutants using catalytic wet air oxidation process **Pd** loaded activated charcoal **(AC)** has been used successfully [146]. Charcoal-supported **Rh** catalyst has been found highly active for the ring hydrogenation of phenol under supercritical carbon dioxide atmosphere [147]. **AC** supported **Cu** catalyst (**Cu/AC**) has been used for low temperature selective catalytic reduction of NO by using response surface methodology [148]. **AC** from renewable sources has been utilized as support to host $\mathbf{CoFe_2O_4}$ nanoparticles as catalyst for methanol decomposition [149]. **AC** supported **Pt–Au** bimetallic catalyst (**Pt-Au/C**) has been successfully employed to minimize the poisoning of **Pt-catalyst** in glucose electro-oxidation for direct glucose fuel cell. Electrochemical analysis such as cyclic voltammetry (CV) and chronoamperometry (CA) performed on **Pt-Au/C** and commercial **Pt/C** and **Au/C** for above mentioned reaction in alkaline media have also been reported which showed that **Pt-Au/C** is capable of electro- oxidation of glucose at low potential as that of **Pt/C** catalyst and more active than **Au/C** catalyst. The poisoning rate of prepared **Pt-Au/C** catalyst is lower than commercial catalysts [150]. **Ag/C** catalyst has been prepared by a novel solution phase-based nanocapsule method as high performance cathode catalyst for H_2/O_2 anion exchange membrane fuel cell (AEMFC). Comparison studies between AEMFCs of **Ag/C** with conventional cathode catalyst **Pt/C** was found that **Ag/C** is a competitive substitute [151].

1.4.2 Carbon Nanotubes as Support

Carbon nanotubes (**CNT**) are tubular structures prepared entirely of rolled-up layers of graphene [152]. In general, the hollow geometry of **CNT**s leads to large specific surface areas, which makes **CNT**s extremely attractive supports

for heterogeneous catalysis (**Figure 1.14**). **CNT**s are tough and tensile, owning good electron conductivity and chemical inertness, as well as thermal conductivity. Therefore, they become ideal and unique templates for nanoparticle immobilization, which allows the construction of designed nano architectures. This makes **CNT**s extremely attractive supports for heterogeneous catalysts and related technologies [153]. Although at an early stage of research, **CNT**s supported metal-nanoparticle catalysts as transition metals **Ru**, **Co**, **Ag**, **Pt**, **Pd**, and **Au** shed new light to catalysis reactions in many fields such as batteries, flat panel displays and chemical sensors [154]. In organic synthesis like Heck reaction or Fischer–Tropsch synthesis, **CNT**s supported **Pd** or **Co** catalysts are applied to improve catalytic activity or to optimize experimental conditions The preparation of magnetic **CNT**s (**Fe_3O_4-coated CNTs**) opens new avenues in nanobiotechnology and biomedical applications as a consequence of their multiple properties embedded within the same moiety [155].

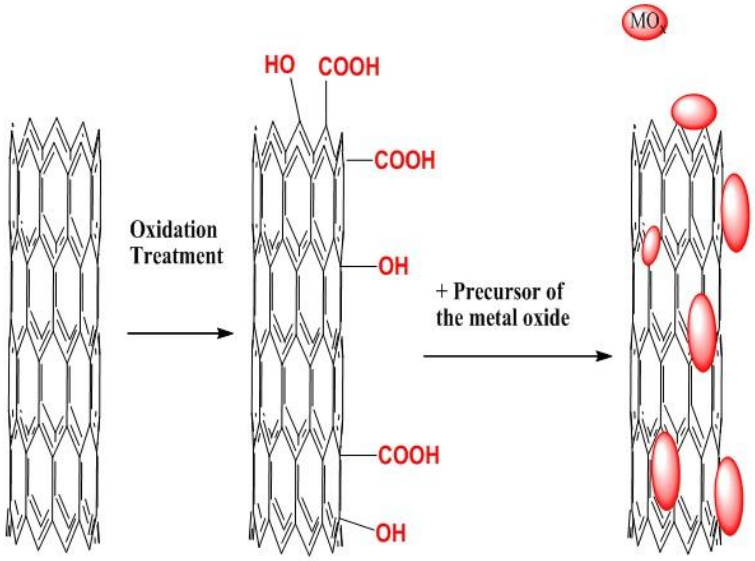

Figure 1.14 Illustration representation of the synthesis of Carbon nanotubes/metal oxide (CNT/MO) composites [156]**.**

For the selective catalytic reduction of NO_x with hydrocarbons, **CNT**s supported **Pt–Rh** catalyst displayed higher NO_x reduction activity [157]. Particularly, with hydrogen carbon-based fuel reserves rapidly running out, fuel

cell and battery with application of **CNT**s-supported metal nanoparticles catalysts have been an active area of research. **CNT**s supported **Pd** catalyst has considerable activity and selectivity for hydrogenation of CO_2 [158]. Carbon nanotubes (**CNT**s) have been widely studied for their potential applications in many fields from nanotechnology to biomedicine.

1.4.3 Al_2O_3 as Support

γ- Al_2O_3 is widely used as catalyst support because of the adjustability of its pore structure and surface acidity. **γ- Al_2O_3** can disperse and stabilize active components over its surface when used as a carrier along with it provides acid alkali active center for effective catalysis. By controlling the properties of **γ-Al_2O_3** high performance catalyst can be synthesized. **Al_2O_3** supported **Ni**-based catalysts for hydrogen production in steam reforming and auto thermal reforming reactions showed good activities and selectivity to hydrogen [159]. **Al_2O_3** supported **Au** nanoparticles has been prepared by various methods like deposition precipitation, potential deposition, without calcination etc. to catalyzed oxidation reactions [160] [161]. **Al_2O_3** supported **Ag** catalyst successfully formed from hydrogel by heat treating for the oxidation of ethylene. An effect of thermal treatment of **Al_2O_3** on catalytic activity has been studied. The catalyst surface area decreased as treating temperature increased simultaneously activity for ethylene oxidation also decreased [162]. **Al_2O_3**-supported **Ni** catalyst prepared through wet impregnation technique is found poorly active in dehydrogenation to acetaldehyde below 673 K, but behaved as a good steam reforming catalyst at this temperature. In **CO_2** methanation the best catalytic activity is obtained at 773 K on **Ni/Al_2O_3** [163]. **MoO_3/ γ-Al_2O_3** has been prepared by wet and dry impregnation of molybdate solutions onto **Al_2O_3** for hydrodesulphurization reactions [164]. **Pd/Al_2O_3** catalyst has been synthesized with pre-adsorbed hydrogen. Pt^{2+} ions in acetone are reduced onto the **Pd** metal using these hydrogen atoms [165]. For Heck and Suzuki reactions **Al_2O_3** - supported **Ru** nanoparticles has been synthesized [4]. Bimetallic **Ni–Ru** nanoparticles loaded onto **γ-Al_2O_3** has been prepared by co-impregnation and sequential impregnation methods and investigated for CO_2 methanation in the temperature range of 250–500 °C under atmospheric pressure to uncover the dependence of activities on

surface species. The activities of CO_2 methanation found very highly dependent on the preparation sequence. The possible reaction mechanism proposed, in which CO_2 dissociated and activated on **Ru** species surfaces to form carbon species, and then reacted with activated hydrogen on **Ni** centers to form methane [166]. **γ-Al_2O_3** supported **Fe_3O_4** nanoparticles have shown efficient catalytic activities as FT catalyst [167].

1.4.4 SiO_2 as Support

SiO_2 supported **Ni**, **Pd, Pt** nanoparticles are successfully employed for benzene hydrogenation and dehydrogenation [168]. **SiO_2** supported **Pd** complexes have been synthesized by immobilizing **Pd** complexes on porous **SiO_2** supports using both grafting and templated sol-gel techniques for various C-C bond forming reactions, including Heck, Suzuki and allylic substitution. The catalysts are stable and can be easily recovered and reused, making them suitable for cleaner processing [169]. A series of **SiO_2** supported transition metal-based bimetallic catalysts **M–M^1/SiO_2** (**M = Co**, **Ni**, and **Cu**; **M^1 = Ni**, **Cu**, and **Co**) has been deposited by deposition–precipitation method for selective hydrogenation of cinnamaldehyde to cinnamyl alcohol in the vapour phase at normal atmospheric pressure. Among the various catalysts investigated, the **Cu–Co/SiO_2** combination catalyst exhibited very promising results for the selective hydrogenation of cinnamaldehyde to cinnamyl alcohol, whereas **Co–Ni/SiO_2** and **Ni–Cu/SiO_2** bimetallic catalysts provided good yields of hydrocinnamaldehyde [170]. The **Cu/SiO_2** serves as an efficient heterogeneous nanocatalyst for the synthesis of a series of 1,4-disubstituted-1,2,3-triazoles and thioethers [171]. Nanometer-sized **Mn** oxide clusters supported on a mesoporous **SiO_2** scaffold have been established as efficient water oxidation catalysts in aqueous solution at room temperature and pH 5.8. The high surface area **SiO_2** support is critical for the integrity of the catalytic system by offering a perfect, stable dispersion of the nanostructured **Mn** oxide clusters. The **SiO_2** environment has protected the active Mn centers of the catalyst from deactivation by surface restructuring [172]. Mesoporous **FeO- SiO_2** composite with a high **SiO_2** content has been synthesized by hydrothermal method. **Au** catalysts have been loaded onto composite by a deposition-precipitation method for CO oxidation. The **Au** nanoparticles

dispersed on the surface of the composites existed in metallic state. The effects of deposition-precipitation pH values on **Au** loading and activity of the catalyst were investigated, and the results indicated that **Au** loading was the highest and the catalyst was the most active for CO oxidation when the synthesis pH was adjusted to 8 [173]. Stable **Au**/mesoporous $\mathbf{SiO_2}$ nanocomposites (with **Au** nanoparticles intercalated in the walls of mesoporous $\mathbf{SiO_2}$) has successfully synthesized by the hydrothermal method using bis[3-(triethoxysilyl)propyl]-tetrasulfide (TESPTS) as coordinating agent (**Figure 1.15**) and applied as catalysts for oxidation of benzyl alcohol and reduction of 4-nitrophenol [174]. Semiconducting microporous solids have been prepared by pillaring layer structured manganese titanate, $\mathbf{Rb_xMn_xTi_{2-x}O_4}$ (x=0.75) with $\mathbf{SiO_2}$. These solids were then chemically modified by loading various kinds of metals by cation exchange and impregnation methods.

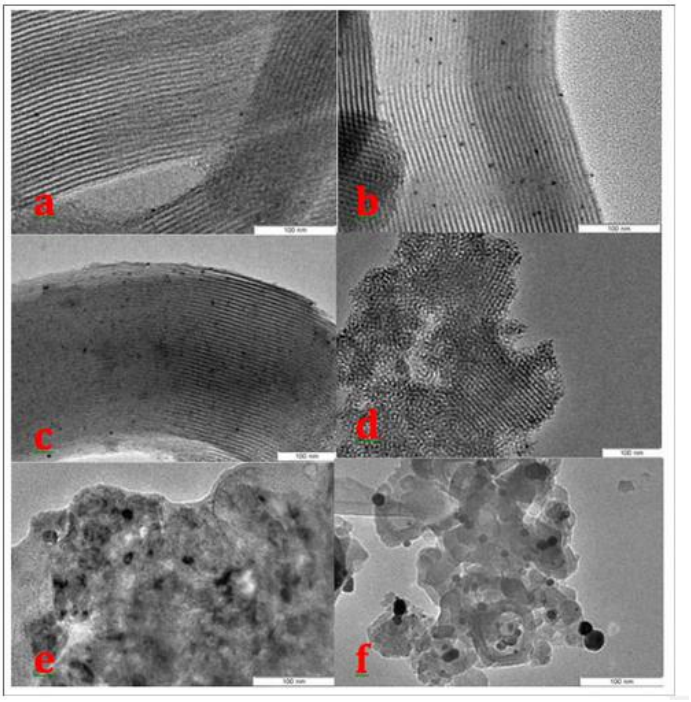

Figure 1. 15 TEM images of Au/mesoporous SiO_2 catalysts synthesized with different molar ratios of TESPTS/polymer template [174]**.**

The samples with **Cu** loaded by the impregnation method showed high catalytic activity for the oxidation of CO with O_2. The highest activity was

obtained for the sample with the **Cu** content, [**Cu**]/[**Cu+Mn**]≈0.3; the CO conversion of more than 90% was achieved at 60°C. The high catalytic activity is attributed to the microporous pillared structure with high porosity and the charge transfer between **Cu** and the manganese titanate layers [175]. **SiO_2** supported **TiO_2** prepared by homogeneous precipitation has been reported as efficient photocatalyst for degradation of phenol and its derivatives in UV range [176] [177]. An effect of **Ag** content on adsorption of hydrogen over **SiO_2** supported **Ru** has been studied. Adsorption of hydrogen increased over catalyst surface as **Ag** metal introduced to **Ru/SiO_2** catalyst. **SiO_2** supported sulfated **ZrO_2** synthesized by grafting sulfated **ZrO_2** on the surface of a **SiO_2** aerogel to generate relatively strong Brønsted and Lewis acid sites on the surface to catalyze n-hexane isomerization reactions [178].

1.4.5 ZrO_2 as Support

Monodispersed **ZrO_2@SiO_2** (**Figure 1.16**) core–shell nanoparticles have been prepared by sol–gel polymerization of TEOS in the presence of **ZrO_2** cores without additional capping agents for extending dispersibility of **ZrO_2** into various organic solvents with adjustable refractive indices [181].

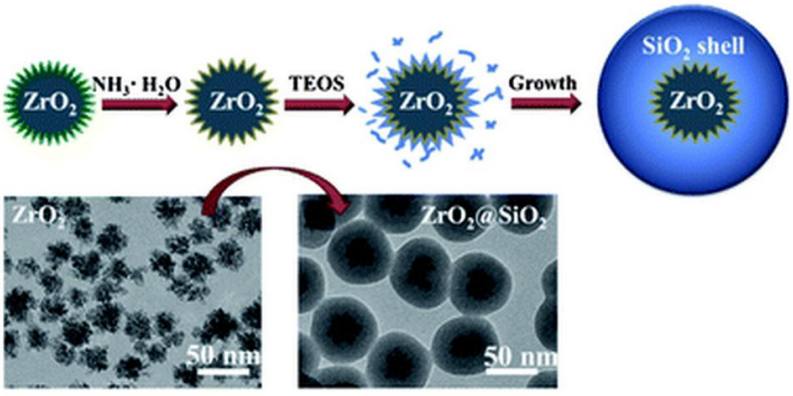

Figure 1. 16 Illustration of preparation process of monodispersed ZrO_2@SiO_2 core–shell nanoparticles (CSNs) by sol–gel polymerization of TEOS in the presence of ZrO_2 cores [181]**.**

CuO/ Ce_2O_3- ZrO_2 catalysts have been prepared, deeply characterized and tested for NO oxidation to NO_2. The behaviour has been compared to that of a

reference **Pt/ Al_2O_3** commercial catalyst. The **Ce_2O_3- ZrO_2** support has been prepared by the co-precipitation method, and different amounts of **Cu** have been loaded by incipient wetness impregnation. It has been found that a very low loading of **Cu** increases significantly the activity for the NO oxidation to NO_2 with regard to the **Ce_2O_3- ZrO_2** support [179]. **Ni** based **Ce_2O_3- ZrO_2** catalysts have been prepared successfully for hydrogen production in sulfur–iodine cycle by sol gel route [180]. Mesoporous **ZrO_2** supported **NiMo** hydrotreating catalyst with EDTA (**NiMo**/Meso-Zr(EDTA)) has been synthesized via incipient wetness impregnation method for hydrotreating of heavy gas oil. Results showed almost comparable activity of **NiMo**/Meso-Zr(EDTA) catalyst with that of **NiMo/γ-Al_2O_3** catalyst indicates that **NiMo**/Meso-Zr(EDTA) has a potential for hydrotreating of heavy gas oil [137]. **Zr** rich **Ce_2O_3- ZrO_2 (CZ)** produced by the co-precipitation is used as support for preparing **Pt** loaded active catalyst (**Pt/CZ**) for improved results of CO oxidation. The property of oxygen release and storage of **Pt/CZ** catalysts were studied which is enhanced by a small amount of **Pt** [182]. A comparative study for catalytic gas-phase dehydration of glycerol to form acrolein (ACL) over dispersed **WO_3** on different supports viz. **Al_2O_3**, **ZrO_2** and **SiO_2** has been carried out and uncovered the effects of **WO_3** dispersion and supporting materials on the catalyst performance. Catalyst offered the highest ACL selectivity (69–72 mol%) on **Al_2O_3** and **ZrO_2** supports [183,184]. The coated **SiO_2** shell, which can be well dispersed in solvents such as methanol and ethanol, can improve the dispersibility of pure **ZrO_2** nanoparticles which can only be dispersed in water. Moreover, the formation of the **SiO_2** shell improved the chemical reactivity of pure **ZrO_2** nanoparticles. After modifying with methyltriethoxysilane (MTES), the CSNs can be well dispersed in various organic solvents, such as dimethylbenzene, chloroform and isoamyl alcohol, which may find applications in optically transparent resins with controllable refractive index or organic silicon packaging materials with high refractive index for LED and so on [181].

1.4.6 Fe_2O_3 as Support

Fe_2O_3 nanodisk supported **Au** nanoparticles has been prepared using the polyvinyl alcohol-protected reduction method for the removal of toluene [185].

The apparent activation energies (46-50 kJ/mol) obtained over the **xAu/ Fe_2O_3** nanodisk smaller than that (65 kJ/mol) obtained over the **Fe_2O_3** nanodisk for toluene oxidation. High oxygen adspecies concentration, good low-temperature reducibility, and strong interaction between **Au** nanoparticles and **Fe_2O_3** nanodisk are responsible for the high catalytic performance of the **Au/ Fe_2O_3** nanodisk [185]. For oxidative esterification of aldehydes and reduction of aromatic nitro compounds an efficient and sustainable protocol has been developed using magnetically separable and reusable maghemite-supported **Au** nanocatalyst (nanocat-**Fe–Au, Figure 1.17**) under mild conditions. The hybrid catalytic system containing 4 wt% of nano **Au** has been generated using simple impregnation methods in aqueous medium from readily available starting materials and was recycled five times without any significant loss in catalytic activity; high yields, 40–95% and 83–94% for oxidative esterification and reduction reactions, respectively, were obtained [186].

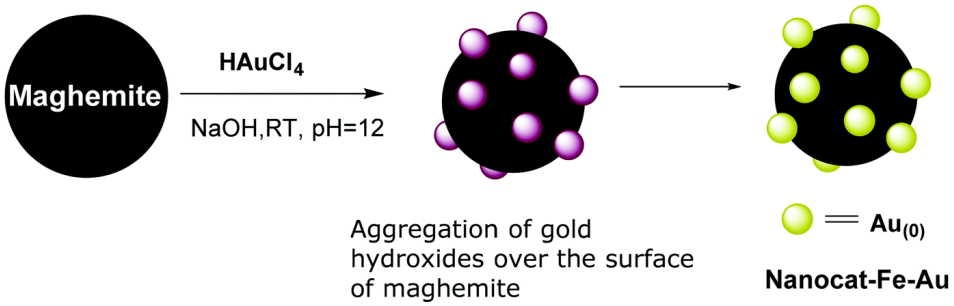

Figure 1. 17 Synthesis of Au loaded Fe_2O_3 nanocatalyst [186]**.**

$NiSO_4$ / Fe_2O_3 catalysts has been found suitable at 500 ˚C for production of 1-butene and 2-butene and with only 20 wt % loading of **$NiSO_4$** [187]. Bimetallic composite nanoparticles of **PtM (M = Au, Cu or Ni)** supported on **Fe_2O_3** has been lucratively synthesized by a radiolytic method employing a 4.8-MeV electron beam to reduce aqueous ions for CO oxidation reaction [188]. All the **Pt-M** systems exhibited activities higher than those of monolithic **Pt** on **Fe_2O_3**. The correlation between the atomic structures and the catalytic activities indicated that

the random alloy structure enhances the catalytic activity. **γ-Fe_2O_3**-supported **Pt-Cu** nanoparticles have also been synthesized by radiolytic process for catalytic CO preferential oxidation. The prepared sample exhibited highest activity with 10 atomic % **Pt** and 90 atomic % **Cu** at 100 °C, which is preferable for low temperature fuel cell applications [133]. **Ag/α-Fe_2O_3** hybrid composites have been fabricated through a self-catalytic growth method by using the aldehyde-modified spindle **α-Fe_2O_3** nanoparticles as supports for enhanced photocatalytic reactions. The size of supported **Ag** nanoparticles can be directly controlled on the surface of **α-Fe_2O_3**. [189].

1.4.7 Zeolites as Support

Different types of zeolites are also used as supports for nanoparticle catalysts. Some of the advantages of zeolites are related to its porous and crystalline structure, which causes its high surface area, high cation exchange capacity as well as the regular nanosized cages and cavities which can act as confinement spaces to stabilize the metal/metal oxide nanoparticles [190]. In this concern so far, several zeolite based nano catalysts have been reported for NO reduction and CO oxidation reactions [191]. In a research, a modified method for preparation of **Au** nanoparticle on Y-type zeolite has been developed. The resulted catalyst possessed higher activity and stability toward CO oxidation reaction in comparison to those catalysts without any surface pretreatment [140], [192]. Zeolite supported active **Ru** catalyst has been prepared and characterized for ammonia synthesis process by controlled thermal activation of **Ru** precursor (**$Ru(NH_3)_6Cl_3$**) under hydrogen environment [193]. Bifunctional catalysts consisting of **Co** and **Ni** supported on HY zeolite has been fabricated by solvent excess impregnation for hydroconversion of n- hexane with selectivity to branched hydrocarbons. Such catalytic activity are related to the acid and metallic properties of the bifunctional catalysts [194]. Catalytic activities of a **Pd** catalyst supported on mesoporous Beta zeolite (Beta-H) has been studied for hydrogenation of naphthalene and pyrene in the absence and presence of 200-ppm sulfur and for the hydrodesulfurization (HDS) of 4,6-dimethyldibenzothiophene (4,6-DMDBT). the catalyst exhibited better sulfur tolerance for hydrogenation of naphthalene and pyrene and higher activity for HDS of 4,6-DMDBT in

comparison with **Pd/Al-MCM-41** [195]. High-performance hydrodesulfurization (HDS) catalysts have been prepared by supporting **Ni-Mo sulfides** on a mixture of mesoporous MCM-41 and microporous HY zeolite. The mixed support were obtained either by physically mixing [**MCM-41-HY(M)**] or by overgrowing **MCM-41** over **HY** zeolite particles [**MCM-41- HY(C)**]. A synergetic effect of the components in the mixed supports on the supported **Ni-Mo** sulfides were observed. **Ni-Mo**/MCM-41-HY(M) exhibited both high HDS activity and hydrocracking activity, whereas **Ni-Mo**/MCM-41-HY(C) showed a comparable HDS activity but a much lower hydrocracking activity [196]. Four **W–Ni** catalysts, containing **Al_2O_3**, chemically treated zeolite Y, hydrothermally treated zeolite beta and the combination of the above zeolite Y and beta were prepared and characterized for hydrodesulfurization (HDS), hydrodenitrogenation (HDN), and hydrodearomatation (HDA) with light cycle oil (LCO) [197]. The zeolite-containing catalysts exhibited much higher HDN, HDS, and HDA activities than the **W-Ni/Al_2O_3**. The three zeolite-containing catalysts had similar HDN activity. The **W-Ni/Beta+Y** and **W-Ni/Beta** catalysts had higher HDS activity than the **W-Ni/Y** catalyst. The higher HDN, HDS, and HDA activities of the three zeolite-containing catalysts are associated primarily with enhanced hydrogenation activity and increased acidity [197]. Dealuminated Y zeolite supported **Pd-Ir** catalysts with different proportions between the metals have been synthesized to evaluate tetralin hydrogenation. For the same proportion between the metals and the same zeolite support, **Pd-Pt** and **Pd-Ir** catalysts were showed similar activities [198].

1.4.8 Mixed Metal Oxides of SiO_2 and Al_2O_3 as Support

Mesoporous **SiO_2** and **Al_2O_3 (MSA)** supported sulfided **Pt** and **Pt–Mo** catalyst has been applied for simultaneous hydrodesulfurization (HDS) of thiophene and hydrodenitrogenation (HDN) of pyridine [138]. The results showed strong positive effect of **Pt** on activity of the promoted catalysts [138]. **Al_2O_3** and **Al_2O_3/SiO_2** coated **TiO_2** nanoparticles have been synthesized in an aerosol flow reactor by chemical vapor deposition. Mesoporous **Co–SiO_2–Al_2O_3** (**MCSA-141, Figure 1.18**) mixed oxides with variable **Co** content have been synthesized through slow evaporation method by using Pluronic F127 non-ionic surfactant as template. Samples have high BET surface areas together with large mesopores

and showed the presence of ferromagnetic correlation at elevated temperature [199]. Uniform and dense coatings of **Al_2O_3/SiO_2** was obtained at 1300 °C when the **Al_2O_3/SiO_2** weight ratio was less than 2:1. The coating took place in two modes: (a) chemical vapor deposition of **$AlCl_3$** and **$SiCl_4$** on the particle surface and (b) gas-phase reactions of the metal chlorides to form **Al_2O_3, SiO_2**, or **Al_2O_3/SiO_2** particles that subsequently collide with the **TiO_2** nanoparticles and sintered into the coating [200]. Physicochemical properties and reducibility of **SiO_2–Al_2O_3** supported **NiO** have been studied keeping all the active phases

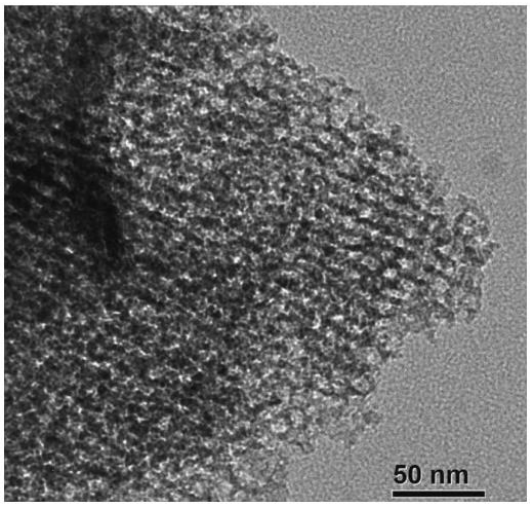

Figure 1. 18 TEM image of mesoporous Co–SiO_2–Al_2O_3 (MCSA-141) sample [199]**.**

constant in all the samples (10 wt % **NiO**) and the **SiO_2** content of the carrier varied from 100 to 15 wt %. It is found that, on **SiO_2** carrier, the active phase is present as a poorly dispersed. Increasing the **Al_2O_3** content in the support leads to an increase of the dispersion of **Ni^{2+}** species manifested by an enhancement of the XPS intensity ratio $I_{Ni}/I_{carrier}$.

1.4.9 Fly Ash as Catalytic Material

Fly ash having **SiO_2** and **Al_2O_3** more than 70% induces the reaction and helps to avoid the use of environmentally unfavorable organic solvents as reaction medium since the reaction proceeds smoothly under solvent-free conditions. A

facile synthesis of α,β-unsaturated acids, α-cyano acrylonitriles and α-cyano acrylates has been achieved with an *E*- geometry via, a stereo selective Knoevenagel reaction by employing fly ash as catalyst [201]. A great variety of amides effectively isolated from ketones in 'One-Pot' via, Beckmann rearrangement under mild conditions during the reactions lead to a clean, efficient, convenient and economical technology [202]. Schiff base, a versatile intermediate in medical and organic chemistry has been synthesized efficiently by activated fly ash. Fly ash is also used as solid catalyst support in the synthesis of 2-mercaptobenzothiazole derivatives under microwave irradiation [203]. **H_2O_2** modified **TiO_2**/fly-ash cenospheres prepared by sol gel route have been used effectively for photocatalytic degradation of methylene blue. [204]. **Ni** coated cenosphere composites have been fabricated by heterogeneous precipitation method for catalysis and electromagnetic wave shielding materials due to their light weight, low cost, ease of processing and good dispersion [205]. Nano-sized **ZnO** particles coated on fly ash have been synthesized by thermal decomposition of **Zn** acetate and Broussonetia papyrifera (L.) vent pulp [206]. Not only this fly ash has also been used for developing several solid acid catalysts for synthesis of aspirin and oil of wintergreen [207], 3,4-dimethoxyacetophenone [208] (anti-neoplastic) and diphenylmethane [209]. Highly active nano-crystalline, thermally stabilized solid acid catalyst (**Figure 1.19**) has been synthesized by loading

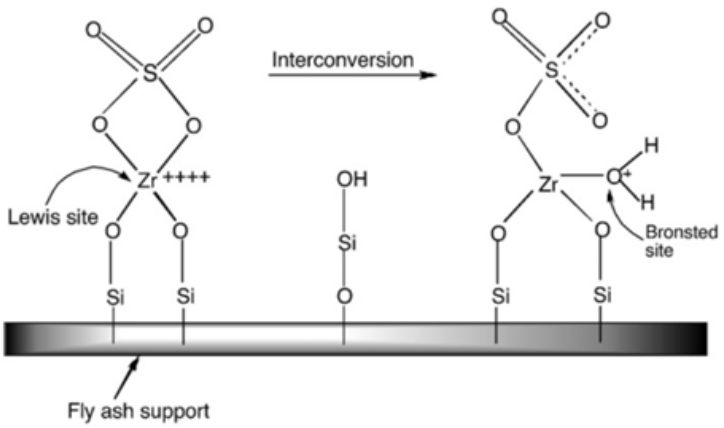

Figure 1. 19 Proposed model structure of SZF catalyst [209]**.**

different weight fractions of sulfated **ZrO_2** on chemically activated fly ash (SZF) through sol gel technique. Liquid phase benzylation of benzene and toluene with benzyl chloride are studied as test reactions for catalytic activity of SZF catalystsgiving very high conversion of benzene (87%) and toluene (93%) [209].

Highly efficient solid Lewis acid has been synthesized by loading **$Ce(OTf)_3$** (7 wt%) on the acid activated fly ash with high **SiO_2** content (81%) (**Scheme 1.20 (a)**). The increased concentration of **SiO_2** surface OH groups on activated fly ash have a major influence on the loading of **$Ce(OTf)_3$**. The catalytic activity of the catalyst tested in the acylation of veratrole using acetic anhydride as the acylating agent. The proposed model structure of catalyst shows that the triflate species withdraws the electron density from the surface cerium making it electron deficit and generate Lewis acidity on the surface of fly ash [208].

In an another report an efficient solid Lewis acid catalyst has been prepared by loading **$Sc(OTf)_3$** on activated fly ash (**Figure 1.20 (b)**). The catalyst showed higher activity for solvent free single pot Friedel–Crafts acylation of 2-methoxynaphthalene (2-MN) using acetic anhydride as an acylating agent achieving conversion up to 84% and selectivity of the desired product, 2-acetyle-6-methoxynaphthalene (6-AMN) up to 73%. 6-AMN is a precursor for anti-inflammatory drug, (S)-(+)-6-mathoxy-α-methyl-2-naphthaleneacetic acid [210].

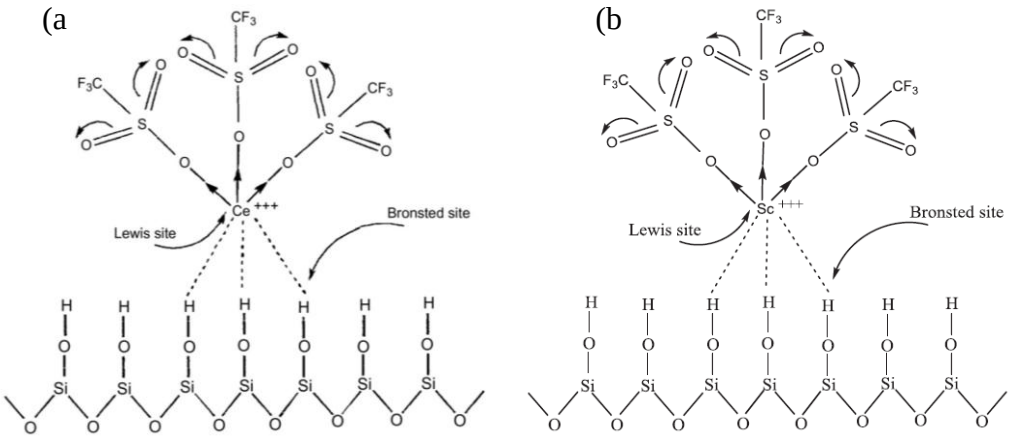

Figure 1. 20 The model of the active site in fly ash-supported (a) $Ce(OTf)_3$ catalyst [208]**, (b) $Sc(OTf)_3$ catalyst** [210]**.**

A new type of solid base catalyst has been synthesized by chemical and thermal activation of fly ash. The chemical activation carried out by 50 wt.% **NaOH** followed by thermal activation at 450 ºC. The basicity of the catalyst measured by liquid phase, solvent free, single step condensation of benzaldehyde with cyclohexanone giving higher conversion (>70%) and selectivity (>80%) of desired product α,α'-dibenzylidenecyclohexanone. [211]. **MgO** loaded fly ash with stable **Si-O-Mg** phase and sufficient hydroxyl group catalyzed liquid phase, solvent free and single step condensation of 4-methoxybenzaldehyde with 2-hydroxyacetophenone giving higher conversion (86%) of desired product (4-methoxy-2-hydroxychalcone) with 93% yield [212] (**Figure 1.21 (a)**). Similarly **CaO** loaded fly ash catalyzed Knoevenagel condensation of benzaldehyde and ethyl cyanoacetate. The catalyst gave very high conversion (87%) of benzaldehyde to desired product ethyl (E)-α- cyanocinnamate with high purity. [213]. A series of solid base catalysts synthesized by functionalization of different weight fractions (5, 10, and 15 wt.%) of 3-aminopropyltrimethoxysilane (APTMS) on fly ash (**Figure 1.22 (b)**). An appropriate amount (10 wt.%) of aminopropyl groups resulted in excellent catalytic performance tested for condensation of ethyl cyanoacetate and cyclohexanone at 120 °C to produce Ethyl (cyclohexylidene) cyanoacetate (92% yield) [214].

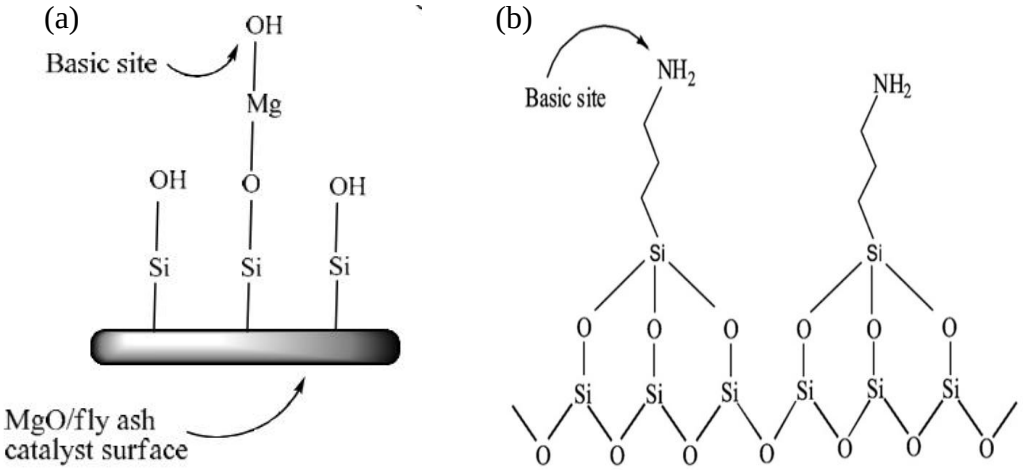

Figure 1. 21 (a) Proposed model structure of MgO/fly ash catalyst [212]**, (b) Proposed structure of NH_2FA catalyst** [214]**.**

Vanadium loaded mechanically activated fly ash (**FAV**) with monolayer vanadia species (monomeric and polymeric) catalyzed gas phase, solvent free selective oxidation of toluene using molecular oxygen as oxidant in a vapor phase micro-reactor under normal atmospheric pressure [215] (**Figure 1.22**).

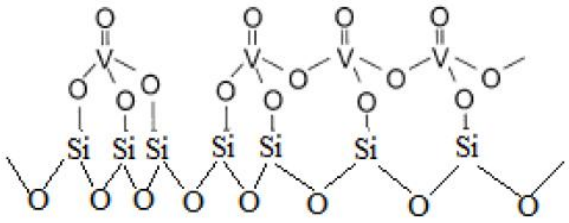

Figure 1. 22 Proposed model structures of supported FAV catalysts [215]**.**

The fly ash supported catalysts are cost effective and recyclable as do not lixiviate active phase during catalytic reactions. The application of solid waste fly ash as solid support after suitable mechanical, thermal and chemical activation can be an effective route of bulk utilization of this material in synthetic industries.

1.5 Objectives of Present Work

In the survey of literature, we found that at present there are plenty of methods available for the synthesis of various fly ash supported and nonsupported metal/metal oxide nanomaterials, especially metal oxides. Our main aim of research is to develop simple, novel synthesis methods for the preparation of metal/metal oxide nanoparticles with and without fly ash support. The work also includes certain industrially as well as environmentally important reactions such as oxidation and photodegradation reactions etc. The comparative study of the effects of fly ash supported and non supported nanoparticles on the catalytic properties of nanoparticles is also investigated during the study.

The main objective of the research work can be described below

1. Preparation of different nano-sized materials by methods reported in the literature.

2. Modification of already existing methods so as to achieve synthesis of nanoparticles more efficiently.

3. To develop techniques to synthesize fly ash supported metal/metal oxides nanoparticles, which are cost effective and less time consuming methods, further these techniques can be utilized at industrial scale.

4. Characterization of the materials using instrumental techniques such as X-ray diffractometer (XRD), Scanning electron microscope (SEM), Fourier transform infrared (FT-IR), Transmission electron microscope (TEM) and Brunner emit teller surface analyzer (BET) etc.

5. To evaluate the catalytic activity of prepared supported nanoparticles for some industrially important reactions.

6. To optimize the reaction condition for maximum conversion of desired product

7. To regenerate and reuse of supported nanoparticles.

The various schemes carried out by using synthesized non supported and fly ash supported nanomaterials are as follows:

1. Synthesis and characterization of nonsupported nano TiO_2, NiO and mesoporous SiO_2 using sol gel, microemulsion and hydrothermal synthesis respectively.

2. Synthesis and characterization of nonsupported and fly ash supported nano TiO_2 by alcoholic sol gel route for photodegradation of congo red dye.

3. Synthesis and characterization of fly ash supported nano Ag using wet impregnation method for liquid phase methanol oxidation.

4. Synthesis and characterization of supported nano NiO using microwave assisted solution combustion synthesis for decomposition of H_2O_2.

1.6 Importance of Present Work

Nanoparticles have found enormous applications in catalytic fields and are used widely in almost every field of industrial synthesis. The present research

work is of great importance as it will develop innovative methodologies for synthesis of industrially important nanoparticles of metal/metal oxides. Such technologies however will be developed at lab scale on suitable modifications can be further converted into pilot and industrial scaled synthesis methods.

Fly ash, a solid waste abundantly available in the world, will be utilized for providing surface to adsorb nanoparticles. Fly ash particles loaded with nanoparticles will be of great importance as they will provide a route to cost effective use of these materials in various sectors. Further the amount of nanoparticles used in catalytic applications will be remarkably reduced if they find suitable support with equally efficient activities. This work is innovative, novel and can generate new path of fly ash utilization.

1.7 References

[1] W. Luther, Industrial Applications of Nanomaterials-Chances and Risks, Germany, 2004.

[2] S. Chaturvedi, P.N. Dave, N.K. Shah, J. Saudi Chem. Soc. 16 (2012) 307.

[3] E.L. Dreizin, Prog. Energy Combust. Sci. 35 (2009) 141.

[4] D. Astruc, in:, D. Astruc (Ed.), Nanoparticles Catal., Wiley-VCH Verlag GmbH & Co. KGaA, Weinheim, Weinheim, 2007, p. 48.

[5] P. Barbaro, F. Liguori, Heterogenized Homogeneous Catalysts for Fine Chemicals Production: Materials and Processes, Springer Science & Business Media, 2010.

[6] S.S. Zalesskiy, V.P. Ananikov, Organometallics 31 (2012) 2302.

[7] E. Spahn, A. Albright, M. Shevlin, L. Pauli, A. Pfaltz, R.E. Gawley, J. Org. Chem. 78 (2013) 2731.

[8] R.R. Schrock, J.A. Osborn, J. Am. Chem. Soc. 98 (1976) 4450.

[9] K. Takaki, K. Sonoda, T. Kousaka, G. Koshoji, T. Shishido, K. Takehira, Tetrahedron Lett. 42 (2001) 9211.

[10] D. Astruc, F. Lu, J.R. Aranzaes, Angew. Chem. Int. Ed. Engl. 44 (2005) 7852.

[11] N. Toshima, Metal Nanoparticles for Catalysis, Kluwer Academic Publishers, Boston, 2004.

[12] Y. Zou, J.S. Zhou, Chem. Commun. 50 (2014) 3725.

[13] G. Hervé, G. Sartori, G. Enderlin, G. Mackenzie, C. Len, RSC Adv. 4 (2014) 18558.

[14] H. Bönnemann, G. Braun, W. Brijoux, R. Brinkmann, A.S. Tilling, K. Seevogel, K. Siepen, J. Organomet. Chem. 520 (1996) 143.

[15] H. Bönnemann, W. Brijoux, Nanostructured Mater. 5 (1995) 135.

[16] M.T. Reetz, S.A. Quaiser, C. Merk, Chem. Ber. 129 (1996) 741.

[17] M. Benmami, K. Chhor, A.V. Kanaev, Chem. Phys. Lett. 422 (2006) 552.

[18] K. Prasad, A.K. Jha, a. R. Kulkarni, Nanoscale Res. Lett. 2 (2007) 248.

[19] Larry N. Lewis, Nathan Lewis, Richard J. Uriarte, Homogeneous Transition Metal Catalyzed Reactions, American Chemical Society, Washington, DC, 1992.

[20] R. Xu, T. Xie, Y. Zhao, Y. Li, Nanotechnology 18 (2007) 055602.

[21] P. Migowski, G. Machado, S.R. Texeira, M.C.M. Alves, J. Morais, A. Traverse, J. Dupont, Phys. Chem. Chem. Phys. 9 (2007) 4814.

[22] M.T. Reetz, R. Breinbauer, P. Wedemann, P. Binger, Tetrahedron 54 (1998) 1233.

[23] A. Martino, M. Stoker, M. Hicks, C.H. Bartholomew, A.G. Sault, J.S. Kawola, Appl. Catal. A Gen. 161 (1997) 235.

[24] X.-B. Fan, N. Yan, Z.Y. Tao, D. Evans, C.X. Xiao, Y. Kou, Chem. Sus. Chem. 2 (2009) 941.

[25] X. Cheng, B. Wu, Y. Yang, Y. Li, Catal. Commun. 12 (2011) 431.

[26] T. Li, S. Li, S. Wang, Y. An, Z. Jin, J. Water Resour. Prot. 1 (2009) 1.

[27] P.G.N. Mertens, F. Cuypers, P. Vandezande, X. Ye, F. Verpoort, I.F.J. Vankelecom, D.E. De Vos, Appl. Catal. A Gen. 325 (2007) 130.

[28] M. Scariot, D.O. Silva, J.D. Scholten, G. Machado, S.R. Teixeira, M.A. Novak, G. Ebeling, J. Dupont, Angew. Chem. Int. Ed. Engl. 47 (2008) 9075.

[29] E. Redel, J. Krämer, R. Thomann, C. Janiak, J. Organomet. Chem. 694 (2009) 1069.

[30] S. Vukojević, O. Trapp, J.-D. Grunwaldt, C. Kiener, F. Schüth, Angew. Chem. Int. Ed. Engl. 44 (2005) 7978.

[31] L. He, H. Liu, C. Xiao, Y. Kou, Green Chem. 10 (2008) 619.

[32] D.D. Evanoff, G. Chumanov, J. Phys. Chem. B 108 (2004) 13948.

[33] S. Vivekanandhan, M. Misra, A.K. Mohanty, J. Nanosci. Nanotechnol. 9 (2009) 6828.

[34] M.K. Schröter, L. Khodeir, M.W.E. van den Berg, T. Hikov, M. Cokoja, S. Miao, W. Grünert, M. Muhler, R.A. Fischer, Chem. Commun. (Camb). (2006) 2498.

[35] Y. Shiraishi, N. Toshima, Colloids Surfaces A Physicochem. Eng. Asp. 169 (2000) 59.

[36] K. Nassau, The Physics and Chemistry of Color: The Fifteen Causes of Color, Wiley, 2001.

[37] W.-R. Li, X.-B. Xie, Q.-S. Shi, H.-Y. Zeng, Y.-S. Ou-Yang, Y.-B. Chen, Appl. Microbiol. Biotechnol. 85 (2010) 1115.

[38] Y. Wang, G. Wei, F. Wen, X. Zhang, W. Zhang, L. Shi, J. Mol. Catal. A Chem. 280 (2008) 1.

[39] Y. Lu, Y. Mei, M. Drechsler, M. Ballauff, Angew. Chem. Int. Ed. Engl. 45 (2006) 813.

[40] T.V.W. Janssens, B.S. Clausen, H. Falsig, C.H. Christensen, Nanotoday 2 (2007) 14.

[41] P.G.N. Mertens, M. Bulut, L.E.M. Gevers, I.F.J. Vankelecom, P.A. Jacobs, D.E. De Vos, Catal. Letters 102 (2005) 57.

[42] A. Roucoux, J. Schulz, H. Patin, Chem. Rev. 102 (2002) 3757.

[43] K.R. Januszkiewicz, H. Alper, Organometallics 2 (1983) 1055.

[44] X. Mu, J. Meng, Z. Li, Y. Kou, J. Am. Chem. Soc. 127 (2005) 9694.

[45] S. Ozkar, R.G. Finke, J. Am. Chem. Soc. 127 (2005) 4800.

[46] W. Yu, H. Liu, M. Liu, Q. Tao, J. Mol. Catal. A Chem. 138 (1999) 273.

[47] N. Yan, C. Zhao, C. Luo, P.J. Dyson, H. Liu, Y. Kou, J. Am. Chem. Soc. 128 (2006) 8714.

[48] C. Xiao, Z. Cai, T. Wang, Y. Kou, N. Yan, Angew. Chem. Int. Ed. Engl. 47 (2008) 746.

[49] F. Launay, A. Roucoux, H. Patin, Tetrahedron Lett. 39 (1998) 1353.

[50] M. Liu, W. Yu, H. Liu, J. Mol. Catal. A Chem. 138 (1999) 295.

[51] X. Yang, H. Liu, Appl. Catal. A Gen. 164 (1997) 197.

[52] L.N. Lewis, N. Lewis, J. Am. Chem. Soc. 108 (1986) 7228.

[53] T. Wang, H. Shou, Y. Kou, H. Liu, Green Chem. 11 (2009) 562.

[54] Ernst Rus. Cent. (n.d.).

[55] H. Hirai, S. Komatsuzaki, N. Toshima, Bull. Chem. Soc. Jpn. 57 (1984) 488.

[56] C. Zhao, W. Gan, X. Fan, Z. Cai, P. Dyson, Y. Kou, J. Catal. 254 (2008) 244.

[57] M. Beller, H. Fischer, K. Kühlein, C.-P. Reisinger, W.A. Herrmann, J. Organomet. Chem. 520 (1996) 257.

[58] M.T. Reetz, R. Breinbauer, K. Wanninger, Tetrahedron Lett. 37 (1996) 4499.

[59] R. Narayanan, C. Tabor, M.A. El-Sayed, Top. Catal. 48 (2008) 60.

[60] J. Watt, S. Cheong, M.F. Toney, B. Ingham, J. Cookson, P.T. Bishop, R.D. Tilley, ACS Nano 4 (2010) 396.

[61] N. Toshima, T. Yonezawa, New J. Chem. 22 (1998) 1179.

[62] J.K.A. Clarke, Chem. Rev. 75 (1975) 291.

[63] W.M.H. Sachtler, R.A. Van Santen, Adv. Catal. 26 (1977) 69.

[64] P. Pervan, M. Milun, Surf. Sci. 264 (1992) 135.

[65] L. Li, Z. Niu, S. Cai, Y. Zhi, H. Li, H. Rong, L. Liu, L. Liu, W. He, Y. Li, Chem. Commun. (Camb). 49 (2013) 6843.

[66] K. Mikkelsen, B. Cassidy, N. Hofstetter, L. Bergquist, A. Taylor, D.A. Rider, Chem. Mater. (2014) 141110163921002.

[67] O. Rahmanpour, A. Shariati, M.R.K. Nikou, Int. J. Chem. Eng. Appl. 3 (2012) 125.

[68] H.C. Stumpf, A.S. Russell, J.W. Newsome, C.M. Tucker, Ind. Eng. Chem. 42 (1950) 1398.

[69] C. Márquez-Alvarez, N. Žilková, J. Pérez-Pariente, J. Čejka, Catal. Rev. 50 (2008) 222.

[70] V. Shashikala, V. Siva Kumar, A.H. Padmasri, B. David Raju, S. Venkata Mohan, P. Nageswara Sarma, K.S. Rama Rao, J. Mol. Catal. A Chem. 268 (2007) 95.

[71] Y. Ono, T. Baba, Catal. Today 38 (1997) 321.

[72] H. Hattori, Chem. Rev. 95 (1995) 537.

[73] K. Tanabe, in:, Solid Acids and Bases, Elsevier, 1970, pp. 35–44.

[74] M. Tajbakhsh, M. Farhang, A.A. Hosseini, J. Iran. Chem. Soc. 11 (2013) 665.

[75] A. Ganguly, P. Trinh, K. V Ramanujachary, T. Ahmad, A. Mugweru, A.K. Ganguli, J. Colloid Interface Sci. 353 (2011) 137.

[76] H. Mirzaei, A. Davoodnia, Chinese J. Catal. 33 (2012) 1502.

[77] R. Ranjbar-Karimi, S. Hashemi-Uderji, A. Bazmandegan-Shamili, Chinese J. Chem. 29 (2011) 1624.

[78] J. Safaei-Ghomi, M.A. Ghasemzadeh, M. Mehrabi, Sci. Iran. 20 (2013) 549.

[79] M. Sadeghi, M.H. Husseini, J. Appl. Chem. Res. 7 (2013) 39.

[80] X. Liu, H. He, Y. Wang, S. Zhu, X. Piao, Fuel 87 (2008) 216.

[81] A. Demirbas, Energy Sources, Part A Recover. Util. Environ. Eff. 30 (2008) 1645.

[82] P.F. Manicone, P. Rossi Iommetti, L. Raffaelli, J. Dent. 35 (2007) 819.

[83] H. Althues, S. Kaskel, Langmuir 18 (2002) 7428.

[84] S. Yu, P. Jiang, Y. Dong, P. Zhang, Y. Zhang, W. Zhang, Bull. Korean Chem. Soc 33 (2012) 524.

[85] S. Samantaray, P. Kar, G. Hota, B.G. Mishra, Ind. Eng. Chem. Res. 52 (2013) 5862.

[86] M. Abdollahi-Alibeik, M. Hajihakimi, Chem. Pap. 67 (2013) 490.

[87] N. Wang, Y. Yao, W. Li, Y. Yang, Z. Song, W. Liu, H. Wang, X.-F. Xia, H. Gao, RSC Adv. 4 (2014) 57164.

[88] G. Chen, C.Y. Guo, H. Qiao, M. Ye, X. Qiu, C. Yue, Catal. Commun. 41 (2013) 70.

[89] R. Malakooti, H. Mahmoudi, R. Hosseinabadi, S. Petrov, A. Migliori, RSC Adv. 3 (2013) 22353.

[90] M. Jafarpour, E. Rezapour, M. Ghahramaninezhad, A. Rezaeifard, New J. Chem. 38 (2014) 676.

[91] M. Lazar, S. Varghese, S. Nair, Catalysts 2 (2012) 572.

[92] C.T. Chen, J.Q. Kao, C.Y. Liu, L.Y. Jiang, Catal. Sci. Technol. 1 (2011) 54.

[93] M.M. Ba-Abbad, A.A.H. Kadhum, A.B. Mohamad, M.S. Takriff, K. Sopian, Int. J. Electrochem. Sci. 7 (2012) 4871.

[94] S. Erdemoğlu, S.K. Aksu, F. Sayilkan, B. Izgi, M. Asiltürk, H. Sayilkan, F. Frimmel, S. Güçer, J. Hazard. Mater. 155 (2008) 469.

[95] A. Bharathi, S.M. Roopan, A. Kajbafvala, R.D. Padmaja, M.S. Darsana, G. Nandhini Kumari, Chinese Chem. Lett. 25 (2014) 324.

[96] S. Onitsuka, Y.Z. Jin, A.C. Shaikh, H. Furuno, J. Inanaga, Molecules 17 (2012) 11469.

[97] W. Huang, A. Duan, Z. Zhao, G. Wan, G. Jiang, T. Dou, K.H. Chung, J. Liu, Catal. Today 131 (2008) 314.

[98] D. Basavaiah, R.M. Reddy, Molecules 17 (2001) 985.

[99] A. Ramzani, K. Dastanra, F.N. Zeinali, Z. Karimi, M. Rouhani, M. Hosseini, Turk J Chem 36 (2012) 467.

[100] S. Banerjee, S. Santra, Tetrahedron Lett. 50 (2009) 2037.

[101] H.T. Chen, Multifunctionalized Mesoporous Silica Nanoparticles for Selective Catalysis, Iowa State University, 2007.

[102] E. Mehrasbi, Y. Sarrafi, A. Vahid, H. Alinezhad, Res. Chem. Intermed. (2014).

[103] A.F. Mingotaud, S. Reculusa, C. Mingotaud, P. Keller, C. Sykes, E. Duguet, S. Ravaine, J. Mater. Chem. 13 (2013) 1920.

[104] J. Wanga, S. He, Z. Li, X. Jing, M. Zhang, Z. Jiangb, J. Chem. Sci. 121 (2009) 1077.

[105] I. Yavari, E. Sodagar, M. Nematpour, Helv. Chim. Acta 97 (2014) 420.

[106] G.R. Chaudhary, P. Bansal, N. Kaur, S.K. Mehta, RSC Adv. 4 (2014) 49462.

[107] M. Zhu, G. Diao, Catal. Sci. Technol. 2 (2012) 82.

[108] B. Shaabani, E. Alizadeh-Gheshlaghi, Y. Azizian-Kalandaragh, A. Khodayari, Adv. Powder Technol. 25 (2014) 1043.

[109] H. Li, J. Liao, T. Zeng, Catal. Commun. 46 (2014) 169.

[110] E. Alizadeh-Gheshlaghi, B. Shaabani, A. Khodayari, Y. Azizian-Kalandaragh, R. Rahimi, Powder Technol. 217 (2012) 330.

[111] L.A. Saghatforoush, S. Sanatia, Gh. Marandib, M. Hasanzadeh, J. Nanostructures 3 (2013) 33.

[112] F. Teng, W. Yao, Y. Zheng, Y. Ma, Y. Teng, T. Xu, S. Liang, Y. Zhu, Sensors Actuators B Chem. 134 (2008) 761.

[113] S. Baruah, J. Dutta, Sci. Technol. Adv. Mater. 10 (2009) 013001.

[114] L. Miao, Y. Ieda, S. Tanemura, Y.G. Cao, M. Tanemura, Y. Hayashi, S. Toh, K. Kaneko, Sci. Technol. Adv. Mater. 8 (2007) 443.

[115] L. Song, Q. Jiang, P. Du, Y. Yang, J. Xiong, Mater. Lett. 123 (2014) 214.

[116] Lamia Saadmary Riad, J. Serbian Chem. Soc. 73 (2008) 997.

[117] H. Sachdeva, R. Saroj, ScientificWorldJournal. 2013 (2013) 680671.

[118] A.S. Adekunle, J.A.O. Oyekunle, O.S. Oluwafemi, A.O. Joshua, W.O. Makinde, A.O. Ogunfowokan, M.A. Eleruja, Eno E. Ebenso, Int. J. Electrochem. Sci. 9 (2014) 3008.

[119] H. Sachdeva, D. Dwivedi, R.R. Bhattacharjee, S. Khaturia, R. Saroj, J. Chem. 2013 (2013) 10.

[120] K. Fominykh, J.M. Feckl, J. Sicklinger, M. Döblinger, S. Böcklein, J. Ziegler, L. Peter, J. Rathousky, E.-W. Scheidt, T. Bein, D. Fattakhova-Rohlfing, Adv. Funct. Mater. 24 (2014) 3123.

[121] M. Jalalian, F. Farzaneh, L.J. Foruzin, J. Clust. Sci. (2014).

[122] F. Wang, W. Ueda, Chemistry 15 (2009) 742.

[123] A. Manivel, G.-J. Lee, C.-Y. Chen, J.-H. Chen, S.-H. Ma, T.-L. Horng, J.J. Wu, Mater. Res. Bull. 62 (2015) 184.

[124] M. Zhang, M. de Respinis, H. Frei, Nat. Chem. Adv. Online Publ. (2014).

[125] S.L. Sharifi, H.R. Shakur, A. Mirzaei, A. Salmani, M.H. Hosseini, Int. J. Nanosci. Nanotechnol. 9 (2013) 51.

[126] I.M. Sadiek, A.M. Mohammad, M.E. El-shakre, M.I. Awad, Int. J. Electrochem. Sci. 7 (2012) 3350.

[127] C.S. Transactions, R. Manigandan, K. Giribabu, R. Suresh, L. Vijayalakshmi, A. Stephen, V. Narayanan, G. Campus, Chem. Sci. Trans. 2 (2013) 47.

[128] M. Risch, D. Shevchenko, M.F. Anderlund, S. Styring, J. Heidkamp, K.M. Lange, A. Thapper, I. Zaharieva, Int. J. Hydrogen Energy 37 (2012) 8878.

[129] R.V. Narayan, V. Kanniah, A. Dhathathreyan, J. Chem. Sci. 118 (2006) 179.

[130] L.X. Yang, Y.J. Zhu, L. Li, L. Zhang, H. Tong, W.-W. Wang, G.-F. Cheng, J.-F. Zhu, Eur. J. Inorg. Chem. 2006 (2006) 4787.

[131] J.Y. Shin, Y.R. Jung, S.J. Kim, S.G. Lee, Bull. Korean Chem. Soc. 32 (2011) 3105.

[132] Y. Chung, G. Xiong, C. Kao, J. Catal. 243 (1984) 237.

[133] J. Kugai, R. Kitagawa, S. Seino, T. Nakagawa, Y. Ohkubo, H. Nitani, H. Daimon, T.A. Yamamoto, Appl. Catal. A Gen. 406 (2011) 43.

[134] C. Milone, M. Trapani, R. Zanella, E. Piperopolulos, S. Galvagno, Mater. Res. Bull. 45 (2010) 1925.

[135] F. Sánchez-De la Torre, J. De la Rosa, B. Kharisov, C. Lucio-Ortiz, Materials (Basel). 6 (2013) 4324.

[136] B.. Min, A.. Santra, D.. Goodman, Catal. Today 85 (2003) 113.

[137] S. Badoga, R. V. Sharma, A.K. Dalai, J. Adjaye, Fuel 128 (2014) 30.

[138] D. Gulková, Y. Yoshimura, Z. Vít, Appl. Catal. B Environ. 87 (2009) 171.

[139] C. Xu, A.S. Teja, J. Supercrit. Fluids 39 (2006) 135.

[140] S. Jafari, H. Asilian Mahabady, H. Kazemian, Catal. Letters 128 (2008) 57.

[141] S. Tsuchiya, S. Sakai, M. Kikugawa, T. Mitsuno, Y. Sakata, Stud. Surf. Sci. Catal. 75 (1993) 2185.

[142] G. Srinivas, A. Lovell, N.T. Skipper, S.M. Bennington, Z. Kurban, R.I. Smith, Phys. Chem. Chem. Phys. 12 (2010) 6253.

[143] P.G. Rodewald, Boron Trifluoride, US3962133, 1976.

[144] M.A.M. Boersma, Catal. Rev. 10 (2006) 243.

[145] Stiles, Alvin B., A.B. Stiles, Catalyst Supports and Supported Catalysts: Theoretical and Applied Concepts, Butterworths, 1987.

[146] P.K. Tripathi, N.N. Rao, C. Chauhan, G.R. Pophali, S.M. Kashyap, S.K. Lokhande, L. Gan, J. Hazard. Mater. 261 (2013) 63.

[147] C. V. Rode, U. D. Joshi, T. Sato, O. Sato, M. Shirai, Carbon Dioxide Utilization for Global Sustainability, Proceedings of 7ththe International Conference on Carbon Dioxide Utilization, Elsevier, 2004.

[148] J. Amanpour, D. Salari, A. Niaei, S.M. Mousavi, P.N. Panahi, J. Environ. Sci. Health. A. Tox. Hazard. Subst. Environ. Eng. 48 (2013) 879.

[149] I. Genova, T. Tsoncheva, M. Dimitrov, D. Paneva, B. Tsyntsarski, R. Ivanova, Z. Cherkezova-Zheleva, T. Budinova, D. Kovacheva, I. Mitov, N. Petrov, Catal. Commun. 55 (2014) 43.

[150] D. Basu, S. Basu, Int. J. Hydrogen Energy 36 (2011) 14923.

[151] L. Xin, Z. Zhang, Z. Wang, J. Qi, W. Li, Front. Chem. 1 (2013) 16.

[152] S. Iijima, T. Ichihashi, Nature 363 (1993) 603.

[153] G.G. Wildgoose, C.E. Banks, R.G. Compton, Small 2 (2006) 182.

[154] G.G. Wildgoose, C.E. Banks, R.G. Compton, J. Am. Chem. Soc. 127 (2005) 10806.

[155] A. Masotti, A. Caporali, Int. J. Mol. Sci. 14 (2013) 24619.

[156] V. Gupta, T.S. A., in:, S. Bianco (Ed.), Carbon Nanotub. - From Res. to Appl., InTech, 2011, p. 368.

[157] E. Santillan-Jimenez, M. Crocker, A. Bueno-López, C. Salinas-Martínez de Lecea, Ind. Eng. Chem. Res. 50 (2011) 7191.

[158] R.S. Oosthuizen, V.O. Nyamor, Platin. Met. Rev 55 (2011) 154.

[159] V. Fierro, O. Akdim, H. Provendier, C. Mirodatos, J. Power Sources 145 (2005) 659.

[160] L. Abahmane, A. Knauer, J.M. Köhler, G.A. Groß, Chem. Eng. J. 167 (2011) 519.

[161] N. Ameur, A. Berrichi, S. Bedrane, R. Bachir, Adv. Mater. Res. 856 (2013) 48.

[162] H. Kanoh, T. Nishimura, A. Ayame, J. Catal. 57 (1979) 372.

[163] P. Riani, G. Garbarino, M. Alberto, F. Canepa, G. Busca, J. Mol. Catal. A Chem. 384 (2014) 10.

[164] M. Zdražil, Catal. Today 65 (2001) 301.

[165] K.P. de Jong, in:, Solid Catal. Porous Solids, 1999, pp. 55–62.

[166] W. Zhen, B. Li, G. Lu, J. Ma, RSC Adv. 4 (2014) 16472.

[167] S. Ali, N.A.M. Zabidi, D. Subbarao, Chem. Cent. J. 5 (2011) 68.

[168] B.K. Min, A.K. Santra, D.W. Goodman, 85 (2003) 113.

[169] D.J. Macquarrie, B. Gotov, S. Toma, Platin. Met. Rev. 45 (2001) 102.

[170] B.M. Reddy, G.M. Kumar, I. Ganesh, A. Khan, J. Mol. Catal. A Chem. 247 (2006) 80.

[171] P. Veerakumar, M. Velayudham, K.L. Lu, S. Rajagopal, Catal. Sci. Technol. 1 (2011) 1512.

[172] F. Jiao, H. Frei, Chem. Commun. 46 (2010) 2920.

[173] W. Zhang, X. Lu, W. Zhou, F. Wu, J. Li, Chinese Sci. Bull. 59 (2014) 4008.

[174] X. Wang, L. Chen, M. Shang, F. Lin, J. Hu, R.M. Richards, Nanotechnology 23 (2012) 294010.

[175] Z. Xu, K. Inumaru, S. Yamanaka, Appl. Catal. A Gen. 210 (2001) 217.

[176] L. Alemany, M. Banares, E. Pardo, F. Martin, M. Galanfereres, J. Blasco, Appl. Catal. B Environ. 13 (1997) 289.

[177] N. Kumar, Ruthenium- Silver Catalysts Supported on Silica, Iowa State University, 1999.

[178] C. Khatri, M.K. Mishra, A. Rani, Fuel Process. Technol. 91 (2010) 1288.

[179] J. Giménez-Mañogil, A. Bueno-López, A. García-García, Appl. Catal. B Environ. 152-153 (2014) 99.

[180] Y. Zhang, R. Wang, X. Lin, Z. Wang, J. Liu, J. Zhou, K. Cen, Int. J. Hydrogen Energy 39 (2014) 10853.

[181] X. Yang, N. Zhao, Q. Zhou, C. Cai, X. Zhang, J. Xu, J. Mater. Chem. C 1 (2013) 3359.

[182] N. Kamiuchi, M. Haneda, M. Ozawa, Catal. Today 232 (2014) 179.

[183] S.-H. Chai, B. Yan, L.-Z. Tao, Y. Liang, B.-Q. Xu, Catal. Today 234 (2014) 215.

[184] S.H. Chai, H.P. Wang, Y. Liang, B.Q. Xu, Green Chem. 9 (2007) 1130.

[185] W. Han, J. Deng, S. Xie, H. Yang, H. Dai, C.T. Au, Ind. Eng. Chem. Res. 53 (2014) 3486.

[186] M.B. Gawande, A.K. Rathi, J. Tucek, K. Safarova, N. Bundaleski, O.M.N.D. Teodoro, L. Kvitek, R.S. Varma, R. Zboril, Green Chem. 16 (2014) 4137.

[187] Y.I. Pae, J.R. Sohn, Bull. Korean Chem. Soc. 28 (2007) 1273.

[188] T.A. Yamamoto, T. Nakagawa, S. Seino, H. Nitani, Appl. Catal. A Gen. 387 (2010) 195.

[189] S. Zhang, F. Ren, W. Wu, J. Zhou, L. Sun, X. Xiao, C. Jiang, J. Colloid Interface Sci. 427 (2014) 29.

[190] J.N. Lin, B.Z. Wan, Appl. Catal. B Environ. 41 (2003) 83.

[191] J.N. Lin, J.H. Chen, C.Y. Hsiao, Y.M. Kang, B.Z. Wan, Appl. Catal. B Environ. 36 (2002) 19.

[192] C. Plaisance, Zeolite and Metal Oxide Catalysts for The Production of Dimethyl Sulfide and Methanthiol, B.S., Louisiana State University, 2005.

[193] J. Wellenbuscher, M. Muhler, W. Mahdi, U. Sauerlandt, J. Schutze, G. Ertl, R. Schlogl, Catal. Letters 25 (1994) 61.

[194] A.M. Garrido Pedrosa, M.J.B. Souza, D.M. a. Melo, A.S. Araujo, Mater. Res. Bull. 41 (2006) 1105.

[195] T. Tang, C. Yin, L. Wang, Y. Ji, F.-S. Xiao, J. Catal. 257 (2008) 125.

[196] J. Ren, A. Wang, X. Li, Y. Chen, H. Liu, Y. Hu, Appl. Catal. A Gen. 344 (2008) 175.

[197] L. Ding, Y. Zheng, Z. Zhang, Z. Ring, J. Chen, J. Catal. 241 (2006) 435.

[198] A. S. Rocha, E.L. Moreno, G.P.M. da Silva, J.L. Zotin, a. C. Faro, Catal. Today 133-135 (2008) 394.

[199] N. Pal, M. Seikh, A. Bhaumik, J. Solid State Chem. 198 (2013) 114.

[200] Q.H. Powell, G.P. Fotou, T.T. Kodas, B.M. Anderson, Chem. Mater. 9 (1997) 685.

[201] M. Gopalakrishnan, P. Sureshkumar, V. Kanagarajan, J. Thanusu, R. Govindaraju, Ark. Gen. Pap. 2006 (2006) 130.

[202] N. Kaur, P. Sharma, D. Kishore, J. Chem. Pharm. Res. 4 (2012) 1938.

[203] H.P. Narkhede, U.B. More, D.S. Dalal, N.S. Pawar, D.H. More, P.P. Mahulikar, Synth. Commun. 37 (2007) 573.

[204] P. Huo, Y. Yan, S. Li, H. Li, W. Huang, S. Chen, X. Zhang, Desalination 263 (2010) 258.

[205] X. Meng, D. Li, X. Shen, W. Liu, Appl. Surf. Sci. 256 (2010) 3753.

[206] C. Liewhiran, S. Phanichphant, J. Microsc. Soc. Thail. 20 (2006) 49.

[207] C. Khatri, A. Rani, Fuel (2008).

[208] C. Khatri, D. Jain, A. Rani, Fuel 89 (2010) 3853.

[209] C. Khatri, M.K. Mishra, A. Rani, Fuel Process. Technol. 91 (2010) 1288.

[210] A. Rani, C. Khatri, R. Hada, Fuel Process. Technol. 116 (2013) 366.

[211] D. Jain, C. Khatri, A. Rani, Fuel 90 (2011) 2083.

[212] D. Jain, A. Rani, Am. Chem. Sci. J. 1 (2011) 37.

[213] D. Jain, C. Khatri, A. Rani, Fuel Process. Technol. 91 (2010) 1015.

[214] D. Jain, M. Mishra, A. Rani, Fuel Process. Technol. 95 (2012) 119.

[215] K. Srivastava, V. Devra, A. Rani, Fuel Process. Technol. 121 (2014) 1.

Synthesis and Characterization of TiO_2, NiO and SiO_2 Nanoparticles

Abstract

This chapter focuses on different chemical and physical synthesis methods mentioned in literature for the preparation of various metal/metal oxide nanoparticles, thin films and coatings. Chapter describes the details of experimental work related to the preparation of (i) TiO_2 nanoparticles synthesized by sol-gel route using ethylene glycol as gelling agent and titanium n-butoxide as titanium precursor. (ii) NiO nanoparticles prepared by novel mixed reverse microemulsion route consisting of aqueous nickel chloride as dispersed phase, unique blend of tween-80 and AOT as surfactant, and cyclohexane as oil phase, (iii) mesoporous silica prepared by a silica source extracted from fly ash by fusion method followed by hydrothermal treatment. Synthesized nanomaterials are characterized for phase and morphological identification. Results based on different characterization techniques such as FT-IR, SEM, TEM, XRD etc., are discussed in this chapter.

Nanoscience and nanotechnology have grown at an enormous rate for the last few decades, and recent advances in nanostructured materials have opened up new opportunities for diverse applications in electronics, catalysis, energy, materials chemistry and even biology [1–8]. Materials in the nanometer-size regime often exhibit properties distinct from their bulk counterparts, because clusters that have small electronic structures have a high density of states but not continuous bands [1]. Nanostructured materials have been prepared by a variety of synthetic methods, including gas phase techniques (e.g., molten metal evaporation, flash vacuum thermal and laser pyrolysis, decomposition of volatile organometallics) [9–11], liquid phase methods (e.g., reduction of metal halides with various strong reductants, colloidal techniques with controlled nucleation) [12,13], and mixed phase approaches (e.g., synthesis of conventional heterogeneous catalysts on oxide supports, metal atom vapor deposition into cryogenic liquids, explosive shock synthesis) [14,15]. Selecting an appropriate synthetic route ultimately determines the success or failure of nanostructured materials synthesis, because physical properties and applications of nanostructured materials are heavily dependent upon how they are prepared. The importance of choosing a proper synthetic route in designing nanostructured materials has been a driving force for the development of new methodologies for several decades [16]. Indeed, this has led scientists' interest to the development of versatile and generalized synthetic methods readily adaptable for the preparation of a variety of nanostructured materials. Among a variety of approaches it is very important to know which method is suitable for specific nanomaterials thus before synthesizing nanomaterials for specific applications basic knowledge of various synthesis methods is essential. Thus an attempt has been made in this chapter to discuss various chemical and physical synthesis methods mentioned in literature for the preparation of various metal/metal oxide nanoparticles, thin films and coatings etc. In the next section of this chapter simple, cost effective, innovative sol gel, microemulsion and hydrothermal synthesis have been discussed to synthesize nanostructure TiO_2, NiO and SiO_2 respectively.

2.1 Various Methods used for Synthesis of Nanoparticles

Nowadays, the attention of many scientists is focused on the development of new methods for synthesis and stabilization of nanoparticles. Moreover, special attention is paid to monodispersed and stable particles formation. Different metals, metal oxides, sulfides, polymers, core-shell and composite nanoparticles can be prepared using a number of synthetic methods, which are broadly classified into two categories, namely, chemical methods and physical methods.

2.1.1 Chemical Methods

1. Chemical vapour deposition
2. Sol-gel route
3. Chemical precipitation
4. Microemulsion route
5. Sonochemical route
6. Hydrothermal synthesis
7. Solution combustion synthesis
8. Spray pyrolysis

1. Chemical Vapour Deposition (CVD)

CVD is a well known process in which a solid is deposited on a heated surface via a chemical reaction from the vapour or gas phase. CVD reaction requires activation energy to proceed. This energy can be provided by several methods. In thermal CVD reaction system the reaction is activated by a high temperature above 900 °C. A typical apparatus comprises of gas supply system, deposition chamber and an exhaust system. In plasma CVD, the reaction is activated by plasma at temperatures between 300 and 700°C. In laser CVD, pyrolysis occurs when laser thermal energy heats an absorbing substrate. In photo-laser CVD, the chemical reaction is induced by ultra violet radiation which has sufficient photon energy, to break the chemical bond in the reactant molecules. In this process, the reaction is photon activated and deposition occurs at room temperature. The thermodynamic instability of the gaseous reactants provides the driving force for the reaction. The total deposition rate depends on the reaction

rate, nucleation rate, and diffusion rate. The rate-determining factor at higher temperatures is diffusion, whereas at lower temperatures it is reaction [17]. The common reactions occurred in the CVD reactor are pyrolysis (thermal deposition), reduction, oxidation, and disproportionation. The main advantages of CVD are that it is a single step chemical process for preparing highly pure, high-performance, shaped nanomaterials and thin films of metal oxides, nitrides and sulphides etc. [18]. It is very promising route for synthesizing single crystals, high purity carbon nanotubes, nanofibres, fullerene [18,19], smooth, columnar, branched and granular thin films of ceramic compounds e.g., TiO_2 [20], NiO [21], and IrO_2 [22] etc. other nanoparticles like metal nitrides of Al, B and Si [23] etc, metal oxides of Ti, [24], Ni [25], and Ir [26] etc , **Figure 2.1** shows hot wire direct current plasma enhanced chemical vapour deposition (HW dc PECVD) set-up for carbon nanotube formation.

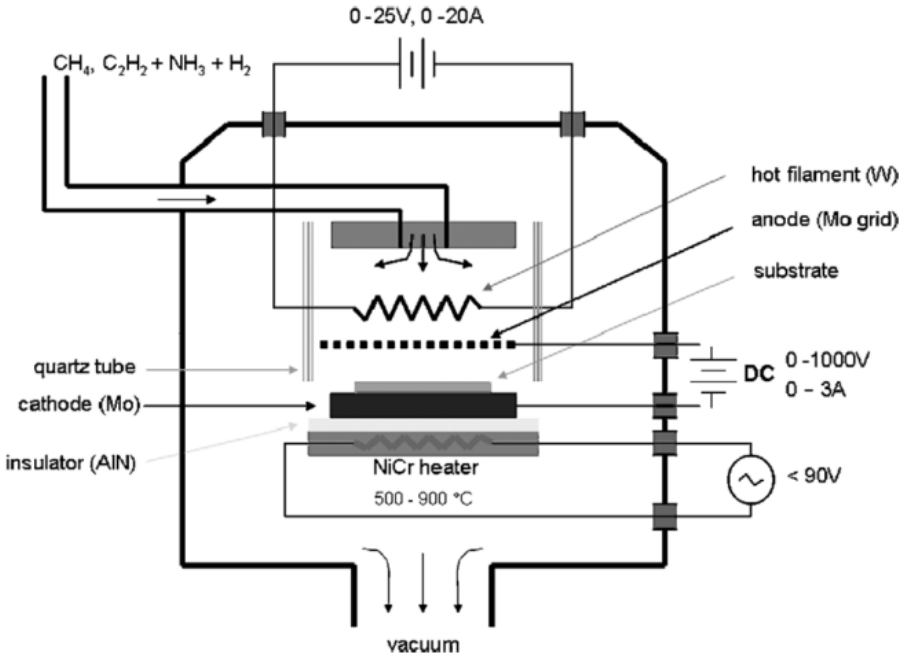

Figure 2. 1 Schematic cross-section of the experimental hot wire direct current plasma enhanced chemical vapour deposition (HW dc PECVD) set-up for carbon nanotube formation [19].

2. Sol Gel Route

Sol-gel processing is a type of wet chemical technique generally, refers to the hydrolysis and condensation of alkoxide-based precursors (**Figure 2.2)**. It can produce ceramic and glasses

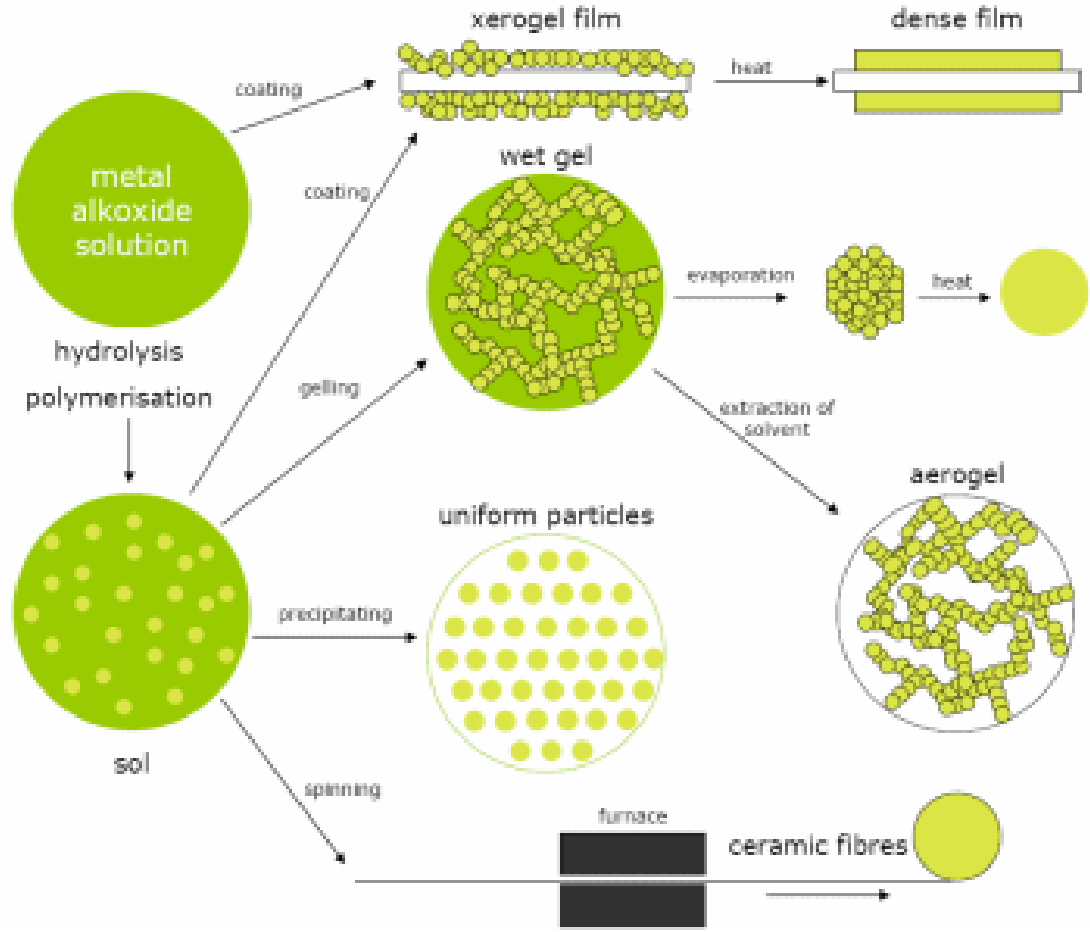

Figure 2. 2 Schematic of sol gel processing.

with better purity and homogeneity than high temperature conventional processes. Sol-gel process can be used to produce a wide range of oxides in various forms, including powders, fibers, coatings, thin films, monoliths and porous membranes. Organic/inorganic hybrids can also be made, where a gel, usually silica, is impregnated with polymer or organic dyes with specific properties. The advantages of sol-gel method are metal oxides which are difficult

to attain by conventional methods can be produced by using the sol-gel process. Another benefit is that the mixing level of the solution is retained in the final product, often in the molecular scale [27]. Sol-gel derived products have numerous applications. One of the promising application areas is for coatings and thin films used in electronics, optical and electro-optical components and devices, such as substrates, capacitors, memory devices, infrared (IR) detectors and wave guides [28]. Antireflection coatings are also used for automotive and architectural applications. Submicron particle size powders of single and multi component composition can be made for structural, electronic, dental, and biomedical applications. A colloid is a suspension in which the dispersed phase is so small (~1-1000 nm) that the gravitational forces are negligible and interactions are dominated by short-range forces, such as Van-der Waals attraction and surface charges. A sol is a colloidal suspension of solid particles in a liquid. An aerosol is a colloidal suspension of particles in a gas [29]. A gel consists of a three dimensional continuous network, which encloses a liquid phase, in a colloidal gel, the network is built from agglomeration of colloidal particles and is limited by the size of container. In a polymer gel the particles have a polymeric sub-structure made by aggregates of sub-colloidal particles. Generally, the sol particles may interact by Van der Waals forces or hydrogen bonds [30].

Gelation

Gelation is freezing in a particular structure (i.e. may be considered as a rapid solidification process). It occurs when links are formed between sol particles produced by hydrolysis and condensation, to such an extent that a giant spanning cluster reaches across the containing vessel. In other words, as the sol particles grow and collide, lead to the condensation and then forming macro particles. This is typically defined as the gelation point or gelation time. All subsequent stages of processing depend on the initial structure of the wet gel formed in the reaction bath during gelation [30].

Aging

When a gel is maintained in its pore liquid, its structure and properties continue to change long after the gel point. This process is called aging. During aging, four processes can occur, singly or simultaneously, including

polycondensation, syneresis, coarsening, and phase transformation [30]. Polycondensation reactions occur continuously, within the gel network as long as neighboring alkoxides are close enough to react. This increases the connectivity of the network and its fractal dimension. Usually in alkoxide-based gels, the chemical hydrolysis reactions are rapid especially when the sol is acid catalyzed and is completed in the early stages of sol preparation. Since the chemical reaction is faster at higher temperatures, aging can be accelerated by hydrothermal treatment, which increases the rate of the condensation reaction [30].

Drying

Drying is nothing but removing of the solvent phase. The method is influenced by the intended use of the dried material. If powdered ceramics are desired, no special care need to be exercised to prevent fragmentation, if monoliths from colloidal gels are desired, the drying procedures are largely determined by the need to minimize internal stresses associated with the volume changes on drying and the capillary forces in the gel pores [31].

There are many studies have been carried out to prepare nanomaterials by sol gel route e.g., Multi component nanoparticles $Si_xAl_yP_zB_wO_q$ [32], $LiTi_2(PO_2)_3$ [33], $Zr_xTi_{1-x}PO_4$ [34], highly ordered oxides (layer by layer) TiO_2-SiO_2 [35], Al_2O_3 [36], ZnO [35], CuO [37], SnO_2 [38] , WO_3 [39], mesostructured binary oxides $AlBO_x$ [40], $TiBO_x$ [41], $SnxTi_{1-x}O_2$ [42] and $Ce_xTi_{1-x}O_2$ [43] etc.

3. Chemical Precipitation

The precipitation technique is probably the simplest and most efficient chemical pathway to obtain oxide nanoparticles e.g., iron oxides (FeOOH, Fe_3O_4 or γ-Fe_2O_3) are usually prepared by addition of alkali to iron salt solutions and keeping the suspensions for ageing. The main advantage of the precipitation process is that a large amount of nanoparticles can be synthesized. However, the control of particle size distribution is limited, because only kinetic factors are controlling the growth of the crystals. In the precipitation process, two stages are involved i.e., a short burst of nucleation occurs when the concentration of the species reaches critical super saturation, and then, there is a slow growth of the nuclei by diffusion of the solutes to the surface of the crystals. To produce mono

dispersed nanoparticles, these two stages should be separated; i.e., nucleation should be avoided during the period of growth [44]. Size control of mono dispersed nanoparticles must normally be performed during the very short nucleation period, because the final particle number is determined by the end of the nucleation and it does not change during particle growth. A wide variety of factors can be adjusted in the synthesis of nanoparticles to control size, physical characteristics, or surface properties. A number of studies have dealt with the influence of these different factors. The size and shape of the nanoparticles can be tailored with relative success by adjusting pH, ionic strength, temperature, nature of the salts (perchlorates, chlorides, sulfates, and nitrates), concentration ratio between metal salt and precipitating agent, addition of binding agent (surfactant) and addition of another salt in lesser amount to increase the nucleation and control growth of nanoparticles [45–48]. **Figure 2.3** is shown a typical process of surfactant mediated chemical precipitation.

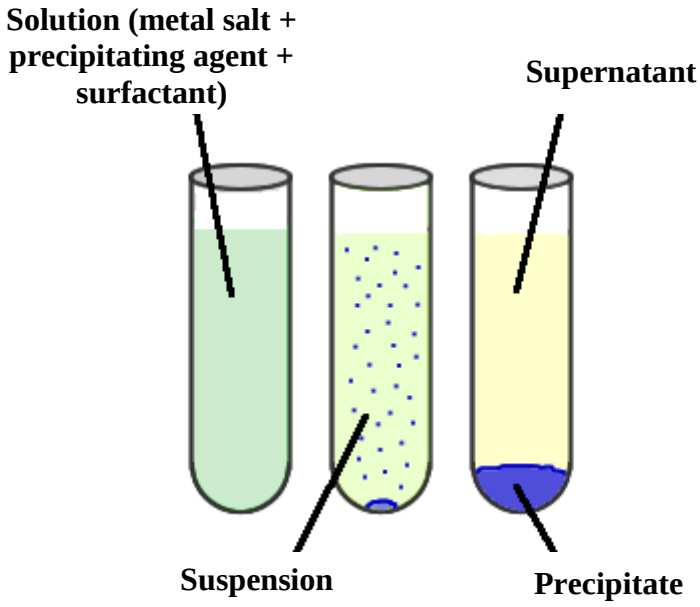

Figure 2. 3 Typical process of surfactant mediated chemical precipitation.

When surfactants are used to control particle size in precipitation process then it is called surfactant mediated chemical precipitation. Surfactants are amphiphilic neutral or charged supramolecules with hydrophilic or lipophobic (water loving) head and hydrophobic or lipophilic (oil loving) tail e.g., Cetyl trimethylammonium bromide (CTAB), span-80, tween-80, docusate sodium (AOT). These molecules are important factors influence the morphology of nanoparticles viz. hexagonal, lamellar, rod, tubes etc. [45]. Surfactants are mixed at room temperature with an aqueous solution of desired salt to yield shaped nanoparticles. For instance, lamellar iron oxide/surfactant composites have been produced by the controlled precipitation and hydrolysis of aqueous iron cations into self-assembled iron/surfactant arrays [49]. These composites were obtained by mixing iron (II) or iron (III) salt solutions with diluted aqueous solutions of sodium n-alkyl sulfates at room temperature. [45]. Many researchers used this method to prepare nanoparticles viz. NiO [46], ZnO [50], CeO_2 [51], Fe_2O_3, Fe_3O_4, [45] Cu doped CeO_2 [52], Ca-Mg doped ferrihydrite [53].

4. Microemulsion Route

This technique allows preparation of ultrafine metal/metal oxide nanoparticles within the size range 5 nm<particle diameter<50 nm. The rate of particle nucleation is a function of the percolation degree of microemulsion droplets. The nature of the stabilizer emulsifier, the surface activity of additives and the colloidal stability of microemulsion droplets play decisive role on the particle size and distribution during the preparation of metal/metal oxide nanoparticles. The traditional method is based on water-in-oil microemulsion (W/O), and it has been used for the preparation of metallic and other inorganic nanoparticles since the beginning of the 1980's [54].

Microemulsions

Microemulsions are thermodynamically stable dispersions of immiscible liquids (aqueous and hydrocarbon liquids) these are stabilized in the presence of an interfacial film of surfactant molecules [55]. The surfactants can (and sometimes co-surfactant) decrease the oil / water interfacial tension. Microemulsions can be described as optically isotropic dispersions that contain

monodispersed spherical droplets of water-in-oil or oil-in-water, which depends on the nature of the surfactants (hydrophobic or hydrophilic) and the composition of the microemulsion. The size of these spherical droplets is in the range of 50-800 Å in diameter [56]. The difference between microemulsions and macroemulsions is based on the optical transparency. This is a direct function of the droplet size. Along with these properties microemulsions are more complicated than other molecular dispersions and colloidal micellar systems.

Reverse micelles are small aggregates (60-800 Å) formed by surfactant molecules that surround a well defined nanometer-sized water core [57]. This unique formation of water droplets in a microemulsion may be characterized as a small reactor used for the synthesis of nanoparticles. The reactants are limited within such dispersed droplets when water-soluble precursors are used. It has been shown that this structure is the most suitable for the preparation of fine inorganic colloidal particles, since the aggregates have very small size and are monodispersed. Additionally, the fact that most metal precursors are water-soluble enhances the particle synthesis procedure, which takes place inside the water core of the reverse micelles. Even though the microemulsions have been considered as being stable systems, it was demonstrated that they are dynamic systems, where the droplets collide continuously with each other, which results sometimes in formation of coalesced droplets that tend to break up. Since they lose their thermodynamic stability, as the particle formation takes place inside the droplet, the nature of the formed colloidal particles will be influenced by the droplet structure and its ability to exchange micellar-containing material [58]. Additionally, the size of the water droplets will determine the size of the catalyst nanoparticles. **Figure 2.4** represents the phase diagram of the microemulsion system cyclohexane-water-cetyl trimethylammonium bromide and the corresponding reverse micelles produced by adding a Ni -containing metal precursor [57]. Generally, a low water to surfactant ratio (w_0) is required to form reverse micelles, it depends also on the type of the surfactant, i.e. number and length of hydrophobic chains. For given surfactants, w_0 will give aggregates of different size and shape (spherical micelles, rod-like micelles).

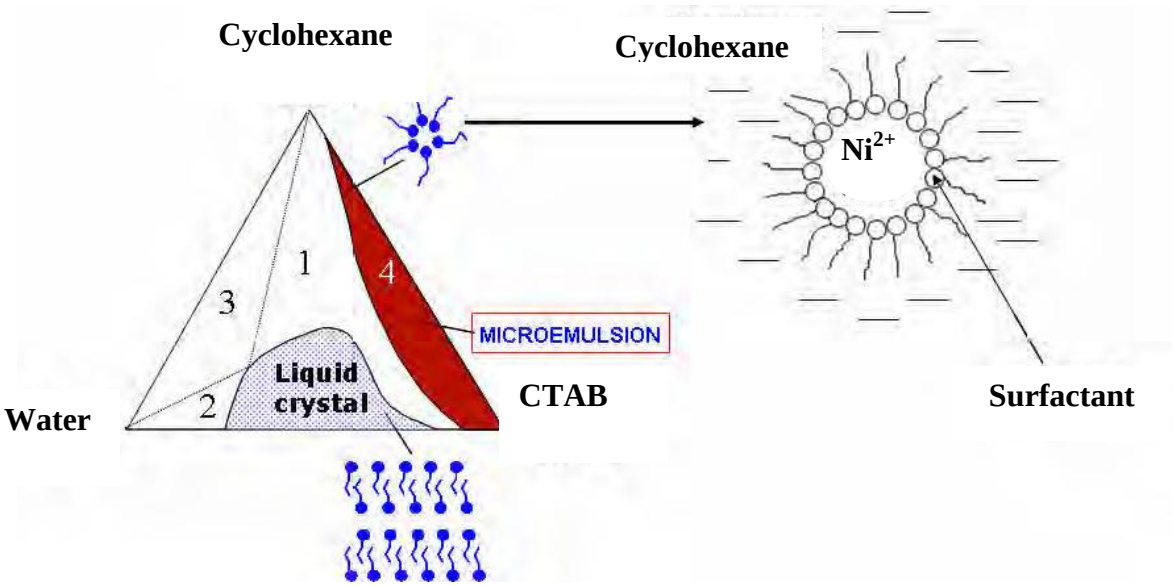

Figure 2. 4 ***Phase diagram at 25 °C of the ternary system cyclohexane-water-CTAB and the reverse micelles with Ni^{2+} ions in water. (CTAB-Cetyl trimethylammonium bromide).***

Numerous investigations have been published on the use of W/O reverse microemulsions for the preparation of a variety of nanomaterials, such as metallic (Ag, Cu, Ag, Fe, Pd, Pt,) [59–63] and bimetallic nanoparticles (PdPt, AgCu, AgNi, CuNi) [64–67], single metal oxide as well as mixed oxides (TiO_2, Fe_2O_3, ZnO, CuO, NiO, ZrO_2) [68–70], quantum dots and even complex ceramic materials [54,71–77].

5. Sonochemical Route

Sonochemical method has been used extensively to generate novel materials with unusual properties [78] because the method causes the formation of highly mono disperse particles of a much smaller size and higher surface area than those reported by other methods [79]. The chemical effects of ultrasound arise from acoustic cavitation, that is, the formation, growth, and implosive collapse of bubbles in a liquid. The implosive collapse of the bubbles generates a localized

hotspot through adiabatic compression or shock wave formation within the gas phase of the collapsing bubble. The conditions formed in these hotspots have been experimentally determined, i.e., transient temperatures of ~5000 K, pressures of 1800 atm [80], and cooling rates in excess of 10^{10} K/s. These extreme conditions result in the chemical excitation of any matter that was inside of, or in the immediate surroundings of the bubble as it rapidly imploded. A broad variety of outcomes can result from acoustic cavitation, including sonoluminescence, increased chemical activity in the solution due to the formation of primary and secondary radical reactions, and increase chemical activity through the formation of new, relatively stable chemical species that can diffuse further into the solution to create chemical effects e.g., the formation of hydrogen peroxide from the combination of two hydroxyl radicals formed following the dissociation of water vapour inside the collapsing bubbles from the water which is exposed to ultrasound, generation of metals [81,82] metal carbides [83], and metal oxides [84,85] from decomposition of metal-carbonyl bonds inside the collapsing bubbles from aqueous solution of carbonyl salt. **Figure 2.5** shows a typical Sonochemical processor.

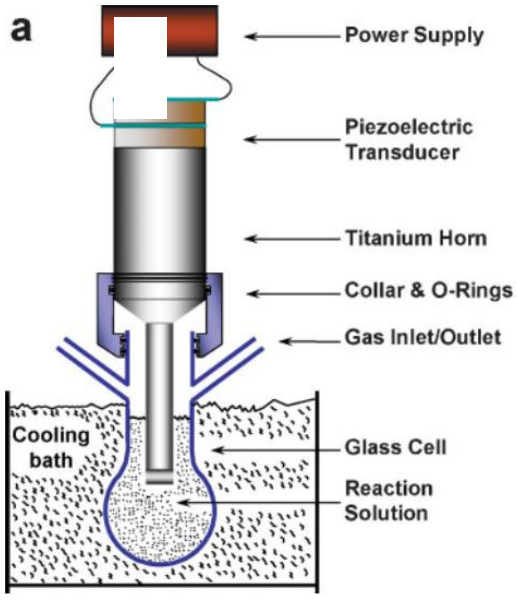

Figure 2. 5 Representation of sonochemical process using high-intensity ultrasonic rig [16]**.**

In this technique, nanoparticles are prepared by irradiating the aqueous or organic dispersion of precursor materials using an ultrasonic probe (rig) at room temperature. The size of the particles obtained in this method mainly depends on the solution concentration and the time of sonication. Nanophasic, amorphous, elemental iron has been synthesized by a sonochemical method involving the irradiation of iron pentacarbonyl by a high-intensity ultrasound radiation. [86], pure nanometer-size paramagnetic Fe_3O_4 powder with particle size of 10 nm has been synthesized by this route [84], TiO_2 microspheres with novel structure have been synthesized by sonochemical-microwave hydrothermal treatment [87].

6. Hydrothermal Synthesis

Hydrothermal processing can be defined as any heterogeneous reaction in the presence of aqueous solvents under high pressure (10-80 MPa, sometimes up to 300 MPa) and temperature (500 °C) conditions to dissolve and recrystallize (recover) materials that are relatively insoluble under ordinary conditions (<100 °C, <1 atm) e.g., some oxides (SiO_2, TiO_2, IrO_2 etc.) Silicates and sulphites [88]. It is widely used for synthesis of single and multi crystalline metal/metal oxide nanoparticles, thin films, hybrid nanoparticles [89,90] and coating of nanomaterials on substrates. Hydrothermal treatment under supercritical water (SCW) condition is an extension of hydrothermal technique. This method relies on high reaction rate of hydrothermal synthesis above the critical temperature of water and lower solubility for prepared metal/metal oxide, which causes an extremely high degree of supersaturation of the metal/metal oxide due to decrease in dielectric constant of water from 78 to below 10 under supercritical condition and thus allows nanoparticle formation [91]. The important parameters of the process that can control dimension and morphology of the produced nanoparticles are solubility of metallic oxides in supercritical water (SCW), pH of starting solution, the initial concentration of the feed and temperature.

In a typical hydrothermal synthesis the crystal growth is performed in an apparatus consisting of a steel pressure vessel called autoclave as given in **Figure 2.6**, in which reactants are supplied along with water. An autoclave is a large pressure cooker containing sealed vessel. It operates by using steam under high

Figure 2. 6 Commercially available magnetic stirrer assembled autoclave [110]**.**

pressure. High pressure enables steam to reach high temperatures, thus increases its heat content and hydrolysing power. Most of the heating power of steam comes from its latent heat of vaporization. A gradient of temperature is maintained at the opposite ends of the growth chamber so that the hotter end dissolves the precursors and the cooler end causes seeds to take additional growth for nanomaterials. Possible advantages of the hydrothermal method over the other types of crystal growth include the ability to create crystalline phases which are not stable at the melting point like Ag_2O [92] and it does not require any calcination or milling steps unlike co-precipitation, solid state and sol gel reactions [93]. The method is also particularly suitable for the growth of large good-quality crystals with controlled composition and morphology. [94,95] [96,97]. The production of various nanoscale metal viz. Ag [98], Au [99], Ru, Os, Rh, Ir, Pd and Pt [100], Pt [101], and Cu [102], etc., nanoscale metallic alloys like CuNi [103], AgPd [104], AuPt and AuPd [105] etc., metal oxide particles such as TiO_2 [94], ZrO_2 [106], Al_2O_3 [107], Fe_2O_3 [108], Fe_3O_4 ZnO [109], Co_3O_4, NiO, CeO_2, $LiCoO_2$, a-$NiFe_2O_4$, and $Ce_{1x}Zr_xO_2$, [28-45]etc. have been synthesized by hydrothermal synthesis systems [90,110].

7. Solution Combustion Synthesis

Solution combustion synthesis (SCS) is an effective low temperature, gas producing, homogeneous, exothermic reaction method for the synthesis of nanosized ceramic oxide powders for a variety of advanced applications. The combustion is carried out in liquid phase and is smouldering type (flameless), accompanied by the evolution of gases resulting in fine, voluminous ceramic oxides [111]. In this process precipitating agent (obtain from fuel decomposition) is added slowly to obtain high purity, mono dispersity, and nanocrystallinity of ceramic oxide powder in a dilute solution of metal salt. The precipitating agent is synthesized in the solution rather than added mechanically. Generally ceramic oxide powders at the nanoscale using SCS can be prepared by the combination of metal nitrates in an aqueous solution with a fuel. Glycine and urea are used as fuels because they evolve high energy while oxidize during exothermic reaction between fuel and oxidizer and these are amino acids that can act as a complexing agent for metal ion in the synthesis of nanocrystalline metal oxides at temperature <500 °C. This method can directly produce the desired final product, although in some cases, a subsequent heat treatment of the synthesized powder is needed to promote the formation of the required phase. The properties of the resulting powders (crystalline structure, amorphous structure, crystallite size, purity, specific surface area and particle agglomeration) depend heavily on the adopted processing parameters (type of fuel, fuel-oxidizer ratio, and use of excess oxidizer, ignition temperature and amount of water contained in the precursor mixture) [112]. Many metal oxides viz. Al_2O_3 [113], CrO_2, Fe and nanocrystalline CoO_2 [114]. $LaBO_3$ [115] Cu/CeO_2 [116], $Ce_{0.98}Pd_{0.02}O_{2-d}$ [117], $Cu/ZnO/ZrO_2/Pd$ [118], Ni [119], $WO_3–ZrO_2$ [120], WO_3 [121], TiO_2 [122], MgO [123], Bi_2O_3 [124] have been synthesized using the solution combustion synthesis.

8. Spray Pyrolysis

Spray pyrolysis is a technique for production of dense and porous oxide films, ceramic coatings and powders even, multi-layered films can be easily prepared using this versatile technique. Unlike many other film deposition techniques, spray pyrolysis represents a very simple and relatively cost-effective

method, especially regarding equipment cost. Spray pyrolysis does not require high quality substrates or chemicals. Spray pyrolysis has been used for several decades in the glass industry [125] and in solar cell production to deposit electrically conducting electrodes [126].

Typical spray pyrolysis equipment consists of an atomizer, precursor solution, substrate heater, and temperature controller. The following atomizers are usually used in spray pyrolysis technique: air blast (liquid is exposed to a stream of air) [127], ultrasonic (ultrasonic frequencies produce the short wavelengths necessary for fine atomization) [128] and electrostatic (liquid is exposed to a high electric field) [129]. Thin film deposition using the spray pyrolysis technique involves spraying a metal salt solution onto a heated substrate **(Figure 2.7)**. Droplets impact on the substrate surface, spread into a disk shaped structure, and undergo thermal decomposition. The shape and size of the disk depends on the momentum and volume of the droplet, as well as the substrate temperature. Consequently, the film is usually composed of overlapping disks of metal salt being converted to oxide on the heated substrate.

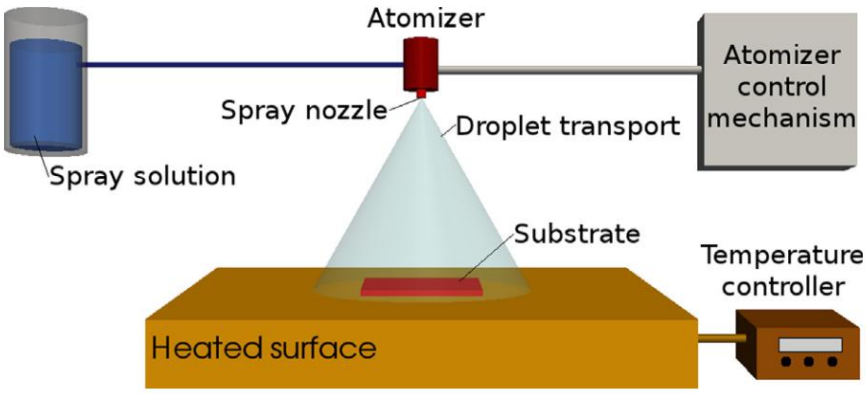

Figure 2. 7 General schematic of a spray pyrolysis deposition process.

Transparent and conducting oxide films (CuO, SnO_2 and TiO_2 etc.) as windows in solar cells had been prepared by spray pyrolysis. Highly transparent ZnO films on glass substrates have been prepared [130]. The properties of the

deposited films can be varied and controlled by changing the spray parameters, the deposition temperature for instance influences the optical and electrical properties of ZnO films [131], [132]. First of all CdS thin films for solar cell applications have been produced by this technique. Since then, the process has been investigated with various materials, such as SnO_2 [133], In_2O_3 [134], indium tin oxide (ITO) [135], PbO [136], ZnO [137], ZrO_2 [138], YSZ [132], [139,140].

2.1.2 Physical Methods

1 Laser ablation

2 Gas condensation and sputtering

3 Inert gas condensation

1 Laser Ablation

In laser ablation, high-power laser pulses are used to evaporate matter from a target surface such that the stoichiometry of the material is preserved in the interaction. As a result, a supersonic jet of particles (plume) is ejected from the target surface as shown in **Figure 2.8** and **2.9**. The plume, similar to the rocket exhaust, expands away from the target with a strong forward-directed velocity distribution of the different particles.

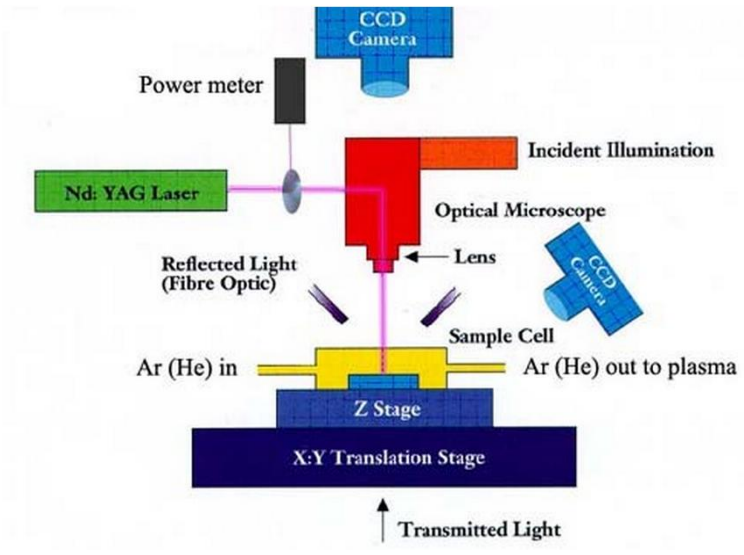

Figure 2. 8 Schematic of laser ablation system.

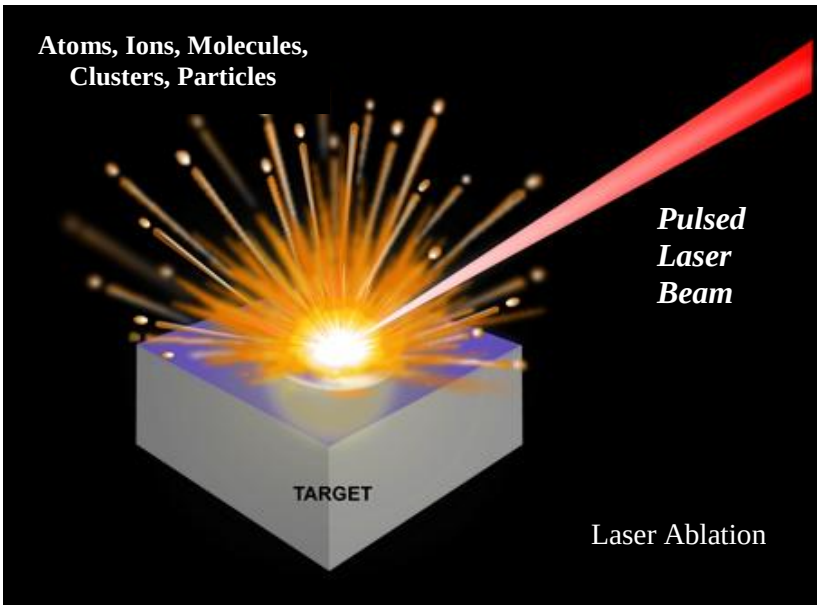

Figure 2. 9 Laser ablation: The removal of a small quantity of mass from a sample's surface using a focused, pulsed laser beam.

The ablated species condense on the substrate placed opposite to the target. The ablation process takes place either in vacuum or in the presence of some background gas. In the case of oxide films, oxygen is the most common background gas. Laser ablation of solids is a top-down method, which has attracted much interest ever since the invention of ruby laser in 1960s [141–144]. Size, shape and morphology of the nanoparticle get affected by energy of laser used. Studies revealed that smaller size nanoparticles are synthesized using lower laser energy (9.3 mJ) and a tendency of agglomeration/cementation is seen at higher laser energy [145]. This may cause a decrease in the reactivity of the nanoparticle. Further, it has been observed that the shape of the nanoparticles is changed with the laser energy, i.e., when the laser energy is increased the shape of the nanoparticles changes from spherical nature to triangular nature. Therefore it has been concluded that the spherical nanoparticles may be synthesized at lower laser energy [145]. Iron has been Synthesis at a liquid‑solid interface by pulsed laser irradiation of iron in water in 1987 [146]. Later, colloids have been synthesized by laser ablation of metallic targets in water and organic solvents, and

this method has been established as a simple yet reliable route to produce clean colloids without residual species [147,148]. Carbon nanotubes, shaped nanoparticles of metal/metal oxides also have been produced using laser ablation technique [149]. In a typical examples of Sb_2O_3 nanostructures, highly pure nanocubic Sb_2O_3, synthesized by pulsed laser ablation for different laser shots of the piece of antimony plate, Sb placed on the bottom of quartz vessel containing 3ml of ultra pure double distilled deionized water. The piece of metal was irradiated by focused energy of 500 mJ and 1064 nm wavelength of Nd:YAG (neodymium-doped yttrium aluminium garnet; $Nd:Y_3A_{l5}O_{12}$) laser. Nanowires of WO_3 growth as nano tree like structure has been synthesized by laser ablation of tungsten foil covered by SiO_2 [150], many other nanoparticles also have been synthesized e.g., metal nanoparticles, Ag, Au, [151], Cu [152],Ti, Pt [153], Al [154] bimetallic nanoparticles, AgAu, CoPt [155], AlAu [156], AgNi [157], metal oxide nanoparticles TiO_2, ZnO, Al_2O_3 [158], Ga_2O_3, In_2O_3[150], FeO [145] etc.

2 Gas Condensation and Sputtering

Gas condensation is a useful technique to synthesize nanocrystalline metals and alloys. In this technique, a metallic or inorganic material is vapourized using evaporation sources such as a Joule heated refractory crucibles, resistive heating, high energy electron beams, low energy electron beam and inducting heating etc., in an atmosphere of 1-50 mbar. In gas evaporation, a high residual gas pressure causes the formation of ultra fine particles (100 nm) by gas phase collision. The ultrafine particles are formed by collision of evaporated atoms with residual gas molecules at gas pressures greater than 3 mPa (10 torr). Clusters in the vicinity of the source by homogenous nucleation in the gas phase grow by incorporation of atoms in the gas phase. It comprises of a ultra high vacuum (UHV) system fitted evaporation source, a cluster collection device of liquid nitrogen filled cold finger scrapper assembly and compaction device. During heating, atoms condense in the supersaturation zone close to Joule heating device. The nanoparticles are removed by scrapper in the form of a metallic plate. Evaporation is to be done from W, Ta or Mo refractory metal crucibles. If the metals react with crucibles, electron beam evaporation technique is to be used. The method is extremely slow. The method

suffers from limitations such as a source-precursor incompatibility, temperature ranges and dissimilar evaporation rates in an alloy. Alternative sources have been developed over the years. For instance, Fe is evaporated into an **inert gas atmosphere** (He). Through collision with the atoms the evaporated Fe atoms loose kinetic energy and condense in the form of small crystallite crystals, which accumulate as a loose powder. Sputtering or laser evaporation may be used instead of thermal evaporation. **Sputtering** is a non-thermal process in which surface atoms are physically ejected from the surface by momentum transfer from an energetic bombarding species of atomic/molecular size. It is a physical vapour deposition (PVD) method of thin film deposition by sputtering. Typical sputtering uses a glow discharge or ion beam as energy source. In case of ion beam sputtering (**DC sputtering**) gaseous plasma is created and then ions are accelerated from this plasma into some source material ("target"), the source material is eroded by the arriving ions via energy transfer and is ejected in the form of neutral particles i.e. either individual atoms, clusters of atoms or molecules. As these neutral particles are ejected they will travel in a straight line unless they come into contact with something i.e. other particles or a nearby surface. **Figure 2.10** shows typical ion beam sputtering process. Other alternate energy sources which have been successfully used to produce clusters or ultra fine particles are sputtering electron beam, heating and plasma methods. If reactive gas is mixed with inert gas in sputtering process then this type of sputtering is called **reactive sputtering,** it is mainly used for the production of Metal oxide, nitride, sulphide etc. whereas for insulators radio frequency voltage is applied on target material then it is called **RF sputtering**. To increase the efficiency of sputtering process magnetron source is used to magnetically confine sputtering source. This type of sputtering is called **magnetron sputtering** and it can be used with DC or RF sputtering. Sputtering is used in low pressure (10^{-1} to 10^{3} Pa) environment to produce a variety of clusters including Ag [159], Fe, Mo and Si etc. [160–162]. Metallic films viz. Al-alloys, Ti, TiW, TiN [163], AlN [164], TaN [165], Nd–Fe–B [166], CrN [167] , NbN [168], Ni, Co, Au [167], Ag [167], Cu [167,169], Pt [170] etc. Typical compounds have been deposited by reactive sputtering e.g., Al_2O_3, TiO_2, MgO [168], Ta_2O_5, and ZnO [171] etc.

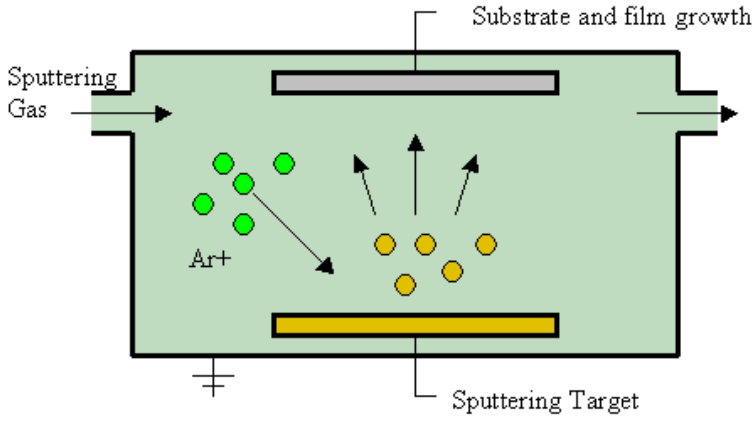

Figure 2. 10 Typical ion beam sputtering process.

3 Inert Gas Condensation

Inert-gas condensation is frequently used to make nanomaterials from metals with low melting points. Cross-section sketch of the inert gas condensation system is given in **Figure 2.11**.

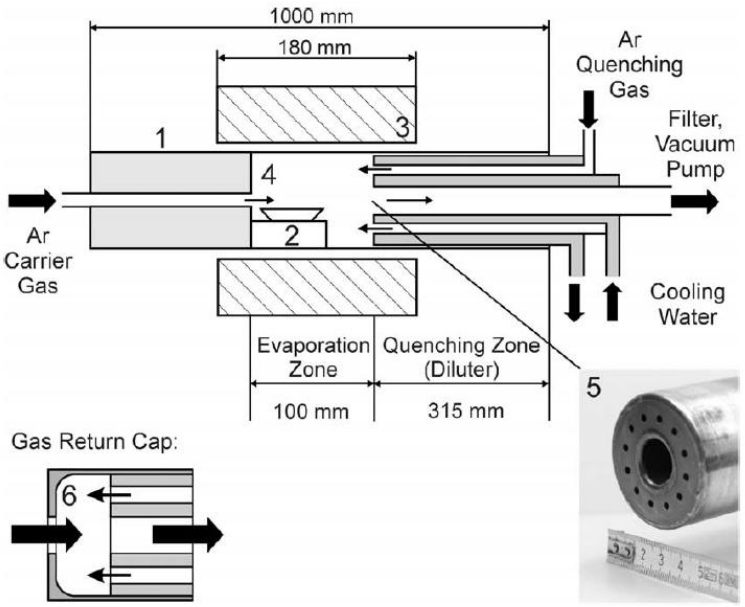

Figure 2. 11 Cross-section sketch of the inert gas condensation system.

The metal is vapourized in a vacuum chamber and then super cooled with an inert gas stream. The super cooled metal vapour condenses into nanometer-size particles, which can be entrained in the inert gas stream and deposited on a substrate It is the most advanced technique, although the technique is costly, it is considered as a controlled process as by this method the exact shape and size of the nanoparticle can be synthesized. In inert gas condensation technique, the nanoparticle as soon as they formed rapidly collides with inert gas in a low-pressure environment and thus smaller and controlled nanoparticles are formed. An inert gas condensation technique has been used to prepare nanometer-sized particles of metallic iron by evaporation and agglomeration in a flowing inert gas stream [172]. Many other nanocrystalline materials such as PbF_2, Mn^{2+}-doped PbF_2, ITO, ZnO, CuO, Al_2O_3, TiO_2 have been prepared by this technique using the ultra high vacuum (UHV) chamber [173].

In the journey of the research work different types of fly ash supported and non supported nanoparticles have been prepared using different chemical methods. The next section of this chapter deals with the preparation of non-supported TiO_2, NiO and mesoporous SiO_2 nanoparticles.

Synthesis of Nanosized Titania by Sol Gel Route using Ethylene Glycol as Gelling Agent

A number of methods for the synthesis of titania (TiO_2) nanoparticle have been reported, such as chemical precipitation [174], microemulsion [175], hydrothermal crystallization [176] and sol-gel [177]. The sol-gel process is the most successful for preparing nanosized metal oxide semiconductors. For example, sol-gel derived TiO_2 powders have been reported to show high catalytic activity due to their fine structure, wide surface area and high porosity. Previously many researchers have prepared titania by hydrolysis of alkoxides, $TiCl_4$, titanyl sulfate and ammonium dihydroxodilactatotitanate (IV) as titanium precursor [178], but titanium tetrabutoxide has not been used to prepare titania in presence of ethylene glycol (EG) as gelling agent. Thus an attempt has been made to prepare titania nanoparticles by simple sol gel route using reactants viz. EG and titanium n-butoxide.

2.2 Experimental Details

2.2.1 Materials and Reagents

The materials used for making nanoparticles of titania included titanium (IV)-n-butoxide (TNBT) as titanium precursor (AR, Merck LTD., 99.5%), n-butanol as diluting agent (AR, Ranbaxy, 99.0%), ethylene glycol as gelling agent (AR, Merck LTD., 99.5%)

2.2.2 Synthesis of Titania by EG Sol Gel Route

Titanium (IV)-n-butoxide (TNBT) (20 g) was added to n-butanol (16 g) to control hydrolysis of butoxide precursor and the mixture was stirred for 5 min using a magnetic stirrer operating at 2000 rpm for proper mixing of precursor and diluting agent. After stirring, above mixture was added to ethylene glycol (EG, 100 mL) for sol formation and mixture was stirred with heating at 85 °C till sol converted to gel then gel was dried in hot air oven at 50 °C. Dried titanium hydroxide sample was calcined at 500 °C for 3 h for proper crystallization of amorphous titanium hydroxide. To see the effect of calcination temperature on crystallinity and crystallite size of as prepared titania nanoparticles the sample

further calcined at 700 °C for 2 h. The whole process of synthesis is given in a flowchart in **Figure 2.12**.

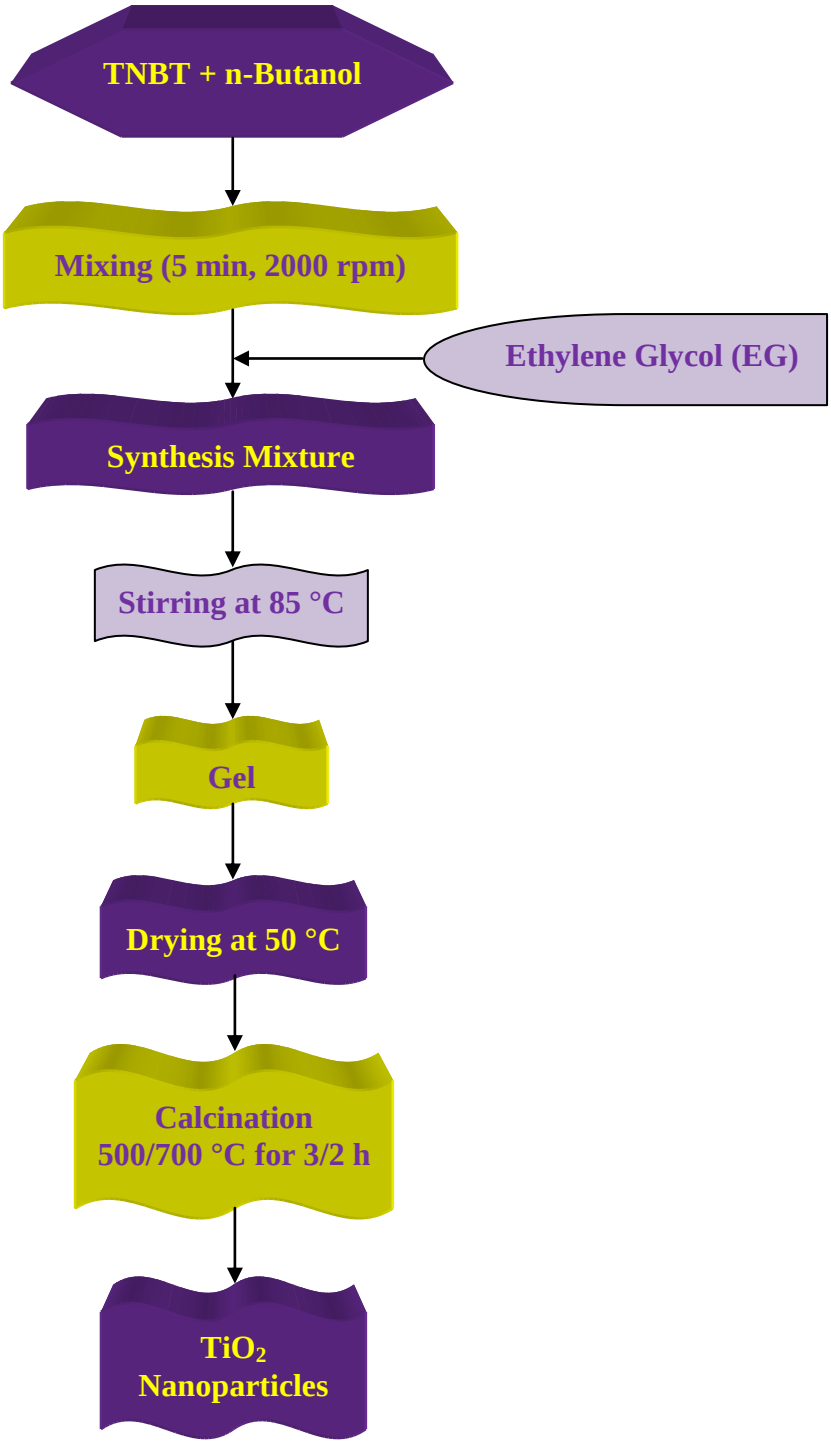

Figure 2. 12 Flowchart for synthesis process of TiO_2 nanoparticles using EG sol gel route.

2.2.3 Characterization

The synthesized materials were characterized by XRD, SEM and FT-IR analytical techniques. Detail of these techniques is given in **Annexure I**.

2.3 Results and Discussion

2.3.1 XRD Analysis

The XRD pattern of nanosized titania particles, prepared by sol gel route using EG as gelling agent calcined at 500 °C for 3 h is shown in **Figure 2.13 a**. The peaks of titania at 'd' values 3.49, 1.88, 2.35 with *hkl* values 101, 004, 200 respectively have been observed in XRD pattern. The d-values of the obtained XRD pattern recorded were compared and matched perfectly with the standard d-values along with the intensity with anatase titania as given in JCPDS card no. 21-1272 [179]. The average crystalline size of nanosized titania has been calculated by X-ray diffraction line broadening using Scherrer's equation [68] to the 100 % intensity peak-

$$d = K\lambda / \beta \cos \theta$$

where *d* represents the grain size; $K = 0.9$ is Scherrer constant related to the spherical shape and the index (hkl) of the crystals; λ represents the wavelength of the X- ray (Cu Kα, 1.54 Å); θ is the diffraction angle of the peak; The parameter β is defined as $\beta = (B^2 - b^2)^{1/2}$ (in radian) where B and b are the linewidths of the most intense TiO_2 reflection ((101) for anatase, (110) for rutile) and most intense standard reflection, respectively. The crystallite size of anatase titania sample is obtained 19 nm. The prepared nanosized powder of TiO_2 was calcined at 500 °C 3 h, leads to its conversion from amorphous phase to nanocrystalline anatase phase. The XRD pattern of titania nanopowder calcined at 700 °C for 2 h shows sharp and intense peaks with lesser peak broadening than sample calcined at 500 °C for 3 h. It can be concluded from **Figure 2.13 b** that calcinations above 500 °C increases the crystallinity as well as crystallite size of as prepared titania. In XRD pattern peaks of titania calcined at 700 °C have been observed at 'd' values 3.24, 1.68, 2.48 with *hkl* values 110, 211, 101 respectively.

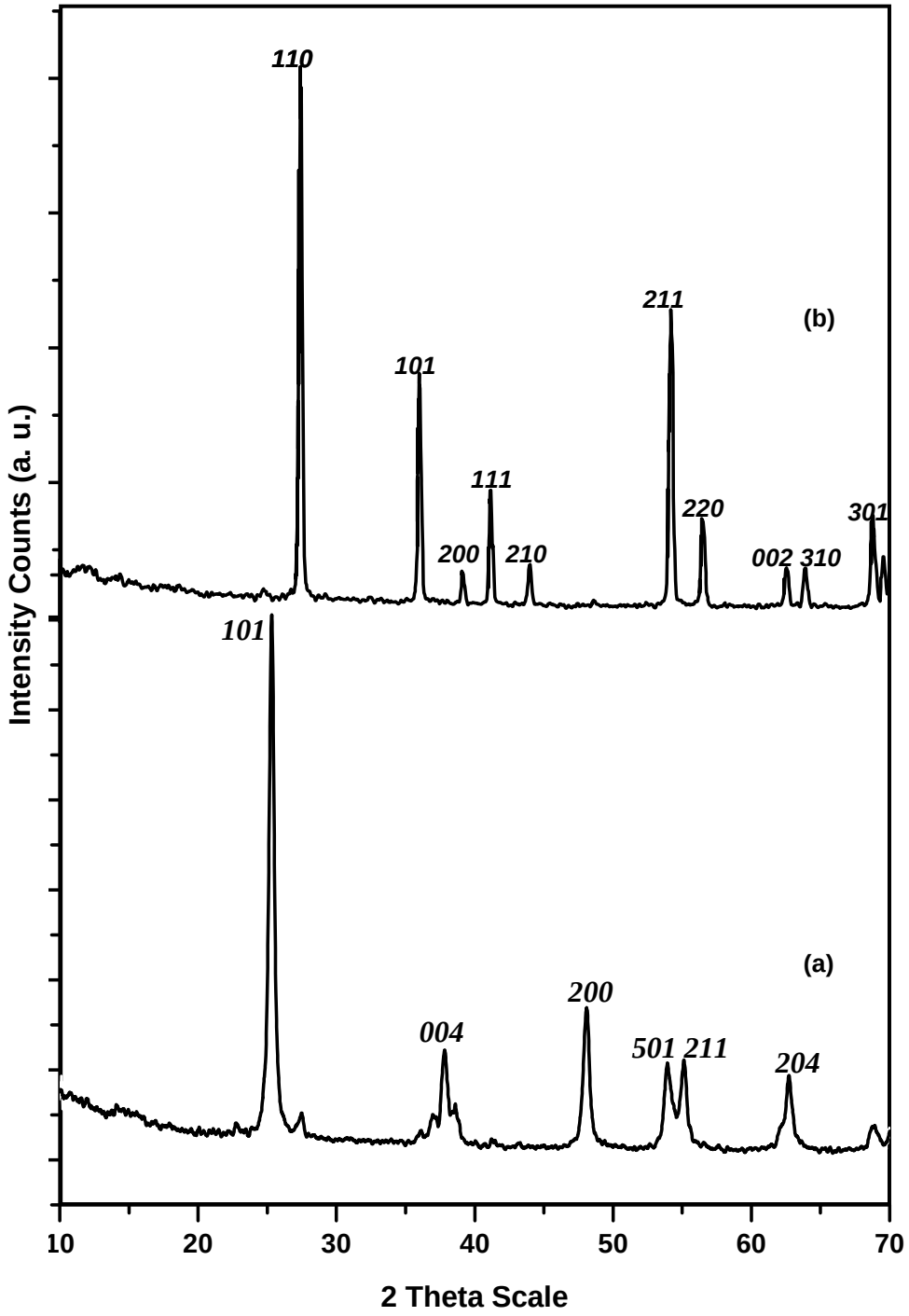

Figure 2. 13 ***XRD patterns of (a) nanosized anatase titania obtained from sol gel route calcined at 500 °C for 3 h, (b) rutile titania calcined at 700 °C for 2 h.***

The d-values of the obtained XRD pattern recorded were compared and matched perfectly with the standard d-values along with the intensity with rutile TiO_2 (JCPDS card no. 21-1276) [179]. As prepared titania at 700 °C completely converted from anatase phase to rutile phase. The average crystallite size of rutile titania is obtained 50 nm as calculated by Scherrer's equation.

2.3.2 SEM Analysis

The SEM image of nanosized titania particles, prepared by sol gel route using EG as gelling agent is shown in **Figure 2.14**. The crystal size of the powder sample of TiO_2 is of 19 nm size as estimated by Scherrer's equation. SEM photograph shows that particles are strongly aggregated which is typical for particles with a size less than 50 nm, so the particle size was estimated to be 20-50 nm. To reduce agglomeration and measure the accurate size and see the accurate shape of as prepared titania nanoparticles dispersion of titania powder has been prepared by mixing pinch of titania powder in 0.01 M aqueous solution of CTAB (cetyltrimethylammonium bromide) the mixture was stirred for half an hour on a magnetic stirrer. One drop of above dispersion was placed on a stub. Then drop was dried under IR lamp prior to SEM study. **Figure 2.14 (b, c)** shows SEM images after proper dispersion in CTAB which shows that titania has rode shaped morphology with 1 µm average rode length. These rods are narrower at both edges than centre. The average width at edges is found 50 nm and at centre it is of approximately 100 nm. It can be seen from **Figure 2.14 b** that some particles are of D shaped plates.

2.3.3 FT-IR Analysis

Figure 2.15 presents the FT-IR spectra of dried gel before and after decomposition at 500 °C for 3h. The broad peaks between 3800 and 2000 cm^{-1} observed in dried gel sample (**Figure 2.15 a**) have signatures of hydroxyl groups. Also, the sharp peaks centred on 1621, 1451, and 1080 cm^{-1} can be attributed to C=C (alkenes) stretching, -C-H bending and –C-O stretching, respectively. A broad peak at 736 cm^{-1} arises due to =C-H bending [180]. After decomposition of gel at 500 °C for 3h, the product depicts a major peak at 506 cm^{-1} (**Figure 2.15 b**) corresponding to Ti-O bond [181]. Another peak at ~3367 cm^{-1}arises due to the adsorbed water after the decomposition.

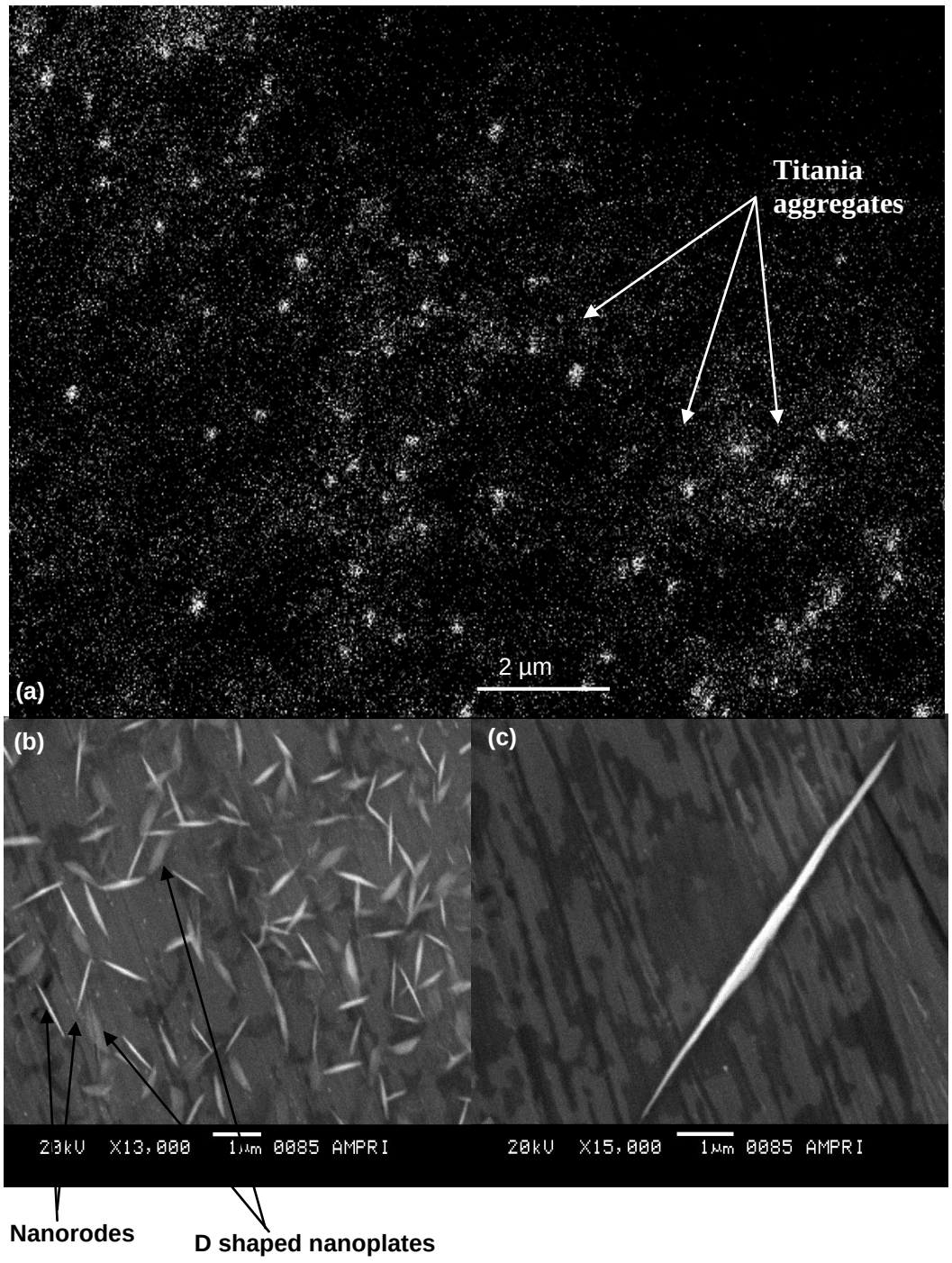

Figure 2. 14 ***SEM photograph of nanosized titania obtained from sol gel route at 500 °C (a) before CTAB dispersion and (b, c) after CTAB dispersion.***

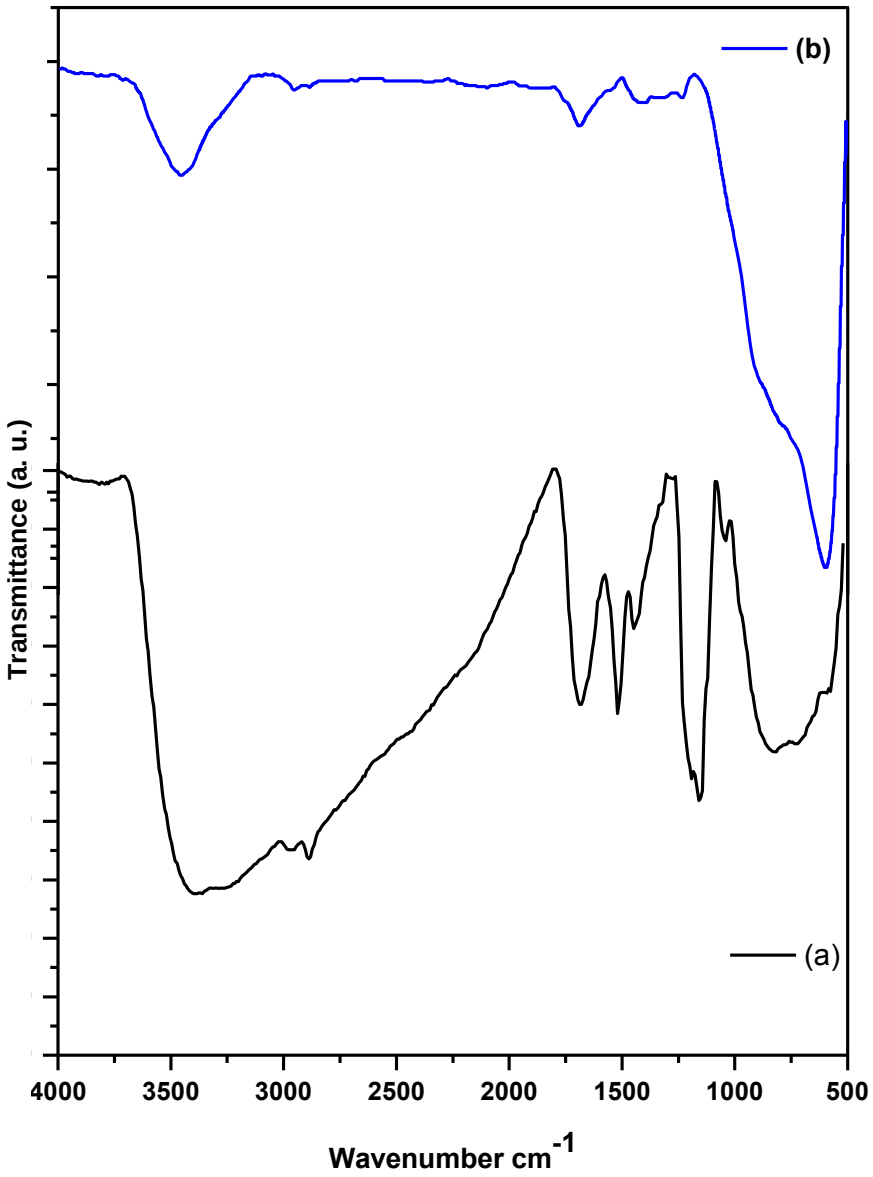

Figure 2. 15 FT-IR spectra of dried gel (a) before and (b) after decomposition at 500 °C for 3h.

2.4 Conclusion

TiO_2 nanoparticles have been synthesized by sol gel route using ethylene glycol as gelling agent. The physical properties, such as crystallite size and crystallinity, morphology were investigated by XRD and SEM. X-ray diffraction pattern shows that TiO_2 particles calcined at 500 °C for 3 h have stable anatase phase with 19 nm average crystallite size, determined according to the Scherrer's equation. TiO_2 particles calcined at 700 °C for 2 h are more crystalline than anatase titania nanoparticles and have stable rutile phase with 50 nm average crystallite size. The SEM image shows that particles have rode shaped morphology. The yield of the prepared titania was quite good. Thus sol gel route using EG is a simple, cost effective, less energy consuming route for synthesis of rode shaped nanosized anatase titania.

Reverse Microemulsion Route for Synthesis of Nickel Oxide Nanoparticles

In the present work nickel oxide nanoparticles have been prepared using the novel single microemulsion system in which mixed reverse microemulsion of aqueous nickel salt solution, blend of anionic and non-ionic surfactant, and oil phase was used. Liquid ammonia was directly added to the above microemulsion system. The synthesis involves hydrolysis of nickel salt in the mixed reverse micelle system leading to the formation of phase pure bunsenite nickel oxide nanoparticles at room temperature. A unique blend of anionic and non-ionic surfactant was used in the preparation of NiO nanoparticles, this blend is more rigid than single moiety of ionic surfactant due to polymer nature of non-ionic surfactant, rigidity of the surfactant layer is essential factor for controlling the size of the nanoparticles in single microemulsion approach [12]. Intermediate values of occupancy the number and surfactant layer rigidity, both intramicellar and intermicellar nucleation and growth contribute to the final particle size [12].

2.5 Experimental Details

2.5.1 Materials and Reagents

The materials used for making phase pure nanoparticles of nickel oxide included cyclohexane as oil phase (AR grade, Merck LTD., 99.5%), distilled water, tween-80 as non ionic surfactant (AR grade, Merck LTD., 99.98%), docusate sodium AOT as anionic surfactant (AR grade, HiMedia Laboratories Pvt. Ltd., 98.0%), n-propanol as co-surfactant (AR grade, Ranbaxy, 99.0%), nickel chloride hexahydrate as nickel precursor (AR grade, Merck LTD, 99.98%), liquid ammonia as hydrolyzing agent (AR grade, Rankem, 25%).

2.5.2 Synthesis of Phase Pure Nanoparticles of Nickel Oxide

The flow chart for the preparation of nanoparticles of nickel oxide powder in mixed reverse microemulsion is given in **Figure 2.16** and the detailed discussion of the same is mentioned below.

First of all a mixed reverse microemulsion was prepared mixing 400 mL cyclohexane, 6 mL aqueous solution of 0.1 M nickel chloride hexahydrate, 8.89 gm AOT, 49.4 mL tween-80, and 20 mL n-propanol. Microemulsion mixture was stirred vigorously using a magnetic stirrer at 1500 rpm at room temperature to obtain transparent green solution revealing the formation of micron size water droplets homogenously dispersed in continuous oil phase. Further the solution of liquid Ammonia was taken in a burette and was added drop wise at the rate of 0.2 mL/min to the mixed reverse microemulsion system using a magnetic stirrer at 1500 rpm at room temperature till the precipitate of the nickel hydroxide was appeared. Then the precipitate of the nickel hydroxide so obtained was filtered using whatman no. 42 filter paper, and was washed repeatedly with 15 mL deionised water in each washing cycle and followed by washing with 15 mL solution of methanol and chloroform in 1:1 volume ratio in each washing cycle, in order to remove the organic residues and surfactant. The washed material was then dried in hot air oven at 80 °C for 10 h. The dried material was powdered with mortar and pestle and then calcined at 450 °C for 3 h in a muffle furnace. The calcined powder was again slightly crushed with mortar and pestle and used for further characterization.

2.5.3 Characterization

The synthesized materials were characterized by XRD, SEM, FT-IR and TGA techniques. Detail is given in **Annexure I**.

2.6 Results and Discussion

2.6.1 XRD Analysis

The purity and crystallinity of as-synthesized nickel oxide nanoparticles were examined using powder X-ray diffraction (XRD) as shown in **Figure 2.17**. It can be seen from XRD that the diffraction peaks are low and broad due to the small size effect and incomplete inner structure of the particles. The peaks appearing at 2θ = 37.185°, 43.223°, and 62.828° are indexed as (111), (200), and (220) respectively and represents face-centered cubic (FCC) crystalline structure of nickel oxide.

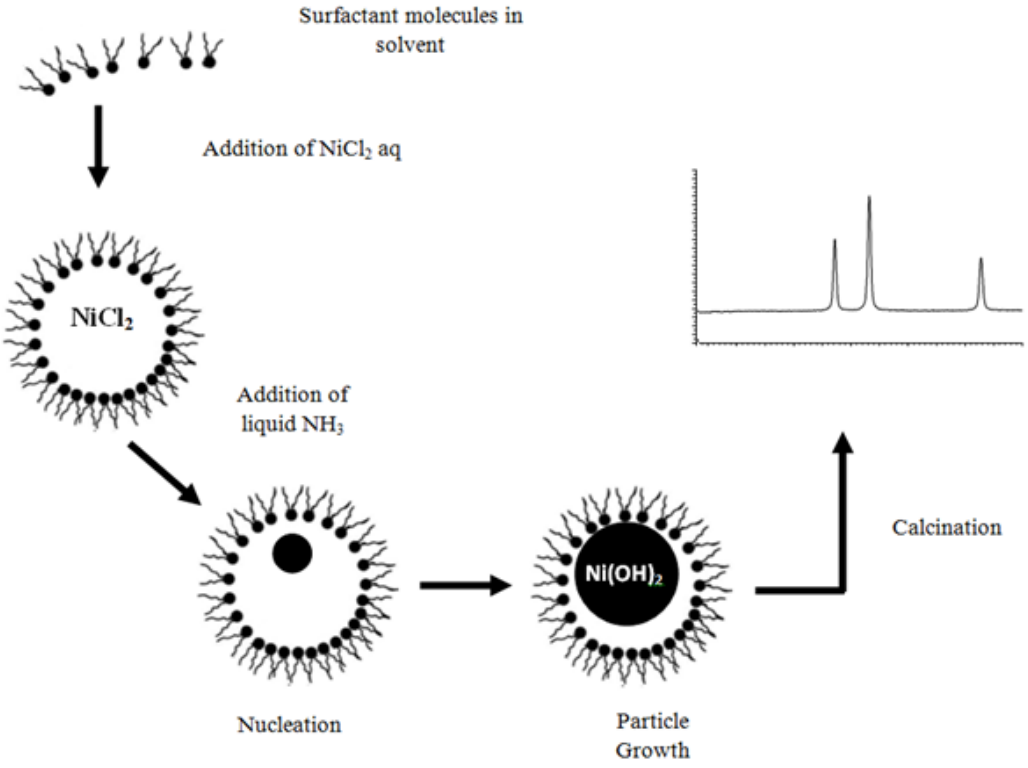

Figure 2. 16 Overall mixed reverse microemulsion process for synthesizing nickel oxide nanoparticles.

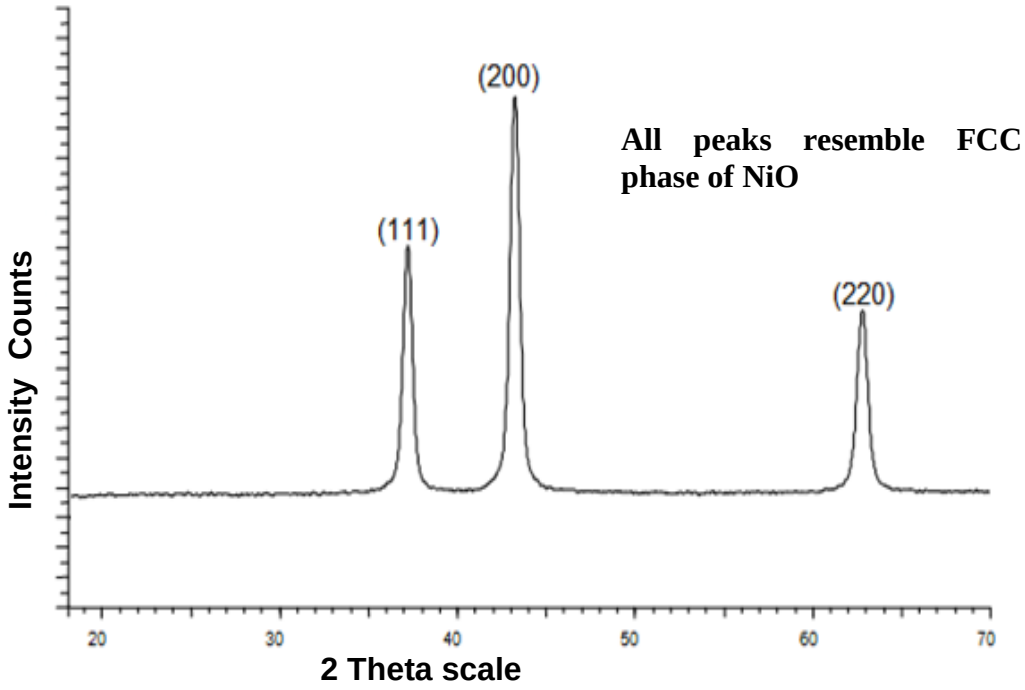

Figure 2. 17 XRD pattern of nickel oxide nanoparticles calcined at 450 °C for 3h.

All these diffraction peaks, not only in peak position but also in their relative intensity, are absolutely matched with the standard spectrum (JCPDS, No. 04-0835) [179]. The XRD pattern shows that the sample is single phase and no any other impurities diffraction peak except the characteristic peaks of FCC phase nickel oxide was detected. The average crystallite size is calculated by X-ray diffraction line broadening using the Scherrer's formula ($d = K\lambda/B \cos\theta$) to 100% intensity peak. The crystallite size of nickel oxide sample is 14 nm which was calculated from measured values for spacing of the (200) plane. In comparison with other microemulsion systems formed in presence of single surfactant, the mixed reverse microemulsion process produced small, less aggregated, and phase pure nickel oxide nanoparticles, due to intermediate effect of both surfactants which causes both inter and intramicellar nucleation and growth [8,182].

2.6.2 SEM Analysis

For microstructural studies samples are prepared for SEM analysis as given in experimental paragraph. **Figure 2.18** presents the SEM image of nanosized nickel oxide powder obtained by mixed reverse microemulsion route, using Tween-80 and AOT as surfactants. It can be seen from the figure that the particles are spherical in shape and the particle size was estimated to be 14-50 nm by SEM image.

2.6.3 FT-IR Analysis

Figure 2.19 shows the FT-IR spectrum of NiO nanoparticles, which showed several significant absorption peaks. The broad absorption band centered at 483 cm^{-1} is assigned to Ni–O stretching vibration mode [183], the broadness of the absorption band indicates that the NiO powders are nanocrystals. The size of samples used in this study was much less than the bulk form NiO, so that NiO nanoparticles have FT-IR peak of Ni–O stretching vibration and shifted to blue direction. Due to their quantum size effect and spherical nanostructures, the FT-IR absorption of NiO nanoparticles is blue-shifted compared to that of the bulk form [184]. Besides the Ni–O vibration, it could be seen from **Figure 2.19** that the broad absorption band in the region of 3000-3700 cm^{-1} is attributable to the O–H stretching vibrations and the weak band near 1628 cm^{-1} is assigned to H–O–H

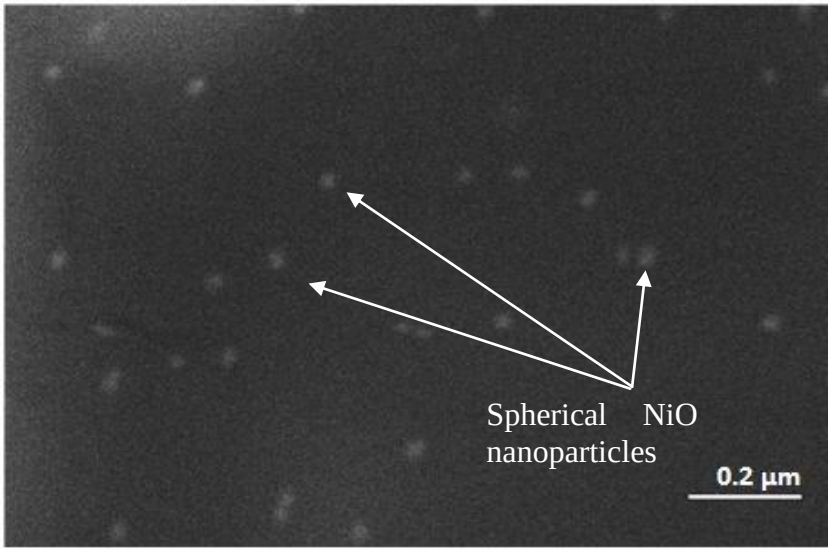

Figure 2. 18 SEM photograph of nickel oxide nanoparticles calcined at 450 °C for 3h.

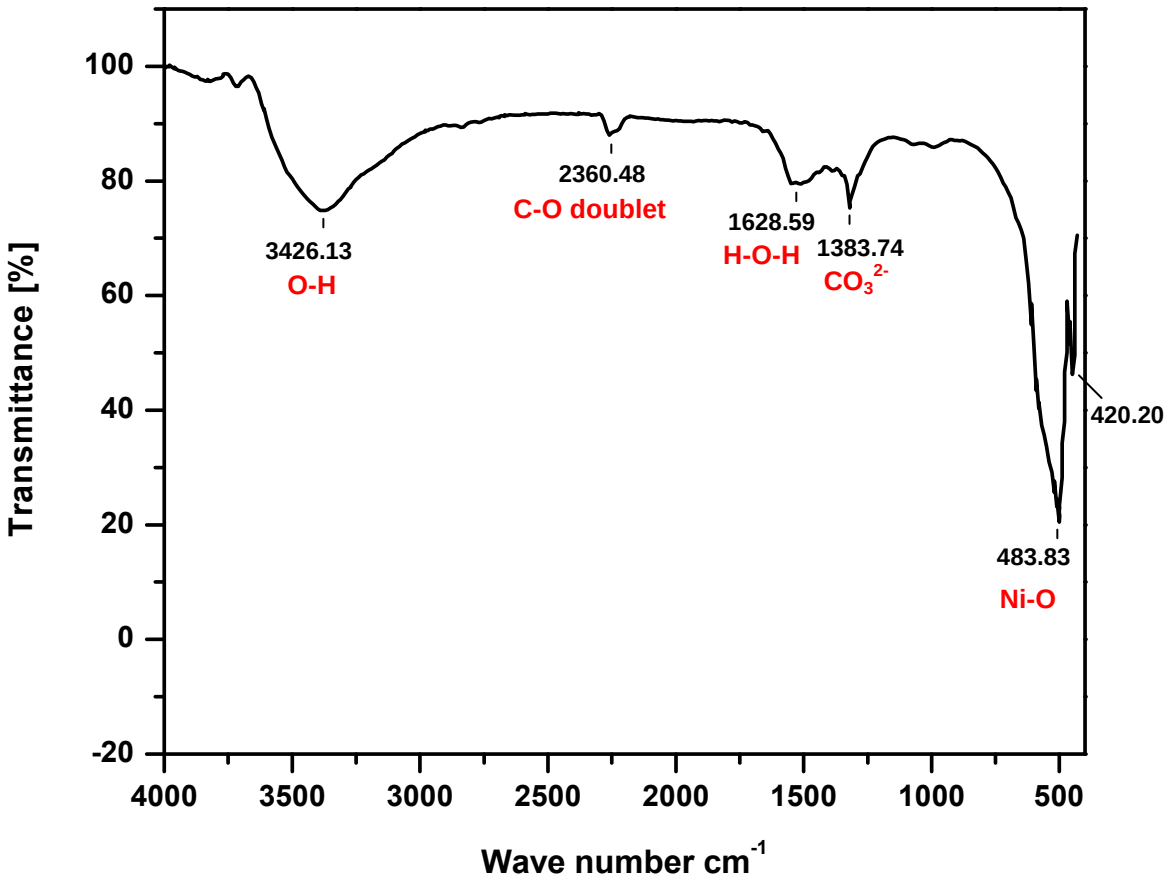

Figure 2. 19 FT-IR Spectrum of nickel oxide nanoparticles calcined at 450 °C for 3h.

bending vibrations mode. These observations provided the evidence to the effect of hydration in the structure. Meanwhile, it implied the presence of hydroxyl in the precursor. The absorption bands 1383 cm^{-1} is assigned to the O–C=O symmetric and asymmetric stretching vibrations and the C–O stretching vibration, but the intensity of the band is weakened, a weak band at 2360 is due to absorption doublet of CO_2 [185], which indicated that the ultrafine powers can have physically absorped H_2O and CO_2 [46].

2.6.4 TGA Analysis

Figure 2.20 shows the TGA curve of NiO precursor ($Ni(OH)_2$). It can be seen that the thermal decomposition of the precursor can be divided into four separated regions. The first region is related to the evaporation of the absorbed water between 50 and 100 °C, at which most of the water will be vanished. In the second region, the residue water will be evaporated by a temperate rate. Appearance of significant weight loss in the third region is due to calcination of structural water. The structural water, which has band structure with nickel and oxygen atoms inside the molecule, will be eliminated before 300 °C. This event may lead to formation pure NiO nanoparticles. In the last region, the molecule will be stable and the weight of molecule is nearly constant without any other of weight loss. **Scheme 2.1** shows the conversion of NiO from $Ni(OH)_2$ form by mixed reverse microemulsion during calcinations.

2.7 Conclusion

Thus a novel process involving mixed reverse microemulsion route has been developed for preparing nickel oxide nanoparticles. The novelty of the process lies in the fact that conventionally either cationic or anionic or non ionic surfactants are used for the synthesis of nickel oxide nanoparticles. Whereas in the present developed novel process preparation of nickel oxide nanoparticles has been carried out using a unique blend system consisting of tween-80 and AOT. The X-ray diffraction pattern confirms the presence of phase pure bunsenite phase with FCC crystal structure where as the SEM image exhibits the particle size of 14 to 50 nm, spherical shape and narrow size distribution of the nickel oxide nanoparticles.

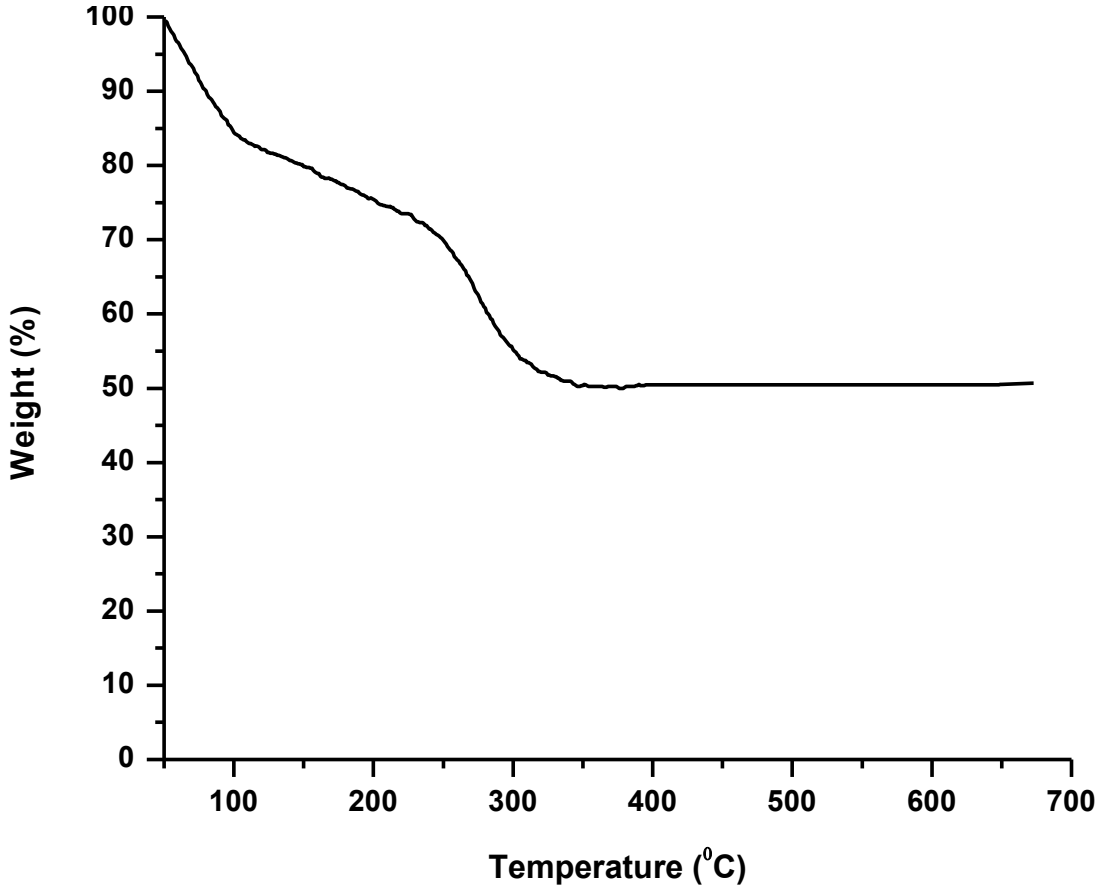

Figure 2. 20 Thermograph of the NiO precursor.

$$NH_4OH_{(aq)} \rightarrow NH_{3(aq)} + H^+ + OH^-_{(aq)}$$

$$Ni(NO_3)_2 \cdot 6H_2O_{(s)} \longrightarrow Ni^{2+}{}_{(aq)} + 2NO_3{}^-{}_{(aq)} + 6H_2O_{(aq)},$$

$$Ni^{2+}{}_{(aq)} + 2OH^-{}_{(aq)} + xH_2O_{(aq)} \longrightarrow Ni(OH)_2 \cdot xH_2O_{(s)} \downarrow,$$

$$Ni(OH)_2 \cdot xH_2O_{(s)} \xrightarrow{50-100} Ni(OH)_{2(s)} + xH_2O_{(g)} \uparrow,$$

$$Ni(OH)_{2(s)} \xrightarrow{300} NiO_{(s)} + H_2O_{(g)} \uparrow .$$

Scheme 2. 1 Conversion of $Ni(OH)_2$ into NiO nanoparticles during calcinations.

Hydrothermal Synthesis of Mesoporous Silica from Coal Fly Ash

In recent times, a significant concentration is given on the mesoporous catalytic materials for ensuring fast synthesis of multipurpose organic compounds owing to their high surface area, large pore size and volume. Mesoporous materials have become an alternative source to make chemical process green and environmentally benevolent. Mesoporous materials can be synthesized using various silica precursors. The present study is concerned with the synthesis of mesoporous silica (MS) from coal fly ash (CFA) and its characterization using various techniques. CFA is mainly composed of some oxides resulting from inorganic compounds, which remain even after the combustion of the coal. SiO_2 and Al_2O_3, are the significant contents of CFA and show few variations with the type of coal. MS synthesis processes engross the addition of Sodium Hydroxide (NaOH) to the CFA slurry at higher temperatures. Blend of the NaOH-CFA mixture facilitates the formation of highly active Sodiumaluminate and silicates, which are eagerly soluble in water and enhance formation of MS. It was thought desirable to collect CFA from thermal power plant at Kota, Rajasthan and renovate it into value added mesoporous material which could be used as catalysts for some industrially important reactions [186].

2.8 Experimental Details

2.8.1 Materials and Reagents

Fly ash was collected from the electrostatic precipitators of the Kota Thermal Power Plant in Rajasthan (India). The representative sample fly ash was prepared by coning and quartering. Cetyl trimethylammonium bromide (CTAB, AR grade, Merck), liquid ammonia (AR grade, Merck), NaOH (LR, grade, RANKEM) were used as the starting materials in the present work. All chemical were used as such without further purification.

2.8.2 Hydrothermal Synthesis of Mesoporous Silica

The whole process of synthesis of mesoporous silica is given in **Figure 2.21** and **Figure 2.22**. In this method fly ash was fused by mixing with crushed NaOH palates in a weight ratio 1:1.2 at 500 °C for five hour using a heating rate of 1°C/minute. After fusion, the powder was mixed with water in a weight ratio of 0.10 to produce the fused fly ash solutions. The fused fly ash solutions were aged for one day at room temperature and ambient pressure with stirring.

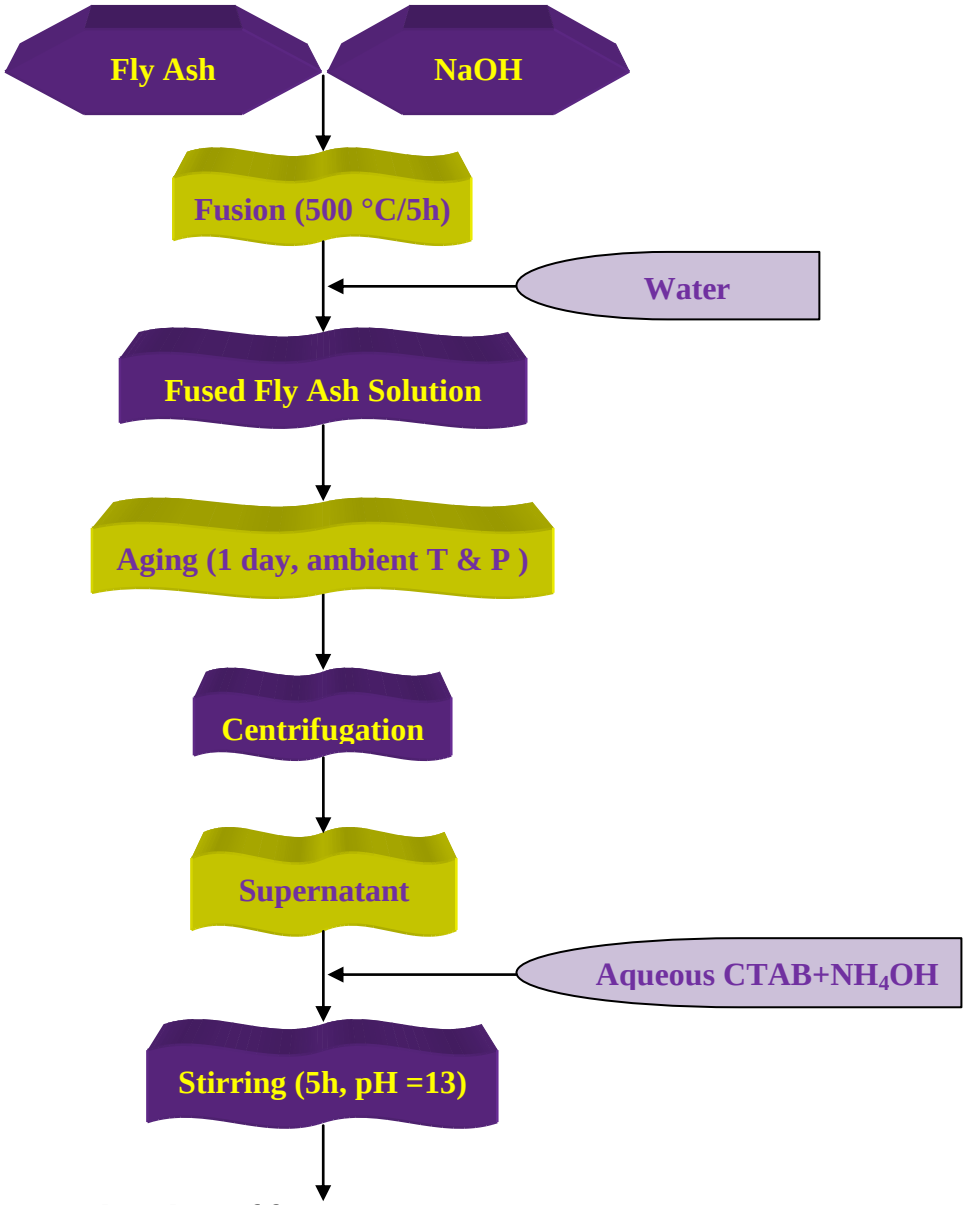

Figure 2. 21 Flow chart of fusion process.

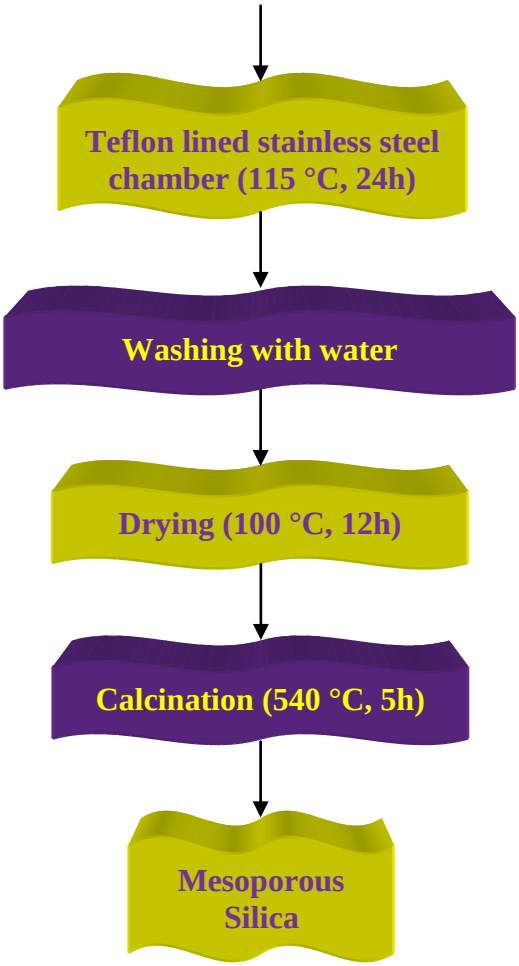

Figure 2. 22 Flow chart of hydrothermal curing used for preparation of mesoporous silica.

The supernatant of the solution was separated by centrifugation. The surfactant solution was prepared by mixing 0.755 g of surfactant (CTAB) with 2.265 g of distilled water at room temperature. When the surfactants were fully dissolved, 5 mL of liquid ammonia solution was added to the surfactant solution and the solution was diluted by adding 12.28 mL of distilled water. The aqueous surfactant solution was then added to 50 mL of supernatant solution and stirred for 5 hrs. The pH value of the mixed solutions was maintained about 13. The mixed solutions were then hydrothermally cured at 115 °C in a Teflon lined stainless steel chamber. Powder samples were taken out after 24 hrs and washed with distilled water. The washed powders were dried at 100 °C for 12 h. The powders were then heated at 540 °C with a heating rate of 5 °C/minute and soaked at 540 °C for 5 h.

2.8.3 Characterization

The synthesized materials were characterized by, XRD, FT-IR, HRTEM and BET analytic techniques. Detail is given in **Annexure I**.

2.9 Results and Discussion

2.9.1 XRD Analysis

The powder X-ray diffraction pattern (XRD) of MS is shown in **Figure 2.23**. XRD is recorded between 2θ values of 1-10°only because amorphous materials do not show Bragg peaks above 2θ =10°, above 10° such materials show only characteristics hump. XRD pattern displayed Bragg peaks in the 2θ = 1.5-8° range, which can be indexed to different *hkl* reflections. The XRD pattern of MS powder consisted of the typical reflection at 2.54° (211) and weak reflections at 2.9° (220), 4.7° (420), and 4.9° (332) which corresponds to the d-spacing of 34.8, 30.3, 18.8, and 19.0 Å, respectively, which matched perfectly with the standard d-values along with the intensity given in JCPDS card no. 42-3143 [179]. Peaks present between 2θ = 1.5-8° range are inferred that prepared MS is contains only pure amorphous phases with no impurity of crystalline phases.

2.9.2 FT-IR Analysis

The FT-IR spectrum of MS sample shown in **Figure 2.24** is relatively simple and well assigned. A sharp absorption band at 3432 cm^{-1} in the spectrum of MS presents single Si-OH and hydrogen-bonded Si-OH groups. Single Si-OH group is also called the "geminal group". These germinal Si-OH groups are supposed to be responsible for the functionalization of mesoporous silica instead of hydrogen bonded Si-OH groups. The strong absorbance at 1085 cm^{-1} and 795 cm^{-1} were associated with Si-O-Si asymmetric and symmetric band stretching, respectively. The band at around 967 cm^{-1} was assigned to the symmetric stretching of Si-OH. The presence of peaks at 454 cm^{-1} and 1639 cm^{-1} were due to the Si-O out of plane deformation and C-O bending vibrations respectively.

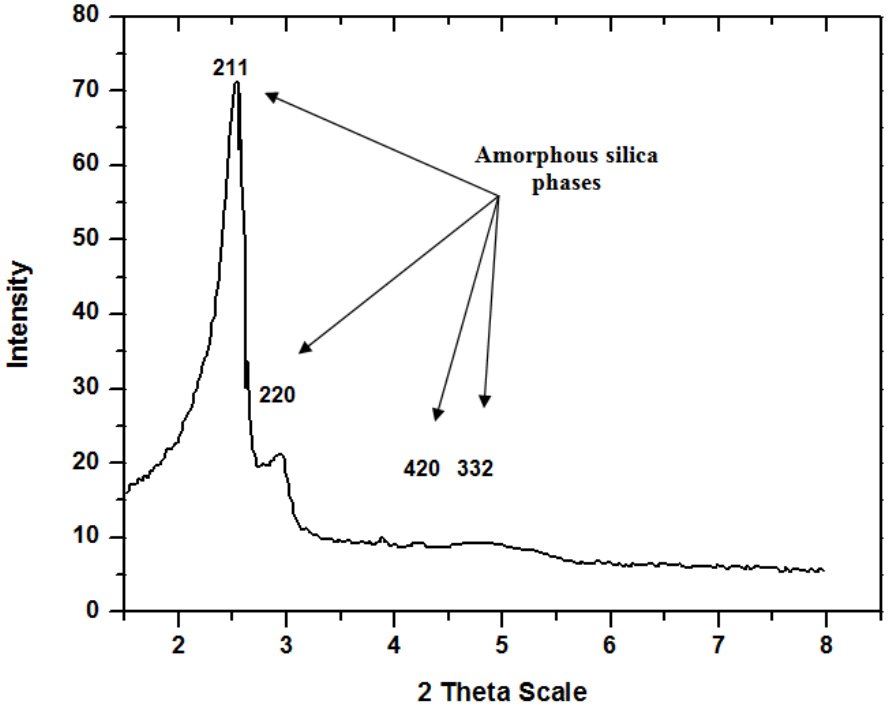

Figure 2. 23 X-ray diffraction spectra of fly ash derived MS using hydrothermal synthesis at 115 °C for 24 h.

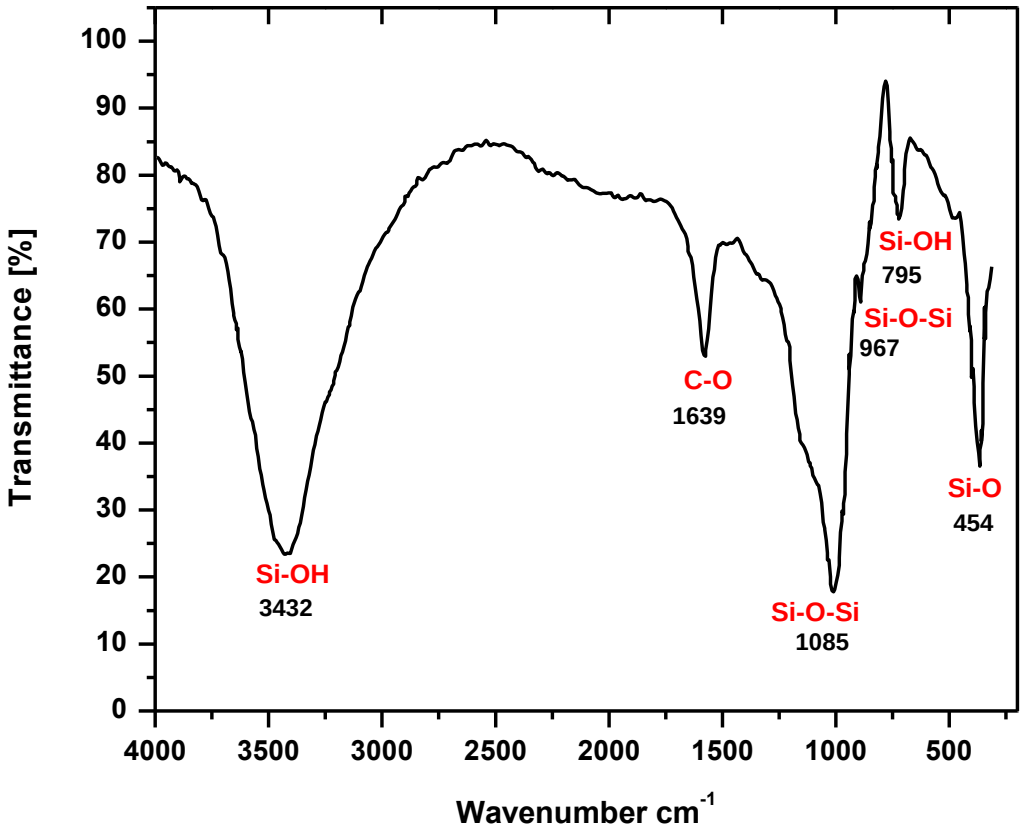

Figure 2. 24 The FT-IR spectra of fly ash derived MS using hydrothermal synthesis at 115 °C for 24 h.

2.9.3 BET Surface Area Analysis

A very higher surface area for the sample observed to be 1250 m^2/g then silica source fly ash. This significant higher surface area provides additional proof that hydrothermally synthesized MS is more amorphous than MS synthesized at room temperature.

2.9.4 TEM Analysis

The morphological studies of synthesized sample were carried out using high resolution transmission electron microscope (HRTEM) shown in the **Figures 2.25 (a, b)**. HRTEM of the sample confirms that the shape of the MS samples is spherical. Porous structure of the surface of mesoporous materials can also be seen in the micrographs. HRTEM of MS shown in the **Figure 2.25 (b)**, shows that pores are regular and in a honeycomb arrangement. Specific pore arrangement is characteristics of specific type of MCM. Honeycomb arrangement of pores is characteristics of MCM-41. Hence synthesized mesoporous silica is MCM-41 [187]. Pore size calculated by HRTEM was observed to be < 3 nm.

2.10 Conclusion

Mesoporous silica was successfully synthesized by fly ash by hydrothermal treatment. The synthesized sample contains the square shaped porous structure confirmed by its XRD, FTIR, HRTEM results. Synthesized mesoporous silica sample belongs to MCM-41 family since are there on the surface of samples. 1250 m^2/g surface area for fly ash assisted hydrothermally synthesized mesoporous silica sample was observed. Hydrothermally synthesized mesoporous silica sample was observed amorphous and less agglomerated. Pore size of the mesoporous silica sample, calculated with help of HRTEM, was observed to be < 3 nm.

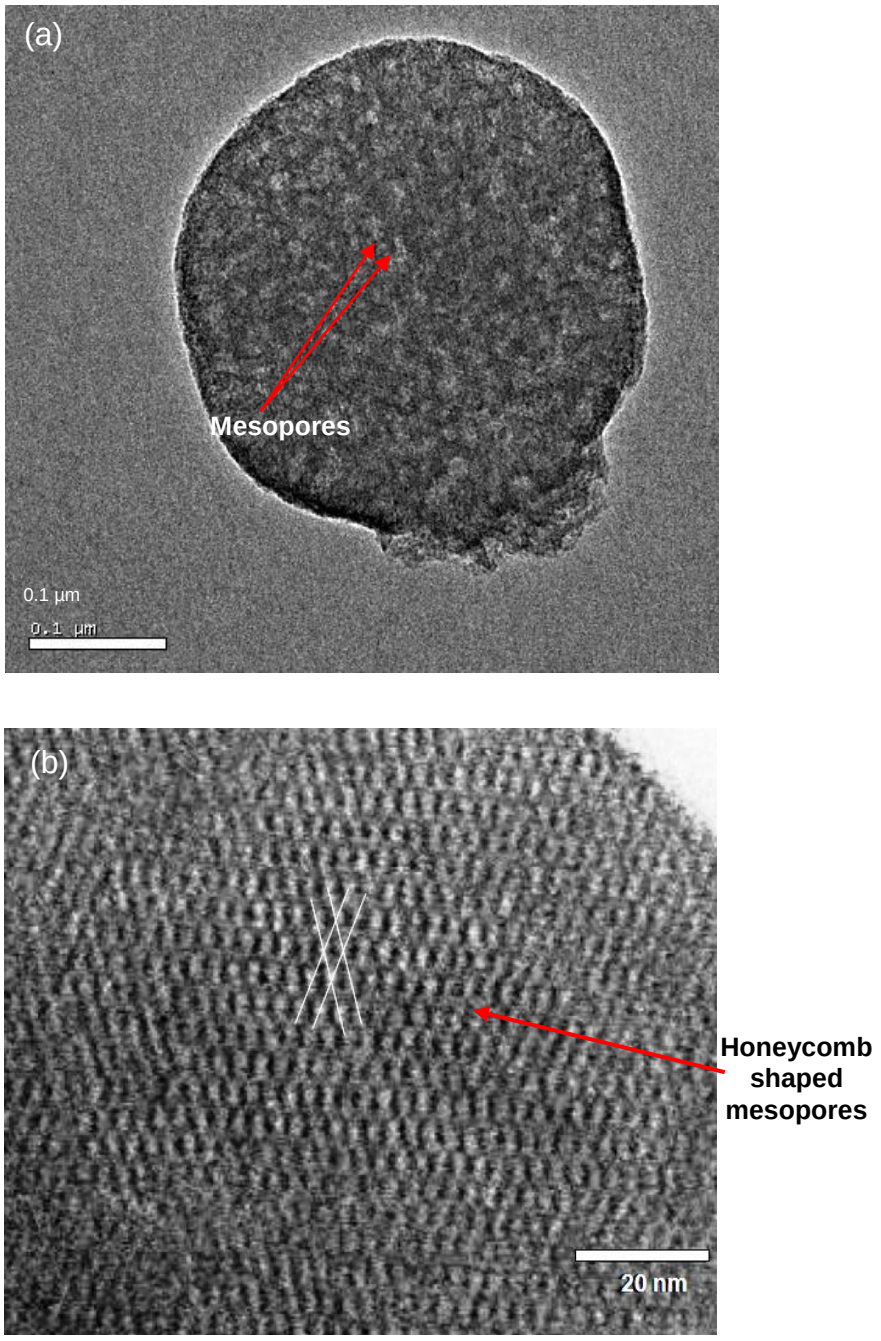

Figure 2. 25 ***HRTEM micrographs of fly ash derived MS using hydrothermal synthesis at 115 °C for 24 h, a) HRTEM micrographs of single MS particle, b) HRTEM micrographs of single MS particle at high magnification.***

2.11 References

[1] V.T. Liveri, Controlled Synthesis of Nanoparticles in Microheterogeneous Systems, Springer Science & Business Media, 2006.

[2] A. Ekimov, J. Lumin. 70 (1996) 1.

[3] P. Tartaj, J. Tartaj, Acta Mater. 50 (2002) 5.

[4] A.P. Alivisatos, J. Phys. Chem. 100 (1996) 13226.

[5] Q.H. Powell, G.P. Fotou, T.T. Kodas, B.M. Anderson, Chem. Mater. 9 (1997) 685.

[6] S. Sahoo, T. De, P. Ghosh, A. Maitra, J. Colloid Interface Sci. 206 (1998) 361.

[7] S. Eriksson, Appl. Catal. A Gen. 265 (2004) 207.

[8] P. Palanisamy, A.M. Raichur, Mater. Sci. Eng. C 29 (2009) 199.

[9] R. D'Amato, M. Falconieri, S. Gagliardi, E. Popovici, E. Serra, G. Terranova, E. Borsella, J. Anal. Appl. Pyrolysis 104 (2013) 461.

[10] Y. Bayazitoglu, R. Cerny, Int. J. Heat Mass Transf. 36 (1993) 3449.

[11] E. Hedaya, M.E. Kent, J. Am. Chem. Soc. 93 (1971) 3283.

[12] E.G. and A.Z. Anna Zielińska-Jurek, Joanna Reszczyńska, in:, R. Najjar (Ed.), Microemulsions - An Introd. to Prop. Appl., InTech, 2012, p. 23.

[13] S. Mahshid, M. Askari, M. Sasani Ghamsari, N. Afshar, S. Lahuti, J. Alloys Compd. 478 (2009) 586.

[14] F. L. Y. Lam, X. Hu, Chem. Eng. Sci. 58 (2003) 687.

[15] X.J. Li, N. Luo, M.L. Bai, in:, Mater. Sci. Forum, 2011, pp. 161–166.

[16] J.H. Bang, K.S. Suslick, Adv. Mater. 22 (2010) 1039.

[17] A. Dip, K.G. Reid, Low-Temperature Dielectric Film Formation by Chemical Vapor Deposition, US7994070 B1, 2011.

[18] F. Farzaneh, N.F. Hamedani, V. Daadmehr, J. Sci. Islam. Repub. Iran 19 (2008) 119.

[19] C. Sorin Cojocaru, D. Kim, D. Pribat, J.-E. Bourée, Thin Solid Films 501 (2006) 227.

[20] X. Chen, S.S. Mao, Chem. Rev. 107 (2007) 2891.

[21] J.R. Vargas Garcia, E.M. Lazcano Ugalde, F. Hernandez Santiago, J.M. Hallen Lopez, J. Nanosci. Nanotechnol. 8 (2008) 2703.

[22] R.-S. Chen, Y.-S. Chen, Y.-S. Huang, Y.-L. Chen, Y. Chi, C.-S. Liu, K.-K. Tiong, A.J. Carty, Chem. Vap. Depos. 9 (2003) 301.

[23] R. Riedel, E. Ionescu, I.W. Chen, in:, R. Riedel, I Wei Chen (Eds.), Ceram. Sci. Technol. Vol. 1 Struct., 1st ed., WILEY-VCH Verlag GmbH & Co. KGaA, Weinheim, 2008, pp. 1–38.

[24] O. Jung, S. Kim, K. Cheong, W. Li, S.I. Saha, Bull. Korean Chem. Soc. 24 (2003) 14.

[25] W.-J. An, E. Thimsen, P. Biswas, J. Phys. Chem. Lett. 1 (2010) 249.

[26] F. Zhang, R. Barrowcliff, G. Stecker, W. Pan, D. Wang, S.-T. Hsu, Jpn. J. Appl. Phys. 44 (2005) L398.

[27] P.S. Leung, in:, A.R. Cooper (Ed.), Ultrafiltr. Membr. Appl., 1st ed., Plenum Press· New York and London, California, 1980, p. 705.

[28] J.D. Wright, N.A.J.M. Sommerdijk, Sol-Gel Materials: Chemistry and Applications, CRC Press, 2000.

[29] C.J. Brinker, G.W. Scherer, Sol-Gel Science: The Physics and Chemistry of Sol-Gel Processing, Gulf Professional Publishing, 1990.

[30] L.L. Hench, J.K. West, Chem. Rev. 90 (1990) 33.

[31] B.L. Cushing, V.L. Kolesnichenko, C.J. O'Connor, Chem. Rev. 104 (2004) 3893.

[32] F. Feil, W. Fürbeth, M. Schütze, Surf. Eng. 24 (2008) 198.

[33] B.L. Bischoff, M.A. Anderson, Chem. Mater. 7 (1995) 1772.

[34] R. Thakkar, U. Chudasama, J. Hazard. Mater. 172 (2009) 129.

[35] T. Moreau, C. Depagne, G. Suissa, H. Gouzi, T. Coradin, J. Mater. Chem. B 1 (2013) 1235.

[36] H. Tan, X. Ma, M. Fu, Bull. Mater. Sci. 36 (2013) 153.

[37] Y. Su, C. Shen, H. tao Yand, H. lin Li, H. jun Gao, Trans. Nonferrous Met. Soc. China 17 (2007) 783.

[38] R. Adnan, N.A. Razana, I.A. Rahman, M.A. Farrukh, J. Chinese Chem. Soc. 57 (2010) 222.

[39] G. Orsini, V. Tricoli, J. Mater. Chem. 21 (2011) 14530.

[40] C.C. Tang, E.M. Elssfah, J. Zhang, D.F. Chen, Nanotechnology 17 (2006) 2362.

[41] S.. Moon, H. Mametsuka, E. Suzuki, Y. Nakahara, Catal. Today 45 (1998) 79.

[42] R. Sui, J.L. Young, C.P. Berlinguette, J. Mater. Chem. 20 (2010) 498.

[43] Y. Jin, Y. Zhu, X. Yang, C. Wei, C. Li, Mater. Chem. Phys. 106 (2007) 209.

[44] P. Tartaj, M.P. Morales, S. Veintemillas-Verdaguer, T. Gonzalez-Carreño, C.J. Serna, Handb. Magn. Mater. 16 (2006) 403.

[45] M. Mohapatra, S. Anand, Sci. Technol. 2 (2010) 127.

[46] Y. Bahari Molla Mahaleh, S.K. Sadrnezhaad, D. Hosseini, J. Nanomater. 2008 (2008) 1.

[47] K. Petcharoen, A. Sirivat, Mater. Sci. Eng. B 177 (2012) 421.

[48] L.T. Shwe, P.P. Win, in:, Int. Work. Nanotechnol. 2013, 2013.

[49] S.H. Tolbert, P. Sieger, G.D. Stucky, S.M.J. Aubin, C.-C. Wu, D.N. Hendrickson, J. Am. Chem. Soc. 119 (1997) 8652.

[50] N. Sahoo, Surfactant Mediated Synthesis and Characterization of Zinc Oxide Nanoparticles, n.d.

[51] M.G. Sujana, K.K. Chattopadyay, S. Anand, Appl. Surf. Sci. 254 (2008) 7405.

[52] E. Gopinathan, G. Viruthagiri, N. Shanmugam, Int. J. Recent Sci. Res. 5 (2014) 1892.

[53] S. Layek, M. Mohapatra, S. Anand, H.C. Verma, J. Nanosci. Nanotechnol. 13 (2013) 1834.

[54] M. Boutonnet, J. Kizling, P. Stenius, G. Maire, Colloids and Surfaces 5 (1982) 209.

[55] M.K. Sharma, D.O. Shah, in:, D.O. Shah (Ed.), Macro- and Microemulsions, American Chemical Society, Washington, D.C., 1985, pp. 1–18.

[56] S. Nassos, Development of Catalytic Nanomaterials for Three Industrial Processes, Chalmers University of Technology, 2007.

[57] J.J. Spivey, G.W. Roberts, S. Rojas, S. Eriksson, M. Boutonnet, in:, J.J. Spivey, G.W. Roberts (Eds.), Catalysis, Royal Society of Chemistry, Cambridge, 2004, pp. 256–292.

[58] I. Lisiecki, M.P. Pileni, J. Am. Chem. Soc. 115 (1993) 3887.

[59] J.N. Solanki, Z.V.P. Murthy, Ind. Eng. Chem. Res. 50 (2011) 12311.

[60] H.R. Ghorbani, Orient. J. Chem. 30 (2014) 803.

[61] M. Mihaly, M.C. Fleancu, N.L. Olteanu, D. Bojin, A. Meghea, M. Enachescu, Comptes Rendus Chim. 15 (2012) 1012.

[62] C.C. Wang, D.H. Chen, T.C. Huang, Colloids Surfaces A Physicochem. Eng. Asp. 189 (2001) 145.

[63] R.A. Martínez Rodríguez, F.J. Vidal Iglesias, J. Solla Gullón, C.R. Cabrera, J.M. Feliu, J. Am. Chem. Soc. 136 (2014) 1280.

[64] M.L. Wu, D.H. Chen, T.C. Huang, J. Colloid Interface Sci. 243 (2001) 102.

[65] H.K. Wang, C.Y. Yi, L. Tian, W. Wang, J. Fang, J.H. Zhao, W.G. Shen, J. Nanomater. 2012 (2012) 1.

[66] J. Feng, C.-P. Zhang, J. Colloid Interface Sci. 293 (2006) 414.

[67] J.A. Adekoya, E.O. Dare, M.A. Mesubi, N. Revaprasadu, J. Mater. 2014 (2014) 1.

[68] R. Hada, A. Amritphale, S.S. Amritphale, S. Dixit, Open Miner. Process. J. 3 (2010) 68.

[69] R. Hada, A. Rani, V. Devra, S.S. Amritphale, Int. Res. J. Pure Appl. Chem. 3 (2013) 111.

[70] M. Fernández-garcia, J.A. Rodriguez, (2007).

[71] J. Eastoe, M.J. Hollamby, L. Hudson, Adv. Colloid Interface Sci. 128-130 (2006) 5.

[72] C. Destrée, F. Debuigne, L. Jeunieau, J.B. Nagy, Adv. Colloid Interface Sci. 123-126 (2006) 353.

[73] K. Holmberg, J. Colloid Interface Sci. 274 (2004) 355.

[74] M.A. López-Quintela, C. Tojo, M.C. Blanco, L. García Rio, J.R. Leis, Curr. Opin. Colloid Interface Sci. 9 (2004) 264.

[75] M.P. Pileni, Langmuir 13 (1997) 3266.

[76] M.-P. Pileni, Nat. Mater. 2 (2003) 145.

[77] M. Sanchez-dominguez, C. Aubery, C. Solans, D. Investigación, M. Avanzados, S.C. Cimav, U. Monterrey, (2011).

[78] K.S. Suslick, J. Acoust. Soc. Am. 87 (1990) 919.

[79] J. Zhu, Y. Koltypin, A. Gedanken, Chem. Mater. 12 (2000) 73.

[80] K.S. Suslick, S.B. Choe, A.A. Cichowlas, M.W. Grinstaff, Nature 353 (1991) 414.

[81] Y. Koltypin, G. Katabi, X. Cao, R. Prozorov, A. Gedanken, J. Non. Cryst. Solids 201 (1996) 159.

[82] Y. Nagata, Y. Mizukoshi, K. Okitsu, Y. Maeda, Radiat. Res. 146 (1996) 333.

[83] T. Hyeon, M. Fang, K.S. Suslick, J. Am. Chem. Soc. 118 (1996) 5492.

[84] X. Cao, Y. Koltypin, R. Prozorov, G. Kataby, A. Gedanken, J. Mater. Chem. 7 (1997) 2447.

[85] N.A. Dhas, A. Gedanken, J. Phys. Chem. B 101 (1997) 9495.

[86] S. Ramesh, Y. Koltypin, R. Prozorov, A. Gedanken, Chem. Mater. 4756 (1997) 546.

[87] Z.F. Zhu, Z.L. He, J.Q. Li, D.G. Liu, N. Wei, Mater. Res. Innov. 14 (2010) 426.

[88] S.O. A, Z. Dmitry, C.B. R, Rusnano (2009) 1.

[89] A. Tiwari, Biosensors Nanotechnology, Wiley, 2014.

[90] H. Hayashi, Y. Hakuta, Materials (Basel). 3 (2010) 3794.

[91] S.J. Nejad, A. Golzary, Int. J. Chem. Eng. Appl. 2 (2011).

[92] M. O'Donoghue, A Guide to Man-Made Gemstones, Van Nostrand Reinhold Company, 1983.

[93] C. Xu, Continuous And Batch Hydrothermal Synthesis Of Metal Oxide, Georgia Institute of Technology, 2006.

[94] H. Hayashi, K. Torii, J. Mater. Chem. 12 (2002) 3671.

[95] R.B. Yahya, H. Hayashi, T. Nagase, T. Ebina, Y. Onodera, N. Saitoh, Chem. Mater. 13 (2001) 842.

[96] Y. Hakuta, K. Shimoyachi, H. Hayashi, K. Armi, J. Ion Exch. 14 (2003) 393.

[97] J. Kim, Y.-S. Park, B. Veriansyah, J.-D. Kim, Y.-W. Lee, Chem. Mater. 20 (2008) 6301.

[98] J. Yang, J. Pan, Acta Mater. 60 (2012) 4753.

[99] H. Liu, Y. Xu, S. Wen, J. Zhu, L. Zheng, M. Shen, J. Zhao, G. Zhang, X. Shi, Polym. Chem. 4 (2013) 1788.

[100] M.H. So, C.M. Ho, R. Chen, C.M. Che, Chem. Asian J. 5 (2010) 1322.

[101] M. Wang, K. Do Woo, D.K. Kim, Energy Convers. Manag. 47 (2006) 3235.

[102] H. Chen, J.H. Lee, Y.H. Kim, D.W. Shin, S.C. Park, X. Meng, J.B. Yoo, J. Nanosci. Nanotechnol. 10 (2010) 629.

[103] B.J. Borah, H. Saikia, P. Bharali, New J. Chem. 38 (2014) 2748.

[104] W. Wang, G. Cao, J. Nanoparticle Res. 9 (2007) 1153.

[105] O. V Belousov, N. V Belousova, A. V Sirotina, L.A. Solovyov, A.M. Zhyzhaev, S.M. Zharkov, Y.L. Mikhlin, Langmuir 27 (2011) 11697.

[106] Y. Hakuta, T. Ohashi, H. Hayashi, K. Arai, J. Mater. Res. 19 (2004) 2230.

[107] T. Noguchi, K. Matsui, N.M. Islam, Y. Hakuta, H. Hayashi, J. Supercrit. Fluids 46 (2008) 129.

[108] C. Xu, A.S. Teja, J. Supercrit. Fluids 39 (2006) 135.

[109] S. Ohara, T. Mousavanda, M. Umetsua, S. Takamia, T. Adschiri, Y. Kurokib, M. Takatab, Solid State Ionics 172 (2004) 261.

[110] K. Byrappa, T. Adschiri, Prog. Cryst. Growth Charact. Mater. 53 (2007) 117.

[111] K.C. Patil, S.T. Arun, S. Ekambaram, Curr. Opin. Colloid Interface Sci. 2 (1997) 158.

[112] J.J. Kingsley, K.C. Patil, Mater. Lett. 6 (1988) 427.

[113] T. Mimani, K.C. Patil, Mater. Phys. Mech. 4 (2001) 134.

[114] A. Kopp Alves, C.P. Bergmann, F.A. Berutti, (2013).

[115] S.T. Aruna, A.S. Mukasyan, Curr. Opin. Solid State Mater. Sci. 12 (2008) 44.

[116] N.F.P. Ribeiro, M.M.V.M. Souza, M. Schmal, J. Power Sources 179 (2008) 329.

[117] S. Roy, M.S. Hegde, Catal. Commun. 9 (2008) 811.

[118] S. Schuyten, P. Dinka, A.S. Mukasyan, E. Wolf, Catal. Letters 121 (2007) 189.

[119] Y. Chen, W. Zhou, Z. Shao, N. Xu, Catal. Commun. 9 (2008) 1418.

[120] M.A. Naik, B.G. Mishra, A. Dubey, Colloids Surfaces A Physicochem. Eng. Asp. 317 (2008) 234.

[121] W. Morales, M. Cason, O. Aina, N.R. de Tacconi, K. Rajeshwar, J. Am. Chem. Soc. 130 (2008) 6318.

[122] T. Aarthi, G. Madras, Catal. Commun. 9 (2008) 630.

[123] B. Nagappa, G.T. Chandrappa, Microporous Mesoporous Mater. 106 (2007) 212.

[124] R.K. Jha, R. Pasricha, V. Ravi, Ceram. Int. 31 (2005) 495.

[125] J.M. Mochel, Electrically Conducting Coatings on Glass and Other Ceramic Bodies, US2564707 A, 1951.

[126] R.R. Chamberlin, J.E. Hill, Process for Making Conductive Film, US3148084 A, 1964.

[127] A.R. Balkenende, A.A.M.B. Bogaerts, J.J. Scholtz, R.R.M. Tijburg, H.X. Willems, Philips J. Res. 50 (1996) 365.

[128] S.P.S. Arya, H.E. Hintermann, Metall. Coatings Thin Film. 1990; Proc. 17th Int. Conf. Metall. Coatings 8th Int. Conf. Thin Film. 2 (1990) 841.

[129] C. Chen, E.M. Kelder, P.J.J.M. van der Put, J. Schoonman, J. Mater. Chem. 6 (1996) 765.

[130] J. Aranovich, J. Vac. Sci. Technol. 16 (1979) 994.

[131] H.H. Afify, S.A. Nasser, S.E. Demian, J. Mater. Sci. Mater. Electron. 2 (1991) 152.

[132] D. Perednis, Solid State Ionics 166 (2004) 229.

[133] G. Korotcenkov, V. Brinzari, J. Schwank, M. Dibattista, A. Vasiliev, 77 (2004) 244.

[134] S.M. Rozati, T. Ganj, Renew. Energy 29 (2004) 1671.

[135] J.C. Manifacier, J.P. Fillard, Thin Silid Film. 77 (1981) 67.

[136] H.Y. Koo, S.K. Hong, S.H. Ju, I.S. Seo, Y.C. Kang, J. Non. Cryst. Solids 352 (2006) 3270.

[137] F.P. D., W.L. Estrada, D.R.N. Acosta, E. Andrade, M. Miki-yoshida, Thin Silid Film. 350 (1999) 192.

[138] G.L. Messing, S.C. Zhang, G. V. Jayanthi, J. Am. Ceram. Soc. 76 (1993) 2707.

[139] L. Filipovic, S. Selberherr, G.C. Mutinati, E. Brunet, S. Steinhauer, A. Köck, J. Teva, J. Kraft, J. Siegert, F. Schrank, Microelectron. Eng. 117 (2014) 57.

[140] J.B. Mooney, S.B. Radding, Annu. Rev. Mater. Sci. 12 (1982) 81.

[141] H.M. Smith, A.F. Turner, Appl. Opt. 4 (1965) 147.

[142] H.W. Kroto, J.R. Heath, S.C. O'Brien, R.F. Curl, R.E. Smalley, Nature 318 (1985) 162.

[143] A.M. Morales, C.M. Lieber, Science (80-.). 279 (1998) 208.

[144] D.B. Chrisey, A. Piqué, R.A. McGill, J.S. Horwitz, B.R. Ringeisen, D.M. Bubb, P.K. Wu, Chem. Rev. 103 (2003) 553.

[145] A. Kebede, A. V. Gholap, A.K. Rai, World J. Nano Sci. Eng. 01 (2011) 89.

[146] P. Patil, D. Phase, S. Kulkarni, S. Ghaisas, S. Kanetkar, S. Ogale, V. Bhide, Phys. Rev. Lett. 58 (1987) 238.

[147] Z. Yan, D.B. Chrisey, J. Photochem. Photobiol. C Photochem. Rev. 13 (2012) 204.

[148] J. Neddersen, G. Chumanov, T.M. Cotton, Appl. Spectrosc. 47 (1993) 1959.

[149] T. Guo, P. Nikolaev, A. Thess, D.T. Colbert, R.E. Smalley, Chem. Phys. Lett. 243 (1995) 49.

[150] L.M.E.L. Nadi, G. Mehena, M.M. Omar, A. Hussein, F.H.A. Taieb, F.M.A. Rahim, (n.d.).

[151] F.B. Verduraz, F. Fievet, J.Y. Piquemal, R. Brayner, K.E. Kabouss, Y. Soumare, G. Viau, G. Shafeev, Brazilian J. Phys. 39 (2009) 134.

[152] V. Amendola, M. Meneghetti, Phys. Chem. Chem. Phys. 11 (2009) 3805.

[153] P. Wagener, S. Barcikowski, N. Bärsch, P. Gmbh, Photonik (2011) 2.

[154] D. Jang, D. Kim, Appl. Phys. A 79 (2003).

[155] S.C. Singh, R. Gopal, Bullatin Mater. Sci. 30 (2007) 291.

[156] R. Singh, R.K. Soni, J. Nanosci. Lett. 3 (2013) 11.

[157] Q. Xiao, Z. Yao, J. Liu, R. Hai, H.Y. Oderji, H. Ding, Thin Solid Films 519 (2011) 7116.

[158] G. Dorcioman, D. Ebrasu, I. Enculescu, N. Serban, E. Axente, F. Sima, C. Ristoscu, I.N. Mihailescu, J. Power Sources 195 (2010) 7776.

[159] P. Asanithi, S. Chaiyakun, P. Limsuwan, J. Nanomater. 2012 (2012) 1.

[160] G.M. Chow, A. Pattnaik, T.E. Schlesinger, R.C. Cammarata, M.E. Twigg, A.S. Edelstein, J. Mater. Res. 6 (2011) 737.

[161] G.M. Chow, C.L. Chien, A.S. Edelstein, J. Mater. Res. 6 (2011) 8.

[162] F.H. Kaatz, G.M. Chow, A.S. Edelstein, J. Mater. Res. 8 (2011) 995.

[163] T.Q. Li, S. Noda, Y. Tsuji, T. Ohsawa, H. Komiyama, J. Vac. Sci. Technol. A Vacuum, Surfaces, Film. 20 (2002) 583.

[164] M. Ishihara, S.. Li, H. Yumoto, K. Akashi, Y. Ide, Thin Solid Films 316 (1998) 152.

[165] C.S. Shin, D. Gall, Y.W. Kim, N. Hellgren, I. Petrov, J.E. Greene, J. Appl. Phys. 92 (2002) 5084.

[166] W.F. Liu, S. Suzuki, K. Machida, J. Magn. Magn. Mater. 308 (2007) 126.

[167] K.P. Almtoft, Structural Characterization of Nanocrystalline Thin Films Grown by Magnetron Sputtering, University of Aarhus, Denmark, 2006.

[168] E. Alfonso, J. Olaya, G. Cubillos, in:, M.R.B. Andreeta (Ed.), Cryst. Sci. Technol., Colombia, 2011.

[169] S. Lee, J.Y. Kim, T.W. Lee, W.K. Kim, B.S. Kim, J.H. Park, J.-S. Bae, Y.C. Cho, J. Kim, M.W. Oh, C.S. Hwang, S.Y. Jeong, Sci. Rep. 4 (2014) 6230.

[170] J.S. Agustsson, U.B. Arnalds, A.S. Ingason, K.B. Gylfason, K. Johnsen, S. Olafsson, J.T. Gudmundsson, J. Phys. Conf. Ser. 100 (2008) 082006.

[171] F.C.M. Van De Pol, F.R. Blom, T.J.A. Popma, Thin Solid Films 204 (1991) 349.

[172] C. Baker, S. Ismat Shah, S.K. Hasanain, B. Ali, L. Shah, G. Li, T. Ekiert, K.M. Unruh, MRS Proc. 746 (2011) Q4.4.

[173] S. Ramasamy, D.J. Smith, P. Thangadurai, K. Ravichandran, T. Prakash, K. Padmaprasad, V. Sabarinathan, Pramana - J. Phys. 65 (2005) 881.

[174] L.K. Campbell, B.K. Na, E.I. Ko, Chem. Mater. 4 (1992) 1329.

[175] U. Selvaraj, A. V. Prasadarao, S. Komarneni, R. Roy, J. Am. Ceram. Soc. 75 (1992) 1167.

[176] T. Sugimoto, K. Okada, H. Itoh, J. Colloid Interface Sci. 193 (1997) 140.

[177] T. Masui, K. Fujiwara, K. Machida, G. Adachi, T. Sakata, H. Mori, Chem. Mater. 9 (1997) 2197.

[178] Z.R. Ismagilov, L.T. Tsikoza, N. V Shikina, V.F. Zarytova, V. V Zinoviev, S.N. Zagrebelnyi, Russ. Chem. Rev. 78 (2009) 873.

[179] A.C.S. JCPDS--International Centre for Diffraction Data, Mineral Powder Diffraction File: Search Manual : Chemical Name, Hanawalt, Fink, Mineral Name Mineral Powder Diffraction File, JCPDS--International Centre for Diffraction Data, 1986, 1986.

[180] A. Chowdhury, J. Kumar, Mater. Sci. Technol. 22 (2006) 1249.

[181] A. Amlouk, L. El Mir, S. Kraiem, S. Alaya, J. Phys. Chem. Solids 67 (2006) 1464.

[182] Y. Du, W. Wang, X. Li, J. Zhao, J. Ma, Y. Liu, G. Lu, Mater. Lett. 68 (2012) 168.

[183] N. Dharmaraj, P. Prabu, S. Nagarajan, C.H. Kim, J.H. Park, H.Y. Kim, Mater. Sci. Eng. B 128 (2006) 111.

[184] H. Qiao, Z. Wei, H. Yang, L. Zhu, X. Yan, J. Nanomater. 2009 (2009) 1.

[185] R.P. Eischens, W.A. Pliskin, in:, Adv. Catal. Proc. Int. Congr. Catal., Elsevier, Pennsylvania, 1957, pp. 662–668.

[186] M.R. Deshpande, N. V Kalyankar, U.D. Joshi, Shodh, Samiksha Aur Mulyankan 2832 (2013) 1.

[187] I. Fechete, Y. Wang, J.C. Védrine, Catal. Today 189 (2012) 2.

Non Aqueous Synthesis of Fly Ash Supported TiO_2 Nanoparticles for Enhanced Photo-Oxidation of Congo Red Dye

Abstract

This chapter addresses the modification of fly ash surface using dispersion of TiO_2 over fly ash surface. A novel methodology has been described for the same which resulted into a cost effective, efficient and highly active photocatalyst. The novel non aqueous sol gel route is used to prepare pure TiO_2 nanoparticles and fly ash supported TiO_2 for photocatalytic oxidation of azo dyes i.e., Congo red where titanium isopropoxide, methanol and glycerol are used as titanium precursor, solvent and gelling agent respectively. The chapter includes the characterization findings by different analytical techniques such as FT-IR, SEM-EDS, TEM and XRD etc., used for the characterization of prepared catalysts. The detailed results of comparative study of photocatalytic activity of fly ash, TiO_2 and fly ash supported TiO_2 as tested by oxidative degradation of Congo-red dye are compiled in this chapter. The results interpret that surface modified fly ash photocatalyst showed enhanced photocatalytic behavior than raw fly ash and pure TiO_2 nanoparticles. The method can be used to waste water treatment at industrial scale. The details of optimization of degradation conditions are also reported in this chapter for the said reaction.

3.1 Introduction

The majority of dyes used in the textile industries are the azo dyes, accounting for more than 50% of all commercial dyes [1]. Many of the azo dyes and their intermediate products, such as aromatic amines, are toxic to aquatic life, carcinogenic and mutagenic to humans [2,3]. Consequently, these dyes have to be removed from textile wastewater before discharge. Dye wastewater is characterized by high concentration, complicated component, deep color, and difficult to biodegrade. Major problems associated with colored effluents are damaging to aesthetic nature of the water surface, lowering light penetration and photosynthesis [4–6]. Thus the need to remove color from wastewater effluents became environmentally important. It is rather difficult to treat dye effluents because of their synthetic origins and mainly aromatic structures, which are biologically non-degradable [7]. Various methods have been used for the treatment of dye-containing wastewater, including biological treatment [8], adsorption [9], chemical oxidation[10], coagulation [8], photocatalysis [11] and reverse osmosis [12]. Although, adsorption of dyes is the most commonly used method for removing dyes from waste water. However, this process does not degrade the dye molecules it only separates the dye molecules form dye contaminated water. There is still a possibility of presence of dye molecules in dye separated water. Thus for proper treatment of waste water both separation and degradation of dyes are essential. There are many adsorbents used for dye separation e.g. activated carbon [13], clay minerals [14], bottom ash, fly ash [15–17], fungi [18] and waste materials from agriculture [19] etc. Although activated carbon adsorption is highly effective for removing dyes and pigments, it is often too expensive to be used in large amount in most of the developing countries [20–24]. Among the above mentioned adsorbents fly ash i.e., a byproduct of thermal power plant industries, is a low cost adsorbent. There are many reports describing the adsorption abilities of fly ash for the removal of dyes from water [15–17].

For the degradation of toxic dyes Photocatalysis (photodegradation) in aqueous medium using photocatalyst is an effective method. Photocatalysis is a method based on irradiation of a solid semiconductor with light of the appropriate

wavelength. The procedure is of high significance as organic pollutants can be efficiently degraded by conversion of solar energy into chemical energy [25–27]. Many researchers used TiO_2, ZrO_2, ZnO, and SiO_2 etc., as photocatalysts for waste water treatment. Titanium dioxide i.e., an inexpensive, non-toxic and biocompatible material, is one of the most important and widely investigated photocatalyst [28]. Crystalline TiO_2 has three modification phases which are rutile (tetragonal), [29] anatase (tetragonal) and brookite (orthorhombic) [30]. Anatase-type TiO_2 has excellent photocatalytic activity and widely used as catalysts for decomposition of a wide variety of organic and inorganic pollutants. Because of these advantages TiO_2 has been selected as photocatalyst in this study.

However, nanosized TiO_2 represents high photo activity and significant quantum effect but there are also problems of separation and recovery of photocatalyst from the reaction media, therefore, supported TiO_2 is one of the choice for the field application of the photocatalyst. Much research has been centered to immobilize TiO_2 nanoparticles photocatalyst on porous supporting matrices, such as silica,[31] alumina, [32] zeolites [33,34] and activated carbon.[35–37] This approach provides a solution to the solid–liquid separation problem yet the porous materials are not cheap because they are artificially synthesized. To treat the huge amount of industrial wastewater by utilizing photocatalyst, a cheaper photocatalyst should be developed. Fly ash is generated in dry form in large quantities as a byproduct of thermal power generation plants and is a major source for environmental pollution. Currently, large quantities of fly ash are land filled. Research is in progress to find out the various ways to utilize this byproduct to prevent any environmental problems as well as effectively use them. Use of fly ash as a substrate for TiO_2 photocatalyst for purifying pollutants in wastewater will be the novel utilization of fly ash progressing towards the fly ash bulk utilization in textile industries [38]. This novel approach uses both separation and degradation processes for proper treatment of dye contaminated water. Separation and regeneration of photocatalyst can be possible after photodegradation of dye molecules which a can be further recycled as photocatalyst in waste water treatment processes.

Many methods have been established for the synthesis of TiO_2 nanoparticles such as sol gel route [39], hydrothermal method [40], chemical vapor deposition [41], direct oxidation [42] and microemulsion [43] etc. Among them, the sol gel route is one of the most suitable methods due to its possibility of deriving unique metastable structure, fine size and excellent chemical homogeneity at low reaction temperatures [44]. For superiority of sol gel process over other nano synthesis processes non aqueous sol gel route has been adopted in this study for the synthesis of photocatalysts viz., TiO_2 nanoparticles and fly ash supported TiO_2 nanoparticles.

Congo red, which is a stable basic azo dye, is a compound that contains azo groups (-N=N-). Due to its high stability, it is commonly used as a titration indicator and a staining agent [3]. Moreover as typical direct azo dye of biphenyl amine, Congo red is commonly used in textile industries. Therefore, it is selected as model pollutant in this research.

Thus the aims of the study are as follows (a) to synthesis TiO_2 nanoparticles (TNP) and fly ash supported TiO_2 nanoparticles ($TiFA_s$) by novel non aqueous sol gel route, (b) to perform accurate characterization for examine physic-chemical properties of fly ash (FA_s) used as support for TiO_2, as synthesized TNP and $TiFA_s$ photocatalyst, (c) to investigate the comparative photodegradation of TNP, FA_s and $TiFA_s$ photocatalyst, (d) optimization of degradation condition for photocatalytic reaction and (e) to check the reuse of the $TiFA_s$ photocatalyst for Congo red adsorption photodegradation cycles. Literature survey reveals that non aqueous sol gel route have not been used to load TiO_2 over coal fly ash surface. The synthesized photocatalyst in such a way have not been used for degradation of Congo red dye earlier. The $TiFA_s$ photocatalyst prepared by this route has large surface area and small particle size which helps in prevention of electron and hole recombination for efficient photodegradation of Congo red dye similarly fly ash used as support also works as adsorbent for Congo red dye which increases the supply of dye molecules to the photocatalyst [45].

3.2 Experimental Details

3.2.1 Materials and Reagents

Fly ash has been collected from Satpura Thermal Power Plant, Sarni, District Betul (M.P.), India and was used as received, after making a representative sample by the method of coining and quartering. It is named as **FA_s**. The FA_s used in the present study was analyzed for their chemical composition by flame atomic absorption spectrophotometer (AA-6300, Shimadzu) and it contains % mass of SiO_2 (62.12), Al_2O_3 (21.30), Fe_2O_3 (5.55), CaO (0.53), MgO (1.58), TiO_2 (1.38), K_2O (4.24) and loss on ignition (3.30).

Methanol (A.C.S., 99.5%), acetic acid (A.C.S., 99.7%), IPA (iso-propyl alcohol, A.C.S., 99.5%), glycerol (spectrophotometric, 99.5%) and TTIP (titanium tetraisopropoxide, AR, 99.99%) were purchased from Sigma Aldrich.

3.2.2 Synthesis of Photocatalyst

Fly ash supported TiO_2 photocatalyst ($TiFA_s$) and pure TiO_2 nanopowder (TNP) were synthesized using sol gel route, both $TiFA_s$ and TNP were prepared by same method but in case of TNP, FA_s was not used as support. 2.66 g FA_s was soaked in IPA for 10 min and used to immobilized 10 weight % TiO_2 over fly ash. TiO_2 sol was prepared by using new solvent system containing methanol and acetic acid in a ratio of 8:3 v/v in presence of glycerol. 1 mL TTIP diluted in 1 mL IPA was added drop by drop in above solvent system at low temperature (10 ºC) followed by vigorous stirring at 1500 rpm for 30 min for TiO_2 sol preparation. FA_s soaked in IPA was added in above mixture at the same temperature followed by vigorous stirring at 2000 rpm for 3 h for proper homogenization. The obtained mixture was then heated at 60 ºC until the gelling reaction was completed. After completion of reaction the liquid phase was decanted from solid phase, then the resulting precipitate was agitated and washed repeatedly with 30 mL deionised water in each washing cycle and followed by washing with 30 mL solution of acetone in each washing cycle, in order to remove the organic residues. The washed precipitate was dried in hot air oven at 60 ºC for 24 h. The dried material was powdered with mortar and pestle and then calcined at 400 °C for 3 h in a

muffle furnace. The calcined powder was again slightly crushed with mortar and mortar and pestle and used for further characterization.

3.2.3 Characterization

TNP, FA_s and $TiFA_s$ were characterized by XRD, FT-IR, SEM and TEM to examine the physico-chemical properties. Detail is given in **Annexure I.**

3.2.4 Evaluation of Catalytic Activity of $TiFA_s$, TNP and FA_s Using Photocatalytic Oxidation of Congo Red Dye

Figure 3.1 shows the schematic diagram of experimental set up for dye oxidation reaction. The photocatalytic oxidation reaction was conducted in a 500 mL cylindrical vessel with a water cooled quartz jacket. Irradiation was provided by a 300 W ultraviolet mercury lamp with major emission at 365 nm, located in the center of the quartz jacket. A magnetic stirrer was equipped at the bottom of the reactor to achieve effective dispersion. Air was bubbled through the reaction solution from the bottom to ensure a constant dissolved O_2 concentration. In the batch reactor the air flow was adjusted to 4.0 mL/min. The temperature of the reaction solution maintained at 20 ºC. The initial concentration of Congo red was adjusted to 20 mg/L. The pH of the suspension was adjusted either with 0.1 mol/L HCl or 0.1 mol/L NaOH. The photocatalyst activated at 400 ºC for 2 h prior to the reaction in static air was added in the reaction mixture. Sixty minutes adsorption time in dark conditions was allowed before the start of the photoreactions. After dark condition photocatalytic experiment was performed under UV irradiation. Then, samples of the suspension were withdrawn after a definite time interval and filtered through filter paper. The filtrates were analyzed for residual Congo red concentration using a UV-Vis spectrophotometer (UV 3000^+, Labindia) at 510 nm. In order to compare the photocatalytic activity of $TiFA_s$, the pure TiO_2 powders and FA_s were also tested. The $TiFA_s$ samples were used repeatedly, and each cycle lasted 240 min. Before the beginning of the next cycle, the remaining dye solution was replaced with fresh.

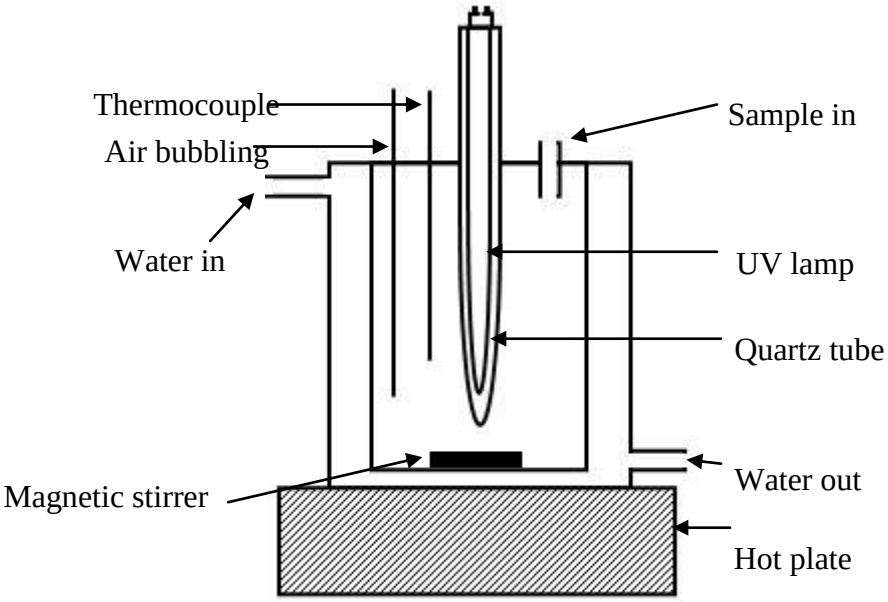

Figure 3.1 Schematic diagram of photocatalytic reactor for Congo red degradation using photocatalyst.

3.2.5 Catalyst Regeneration

After initial use, spent catalyst from the reaction mixture was recovered by filtration and regenerated for further use. The recovered catalyst was washed thoroughly with acetone and dried in oven at 110 ºC for 12 h followed by activation at 400 ºC for 2 h in static condition prior to the reaction. Thus, regenerated catalyst was used for further reaction cycles under the similar reaction conditions.

3.3 Results and Discussion

3.3.1 EDS Analysis

The EDS survey spectra of TNP, FA_s before and after loading of TiO_2 are shown in **Figure 3.2 (a, b** and **c)**. The compositions for the FA_s by mass percent were Al 27.29%, Si 66.23% and Fe 3.33 % and after loading of TiO_2 the composition by mass percent were Al 32.59%, Si 57.46%, Fe 4.60 % and Ti 5.35%. The presence of Ti peaks in the EDS spectrum of $TiFA_s$ photocatalyst confirms the loading of TiO_2 over fly ash.

3.3.2 XRD Analysis

XRD patterns of FA_s, TNP and $TiFA_s$ are represented in **Figure 3.3 (a, b** and **c)**. It can be seen that FA_s used in the experiments is well crystalline in nature and poses higher percentage of quartz and mullite phases. The XRD pattern of TNP indicates that the position and intensity of characteristic peaks are well confirmed by comparison with the JCPDS card no. 83-2243 which are related to the (101), (004), (200), (501), (211) and (204) plans of TiO_2 anatase structure at 2 theta 25º, 38º, 48º, 53º, 55º, 62º respectivety no other impurities of rutile or brookite were detected at calcination temperature 400 °C for 3h. The average crystalline size of TNP has been calculated by applying Scherrer's equation [43] ($d = k \alpha / \beta \cos$) to highest intensity diffraction peak (101) and is in the range of 5-10 nm. **Figure 3.3 (b)** shows the XRD pattern of $TiFA_s$ calcined at 400 °C for 3h which clearly indicates decrease in crystalline nature of fly ash after TiO_2 loading as compared to pure FA_s used in the experiment. Peaks corresponding to anatase TiO_2 phase were presented in the XRD of $TiFA_s$ which is very small in intensity

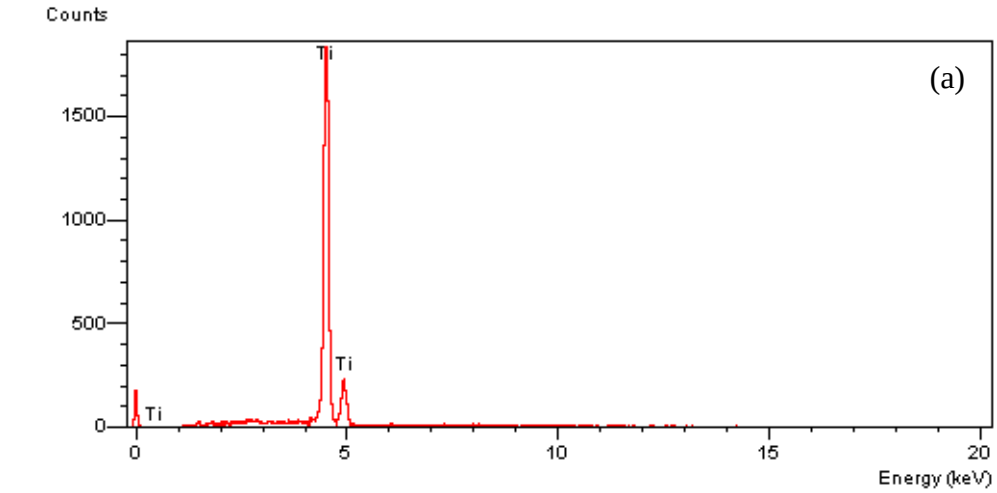

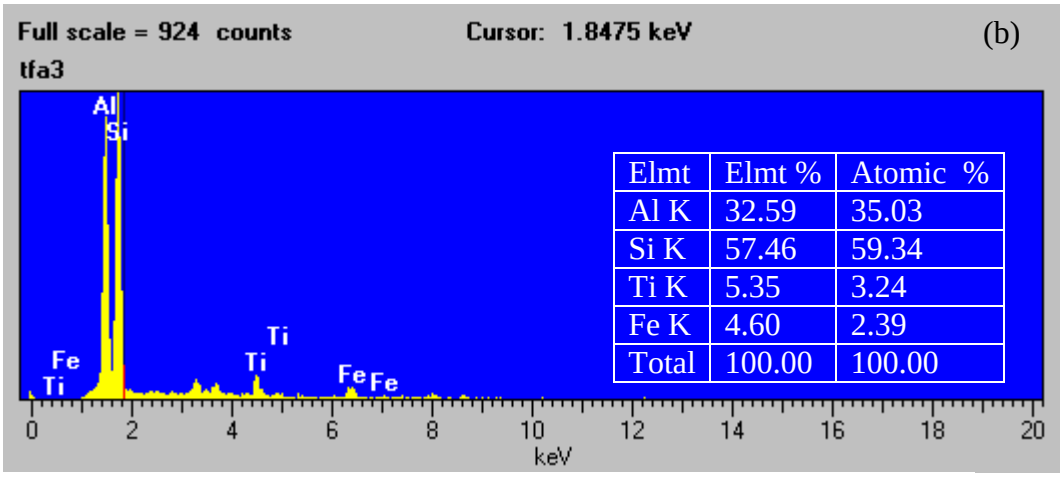

Elmt	Elmt %	Atomic %
Al K	32.59	35.03
Si K	57.46	59.34
Ti K	5.35	3.24
Fe K	4.60	2.39
Total	100.00	100.00

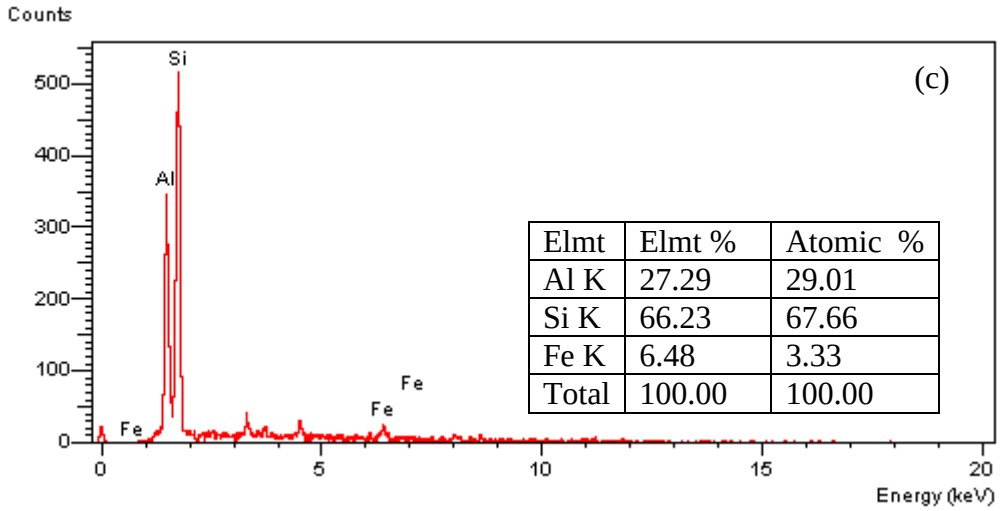

Elmt	Elmt %	Atomic %
Al K	27.29	29.01
Si K	66.23	67.66
Fe K	6.48	3.33
Total	100.00	100.00

Figure 3.2 EDS spectra of (a) TNP, (b) $TiFA_s$ synthesized by sol gel route, calcined at 400 °C for 3 h and (c) FA_s.

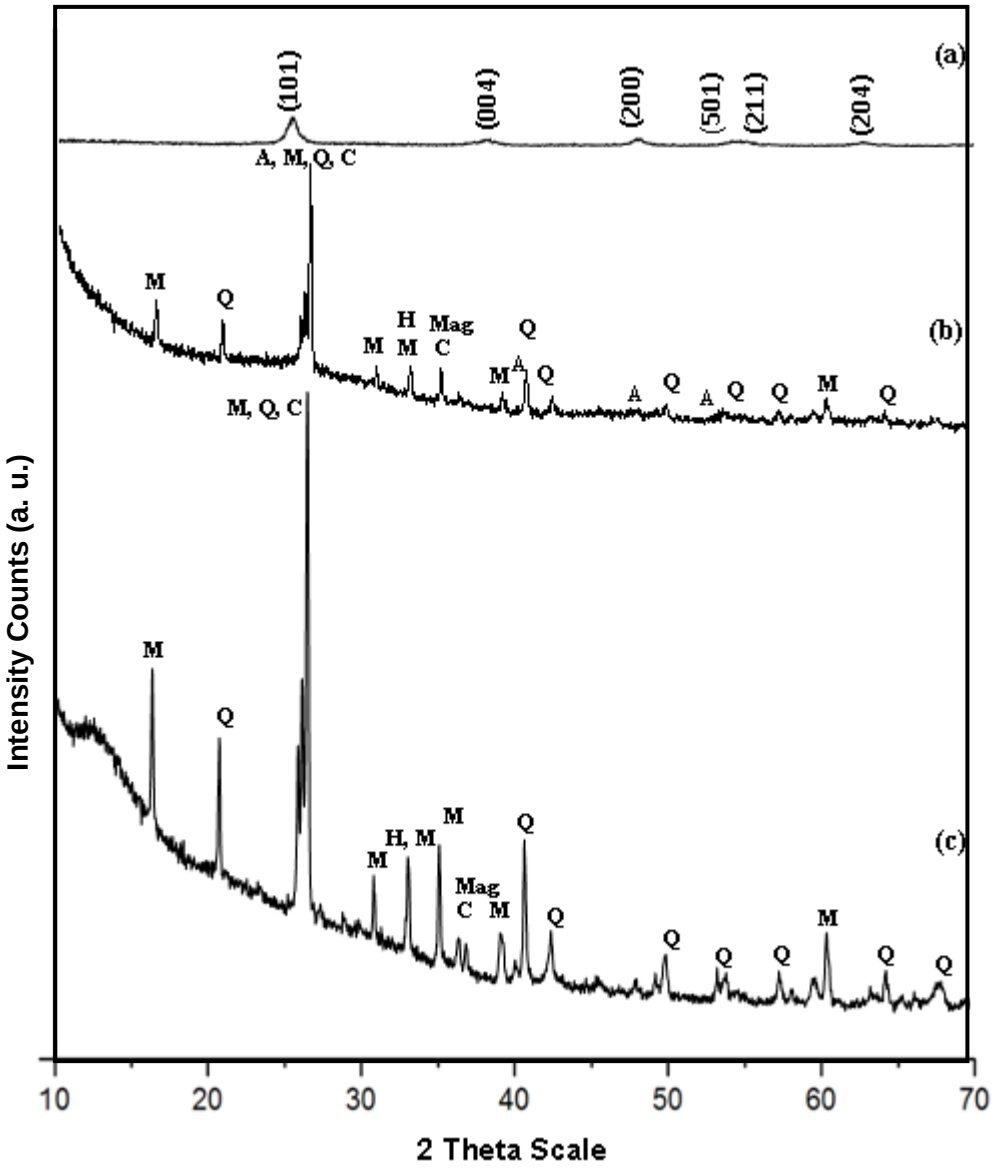

Figure 3.3 **XRD pattern of (a) anatase TNP and (b) $TiFA_s$ synthesized through sol gel route, calcined at 400 ºC for 3h, (c) as received FA_s. (A-anatase, M-mullite, Q-quartz, H-hematite, Mag-magnatite, C-calcite).**

denoted as 'A' at 2 theta value 25º, 38º, 48º, 53º in **Figure 3.3 (b)**. The presence of these peaks confirms the loading of TiO_2 over fly ash which is further confirmed by EDS analysis of $TiFA_s$.

3.3.3 FT-IR Analysis

The FT-IR spectrum of TNP, FA_s, $TiFA_s$ is given in **Figure 3.4**. FT-IR Spectrum of TNP shows broad band between 3800 and 2000 cm^{-1} indicates the presence of surface –OH groups, –Ti-OH and absorbed water molecules as moisture on surface of TNP. The frequency separation between 1539 and 1436 cm^{-1} suggests the presence of acetate and glycerol groups as chelating ligands [46–48] which have bonded to Ti. The chelating ligands are very stable and still exists after calcination of TiO_2 nanopowder [49]. The residual acetate and glycerol ligands on the surface of TiO_2 make the as-prepared TiO_2 particles small in size due to anti agglomeration effect of these ligands. Broad band between 600 and 1100 cm^{-1} corresponds to Ti-O-Ti suggesting the formation of TiO_2. Small bands at 588 and 576 cm^{-1}, confirms the existence of anatase polymorph of TiO_2, can be assigned to the vibration of the Ti–O–Ti moiety of the anatase titanium oxide network [50]. The FT-IR spectrum of FA_s as given in **Figure 3.4 (b)** shows a broad band between 3800 and 3000 cm^{-1} indicates the presence of surface –OH groups, –Si-OH and absorbed water molecules on surface. The spectrum shows a broad range of bands from 1000 cm^{-1} to 1190 cm^{-1} are attributed to the modes of asymmetric Si–O–Si stretching vibrations which is extended up to 1298 cm^{-1} can be assigned to the double Si=O bond. A broad band between 700–1000 cm^{-1} resulted due to overlapped modes of symmetric stretching vibrations of Si–O–Si bridges and the vibration of Al-OH connection for octahedrally coordinated Al. The absorbance at 1609 cm^{-1} is assigned to the surface hydroxyl groups of Si-OH. In addition, the small band at 643 cm^{-1} is due to Al–O– stretching modes in AlO_6 units [51]. A band at 1869 cm^{-1} can be assigned to carbon-oxygen double bond, C=O due to adsorption of CO_2 over fly ash surface. **Figure 3.4 (c)** illustrates the FT-IR spectrum of $TiFA_s$ photocatalyst. A broad band between 3800 and 2200 cm^{-1} indicates the presence of surface –OH groups, –Ti-OH, –Si-OH and absorbed water molecules as moisture on surface.

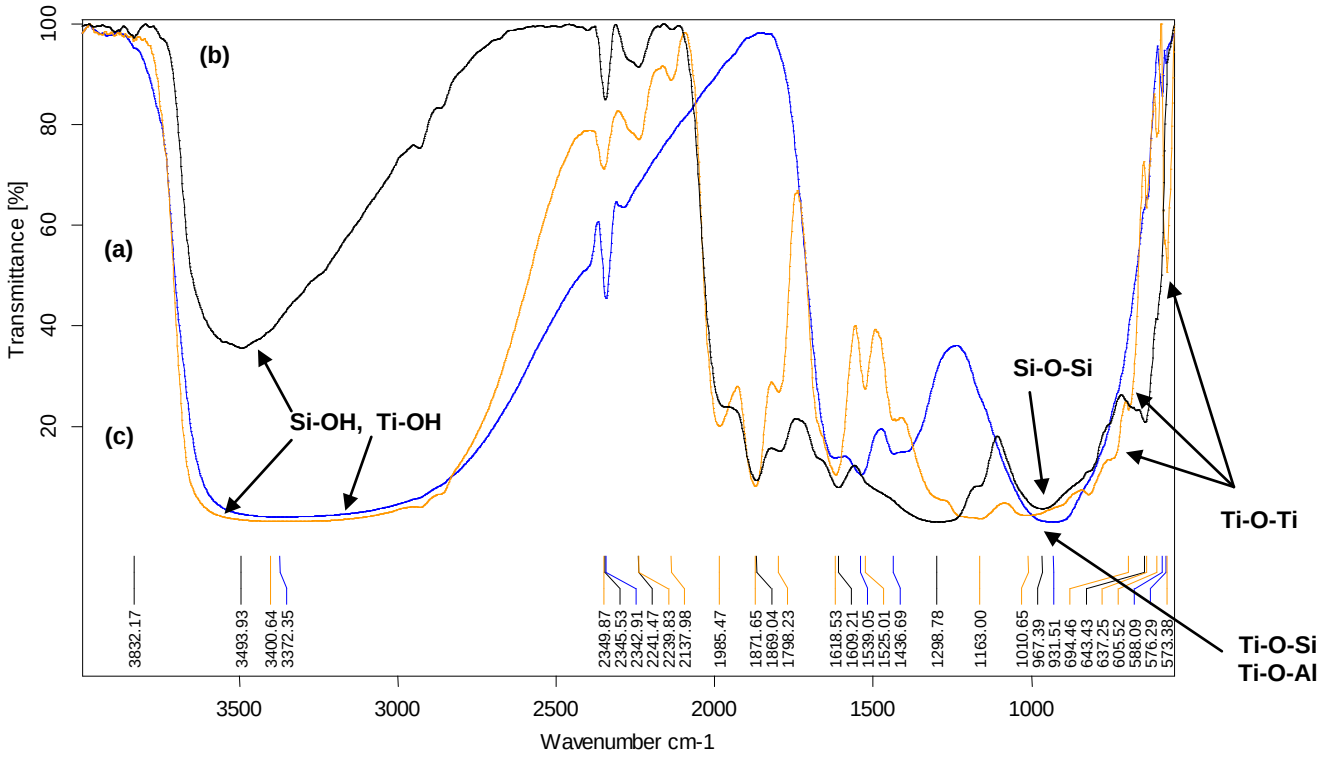

Figure 3.4 FTIR spectra of (a) TNP, (b) FA_s and (c) $TiFA_s$ synthesized through sol gel route, calcined at 400 °C for 3h.

The frequency separation between 1525 and 1444 cm^{-1} suggests the presence of acetate and glycerol groups as chelating ligands. It means that the acetate and glycerol ligands are not removed completely during the sol gel reaction, which is in accordance with former research result [52]. The residual acetate and glycerol ligands on the surface of TiO_2 make the as-prepared TiO_2 particles small and well dispersed on fly ash surface. The signal at 1163 cm^{-1} is attributed to the presence of Si–O–Si bands of fly ash [53]. Change in peak area between 800 and 1010 cm^{-1}, can be assigned to stretching vibrations of Ti-O-Si and Ti-O-Al [54,55], confirms the strong interaction due to chemical bonding between TiO_2, SiO_2 and Al_2O_3. Small peaks at 694, 637 and 605 cm^{-1} corresponds to the presence Ti-O-Ti network over fly ash surface. Small band at 573 cm^{-1} confirms the modification of fly ash surface by means of anatase TiO_2 responsible for higher photocatalytic activity of $TiFA_s$ catalyst.

3.3.4 SEM and TEM Analysis

The SEM images of FA_s, TNP and $TiFA_s$ are illustrated in **Figure 3.5, 3.6** and **3.7** respectively and TEM images of TNP, FA_s and $TiFA_s$ are shown in **Figure 3.8 (a** and **b)** and **3.9 (a** and **b).** The SEM and TEM images of FA_s clearly indicate that the fly ash mainly consists of spherical smooth surface of silica particles, which is also confirmed by the XRD patterns of fly ash (**Figure 3.3 (c)**). It can be concluded from **Figure 3.6** and **Figure 3.8** (**a** and **b**) that TNP are almost spherical in shape, the anatase TiO_2 are not hard grained clusters but consisting of many nearly spherical particles which is confirmed by HRTEM images of TNP. The average crystallite size of TNP is in the range of 5-10 nm calcined at 400 °C for 3h. Loading of TNP over FA_s increased the surface roughness of FA_s as indicated by **Figure 3.7 and 3.9 (b)**. This roughness contributed to the increase in specific surface area of $TiFA_s$ [37].

3.4 Catalytic Performance

3.4.1 Effect of Photocatalyst

To evaluate the factual photocatalytic activity of the $TiFA_s$ photocatalyst calcined at 400 °C for 3 h, five Congo red removal processes were compared viz. photolysis, photocatalytic degradation by TNP, FA_s, $TiFA_s$, and absorption of

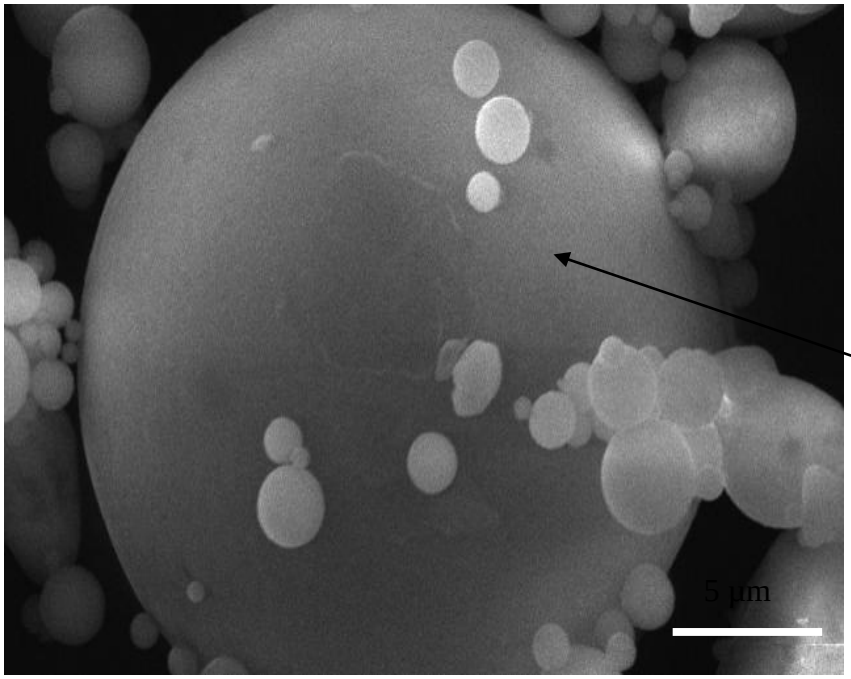

Figure 3.5 SEM image of as received FA_s.

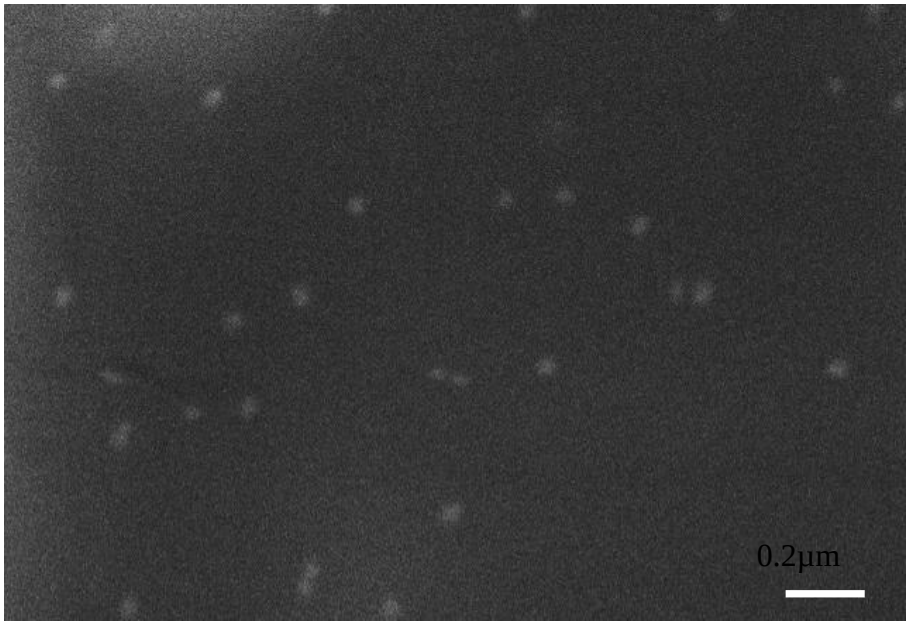

Figure 3.6 SEM image of TNP synthesized through sol gel route calcined at 400 ºC for 3h.

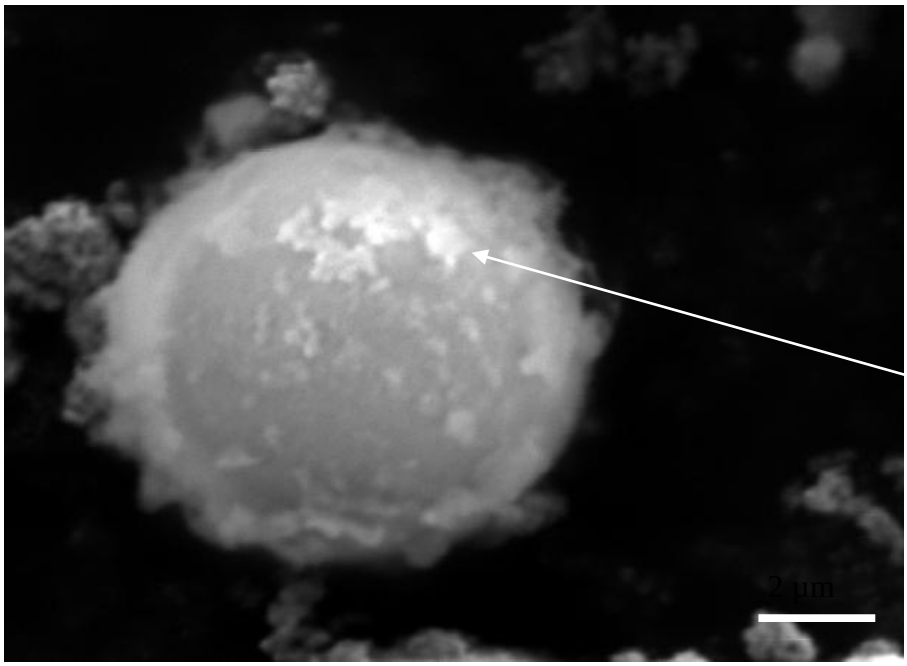

Figure 3.7 SEM image of $TiFA_s$ synthesized through sol gel route calcined at 400 ºC for 3h.

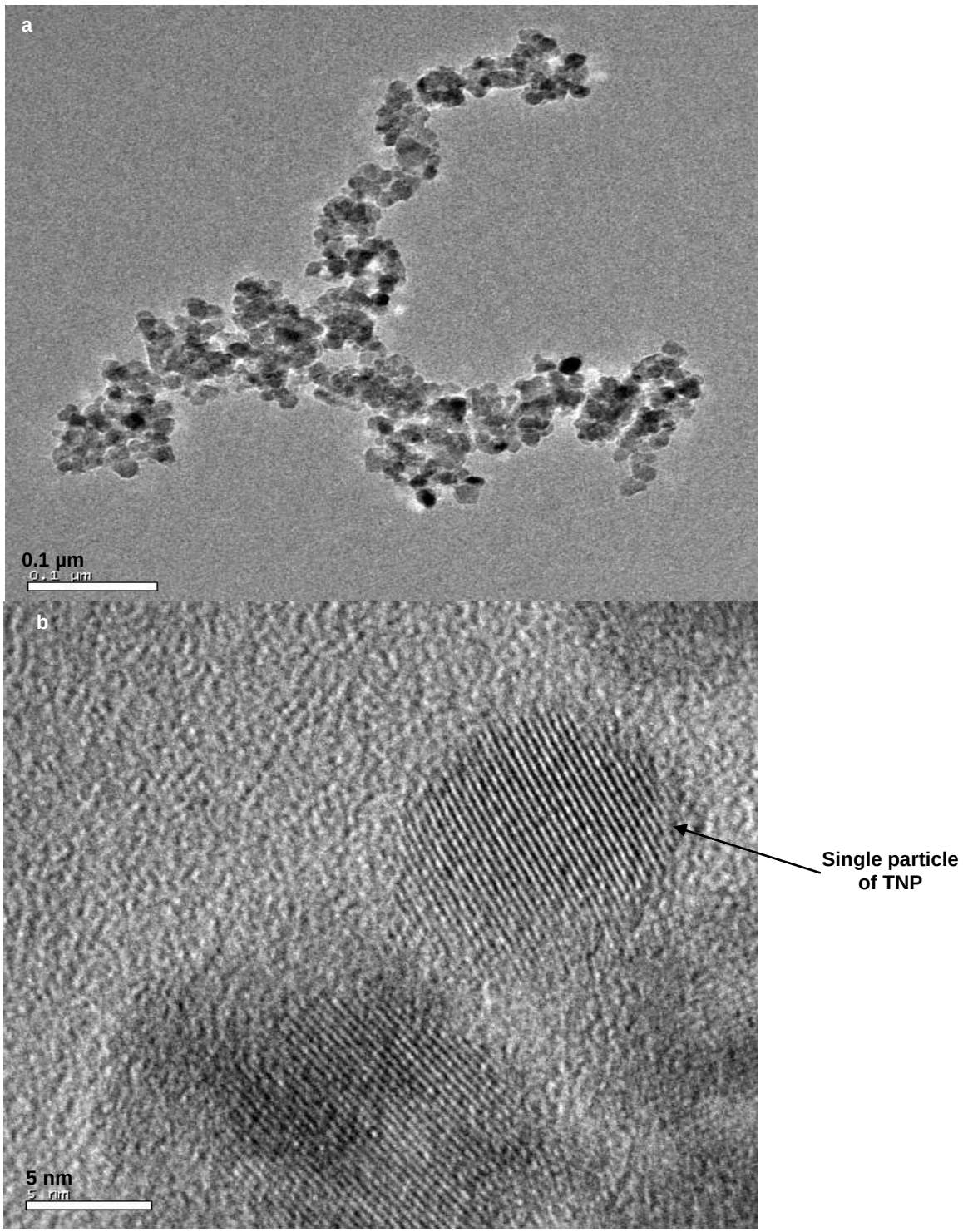

Figure 3.8 **HRTEM images of (a) TNP and (b) HRTEM image at high magnification of TNP synthesized through sol gel route calcined at 400 ºC for 3 h.**

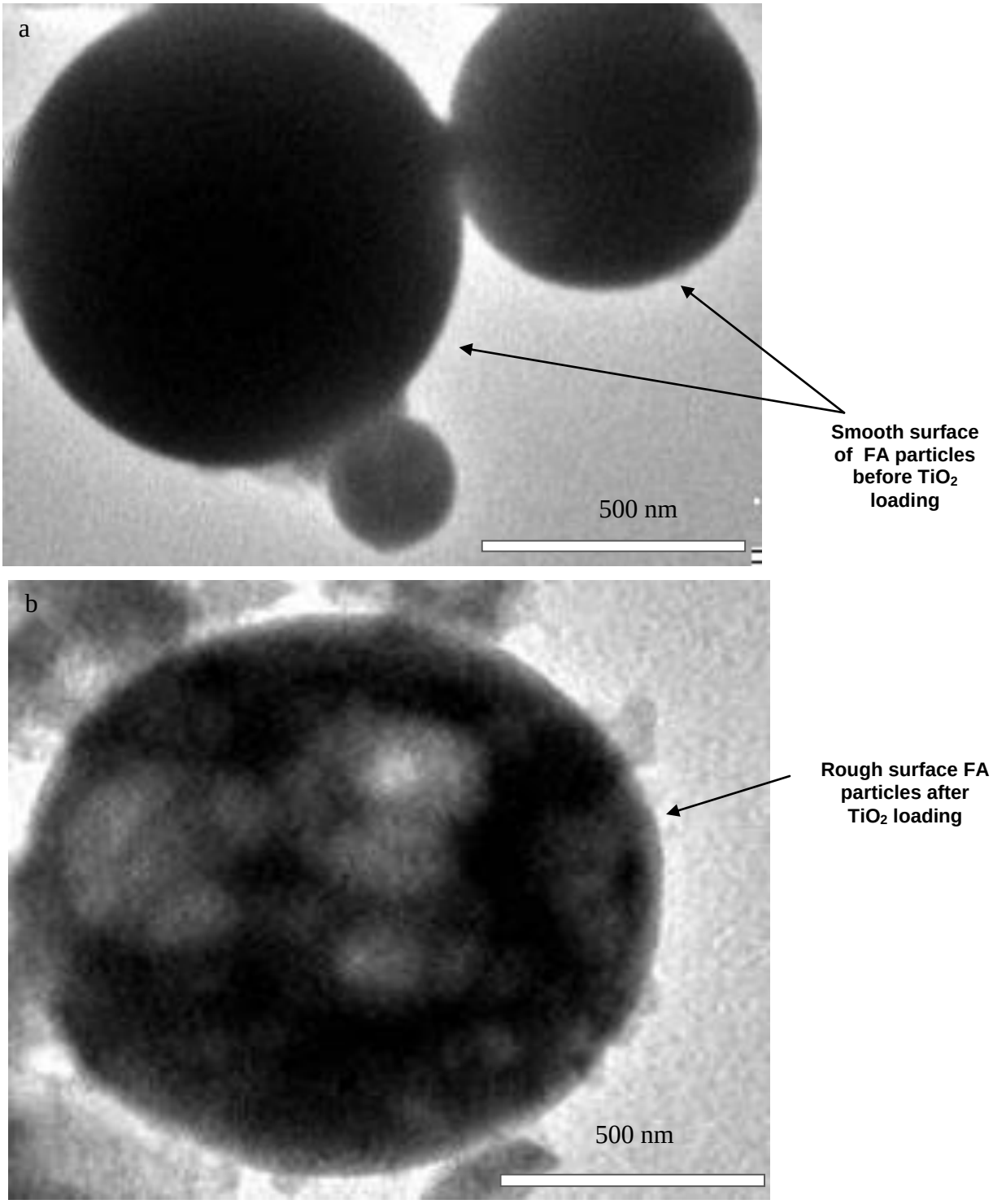

Figure 3.9 TEM images of (a) as received FA_s and (b) $TiFA_s$ synthesized through sol gel route calcined at 400 ºC for 3h.

$TiFA_s$, by corresponding experiments to evaluate the effect of catalyst on the overall degradation rate for Congo red, as shown in **Figure 3.10**. Experimental results show that Congo red could be decolorized to a certain degree under UV irradiation (see **Figure 3.10 (a)**). The adsorption of Congo red on FA_s was saturated after 120 min under UV light irradiation, the degradation rate of Congo red did not increase any further with prolonged UV light irradiation time. This indicated that pure FA_s does not have photocatalytic activity (**Figure 3.10 (b)**). Similarly, the $TiFA_s$ showed little photocatalytic activity without irradiation of UV light, and the saturated adsorption capacity of $TiFA_s$ is higher than that of pure FA_s (**Figure 3.10 (c)**). This was a result of the higher surface area and polarity of the FA_s after the deposition of TiO_2 [37]. The Congo red degradation rates increased with UV light irradiation for the Congo red/TNP and Congo red/$TiFA_s$ system, but the degradation percentages of Congo red with $TiFA_s$ are higher than those of TNP (**Figure 3.10 (d)** and **(e)**). By comparison of the amounts of Congo red removed with and without UV irradiation (**Figure 3.10**), it is affirmed that the oxidation of Congo red was due to photocatalytic degradation instead of only to adsorption.

3.4.2 Effect of Calcination Temperature

The photocatalytic activities of $TiFA_s$ photocatalysts at different calcination temperatures are shown in **Figure 3.11**. It can be seen that the calcination temperature significantly affects the photocatalytic activity of $TiFA_s$ photocatalyst. The samples exhibited some differences in Congo red degradation rate, it is increased notably with increasing calcination temperature from 300 to 400 °C, but decreased when temperature was further raised to 500 °C, much in accordance with a previous report [37]. This phenomenon can be attributed to the improvement in crystallinity of the anatase structure of TiO_2 as calcination temperature increases. However, when the calcination temperature increases to 500 °C, the anatase is transformed to rutile, with a decrease in photocatalytic activity [37]. Hence, the $TiFA_s$ calcined at 400 °C found the best photocatalyst for Congo red degradation.

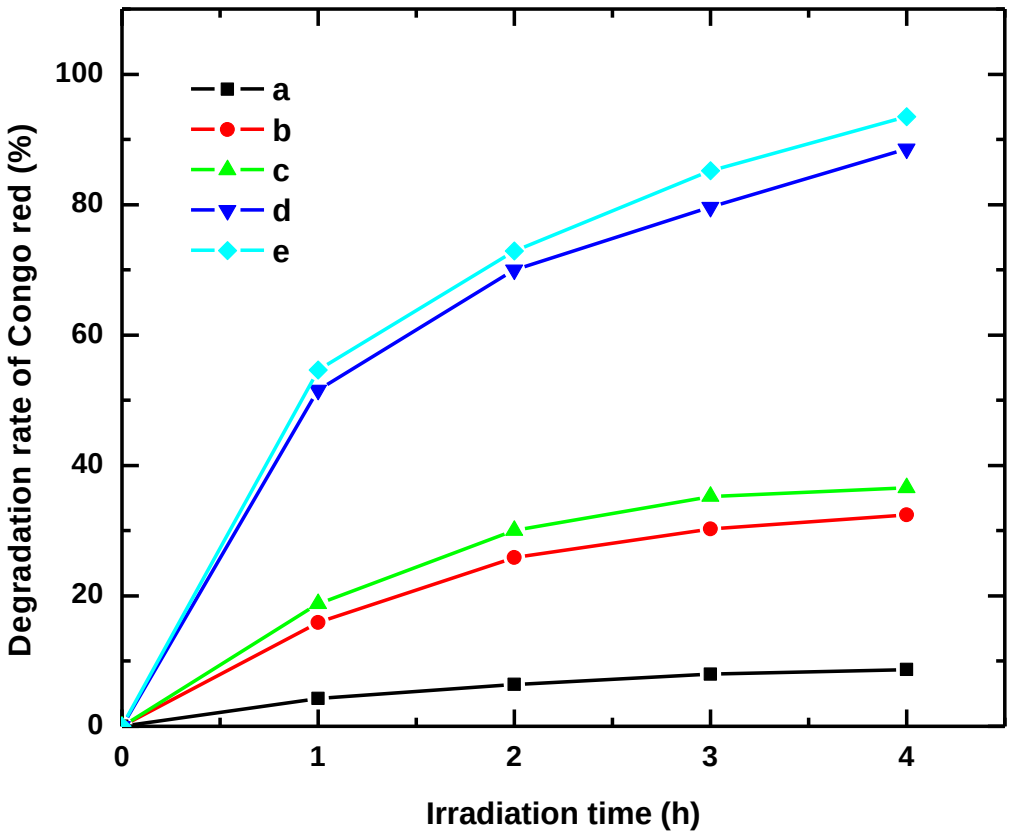

Figure 3.10 **Effect of photocatalyst on the degradation rate of Congo red. (a) only with UV irradiation; (b) FA_s with UV irradiation; (c) FA_s without UV irradiation; (d) TNP with UV irradiation; (e) $TiFA_s$ with UV irradiation. Initial conditions: Congo red concentration = 20 mg/L, photocatalyst dose = 2.0 g/L, pH = 6, calcination temp = 400 °C.**

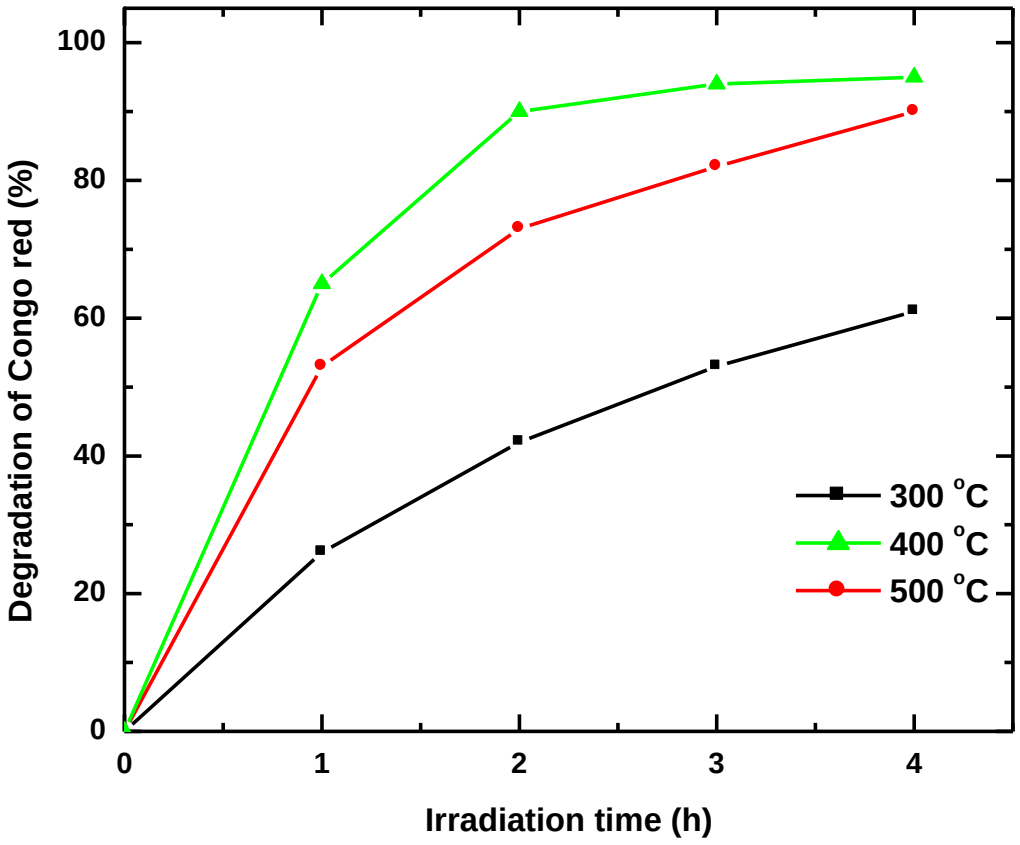

Figure 3.11 **Effect of calcination temperature on the degradation rate of Congo red. Initial conditions: Congo red concentration = 20 mg/L, photocatalyst dose = 2.0 g/L, pH = 6.**

3.4.3 Effect of Photocatalyst Dosages

Photocatalytic activity rises with catalyst dosage although, when the dosage exceeds the optimal amount, the suspension becomes too thick to admit enough light for photocatalysis. **Figure 3.12** shows the effect of $TiFA_s$ photocatalyst dosage (1.0 – 2.5 g L^{-1}) on Congo red degradation rates to increase markedly with catalyst dosage. At 2.0 g L^{-1}, the degradation reaction rate is the highest, and this dosage was found best suitable for photodegradation of Congo red dye.

3.4.4 Cyclic Performance of $TiFA_s$ for Oxidation of Congo Red

In order to test the workability of the cyclic use of $TiFA_s$ photocatalyst, four cycles of photocatalytic degradation of Congo red were performed. The change in relative degradation percentage of Congo red with cycling operation was shown in **Figure 3.13**. It was observed that Congo red could be degraded by the present photocatalyst under UV irradiation. The photocatalytic reactivity of the present photocatalyst was just slightly reduced in stirred aqueous solution, and the $TiFA_s$ photocatalyst, after being used four times, remained at 90% of photocatalytic activity of the fresh sample. The degradation percentage of Congo red could reach 83.58% when the irradiation time was 4 h, and the amount of Congo red removal was slightly lower than that for pure TiO_2. Thus it is suggested that the deposited anatase TiO_2 has firmly attached to the coal fly ash surface, and cannot be easily withdrawn from fly ash with mechanically stirred solutions for a long period. At the same time, it was also proved that the final removal of Congo red from solutions was caused by the photocatalytic degradation rather than the adsorption process that leads to saturated adsorption of Congo red on the photocatalyst. These results indicated that cyclic usage of the $TiFA_s$ photocatalyst was feasible and its immovability in treating polluted water was acceptable. Therefore, it is potentially employable for continuous photocatalytic degradation processes.

3.4.5 Proposed Reaction Mechanism

Although the detailed mechanism differs from one pollutant to another, it has been widely recognized that hydroxyl radicals $^{\bullet}OH$ act as active reagent for the complete mineralization of organic compounds. The radicals are formed by

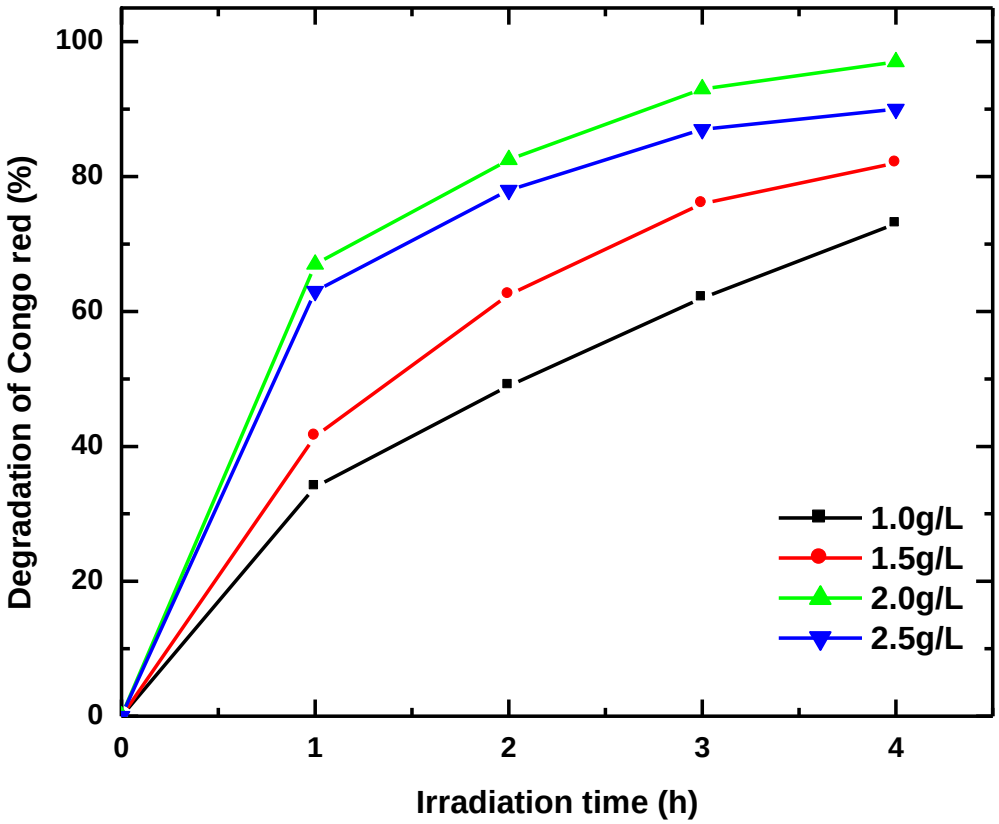

Figure 3.12 **Effect of photocatalyst dosage on the degradation rate of Congo red. Initial conditions: Congo red concentration = 20 mg/L, pH = 6, calcination temp = 400 °C.**

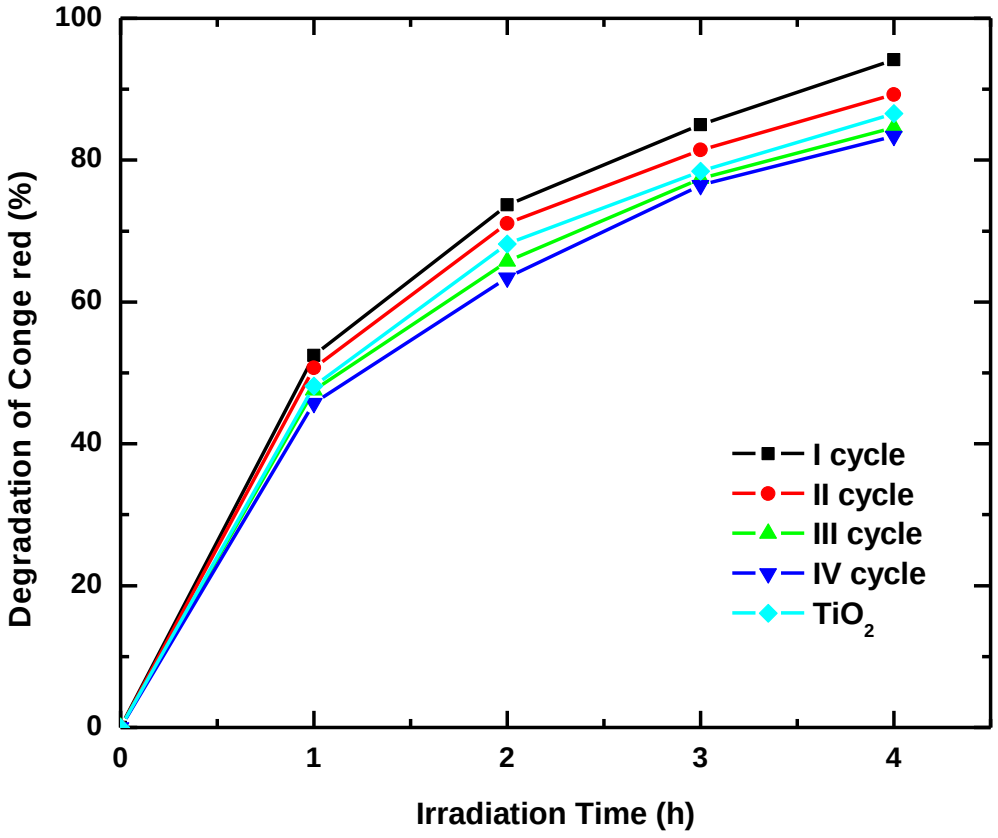

Figure 3.13 **The cyclic performance of the photocatalyst. Initial conditions: Congo red concentration = 20 mg/L, pH = 6, photocatalyst dosage = 2.0 g/L, calcination temp = 400 ºC.**

the scavenging of electron-hole pair by molecular oxygen and water adsorbed on catalyst surface **(eq. 1-3)**. Under UV irradiation, most of the $^{\bullet}OH$ radicals are generated directly from the reaction between the holes and surface adsorbed H_2O or OH^- ion **(eq. 1.2, 1.3)** [56].

When $TiFA_s$ is irradiated within UV range of electromagnetic radiation, electrons (e-) and holes (h+) are generated in the conduction band (CB) and the valence band (VB), respectively. These electrons and holes are thought to have the respective abilities to reduce and oxidize chemical species adsorbed on the surfaces of $TiFA_s$ photocatalyst **(eq. 1)**

$TiFA_s + h\nu \longrightarrow TiFA_s^* (e^-_{CB} + h^+_{VB})$ **(eq. 1)**

formation of electron-hole pair

$H_2O + h^+ \longrightarrow {}^{\bullet}OH + H^+$ **(eq. 2)**

formation of hydroxyl radical

$OH^- + h^+ \longrightarrow {}^{\bullet}OH$ **(eq. 3)**

formation of hydroxyl radical

•OH radicals produced in eq. 2 and 3 are strong oxidant. They are most important reactive species responsible for the complete mineralization of organic chemicals **(eq. 4).**

dye + $^{\bullet}OH \longrightarrow$ degradation of the dye **(eq. 4)**

h^+ also may act as oxidant, especially when available at high concentration **(eq. 5)**.

dye + $h^+ \longrightarrow$ oxidation products **(eq. 5)**

Electrons present in the conduction band (e_{CB}^-) on the catalyst surface can reduce molecular oxygen to superoxide anion **(eq. 6)**. This radical, in the presence

of organic scavengers, may form organic peroxides **(eq. 7)** or hydrogen peroxide **(eq. 8)**.

$e_{CB}^- + O_2 \longrightarrow {}^{\bullet}O_2^-$ **(eq. 6)**

${}^{\bullet}O_2^- + Dye \longrightarrow Dye–OO^{\bullet-}$ **(eq. 7)**

${}^{\bullet}O_2^- + HO_2^{\bullet} + H^+ \longrightarrow H_2O_2 + O_2$ **(eq. 8)**

Electrons present in the conduction band are also responsible for the production of hydroxyl radicals which have been shown to be the primary cause of organic matter mineralization (eq. 9).

${}^{\bullet}OH + Dye \longrightarrow$ degradation of the dye **(eq. 9)**

As revealed by various studies on the photo degradation of azo dyes such as Congo red, the chromophore azo group in the presence of ${}^{\bullet}OH$ radical is easily broken to generate N_2 gas [57]:

$R–N = N–R' + 2\ {}^{\bullet}OH \longrightarrow N_2\ (g) + ROH + R'OH$ **(eq. 10)**

Also Congo red is oxidized by oxidative species and converted into fatty acids and finally into CO_2. Among the oxidative species, ${}^{\bullet}OH$ is the major oxidative transient and is known to react with benzene and azo moieties with high rate coefficients [58]. The resulting intermediates are degraded progressively through hydroxylation of aromatic rings by ${}^{\bullet}OH$, ring openings and photo–Kolbe decarboxylation reactions until total mineralization [59,60]. Thus on this way complete degradation of Congo red is achieved by using cost effective, recyclable, green photocatalyst $TiFA_s$. This catalyst can be efficiently used at large scale in textile industries for waste water treatment. The plausible model structure of $TiFA_s$ photocatalyst, structure of Congo red dye before and after photo-oxidation is given in **scheme 3.1-3.3.**

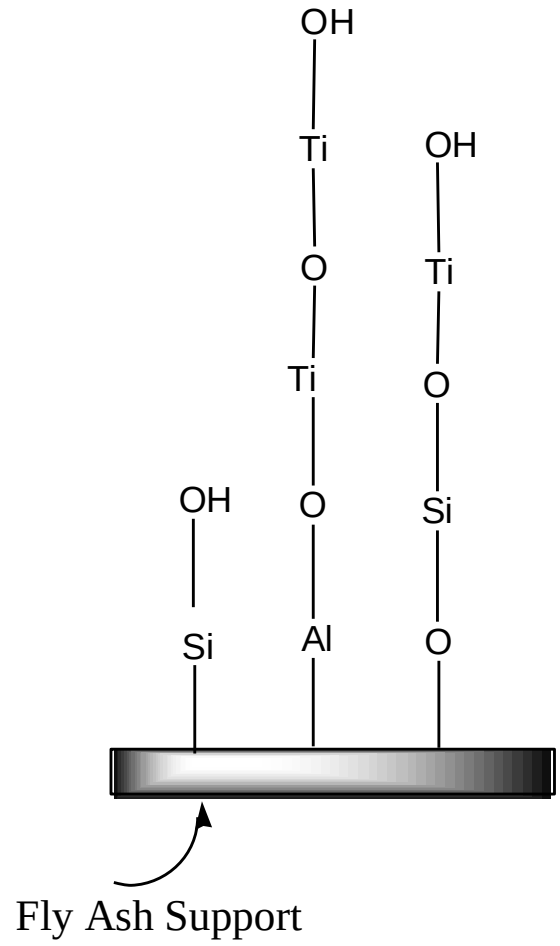

Scheme 3.1 Proposed model structure of $TiFA_s$ photocatalyst.

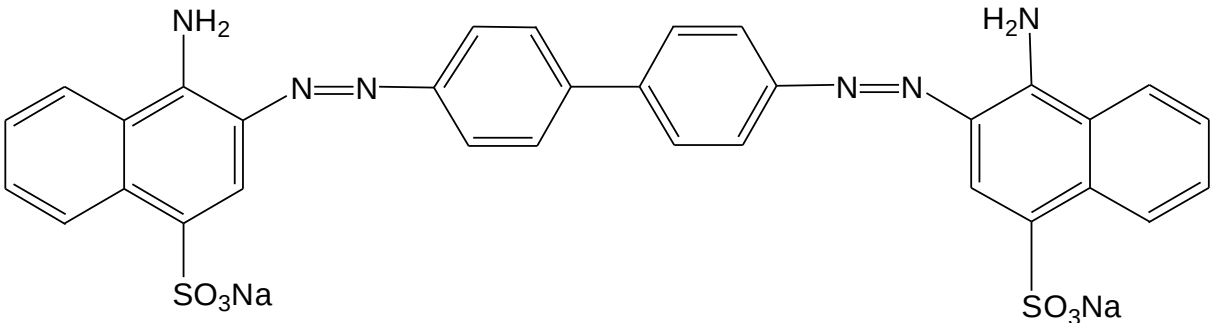

Scheme 3.2 Structure of Congo red molecule.

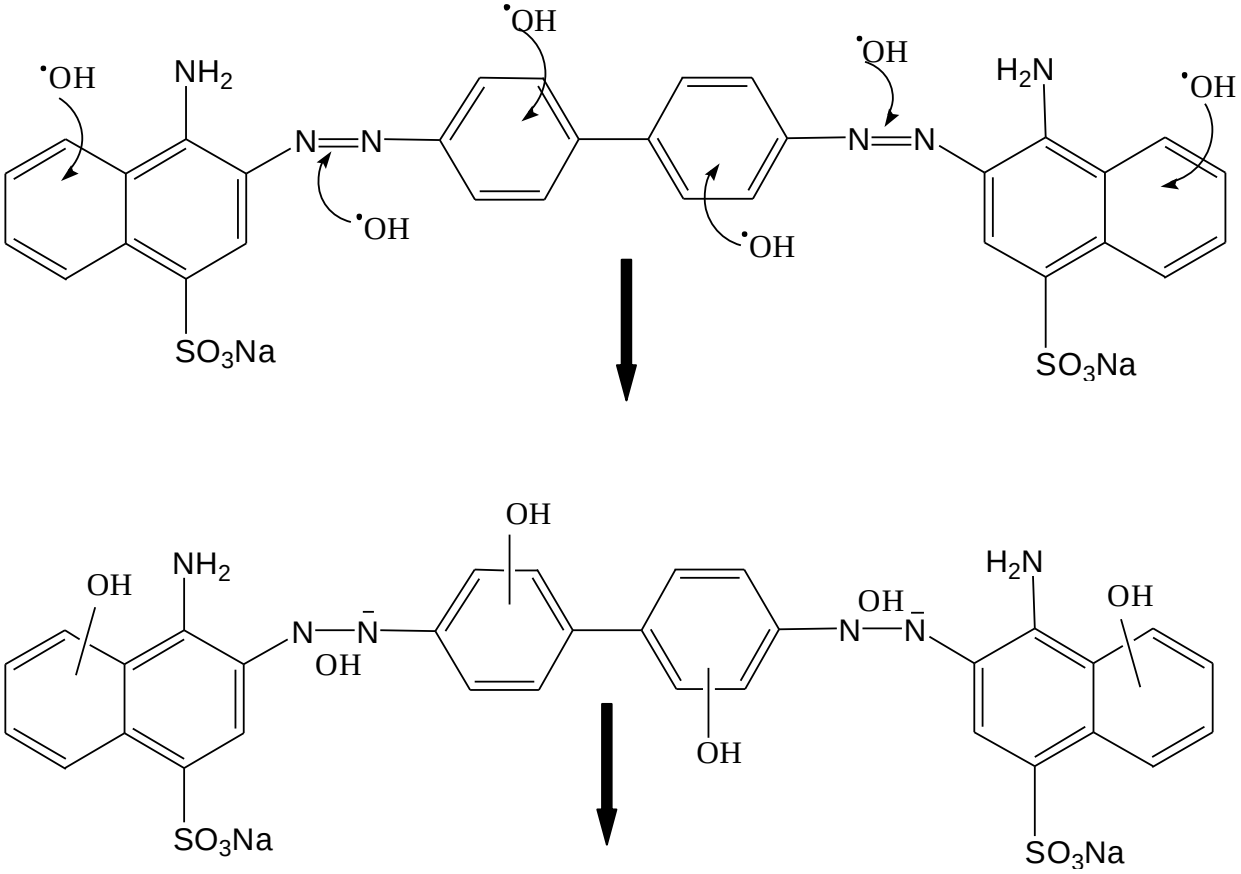

Mineralizaed Products

Scheme 3.3 Proposed mechanism of Congo red photo degradation mechanism UV irradiation in aqueous $TiFA_s$ photocatalyst dispersions.

3.5 Conclusion

In the present study, a supported photocatalyst was developed by immobilizing TiO_2 onto thermal power plant generated solid waste fly ash by sol gel route, followed by calcination at 400 ºC for 3h. The TiO_2 coating showed an enhancement of the adsorption of Congo red in the photodegradation process. Photocatalytic oxidation tests showed that Congo red can be effectively degraded and mineralized by the synthesized TiO_2 and $TiFA_s$ photocatalyst. The as-prepared $TiFA_s$ photocatalyst showed high photocatalytic activities in the photodegradation of Congo red in comparison with FA_s and as prepared TNP. From the viewpoint of efficient mineralization of wastewater, the best dosage of $TiFA_s$ was 2.0 g L^{-1} Moreover, after repeated use for four cycles, the photocatalytic ability of $TiFA_s$ was just slightly reduced in stirred aqueous solution, and the separation of photocatalyst from solution was avoided. Therefore, it is potentially employable for continuous photocatalytic degradation processes. The cost effective, recyclable, green and novel photocatalyst $TiFA_s$ finds applications in textile industries where large amount of azo dyes are used to dying and consequently purify the polluted drinking water.

3.6 References

[1] S. Atchariyawut, J. Phattaranawik, T. Leiknes, R. Jiraratananon, Sep. Purif. Technol. 66 (2009) 153.

[2] S. Figueroa, L. Vázquez, A. Alvarez-Gallegos, Water Res. 43 (2009) 283.

[3] L. iu Jian hua, W. Hai jun, J. Chongqing Univ. 8 (2009) 165.

[4] M. Soni, A. K.Sharma, J. K.Srivastava, J.S. Yadav, Int. J. Chem. Sci. Appl. 3 (2012) 338.

[5] A.A. Giwa, I.A.. Bello, A.A. Olajire, Chem. Process Eng. Res. 13 (2013) 51.

[6] J. Sheng, Y. Xie, Y. Zhou, Appl. Clay Sci. 46 (2009) 422.

[7] M.A. Mohammed, A. Shitu, A. Ibrahim, Res. J. Chem. Sci. 4 (2014) 91.

[8] Z. Wang, M. Xue, K. Huang, Z. Liu, in:, P.P. Hauser (Ed.), Advsnces Treat. Text. Effl., InTech, Shanghai, 2011, p. 154.

[9] I.D. Mall, V.C. Srivastava, N.K. Agarwal, Dye. Pigment. 69 (2006) 210.

[10] S. Wang, Z.H. Zhu, J. Hazard. Mater. B 136 (2006) 946.

[11] Y. Arai, K. Tanaka, A.L. Khlaifat, J. Mol. Catal. A Chem. 243 (2006) 85.

[12] V.K.K. Gupta, A. Mittal, L. Krishnan, V. Gajbe, Sep. Purif. Technol. 40 (2004) 87.

[13] W.T. Tsai, C.Y. Chang, M.C. Lin, S.F. Chien, H.F. Sun, M.F. Hsieh, Chemosphere 45 (2001) 51.

[14] C.C. Wang, L.C. Juang, T.C. Hsu, C.K. Lee, J.F. Lee, F.C. Huang, J. Colloid Interface Sci. 273 273 (2004) 80.

[15] S. Wang, H. Wu, J. Hazard. Mater. B 136 (2006) 482.

[16] Shaobin Wang, Y. Boyjoo, A. Choueib, Z.H. Zhu, Water Res. 39 (2005) 129.

[17] A.R. Dincer, Y. Gunes, N. Karakaya, J. Hazard. Mater. 141 (2007) 529.

[18] M. Chander, D.S. Arora, Dye. Pigment. 72 (2007) 192.

[19] T. Robinson, Water Res. 36 (2002) 2824.

[20] V.K. Gupta, I. Ali, V.K. Saini, J. Colloid Interface Sci. 315 (2007) 87.

[21] A.. Jain, V.. Gupta, A. Bhatnagar, J. Hazard. Mater. 101 (2003) 31.

[22] V.K. Gupta, I. Ali, V.K. Saini, Ind. Eng. Chem. Res. 43 (2004) 1740.

[23] V.. Gupta, I. Ali, D. Mohan, J. Colloid Interface Sci. 265 (2003) 257.

[24] T.-C. Hsu, Fuel 87 (2008) 3040.

[25] M.R. Hoffmann, S.T. Martin, W. Choi, D.W. Bahnemannt, (1995) 69.

[26] I. Ilisz, A. Dombi, K. Mogyorósi, A. Farkas, I. Dékány, Appl. Catal. B Environ. 39 (2002) 247.

[27] J. Theurich, M. Lindner, D.W. Bahnemann, Langmuir 12 (1996) 6368.

[28] B. Tryba, A.W. Morawski, M. Inagaki, Appl. Catal. B Environ. 46 (2003) 203.

[29] B.L. Bischoff, M.A. Anderson, Chem. Mater. 7 (1995) 1772.

[30] P. Van Nho, T.K. Cuong, VNU J. Sci. Math. - Phys. 24 (2008) 24.

[31] L. Alemany, M. Banares, E. Pardo, F. Martin, M. Galanfereres, J. Blasco, Appl. Catal. B Environ. 13 (1997) 289.

[32] W. Huang, A. Duan, Z. Zhao, G. Wan, G. Jiang, T. Dou, K.H. Chung, J. Liu, Catal. Today 131 (2008) 314.

[33] S. Fukahori, H. Ichiura, T. Kitaoka, H. Tanaka, Environ. Sci. Technol. 37 (2003) 1048.

[34] H. Yamashita, M. Anpo, Curr. Opin. Solid State Mater. Sci. 7 (2003) 471.

[35] J. Matos, J. Laine, J.-M. Herrmann, J. Catal. 200 (2001) 10.

[36] T. Tsumura, N. Kojitani, H. Umemura, M. Toyoda, M. Inagaki, Appl. Surf. Sci. 196 (2002) 429.

[37] Z. Shi, S. Yao, C. Sui, Catal. Sci. Technol. 1 (2011) 817.

[38] Y. Yu, Powder Technol. 146 (2004) 154.

[39] S. Mahshid, M. Askari, M. Sasani Ghamsari, N. Afshar, S. Lahuti, J. Alloys Compd. 478 (2009) 586.

[40] C.-C. Wang, J.Y. Ying, Chem. Mater. 11 (1999) 3113.

[41] H. Liu, W. Yang, Y. Ma, Y. Cao, J. Yao, J. Zhang, T. Hu, Langmuir 19 (2003) 3001.

[42] D. Byun, Y. Jin, B. Kim, J. Kee Lee, D. Park, J. Hazard. Mater. 73 (2000) 199.

[43] R. Hada, A. Amritphale, S.S. Amritphale, S. Dixit, Open Miner. Process. J. 3 (2010) 68.

[44] K. Thangavelu, R. Annamalai, D. Arulnandhi, Int. J. Emerg. Technol. Adv. Eng. 3 (2013) 636.

[45] S. Dafare, P.S. Deshpande, R.S. Bhavsar, Indian J. Chem. Technol. 20 (2013) 406.

[46] S. Doeuff, M. Henry, C. Sanchez, J. Livage, J. Non. Cryst. Solids 89 (1987) 206.

[47] J.C.S. Wu, I.H. Tseng, W.C. Chang, J. Nanoparticle Res. 3 (2001) 113.

[48] Z. Zhang, X. Zhong, S. Liu, D. Li, M. Han, Angew. Chem. Int. Ed. Engl. 44 (2005) 3466.

[49] D. Jiang, Y. Xu, B. Hou, D. Wu, Y. Sun, Eur. J. Inorg. Chem. 2008 (2008) 1236.

[50] A. Jaroenworaluck, N. Pijarn, N. Kosachan, R. Stevens, Chem. Eng. J. 181-182 (2012) 45.

[51] A. Adamczyk, E. Długon, Spectrochim. Acta Part A 89 (2011) 11.

[52] M. Gotić, M. Ivanda, S. Popović, S. Musić, A. Sekulić, A. Turković, K. Furić, J. Raman Spectrosc. 28 (1997) 555.

[53] Y. Zhang, Y. Wu, M. Chen, L. Wu, Colloids Surfaces A Physicochem. Eng. Asp. 353 (2010) 216.

[54] X. Gao, I.E. Wachs, Catal. Today 51 (1999).

[55] H. Faghihian, A. Bahranifard, Iran. J. Catal. 1 (2011) 45.

[56] J. Fernández, J. Kiwi, C. Lizama, J. Freer, J. Baeza, H.D. Mansilla, J. Photochem. Photobiol. A Chem. 151 (2002) 213.

[57] H. Lachheb, E. Puzenat, A. Houas, M. Ksibi, E. Elaloui, C. Guillard, J.-M. Herrmann, Appl. Catal. B Environ. 39 (2002) 75.

[58] H. Ma, M. Wang, R. Yang, W. Wang, J. Zhao, Z. Shen, S. Yao, Chemosphere 68 (2007) 1098.

[59] A. Akyol, M. Bayramoglu, Chem. Eng. Process. Process Intensif. 47 (2008) 2150.

[60] M. Alaei, Iran. J. Chem. Chem. Eng. 31 (2012) 23.

Synthesis and Characterization of Fly Ash Supported Silver Nanoparticles for Partial Oxidation of Alcohols

Abstract

The chapter describes the novel use of solid waste fly ash for the synthesis of innovative, highly efficient, cost effective, re-generable heterogeneous catalyst by loading different weight percents (1, 3 and 5 %) silver nanoparticles on thermally activated fly ash to intensify oxidation of alcohols (benzyl alcohol and methanol). Chemical reduction method, followed by calcination at appropriate temperature, has been used to load Ag nanoparticles over surface of thermally activated fly ash. Partial oxidation of alcohols under liquid phase condition has been used to evaluate catalytic activity of fly ash supported Ag catalyst. Results of textural, structural and morphological properties of prepared catalysts interpreted by XRD, SEM-EDS, FT-IR, UV-Vis and BET surface area analyzer, the plausible reaction mechanism for partial oxidation of benzyl alcohol over prepared catalyst are discussed.

4.1 Introduction

The preparation and study of metal nanoparticles is of interest in both research and technology. Silver nanoparticles have attracted considerable interest because of their potential applications in areas such as catalysis, nanoelectronics, optical filters, electromagnetic interference shielding and surface Raman scattering [1,2]. The method of preparation of nanoparticles in aqueous medium involves reduction of metal precursor salt by suitable reducing agent (sodium borohydride, ascorbic acid, etc.), or UV photons [3] or ionizing agents [4] or radiations [5]. All these synthesis methods require a stabilizing (capping) agent, for example polymers having functional groups such as -NH_2, -COOH and -OH, that have high affinity for metal atoms. The use of stabilizer is not desirable for some applications such as catalysis, where their presence may have detrimental effect on the performance of the catalyst. One significant approach to achieve this is to synthesize nanoparticles in the presence of suitable solid support such as silica, titania and alumina. Metal nanoclusters have been formed in silica aerogels by adding colloidal metal particles directly into the sol during gelation [6]. Recently, a gamma radiation-induced synthesis of Ag nanoclusters in silica aerogel has been reported [7] where Ag^+ ions were exchanged in the silica gel prior to drying and irradiated with gamma radiation followed by supercritical drying. The silver nanoclusters formed upon irradiation get embedded into silica matrix. Pulse radiolytic studies [8] on the reduction of Ag^+ ions at the surface of silica gel and gamma radiation preparation [9] of Ag nanocluster on SiO_2 have also been reported. For selective oxidation of CO, carbon and silica supported silver catalysts were formed by wet impregnation method using silver nitrate [10,11]. CuO/SiO_2 supported silver nanoparticles prepared by sol-gel route [12], silver loaded zeolites were also prepared by ion exchange for antibacterial application [13], for low temperature methane oxidation SnO_2 supported silver was prepared by wet impregnation method [14], silica alumina supported silver composite were synthesized by sol-gel route for partial oxidation of methanol to formaldehyde and the researcher claimed 97 % of methanol conversion over this sol-gel composite [15] Silver is 68^{th} most abundant and widely distributed metal in the earth's crust [16]. The most dominant non-metallurgical use of silver as

catalyst is in production of ethylene oxide from ethylene [17]. Supported silver catalysts have been widely investigated as promising oxidative catalytic materials for various reactions such as for partial oxidations [17–19] and oxidative dehydrogenation of hydrocarbons [20–22], epoxidation of alkenes [17], selective reduction of compounds [23,24] etc.

Most of the silver supported catalysts consist of silver metallic and ionic phase deposited on the surface of an oxide support which tend to be present as isolated silver species, and/or as small clusters of silver [25]. Supporting a metal on the surface of another oxide improves the catalytic activity of the active metal phase due to gain in surface area and mechanical strength [25]. Generally, during the preparation of the supported silver, the state of silver is non-uniform and the monolayer silver species are responsible for the catalytic activity and selectivity of the products. The advantage of these methods are that they do not require capping agent for stabilizing the metal nanoparticles [26]. The selectivity and activity of these catalysts depend on various factors such as the metal-support interaction, silver loading, methodology, state of silver on the support, calcination temperatures, types of support and its surface activity [27,28].

The use of solid waste FA as support in catalyst synthesis reduces the cost of bulk production of catalyst as it replaces commercially used costly metal supports viz. SiO_2, TiO_2, ZrO_2, Al_2O_3 etc. In our previous work, the surface activity has been generated over FA after suitable morphological and mineralogical modifications converting it into desired catalytic materials for Friedal-Crafts acylation[29,30], benzylation [31], esterification [32] and various type of condensation reactions [33–36] under liquid phase condition and oxidation under vapour phase [37].

Selective catalytic oxidation of alcohols to carbonyls is one of the most important chemical transformations in industrial chemistry. Carbonyl compounds such as ketones and aldehydes are the precursors for many drugs, vitamins, and fragrances and they are also important intermediates for many complex syntheses [38]. Numerous methods are available for alcohol oxidations such as metal salts in the form of homogeneous catalysts [39–42] or supported metal ions as

heterogeneous catalysts [43–46]. However, the common methods of alcohol oxidation may use toxic, corrosive, expensive oxidants such as chromium (VI), and setting up a severe condition, like high pressure or temperature, using strong mineral acids. Potentially, supported catalysts have advantages over the unsupported ones, including better heat transfer character, larger surface area to volume ratio of active component, better mechanical strength, and controllable catalyst textures.

In this series, we have introduced an innovative, highly efficient, cost effective, re-generable heterogeneous catalyst ($AgFA_j$) by supporting silver (1%, 3% and 5%) over thermally activated solid waste fly ash. The structural, morphological, thermal and surficial properties of $AgFA_j$ catalyst are presented in this work. Catalytic activity has been evaluated using partial oxidation of alcohols (benzyl alcohol and methanol) with *tert*-butylhydroperoxide in the liquid phase. The product are used largely as intermediates in the fine chemicals and pharmaceutical industries.

4.2 Experimental Details

4.2.1 Materials and Reagents

Fly ash collected from Tata thermal power plant, Jamshedpur, Jharkhand was used as catalytic support for silver nanoparticles. It is named as **FA_j** Silver nitrate ($AgNO_3$, A.C.S., 99.0%), sodium borohydride ($NaBH_4$, granular, 98%), benzyl alcohol (C_7H_7OH, HPLC, 99.99%) and methanol (CH_3OH, HPLC, 99.99%) were purchased from Sigma Aldrich. Oxidant *tert*-butylhydroperoxide (*t*-butOOH, AR, 80% in *ditert*-butylperoxide), acetonitrile (CH_3N, AR, 99.8%), chloroform ($CHCl_3$, AR, 99.5%), toluene ($C_6H_5CH_3$, AR, 99.5%) and *p*-dioxane ($C_4H_8O_2$, AR, 99.0%) were purchased from Merck Company and used without further purification.

4.2.2 Synthesis of $AgFA_j$ Catalyst

Fly ash supported Ag catalysts ($AgFA_j$) of 1, 3 and 5 weight % (wt%) of Ag were synthesized using chemical reduction method. Fly ash was activated thermally at 800 °C for 3 h prior to use for catalyst preparation for removing

carbon, sulfur and other impurities. In typical procedure for 5 weight % loading of Ag over fly ash, 2 gm thermally activated fly ash (TFA_j) was added to the 50 mL aqueous solution of 0.36 gm $AgNO_3$ (0.042 M) containing in a 250 mL reaction vessel with stirring at 750 rpm on a magnetic stirrer. Stirring was continued for 2 h for proper dispersion of Ag ions over fly ash surface. Simultaneously, 0.0846 M aqueous $NaBH_4$ solution was made by adding 0.16 g of $NaBH_4$ to 50 mL of ice cold deionized water. Freshly prepared $NaBH_4$ solution was added dropwise using burette at approximately 1 drop per second to the suspension of fly ash and $AgNO_3$ solution with vigorous stirring. The resulting suspension was stirred at ambient temperature for additional 15 min for proper reduction of Ag ions. Finally the reduced material was filtered and washed with 200 mL deionized water for removing Na and nitrate ions. The washed material was dried in hot air oven at 60 ^oC for 24 h. The dried material was powdered with mortar and pestle and then calcined at 550 °C for 2 h in a muffle furnace. The calcined powder was again slightly crushed with mortar and pestle and used for further characterization. Catalysts are denoted as $AgFA_j$ -x, where x = 1, 3 and 5 wt% of the silver content.

4.2.3 Characterization

The TFA_j and prepared $AgFA_j$ catalysts were characterized by WD-X-ray fluorescence, powder XRD, FT-IR, SEM-EDS, UV-VIS-DRS and BET surface area analyzer. Detail is given in **Annexure I**.

4.2.4 Evaluation of Catalytic Activity Using Partial Oxidation of Methanol in Presence of $AgFA_j$ Catalyst

Liquid phase oxidation of alcohol (benzyl alcohol or methanol) was carried out in a three necked round bottom flask connected with a spiral condenser containing 0.2 g catalyst, 15 mL acetonitrile solvent and 30 mmol of alcohol to which 30 mmol of *tert*-butylhydroperoxide (TBHP) used as oxidant was added. Before adding oxidant reaction mixture was stirred under nitrogen atmosphere at 50 °C for 30 min. The rotation rate of the reaction mixture was set at 750 rpm then after adding the oxidant, the mixture was refluxed at 90 °C temperature in an oil bath for 8 h under nitrogen atmosphere. Small aliquots of the sample were withdrawn from the reaction mixture at regular intervals for analysis. At the end

of the reaction, the solid particles (catalyst) were separated by filtration during the hot condition and products were analyzed by gas chromatograph (GC, 7820) Agilent Technologies, Inc, equipped with a flame ionization detector (FID) and a 19019J-413 column (30 m length, 0.32 mm id and 0.25 µm film thickness). For the reusability test, after completion of the reaction, the catalyst was recovered from the reaction mixture by filtration and washed thoroughly with acetone and reused as such for multiple circles.

The conversion of the alcohol and the selectivity of the products in the reaction are calculated as:

Conversion = (moles of alcohol reacted/moles of alcohol in the feed) × 100
Selectivity = (moles of alcohol converted to p/moles of alcohol reacted) × 100.
Where P = product.

4.3 Results and Discussion

4.3.1 XRF Analysis

The chemical composition of TFA_j and $AgFA_j$-5 evaluated using WD-XRF as given in **Table 4.1** has revealed that high percentage of SiO_2, Al_2O_3, Fe_2O_3 present in TFA_j and $AgFA_j$-5, other inorganic oxides remain in low percentage. In TFA_j no percentage of Ag is detected but the amount of Ag incorporated in the $AgFA_j$-5 is found 4.6 weight percent inferred the loading of Ag over TFA_j.

Table 4. 1 Chemical Composition of TFA_j and $AgFA_j$-5.

Chemical Components	TFA_j	AgFA-5
SiO_2	61.9	62.0
Al_2O_3	29.7	26.0
Fe_2O_3	3.65	3.55
Ag_2O	-	4.6
CaO	0.4	0.6
MgO	0.31	0.41
TiO_2	1.43	1.33
Na_2O	0.14	0.24
K_2O	0.71	0.54
Other elements	1.61	1.53
LOI	0.15	0.2

4.3.2 XRD Analysis

The X-ray diffraction patterns of TFA_j and silver loaded fly ash catalysts viz. $AgFA_j$-1, $AgFA_j$-3 and $AgFA_j$-5 are shown in **Figure 4.1** (**a**, **b, c** and **d**) figure shows that fly ash is nano-crystalline in nature [29] the crystallinity and crystallite size (33 nm) of the thermally activated fly ash is higher than silver loaded samples. The TFA_j contained an amorphous phase, mullite ($Al_6Si_2O_{13}$, ICDD pdf number, 15-0776) and quartz (SiO_2, ICDD pdf number, 46-1045), calcite ($CaCO_3$, ICDD pdf number, 47-1743), hematite (Fe_2O_3, ICDD pdf number, 33-0664), magnetite (Fe_2O_4, ICDD pdf number, 19-0629). After silver loading the amount of amorphous material increased considerably and the intensity of the quartz and mullite peaks decreased. For the samples with silver content below 5 wt % clear diffraction peaks were not observed. The absence of crystalline peaks associated with metallic silver indicates that the silver species are either highly dispersed or present as ionic state [15]. However, with increasing silver concentration, the characteristic diffraction peaks due to the crystalline Ag (111) (38º), Ag (200) (44.3º) and Ag (220) (64.4º) (Ag, ICDD pdf number, 04-0783) appear at low intensity in the XRD spectrum [15].

4.3.3 FT-IR Analysis

The FT-IR spectrum of TFA_j as given in **Figure 4.2 (a)** shows broad band between 3400 and 3000 cm^{-1}, which is attributed to the surface -OH groups of Si-OH and adsorbed water molecules on surface. A peak at 1650 cm^{-1} in the spectra of fly ash is assigned to bending mode (δO-H) of water molecule. The main absorption band of the valence oscillations of Si-O-Si groups in quartz appears with an absorption maximum at 1100 cm^{-1} [33].

The FT-IR spectrum of $AgFA_j$-5 catalyst as shown in **Figure 4.2 (b)** shows -OH peaks characteristics of Si-OH of Fly ash and incorporated Silver species on its surface. The increased amorphous silica in the silver loaded fly ash can be characterized by an intense band in the range 1000 – 1300 cm^{-1}, corresponding to the valence vibrations of the silicate oxygen skeleton. It can be noticed that slight changes in the intensities of some absorption bands in the range 1100–500 cm^{-1} (fingerprint region) confirms the presence of Si-O-Ag bond.

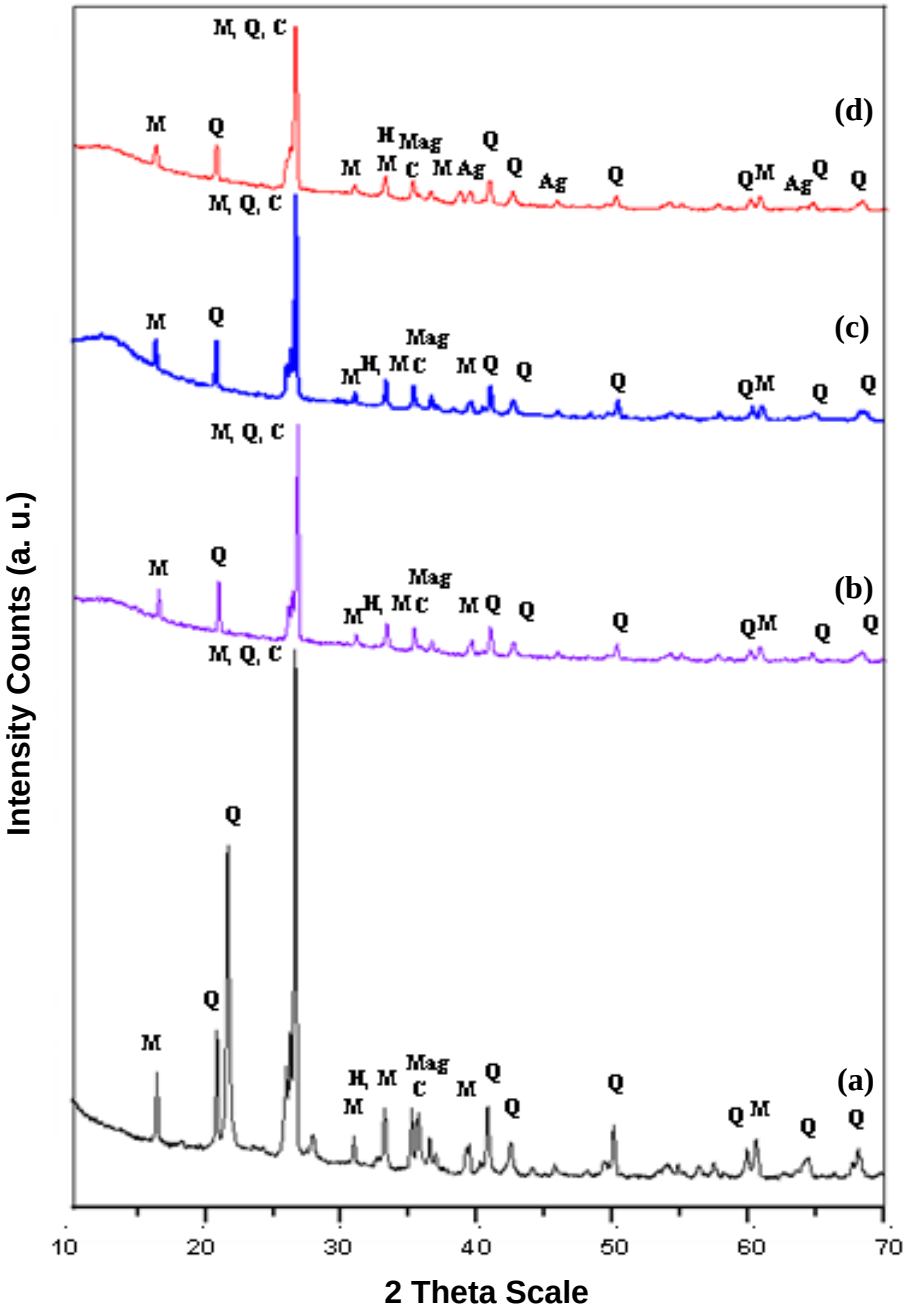

Figure 4. 1 **XRD patterns of (a) TFA_j heated at 800 °C for 3h, (b) $AgFA_j$-1, (c) $AgFA_j$-3 and (d) $AgFA_j$-5 prepared using chemical reduction method, calcined at 550 °C for 2h.**

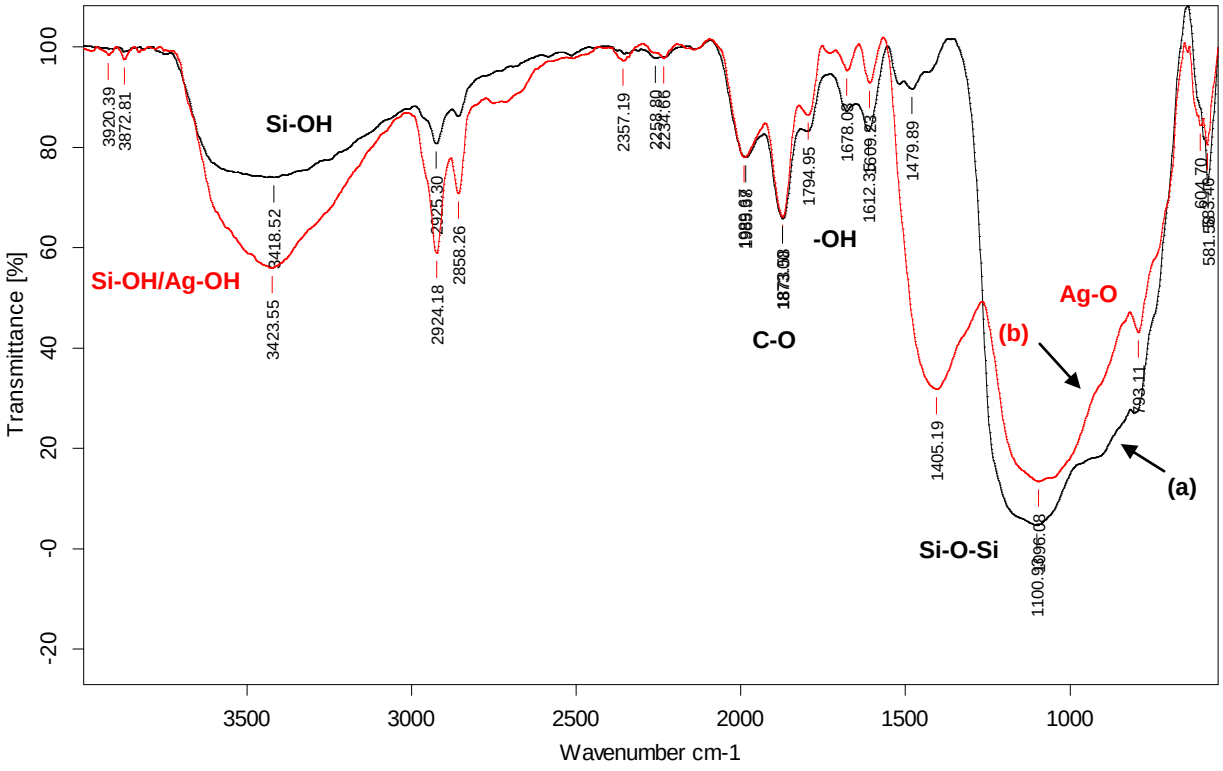

Figure 4. 2 FT-IR spectra of (a) TFA_j and (b) $AgFA_j$-5.

Further, the vibrational peaks found in the range 1130–650 cm^{-1} may be attributed to Ag–O, which indicates that silver nanoparticles are loaded over fly ash surface [47].

4.3.4 UV-Visible Analysis

Figure 4.3 (a, b and **c)** shows UV-VIS spectra of $AgFA_j$-1, $AgFA_j$-3 and $AgFA_j$-5. The spectra show distinct absorption signals around 257 nm indicates the presence of ionic silver species, peak at around 390 to 394 nm indicate the appearance of plasmon resonance bands of Ag nanoparticles due to collective oscillation of conduction electrons on the Ag metal nanoparticles surface. As increasing the Ag content over fly ash peak intensity of plasmon resonance band (394) increases but peak corresponding to ionic Ag (Ag^+ and Ag_n^+) decreases from 1 wt % loading to 3 wt % loading and then increases which indicates the presence of highest % of ionic Ag species and Ag nanoparticles over AgFA-5 surface. Similarly surface plasmon resonance band shifts to higher wave number indicates an increase in particle size of Ag nanoparticles [48,49] with increase in loading wt % of Ag.

4.3.5 N_2 - Adsorption-Desorption Analysis

Table 4.2 indicates the effect of silver wt% on surface area of catalyst with increasing silver content from 1 to 5 wt% on TFA_j support, the surface area is decreased from 9000 to 8000 m^2/Kg. This was mainly due to the blockage of fly ash surface pores by loading of silver nanoparticles [50].

Table 4. 2 Effect of silver loading on BET surface area for $AgFA_j$ catalysts.

Catalysts	Ag content (wt. %)	Specific surface Area(m^2/Kg)
TFA_j	0	9000
$AgFA_j$-1	1	8800
$AgFA_j$-3	3	8500
$AgFA_j$-5	5	8000

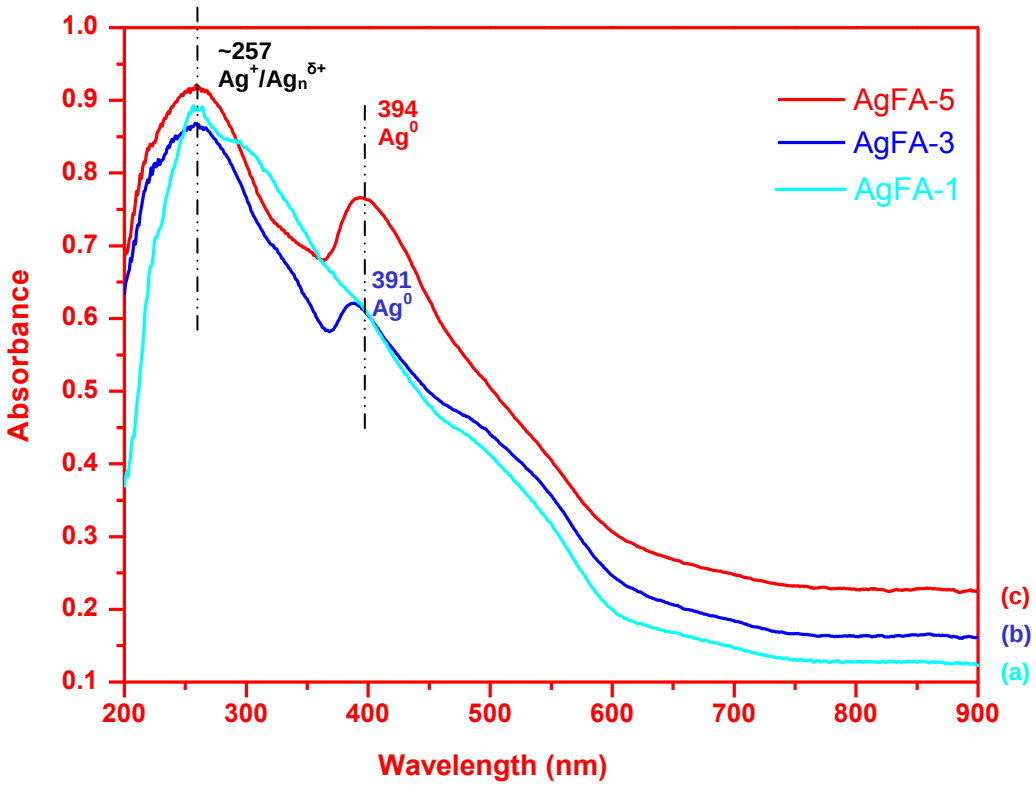

Figure 4. 3 **UV-Vis spectra of (a) AgFA$_j$-1, (b) AgFA$_j$-3 and (c) AgFA$_j$-5 synthesized using chemical reduction method, calcined at 550 °C for 2h.**

4.3.6 SEM-EDS Analysis

The EDS analysis of TFA_j also shows that fly ash mainly contains Si, Al and Fe elements in higher percentage as given in **Figure 4.4**, after loading of silver over fly ash the particles surface shows the presence of Ag along with the other elements i.e., Si, Al and Fe as shown in **Figure 4.5**. It is also to be noted that peak corresponding to Ag is not present in EDS of TFA_j and it appears only after loading process, indicating successful Ag deposition on the fly ash surface using the chemical reduction method.

The scanning electron micrograph (SEM) of TFA_j and 5 wt% silver loaded fly ash ($AgFA_j$-5) are shown in **Figure 4.6** to **4.8**. SEM photographs of the TFA_j revealed smooth spherical particles of silica with diameter of 840 nm to 6.95 µm interspersed with aggregates of crystalline compounds **(Figure 4.6)**. The majority of the particles consisted of solid spheres, mineral aggregates, hollow cenospheres and irregularly shaped unburned carbon particles and amorphous particles [51]. After silver loading the fly ash surface get rougher and agglomerated as shown in **Figure 4.7** and **4.8.**

4.4 Catalytic Performance

At first, the reactivity of a model compound, benzyl alcohol, was examined under a variety of experimental conditions. The results of the oxidation of benzyl alcohol with TBHP in the presence of $AgFA_j$ with 1, 3 and 5 wt% of Ag, are shown in **Table 4.3**. The conversion percentage was calculated with respect to substrate (benzyl alcohol). The result shows that the reaction with $AgFA_j$-5 has relatively higher conversion (65.8 %) compare to $AgFA_j$-1 and $AgFA_j$-3. The highest activity of $AgFA_j$-5 is due to availability of highest active sites over its surface. However, with increasing the loading of Ag from 1 to 3 wt % on TFA_j the selectivity with respect to benzaldehyde increased but further increasing the loading of Ag from 3 to 5 wt % on TFA_j the selectivity with respect to benzaldehyde was decreased. The selectivity of benzaldehyde and benzoic acid on $AgFA_j$-5 catalyst were obtained 78.7% and 21.3% respectively. It may be a better catalyst with respect to catalysts with lower wt % of Ag.

Table 4. 3 **Oxidation of benzyl alcohol with TBHP in the presence of $AgFA_j$ catalyst. Reaction condition: catalyst 0.2 g; benzyl alcohol 30 mmol; TBHP 30 mmol; acetonitrile 15 mL; reflux temperature 90 °C; reaction time 8 h.**

Sample	Conversion (%)	Selectivity of benzaldehyde (%)
$AgFA_j$-1	46.3	77.5
$AgFA_j$-3	57.5	80.7
$AgFA_j$-5	65.8	78.7[a]

[a] Selectivity of benzoic acid is 21.3%.

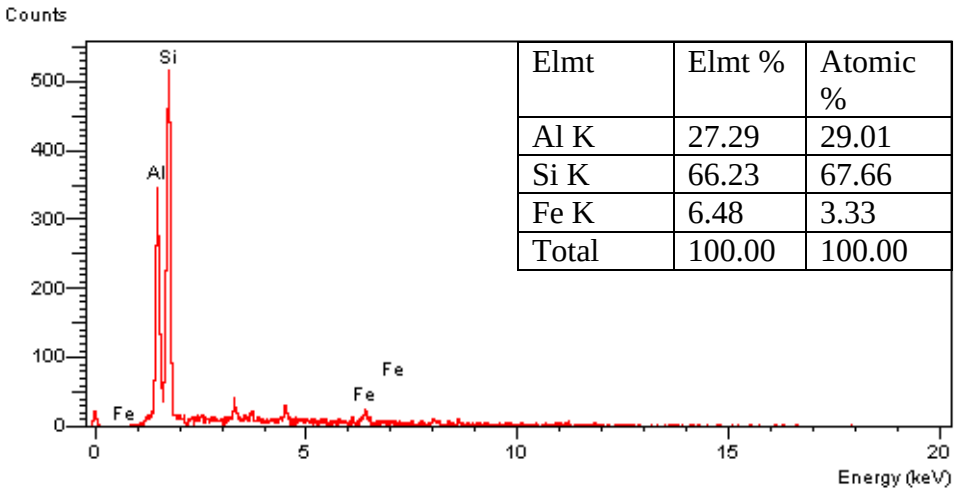

Elmt	Elmt %	Atomic %
Al K	27.29	29.01
Si K	66.23	67.66
Fe K	6.48	3.33
Total	100.00	100.00

Figure 4. 4 **EDS spectra of TFA_j heated at 800 °C for 3h.**

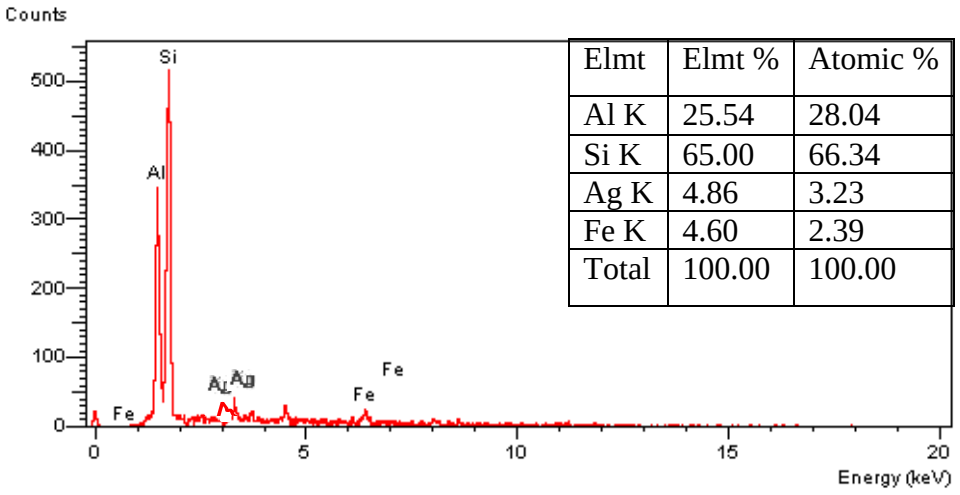

Elmt	Elmt %	Atomic %
Al K	25.54	28.04
Si K	65.00	66.34
Ag K	4.86	3.23
Fe K	4.60	2.39
Total	100.00	100.00

Figure 4. 5 **EDS spectra of $AgFA_j$-5 catalyst prepared using chemical reduction method, calcined at 550 °C for 2h.**

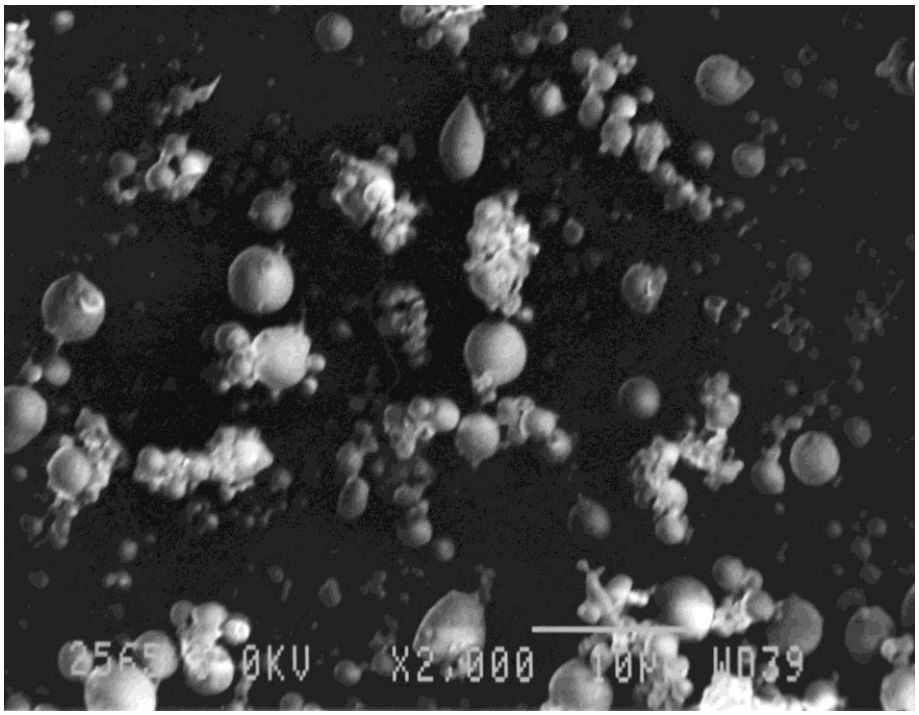

Figure 4. 6 SEM micrograph of TFA_j heated at 800 °C for 3h.

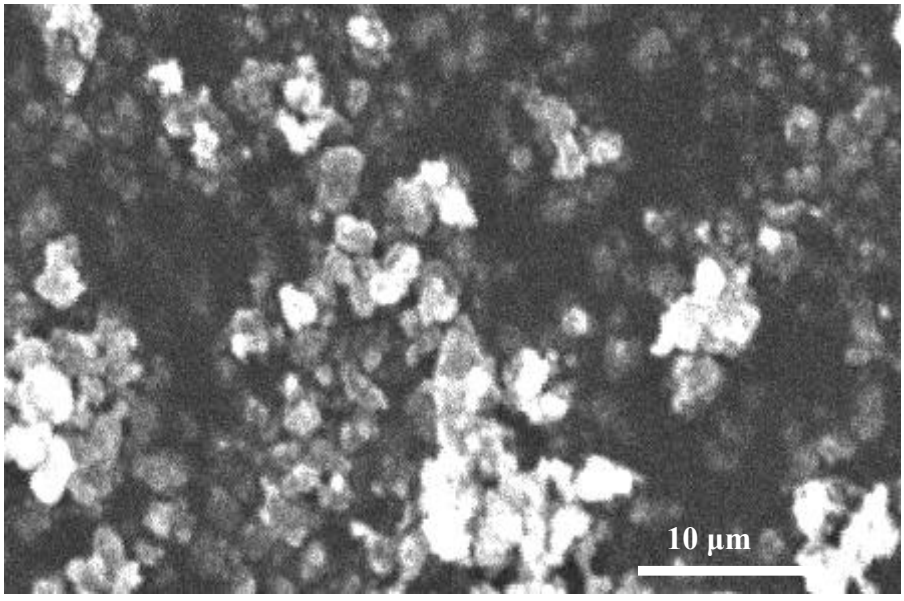

Figure 4. 7 SEM micrograph of $AgFA_j$-5 synthesized using chemical reduction method, calcined at 550 °C for 2h.

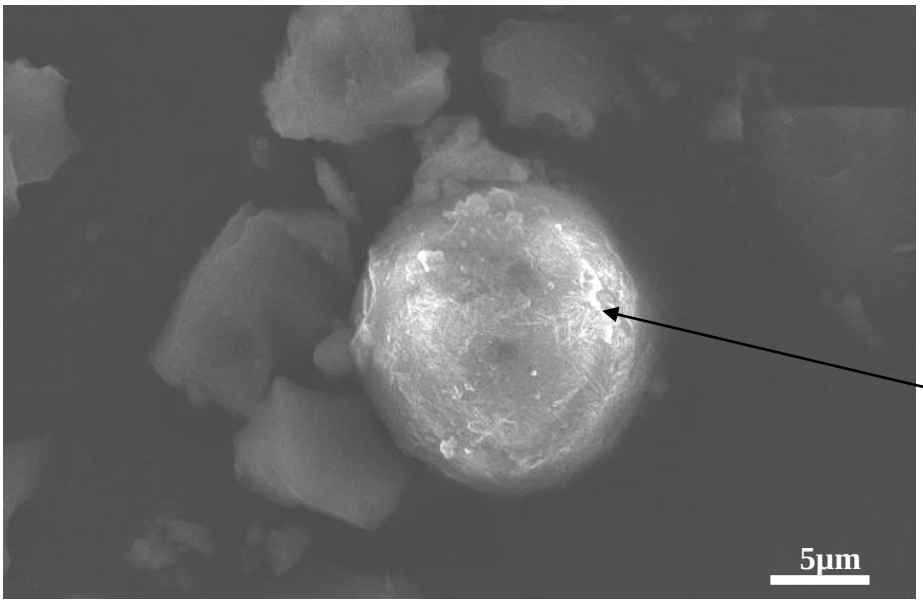

Figure 4. 8 SEM micrograph of AgFA$_j$-5 synthesized using chemical reduction method, calcined at 550 °C for 2h (at high magnification).

4.4.1 Effects of Reaction Time and Oxidant/Alcohol Molar Ratio

The change in conversion (%) of benzyl alcohol in the presence of TBHP and $AgFA_j$-5 catalyst with 1, 2 and 3 TBHP/benzyl alcohol molar ratios, was monitored with respect to the time (**Figure 4.9**). The conversion of benzyl alcohol increases continuously as time and TBHP/benzyl alcohol molar ratios increases and then remains constant. The lowest TBHP/Benzyl alcohol ratio, results 54% (at 3 h) conversion of benzyl alcohol and the other two ratios (i.e. 2:1 and 3:1) give considerably higher conversion, 84% and 99% respectively.

4.4.2 Effect of Substrates

Regarding conversions and selectivity of the products, the experiments were compared with respect to substrates (benzyl alcohol and methanol) and the results are shown in **Table 4.4**. Higher conversion was obtained for benzyl alcohol on $AgFA_j$-5 catalyst. The reactivity of the alcohols toward oxidation with TBHP on $AgFA_j$ catalyst depends on the particular structure of the substrate. $AgFA_j$ catalyst is more active towards benzyl alcohol than methanol.

Table 4. 4 Effect of the $AgFA_j$-5 catalyst in the oxidation of different alcohols. Reaction condition: catalyst 0.2 g; Alcohol 30 mmol; Oxidant TBHP 30 mmol; acetonitrile 15 mL; reflux temperature 90 °C; reaction time 8 h.

Alcohol	Product	Conversion (%)	Selectivity (%)
Benzyl alcohol	Benzaldehyde	65.8	78.7[a]
Methanol	Formaldehyde	40.5	100

[a] Selectivity of benzoic acid is 21.3%.

4.4.3 Effect of Solvents

The results of conversion of benzyl alcohol with various solvents (polar to nonpolar) are shown in **Table 4.5**. The behavior of benzyl alcohol oxidation in various solvents is strikingly different. Acetonitrile gives the best conversion results, followed by toluene. The selectivity toward benzaldehyde was not varied

Table 4. 5 Effect of solvents on oxidation of benzyl alcohol. Reaction condition: $AgFA_j$-5 catalyst 0.2 g; benzyl alcohol 30 mmol; Oxidant TBHP 30 mmol; solvent 15 mL; reflux temperature 90 °C; reaction time 8 h.

Solvent	Dielectric constant	Dipole moment (D	Conversion (%)	Selectivity (%)
Acetonitrile	37.5	3.92	65.8	78.7
Chloroform	3.7	1.04	39.4	90
Toluene	2.4	0.37	48.9	100
p-Dioxane	2.2	0	33.6	62

significantly in various solvents. However, the conversion was low when the p-dioxane and chloroform were used as solvent. The decrease in conversion of benzyl alcohol in toluene may be explained by the low solubility of TBHP in a non polar solvent as a result of which the reaction could not proceed. Even though acetonitrile is a polar and has very high dielectric constant may readily dissolve TBHP along with the benzyl alcohol and consequently will direct the reactants in such a way that properly be adsorbed on the catalyst surface and increasing the efficiency of the conversion.

4.4.4 Effect of Temperature

Oxidation of benzyl alcohol was carried out at 27, 60 and 90 °C in same reaction condition, and it was found that conversion is simultaneously increased as temperature is increased from 27 to 90 °C (**Figure 4.10)**.

4.4.5 Catalyst Recycling and Leaching

Loading of Ag over TFA_j enhances the dispersion of Ag over the TFA_j and increases the activity and life of the resulting catalyst. $AgFA_j$-5 and benzyl alcohol as a model substrate have selected for the recycling and leaching study. The leaching of the catalyst was tested by filtering the catalyst during the reaction and studying the catalytic activity of the filtrate. In this study, a mixture of 0.2 g catalyst $AgFA_j$-5, 15 mL acetonitrile, 30 mmol TBHP and 30 mmol of benzyl alcohol was refluxed for 4 h, then the reaction mixture was filtered, filtrate

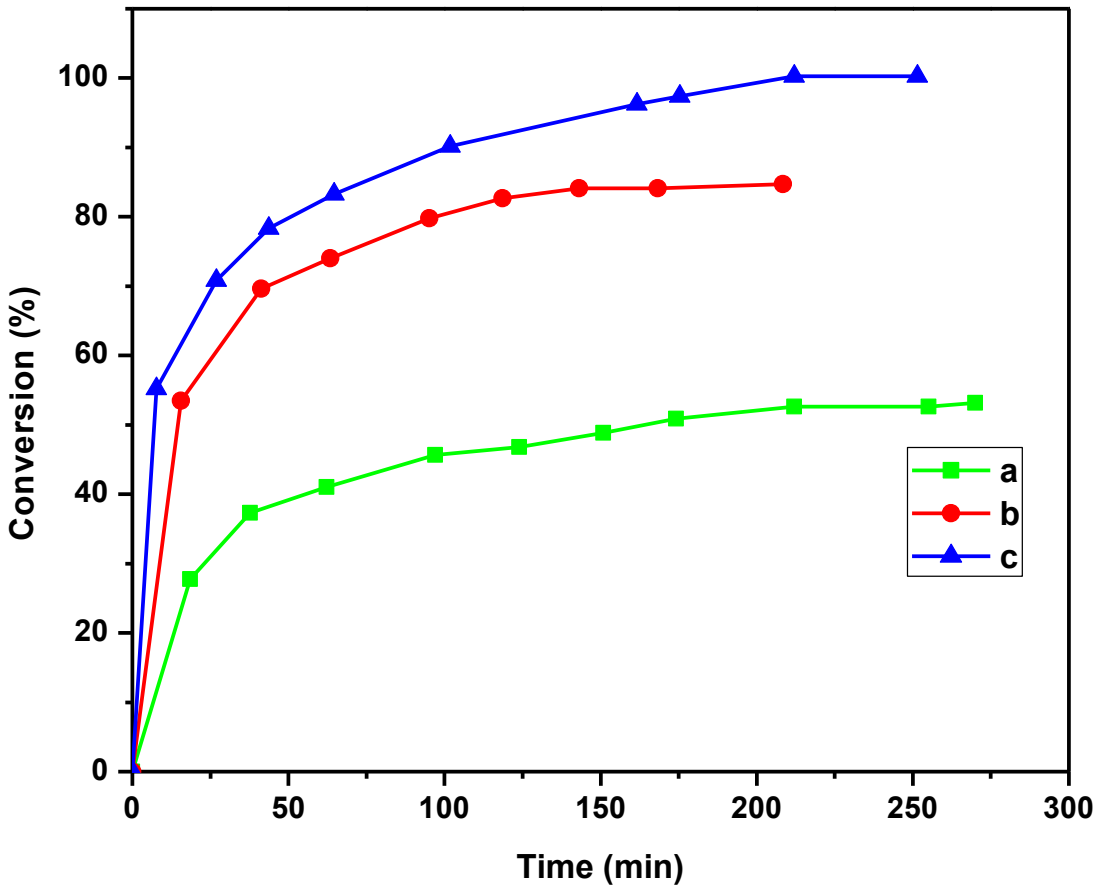

Figure 4. 9 **The effect of reaction time and oxidant/alcohol molar ratio on benzyl alcohol conversion. Reaction condition: acetonitrile 15 mL, $AgFA_j$-5 catalyst 0.2 g; reflux temperature 90 °C; benzyl alcohol 30 mmol; TBHP/ Benzyl alcohol molar ratio: (a) 1, (b) 2 and (c) 3.**

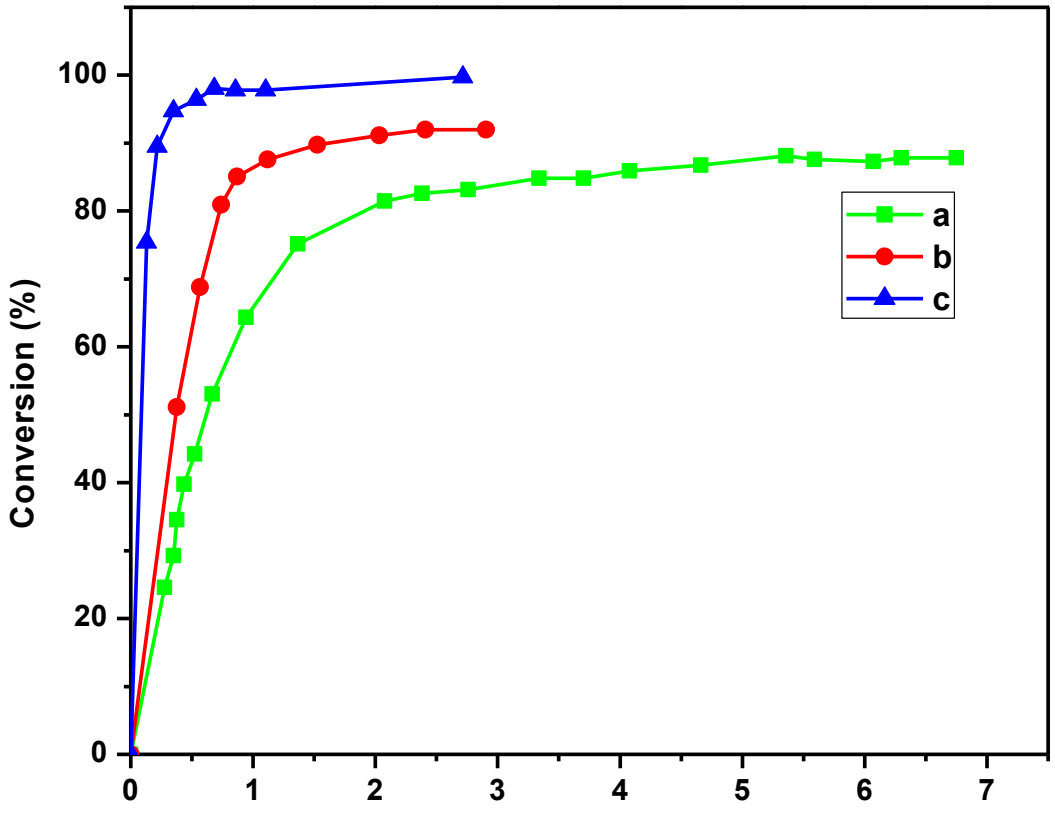

Figure 4. 10 **Conversion of benzyl alcohol as a function of time at (a) 27, (b) 60 and (c) 90 °C with $AgFA_j$-5 catalyst in the presence of excess TBHP. Reaction condition: catalyst 0.2 g; Alcohol 30 mmol; Oxidant TBHP 30 mmol; acetonitrile 15 mL; reaction time 8 h.**

solution was refluxed for next 4 h. The conversion of 54.2% and 55.3 % were obtained for reaction with catalyst and filtrate. The results demonstrate that the amount of leaching of Ag from solid catalyst during liquid phase reaction is low and catalyst is stable. In recycling study, the catalyst was separated from the reaction mixture after each experiment by filtration, washed with the solvent and dried carefully before using it in the subsequent run. The catalyst may be recycled for five times, there is a low loss of activity with lowering in conversion of benzyl alcohol (without any loss in selectivity), indicating that leaching of Ag species from the support was happened but in less amount. Only 10% decrease in conversion was observed after four cycles.

4.4.6 Proposed Mechanism

Proposed mechanism of catalytic partial oxidation of benzyl alcohol is depicted in **Scheme 4.1**. In presence of $AgFA_j$ catalyst, it is hypothesize that TBHP is broken down into t-butoxide and hydroxyl radicals. Abstraction of a hydrogen radical from benzyl alcohol afforded a benzyl alcohol radical which combines with a hydroxyl radical to yield benzaldehyde. The adsorption of alcohol over catalyst surface increases the availability of benzyl alcohol radical nearby hydroxyl radicals thus fascilites the conversion of benzyl alcohol into benzaldehyde. Further oxidation could lead to benzoic acid [38,52]. Therefore, proposed mechanism suggested that the oxidation pathway may be as follows (**eq. 4.1** to **eq. 4.4**).

$$AgFA_j + t\text{–}butOOH \rightarrow t\text{–}butO^{\bullet} + OH^{\bullet} \qquad \textbf{(eq. 4.1)}$$

$$t\text{–}butO^{\bullet} + PhCH_2\text{–}OH \rightarrow t\text{–}butOH + PhCH^{\bullet}\text{–}OH \qquad \textbf{(eq. 4.2)}$$

$$PhCH^{\bullet}\text{–}OH + OH^{\bullet} \rightarrow PhCH(OH)_2 \qquad \textbf{(eq. 4.3)}$$

$$PhCH(OH)_2 \rightarrow \underset{\textbf{Benzaldehyde (76.5\%)}}{PhCHO} + \underset{\text{Benzoic Acid (23.5\%)}}{PhCOOH} \qquad \textbf{(eq. 4.4)}$$

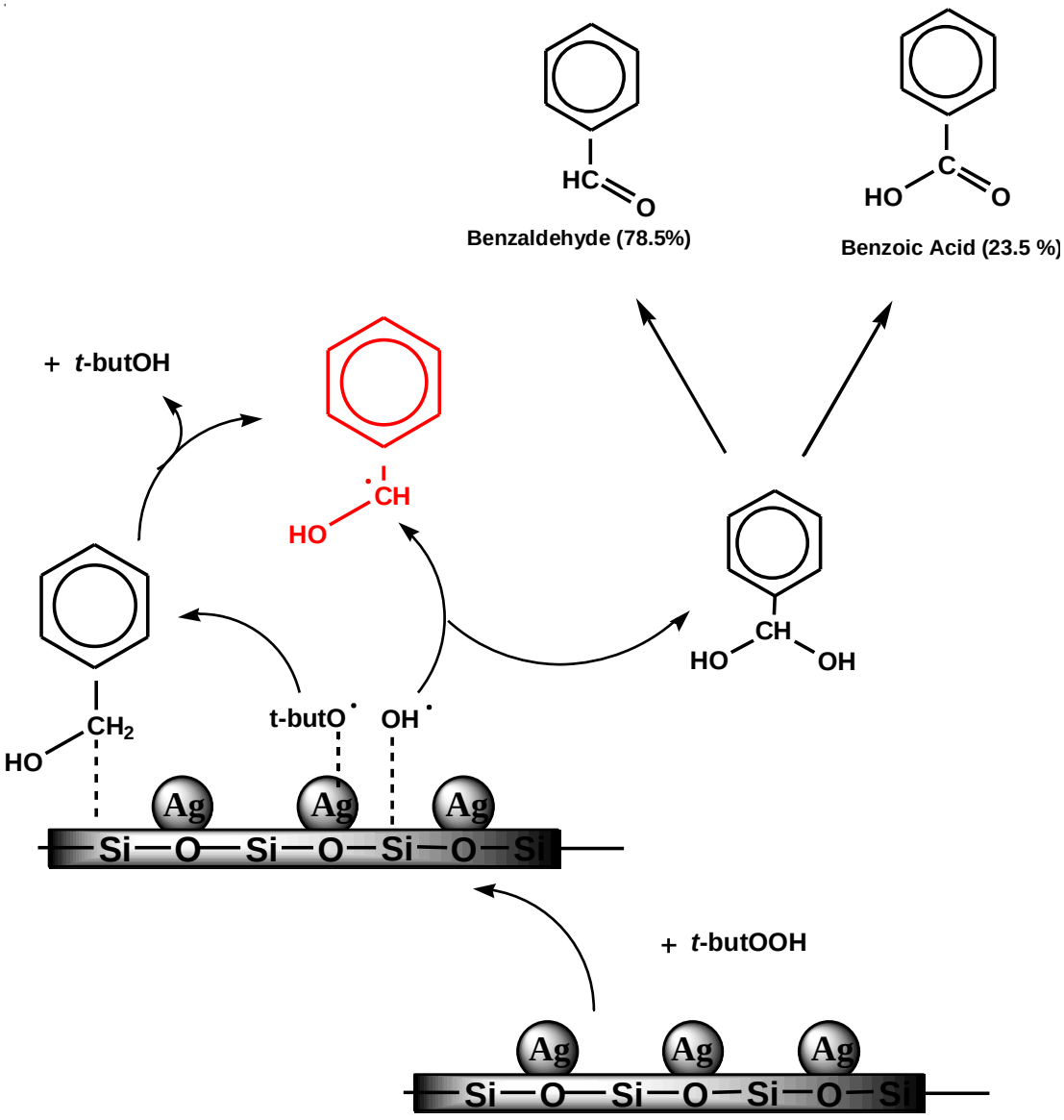

Scheme 4. 1 The mechanistic pathways of oxidation of benzyl alcohol to benzaldehyde over $AgFA_j$-5 catalyst.

4.5 Conclusion

In the present study, an efficient solid oxidation catalyst was synthesized by loading of silver over thermally activated fly ash. The thermal activation of fly ash removes C, S and other impurities, thus increases silica percentage. The characterization of the catalysts confirmed the loading of fly ash surface with significant amount of silver by surface reaction of silver nitrate and surface silanols of the fly ash. The prepared $AgFA_j$ catalyst was found to possess significant oxidation capacity which catalyzes the aldehyde production from the catalytic oxidation of alcohols with tert-butylhydroperoxide (TBHP) in the liquid phase. Only 0.2 g of the catalyst in mild conditions may be able to carry out the oxidation reaction successfully. In addition, the catalyst can be recycled several times without any loss in selectivity and a nearly identical conversion percentage of the recovered catalyst, suggests its reusability and stability.

4.6 References

[1] A.N. Shipway, E. Katz, I. Willner, Chemphyschem 1 (2000) 18.

[2] A.C. Templeton, W.P. Wuelfing, R.W. Murray, Acc. Chem. Res. 33 (2000) 27.

[3] A. Henglein, Chem. Mater. 10 (1998) 444.

[4] L. Hermida, A.Z. Abdullah, A.R. Mohamed, 2013 (2013) 52.

[5] S.S. Gasaymeh, S. Radiman, L.Y. Heng, E. Saion, G.H.M. Saeed, African Phys. Rev. 4 (2010) 31.

[6] M.L. Anderson, C.A. Morris, R.M. Stroud, C.I. Merzbacher, D.R. Rolison, Langmuir 15 (1999) 674.

[7] J.F. Hund, M.F. Bertino, G. Zhang, C. Sotiriou-Leventis, N. Leventis, A.T. Tokuhiro, J. Farmer, J. Phys. Chem. B 107 (2003) 465.

[8] D. Lawless, S. Kapoor, P. Kennepohl, D. Meisel, N. Serpone, J. Phys. Chem. 98 (1994) 9619.

[9] A. Sárkány, I. Sajó, P. Hargittai, Z. Papp, E. Tombácz, Appl. Catal. A Gen. 293 (2005) 41.

[10] L. Chen, D. Ma, B. Pietruszka, X. Bao, J. Nat. Gas Chem. 15 (2006) 181.

[11] X. Zhang, Z. Qu, X. Li, M. Wen, X. Quan, D. Ma, J. Wu, Sep. Purif. Technol. 72 (2010) 395.

[12] Y.-W.C. T.I. Izaak, D.O. Martynova1, V.V. Maas1, E.M. Slavinskaya, A.I. Boronin, Proc. Int. Conf. Nanomater. Appl. Prop. 2 (2013) 01001.

[13] L. Tosheva, A. Brockbank, B. Mihailova, J. Sutula, J. Ludwig, H. Potgieter, J. Verran, J. Mater. Chem. 22 (2012) 16897.

[14] T. Suttikul, T. Sreethawong, P. Ouraipryvan, J. Chamnanmanoontham, S. Chavadej, Polish J. Environ. Stud. 17 (2008) 433.

[15] Y. Cao, W. Dai, J. Deng, (2001) 12.

[16] M. Van Roy J. Irwin, Mouwerik, L. Stevens, M.D. Seese, W. Basham, Environ. Contam. Encycl. Silver Entry (1997) 88.

[17] M. Stoukides, S. Pavlou, Chem. Eng. Commun. 44 (1986) 53.

[18] A. Schlunke, Mechanism and Modelling of the Partial Oxidation of Methanol over Silver, The University of Sydney, 2007.

[19] J.L. Bronkema, a. T. Bell, J. Phys. Chem. C 111 (2007) 420.

[20] J.G. van O. and J.R.H.R. L. Lefferts, Appl. Catal. 23 (1986) 385.

[21] Y. Zhi, L.I. J, Y. Xiang, Chem. Res. Chinese Univ. 21 (2005) 5.

[22] D. Astruc, in:, D. Astruc (Ed.), Nanoparticles Catal., WILEY-VCH Verlag GmbH & Co. KGaA, Weinheim, Weinheim, 2007, p. 48.

[23] Y. Chen, C. Wang, H. Liu, J. Qiu, X. Bao, Chem. Commun. (Camb). 2 (2005) 5298.

[24] P. Claus, H. Hofmeister, J. Phys. Chem. B 103 (1999) 2766.

[25] C.N. Satterfield, Heterogeneous Catalysis in Practice, McGraw-Hill Company, 1980.

[26] S.P.P.Ã. Ramnani, J. Biswal, S. Sabharwal, Radiat. Phys. Chem. 76 (2007) 1290.

[27] T. Mallat, A. Baiker, Chem. Rev. 104 (2004) 3037.

[28] N. Kumar, Ruthenium- Silver Catalysts Supported on Silica, Iowa State University, 1999.

[29] A. Rani, C. Khatri, R. Hada, Fuel Process. Technol. 116 (2013) 366.

[30] C. Khatri, D. Jain, A. Rani, Fuel 89 (2010) 3853.

[31] C. Khatri, M.K. Mishra, A. Rani, Fuel Process. Technol. 91 (2010) 1288.

[32] C. Khatri, A. Rani, Fuel (2008).

[33] D. Jain, R. Hada, A. Rani, J. Catal. 2013 (2013) 1.

[34] D. Jain, C. Khatri, A. Rani, Fuel Process. Technol. 91 (2010) 1015.

[35] D. Jain, C. Khatri, A. Rani, Fuel 90 (2011) 2083.

[36] D. Jain, M. Mishra, A. Rani, Fuel Process. Technol. 95 (2012) 119.

[37] K. Srivastava, V. Devra, A. Rani, Fuel Process. Technol. 121 (2014) 1.

[38] R.A. Sheldon, J.K. Kochi, Metal-Catalyzed Oxidations of Organic Compounds, Elsevier, 1981.

[39] R.. Sheldon, I.W.C.. Arends, A. Dijksman, Catal. Today 57 (2000) 157.

[40] C.Y. Lorber, J.A. Osborn, Tetrahedron Lett. 37 (1996) 853.

[41] C. Sheu, D.T. Sawyer, J. Am. Chem. Soc. 112 (1990) 8212.

[42] W. Nam, R. Ho, J.S. Valentine, J. Am. Chem. Soc. 113 (1991) 7052.

[43] R.S. Chandran, W.T. Ford, J. Chem. Soc. Chem. Commun. (1988) 104.

[44] S. IVANOV, J. Catal. 56 (1979) 150.

[45] H. Turk, W.T. Ford, J. Org. Chem. 53 (1988) 460.

[46] T.J. Pinnavaia, M.S. Tzou, S.D. Landau, J. Am. Chem. Soc. 107 (1985) 4783.

[47] M. Ghanipour, D. Dorranian, J. Nanomater. 2013 (2013) 1.

[48] S.K. Ghosh, T. Pal, Chem. Rev. 107 (2007) 4797.

[49] R. Desai, V. Mankad, S.K. Gupta, P.K. Jha, Nanosci. Nanotechnol. Lett. 4 (2012) 30.

[50] A.C.S. JCPDS--International Centre for Diffraction Data, Mineral Powder Diffraction File: Search Manual : Chemical Name, Hanawalt, Fink, Mineral Name Mineral Powder Diffraction File, JCPDS--International Centre for Diffraction Data, 1986, 1986.

[51] B.G. Kutchko, A.G. Kim, Fuel 85 (2006) 2537.

[52] V. Mahdavi, M. Mardani, J. Chem. Sci. 124 (2012) 1107.

Microwave Assisted Solution Combustion Synthesis of Activated Fly Ash Supported NiO Nanoparticles for Hydrogen Peroxide Decomposition

Abstract

This chapter illustrates the synthesis of fly ash supported nickel oxide nanoparticles as cost effective catalyst for generation of reactive oxygen species for waste water treatment. A novel microwave assisted solution combustion synthesis is described in which urea is used as fuel and nickel nitrate as oxidizer. Fly ash is chemically activated prior to being used as support material for catalyst synthesis. The experimental details of thermal and chemical activation of fly ash are reported which modified neutral surface of fly ash into basic surface responsible for intensified bonding and dispersion of NiO nanoparticles over fly ash surface. The results of physico-chemical and morphological characterization of fly ash, chemically activated fly ash and fly ash supported nickel oxide, decomposition reactions of hydrogen peroxide to evaluate the catalytic activity of the catalyst, effects of different parameters such as pH, calcination temperature, nature of catalyst etc., are also discussed in this chapter.

5.1 Introduction

Fast decomposition of hydrogen peroxide has wide applications in waste water treatment, health supplementation (altitude sickness, breathing problems, blood circulation problems, and "well-being" oxygen supplementation), fish tank aeration, water aeration, agricultural, horticultural, rocket propellants, fuel cells, and bleaching etc. [1–4], where it is used as a source of oxygen [4]. Hydrogen peroxide is also used in advanced oxidation processes (AOP) and can be combined with catalysts or other oxidizers to produce reactive oxygen species (ROS i.e. O_2 and OH radical) able to attack a wide range of organic compounds and microorganisms [5]. Advanced oxidation processes (AOPs) are attractive alternatives to conventional treatment methods. They have been used more frequently due to the high oxidizing power of free radicals. Production of these radicals is achieved using either single oxidants or combinations of ozone, H_2O_2 and UV radiation [6] and a combination of H_2O_2 with homogeneous catalyst viz., ferrous ions in Fenton's reagent, TiO_2 etc. [7,8]. It is well known that catalysts of metal ions in solution or powder metal oxides create an unstable state because the surface tension favours a smaller interfacial area for a given mass. Catalysts also cause a secondary pollutant problem that requires further treatment to remove the metal ion from water [9]. Therefore, attempts have been made to improve the catalysis process by replacing the homogeneous catalysts with a heterogeneous catalyst. For this purpose, supported metal catalysts can be prepared [10]. Fly ash (FA) is one of the most widely used catalyst supports in recent years [11–20] because of its high surface area, well-defined porous structure, the presence of various surface functional groups and its inertness in many catalytic processes [16].

Many physical and chemical methods are used for synthesis of non supported and supported metal/metal oxide nanoparticles like CVD [21], PVD [22], spray pyrolysis [23], sol gel [24] and solution combustion [25] etc., among them solution combustion synthesis is a quick and easy process, which saves time and energy. This process is used directly in the production of high purity, homogeneous ceramic oxide powders. This method is versatile for the synthesis of

a wide size range of particles, including nanometer size Al_2O_3 powders [26], Cr^{3+}-doped α-Al_2O_3, spinels, MAl_2O_4 (M = Ca, Mg, Zn and Ni), perovskites, $LaMO_3$ (M = Mn, Cr and Al), $La_{0.67}Sr_{0.33}MnO_3$, and $La_{0.67}Ca_{0.33}MnO_3$ [27] and Bi_2O_3 [28] etc. Interestingly, the combustion of a mixture of redox metal nitrate-glycine-nitrate ammonium acetate or mixtures of metal nitrate-urea combustion systems, showed no presence of a flame for obtaining oxide nanoparticles. The characteristics of the powders, such as crystallite size, surface area, nature of agglomeration for both strong and weak, are governed mainly by the enthalpy and temperature generated during combustion, which is dependent on the nature of the fuel and the kind of fuel-oxidizer used in the reaction. The rapid generation of a large volume of gases during combustion dissipates the heat from the process and limits the temperature rise, reducing the possibility of premature sintering between the primary particles. The generation of gases also helps to limit interparticle contact, resulting in a more powdery product.

In recent years, microwave-assisted synthesis is emerging as one of the efficient method to produce nanomaterial with controlled size and shape, because of its characteristics of rapid volumetric heating, short reaction time, high reaction rate, and energy savings. [29–32]. Microwave irradiation is becoming widely used as a rapid heating method for the synthesis of metal oxides [33]. Beyond rapid heating, microwave irradiation also reduces the reaction time and increases product yield when compared to conventional heating methods.

The present study introduces an innovative, highly efficient, cost effective, re-generable fly ash supported nanosized NiO catalyst ($NiFA_k$) by supporting NiO over chemically activated fly ash (CFA_k) using microwave assisted solution combustion synthesis. Urea and $NiNO_3$ are used as fuel and oxidizer respectively. To get information about the catalytic activity of the catalyst, decomposition of hydrogen peroxide has been used as model test reaction [34–37]. The microwave assisted synthesis is a green, efficient, simple, fast and high yielded method. The novelty of the study is the use of chemically activated fly ash as support for NiO loading and presence of microwave radiation during synthesis of supported NiO catalyst.

5.2 Experimental Details

5.2.1 Materials and Reagents

Fly ash has been collected from Kota super thermal power station (Kota, Rajasthan, India) and was used after chemical activation, after making a representative sample by the method of coining and quartering. It is named as **FA_k**. Nickel nitrate ($NiNO_3.6H_2O$, ACS, Merck, 99.0%), calcium carbonate ($CaCO_3$, AR, S.D. fine chemicals, 98.9%) and urea (CH_4N_2O, AR, Rankem, 98.9%) were used for catalyst preparation and hydrogen peroxide (H_2O_2, AR, Merck, 30%) was used for evaluation of catalytic activity of prepared catalyst.

5.2.2 Synthesis of $NiFA_k$ Catalyst using Novel Microwave Assisted Combustion Synthesis

Fly ash supported NiO catalyst ($NiFA_k$) of 20 weight % was prepared using microwave assisted solution combustion synthesis (MWSCS) in CEM discover microwave synthesizer as shown in **Figure 5.1**. For this fly ash was activated by means of thermal and chemical activation techniques prior to use for catalyst preparation. For thermal activation, as received fly ash (FA_k) was calcined at 900 ^{0}C for 3 hrs to remove C, H, S and other impurities enhancing the surface hydroxyl groups over thermally activated fly ash (TFA_k) surface. For preparing chemically activated fly ash (CFA_k) 1 g TFA_k was added to 0.25 g $CaCO_3$, dissolved in hot de-ionized water, in a stirred reactor. The above suspension was refluxed at 110 °C for 2 days followed by washing and drying at 110 °C for 24 h. The dried sample was calcined at 700 °C for 2 h in order to get CaO from $CaCO_3$. This resulted in coating of CaO over TFA_k surface availing its surface most suitable for homogeneous loading of NiO nanoparticles.

Then for 20 weight % loading of NiO over CFA_k surface 1.6 g CFA_k preheated at 400 °C for 4 h was added to 50 mL aqueous solution of 1.5 g $Ni(NO_3)_2.6H_2O$ (0.1 M) containing in a 100 mL single necked round bottom flask equipped with vertical air glass condenser placed in a sample holder of CEM discover microwave synthesizer. Aqueous solution of urea was added in 1:5 molar ratios in the above suspension as fuel for combustion of nickel nitrate.

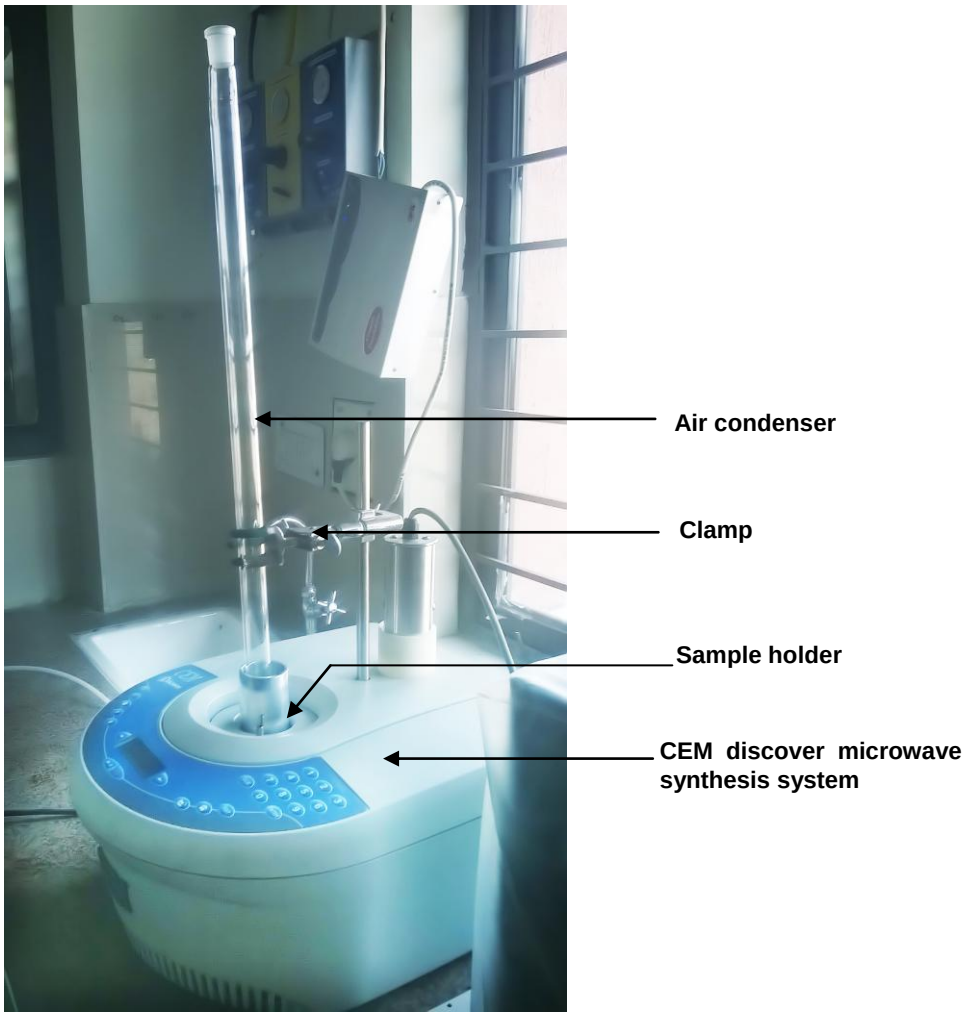

Figure 5. 1 Experimental setup for synthesis of $NiFA_k$ catalyst using CEM discover microwave synthesis system.

After adding urea the above suspension was stirred for 5 min for proper mixing of ingredients. Further the suspension was heated to 100 °C for 2 h with continuous stirring set to medium under microwave irradiation of 100 W powers. Urea was slowly decomposed at 100 °C into CO_2 and liquid ammonia in aqueous medium. Thus prepared liquid ammonia hydrolyzed the $Ni(NO_3)_2$ into $Ni(OH)_2$ in this way green precipitate of $Ni(OH)_2$ was formed over surface of CFA. After completion of reaction the liquid phase was decanted from solid phase, then the resulting precipitate was agitated and washed repeatedly with 200 mL deionised water in order to remove the ammonia and undecomposed urea if any. The washed precipitate was dried in hot air oven at 60 ºC for 24 h. The dried material was powdered with mortar and pestle and then calcined at 400 °C for 3 h in a muffle furnace. The calcined powder was again slightly crushed with mortar and pestle and used for further characterization.

5.2.3 Characterization

FA_k, CFA_k and $NiFA_k$ were characterized by AAS, XRD, FT-IR and SEM-EDX analysis to evaluate physico-chemical properties of catalyst and support. Detail is given in **Annexure I**.

5.2.4 Evaluation of Catalytic Activity by Decomposition of Hydrogen Peroxide

To evaluate the catalytic activity of as synthesized $NiFA_k$ catalyst decomposition of H_2O_2 was studied. In a typical experiment 0.0206 g $NiFA_k$ catalyst was added to 60 mL solution of 0.002 M H_2O_2 in a 100 mL double walled glass vessel at 10 pH with stirring at 700 rpm on a magnetic stirrer. Reaction temperature was maintained at 55 °C by circulating water through double wall jacket of glass vessel. pH of reaction mixture was adjusted using NH_4OH. The stirring was continued during decomposition reaction. After suitable time interval (1 min) a known amount of the reaction mixture was withdrawn from the reaction vessel and was rapidly added to 5 mL of ice cooled 5 M sulfuric acid solutions to quench the decomposition reaction. The catalyst was separated from the mixture by centrifugation. Thus obtained centrifuge was titrated against 0.02 M $KMnO_4$ solution to estimate the amount of un-decomposed H_2O_2. Blank experiments were

also performed in the absence of the catalytic material in order to evaluate the effect, if any, of the experimental conditions on the decomposition of hydrogen peroxide. To optimize the reaction conditions catalytic decompositions of H_2O_2 were performed at different reaction temperature and pH values. To see the effect of catalyst decomposition were also performed on FA_k and CFA_k. Effect of catalyst calcination temperature was studied using catalysts calcined at different temperatures.

5.2.5 Catalyst Regeneration

After first use, spent $NiFA_k$ catalyst from the reaction mixture was recovered by filtration and regenerated for further use. The recovered catalyst was washed thoroughly with water and dried in oven at 110 ºC for 12 h followed by activation at 300 ºC for 1 h in static condition prior to use for catalytic reaction. Thus, regenerated catalyst was used for further reaction cycles under the similar reaction conditions.

5.3 Results and Discussion

5.3.1 AAS Analysis

The chemical composition evaluated by atomic absorption spectrophotometer (AAS) shows that FA_k having SiO_2 (54%), Al_2O_3 (21%), Fe_2O (9%), CaO (1.6%), MgO (0.8%), TiO_2 (1.3%), Na_2O (4.8%), K_2O (3.2%) and trace elements (4.0%). In FA_k only 0.6 weight percent of CaO is detected but the amount of Ca incorporated in the CFA_k is found 11.7 weight percent. The increase in Ca is responsible for more CaO-SiO_2 phases in CFA_k resulting in increased basicity consequently production of active sites for NiO loading.

5.3.2 XRD Analysis

The XRD pattern of FA_k, CFA_k and $NiFA_k$ is given in **Figure 5.2** and detail of different phases present in XRD is given in **Table 5.1**. The diffraction pattern of FA_k **(Figure 5.2 (a))** shows the presence of both amorphous and crystalline phases which poses higher percentage of quartz and mullite phases the detailed description of diffraction pattern of fly ash is given in **Figure 4.3 (a)** of **Chapter 4**. The XRD pattern of CFA_k in **Figure 5.2 (b)** shows the appearance of all peaks

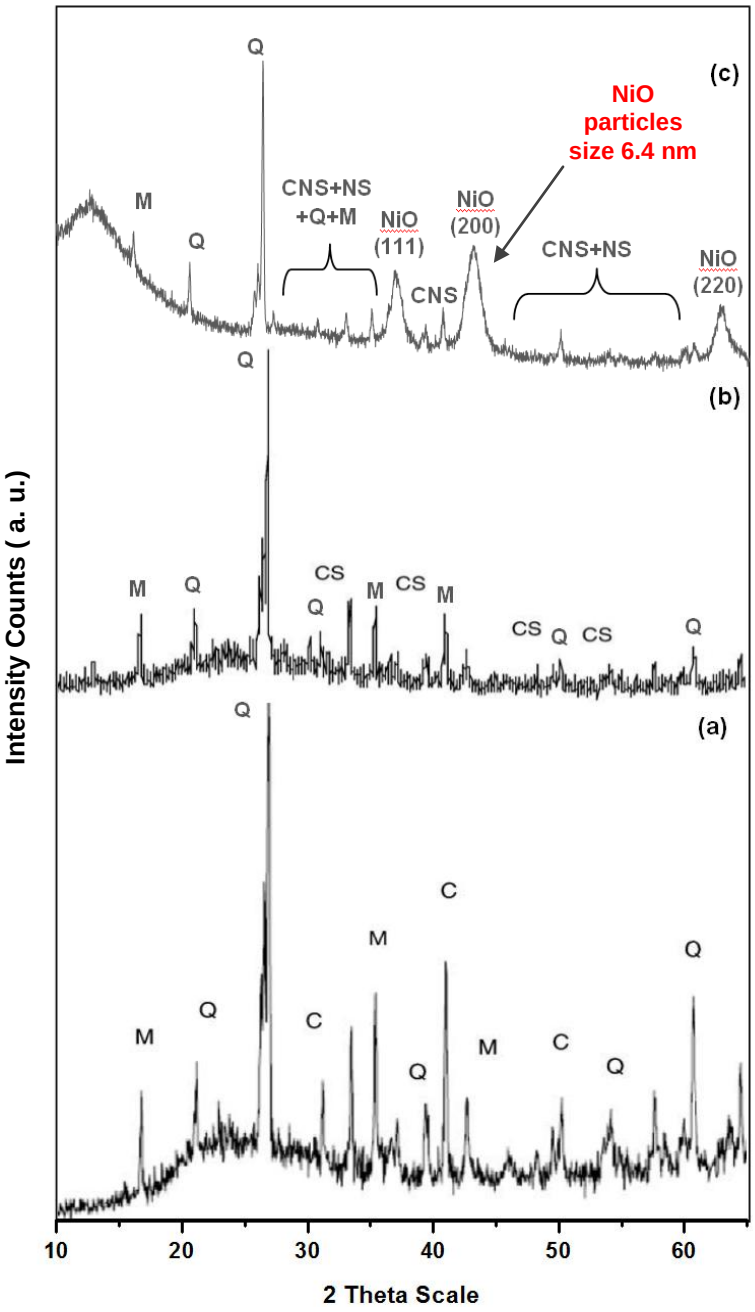

Figure 5. 2 **X-ray diffraction patterns of (a) FA_k collected from Kota, (b) CFA_k activated by CaO, heated at 700 ºC for 2 h, (c) $NiFA_k$ catalyst prepared using microwave assisted combustion route, calcined at 400 ºC for 3h. (M-mullite, Q-quartz, C-calcite, CS-calcium silicate, CNS-calcium nickel silicate phase, NS-Nickel silicate phase, NiO-Nickel oxide phases).**

Table 5. 1 Comparison of crystalline phases present in FA_k, CFA_k and $NiFA_k$.

2 Theta	Crystalline phases FA_k	Crystalline phases CFA_k	Crystalline phases $NiFA_k$
~16	Mullite	Mullite	Mullite
~20	Quartz	Quartz	Quartz
~22	-	-	-
~23	-	-	-
~26	Quartz	Quartz	Quartz
~26.5	-	-	**CNS/NS**
~28	-	-	**CNS/NS**
~30	-	-	Calcite/ **CNS/NS**
~31	Calcite	Calcite/**CS**	**CNS/NS**
~33	Hematite	Hematite/**CS**	Hematite/ **CNS/NS**
~35	Magnetite	Magnetite	Magnetite
~37	-	**CS**	**NiO**
~39	Quartz	Quartz	Quartz
~40	Calcite	Calcite	Calcite
~42	Mullite	Mullite	Mullite/**CNS**
~43	-		**NiO**
~47	-	**CS**	CNS
~50	Calcite	Calcite/**CS**	Calcite
~53	-	-	**CNS/NS**
~54	-	**CS**	**CNS/NS**
~57	-	-	**CNS/NS**
~60	Quartz	Quartz	Quartz
~62	-	-	**CNS/NS**
~63	-	-	**NiO**

of FA_k along with new peaks of calcium silicate phases at 2 theta 31°, 32°, 37°, 47° and 54° [38] arise due to reaction between silica present in FA_k and CaO obtained by $CaCO_3$ decomposition during chemical activation of FA_k. The amorphous nature of the CFA_k increases which is evident from the decrease in the intensity of crystalline phases in CFA_k. **Figure 5.2 (c)** illustrates the X-ray diffraction pattern of $NiFA_k$ catalyst prepared using MWSCS. XRD analysis showed the presence of crystalline and amorphous phases of FA_k and CFA_k together with calcium nickel silicate, nickel silicate and nickel oxide phases which are observed from the new peaks appeared in diffraction pattern of $NiFA_k$ (match with JCPDF file no 47-1049 of NiO, 24-0186 of $CaNiSi_4O_{10}$, 15-0388 of Ni_2SiO_4) [39] as shown in **Table 5.1** confirms the loading of Ni over CFA_k. The amorphous phase of fly ash is increased by NiO loading which results in decreased crystallinity [12]. The mean crystallite size of NiO is obtained 6.4 nm calculated by highest intensity NiO peak of $NiFA_k$ (200) peak of $NiFA_k$ has been calculated by using Scherrer's equation. Results indicate that MWSCS as well as activation using Ca of support is another alternative way for metal oxide loading over fly ash surface. Ca activation of fly ash introduces the active basic sites over fly ash responsible for enhanced loading of Ni on fly ash surface as well as microwave irradiation increases the nucleation of nickel oxide over fly ash surface responsible for homogeneous loading of nanosized NiO particles over fly ash surface.

5.3.3 FT-IR Analysis

The FT-IR spectra of FA_k, CFA_k is given in **Figure 5.3** and $NiFA_k$ is given in **Figure 5.4.** The spectrum of FA_k (**Figure 5.3 (a)**) matches well with the spectrum reported in the literature [40], shows a broad band between 3400 and 3000 cm^{-1} indicates the presence of surface –OH groups, –Si-OH and absorbed water molecules on surface. The spectrum also shows a broad range of bands from 1055 cm^{-1} to 1100 cm^{-1} are attributed to the modes of asymmetric Si–O–Si stretching vibrations. The low frequency band at around 794 cm^{-1} is due to symmetric Si–O–Si stretching vibrations. The FT-IR spectrum of CFA_k in **Figure 5.3 (b)** shows a band at around 3740-3742 cm^{-1} refer to the Si–OH stretching in

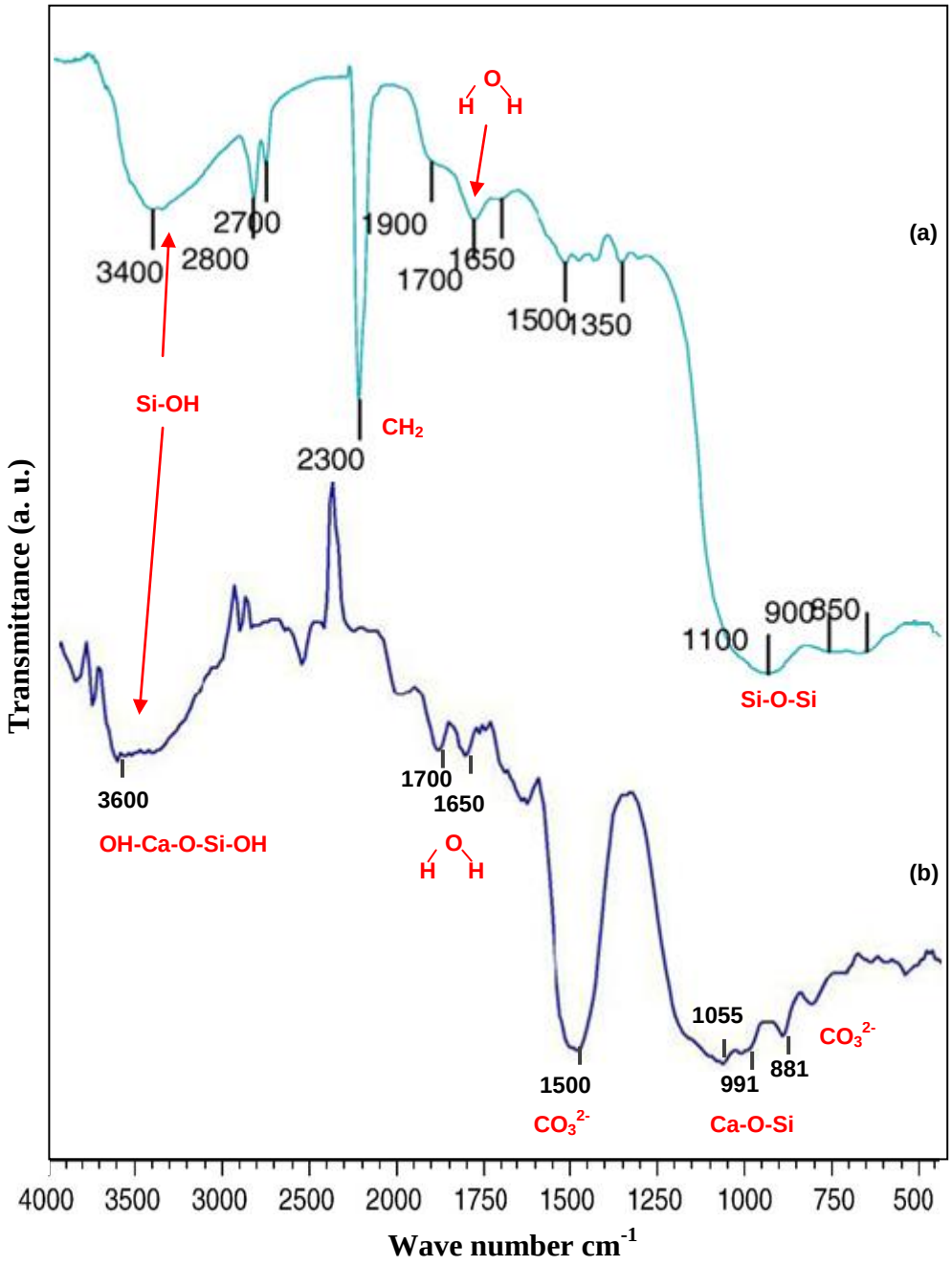

Figure 5. 3 **FT-IR spectrum of (a) FA_k, (b) CFA_k chemically activated using $CaCO_3$, heated at 700 °C for 2h.**

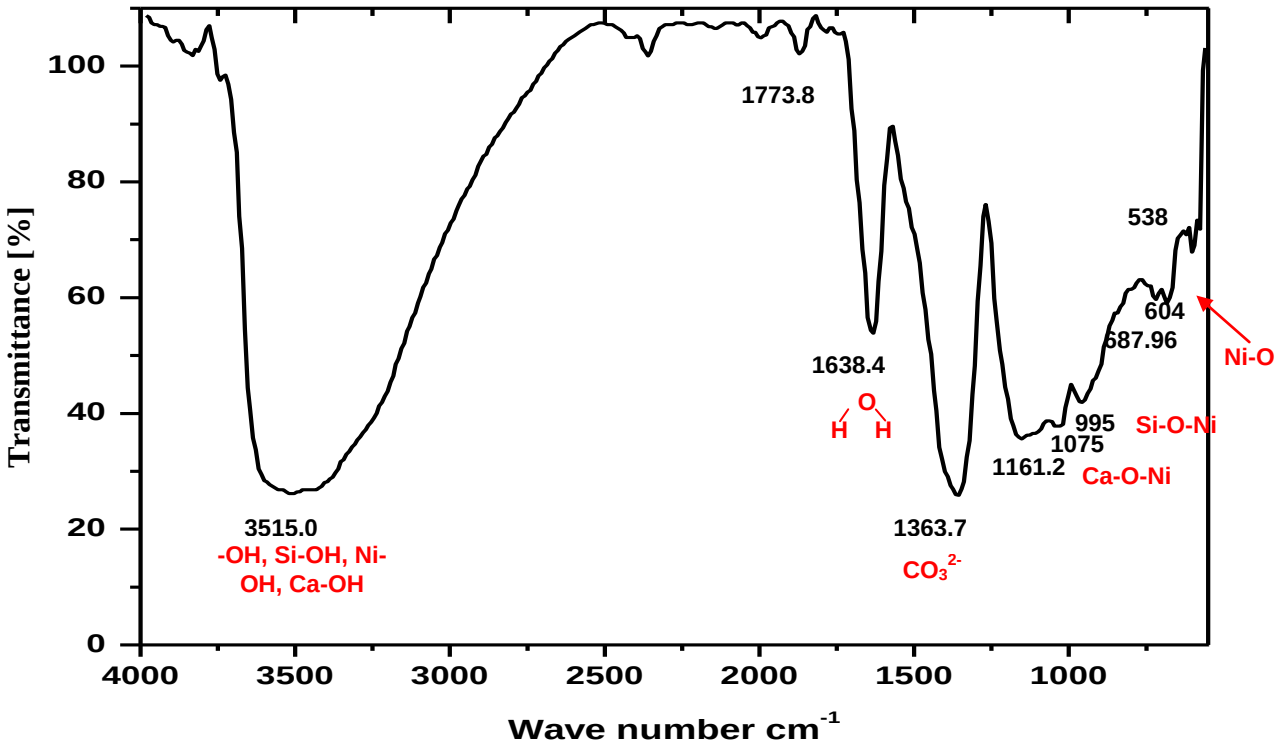

Figure 5. 4 **FT-IR spectrum of $NiFA_k$ catalyst prepared using MWSCS, calcined at 400 ºC for 3h.**

isolated Si–OH species [41]. A peak at 1650 cm^{-1} is due to the bending mode of water molecule. The adsorption peak at around 991 cm^{-1}, shows the presence of Si–O–Ca bond [42], is an evidence for loading of CaO on fly ash surface. This band is due to the formation of calcium silicate hydrate (CSH), a new phase found after loading of CaO. Intense band between 3400 and 3640 cm^{-1} also indicates the associated –OH groups on the surface of the support silica or with the calcium silicate. The presence of CSH is responsible for the increase in basicity of CFA_k. At high temperature up to 700 °C the molecular water is removed while structural –OH ions remain associated in the Ca and SiO_2 skeleton [43]. The low coordinated O^{-2} ions on the edges/corners of CaO particles loaded on FA_k are less stabilized by adjacent Ca^{+2} ions and could also exhibit higher basicity in CFA_k [44]. A broad and intense band at 1500 cm^{-1} and at 881 cm^{-1} is due to asymmetric stretching of CO_3^{-2} which remains in CFA_k owing to incomplete decomposition of $CaCO_3$ even at high temperature up to 700 °C [45].

Infrared spectra of $NiFA_k$ catalyst calcined at 400 ˚C for 3h is given in **Figure 5.4** shows a broader and intense band with higher absorbance than FA_k and CFA_k between 3600 and 3000 cm^{-1} indicates the presence of surface –OH groups, –Si-OH, -Ni-OH and absorbed water molecules on the surface. New peaks are observed between 700 and 500 cm^{-1} due to Ni-O stretching confirms the loading of NiO over fly ash surface. Broad band due to Si-O-Si, T-O (T= Al, Si) stretching spread to lower wave number is inferred that the strength of Si-O-Si and T-O bond is decreased as a result of new Si – O – Ni bond formed during the preparation of $NiFA_k$ catalyst [46]. In **Figures 5.3** and **5.4** comparing the FT-IR spectra at neighborhood of wave number 1000 cm^{-1}, it is found that the $NiFA_k$ catalyst has additional peaks at 1075 and 995 cm^{-1}. These additional peaks are speculated to correspond to the bending motion of Si-O-Ni bond and Ca-O-Ni bond. There has been speculation of the existence of a Si-O-Ni bond. However, no direct evidence has been shown in the literature [47]. It may be expected from previous studies that Ni^+ fragments react with the free surface silanols on the surface of CFA_k to form Si-O-Ni and Ca-O-Ni species, which in turn may serve as nucleating sites for the further aggregation of nickel oxide [48].

5.3.4 SEM-EDS Analysis

A typical EDX spectrum of the CFA_k is given in **Figure 5.5.** The elements detected are Si- 21.52%, Al-8.66%, O-56.79%, C-1.61%, Na-1.21%, Mg-0.12% Ca-11.19%, K-0.09%, Fe-0.30% and Ti-0.12%. The presence of calcium (Ca-11.19%) in the CFA_k confirms the loading of CaO on FA_k surface, as well as the EDS spectrum of $NiFA_k$ catalyst is shown in **Figure 5.6** shows 20 % deposition of Ni over fly ash confirms the loading of NiO over CFA_k surface.

To study the surface topography and to assess the surface dispersion of active components over the supports, SEM investigations were performed on FA_k, CFA_k and $NiFA_k$. The obtained representative electron micrographs are presented in **Figure 5.7** to **5.9**. SEM micrographs of FA_k (**Figure 5.7)** revealed the presence of smooth and spherical silica particles, while the typical SEM images of the CFA_k in **Figure 5.8** shows dense particles with distribution of varying particle sizes. SEM micrographs of $NiFA_k$ catalyst is shown in **Figure 5.9** depicts the loaded and rougher surface of support due to deposition of NiO over CFA_k surface, corroborating the conclusion extracted from the XRD pattern and FT-IR spectra.

5.3.5 Effect of Microwave Radiation on Reaction Rate of Loading of NiO Over Fly Ash Surface

One new finding of this research is intensification of the reaction-rate by microwave- assistance. The Arrhenius law explains the specific rate:

$$k = A \exp(-Q/RT) \qquad \textbf{(eq. 5.1)}$$

Where k is the rate constant, A is the frequency factor indicating the molecular mobility, Q is the activation energy, R is the universal gas constant and T is the absolute temperature at the reaction interface. According to **eq. 5.1**, there are two ways to increase the rate of a chemical reaction: increasing A or decreasing Q.

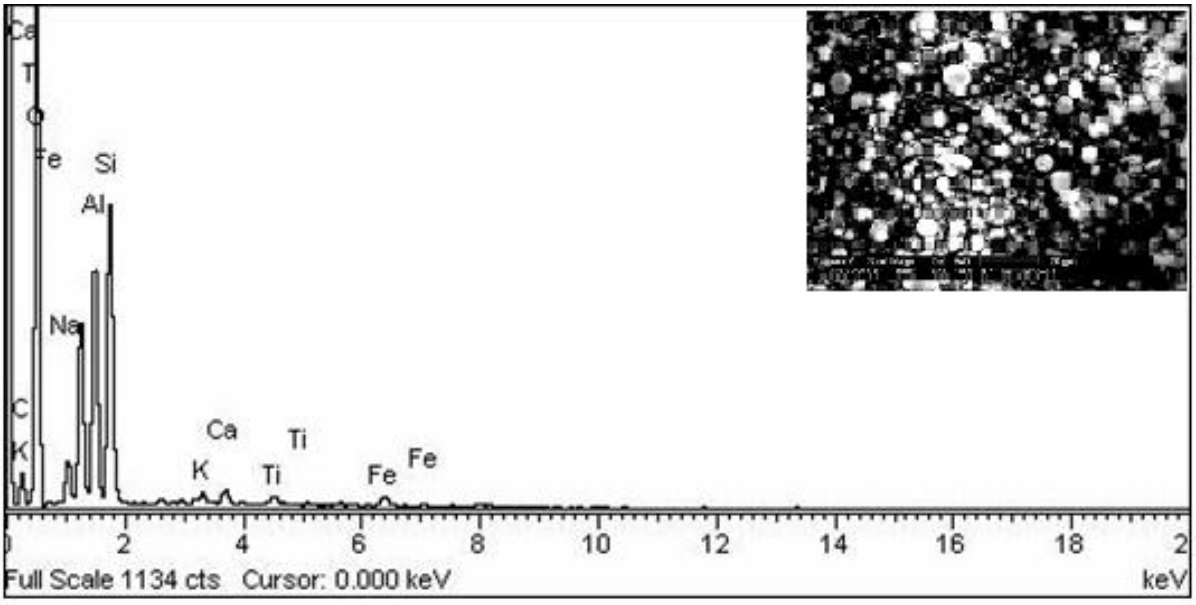

Figure 5. 5 EDS spectrum of CFA_k chemically activated using $CaCO_3$, heated at 700 ºC for 2h.

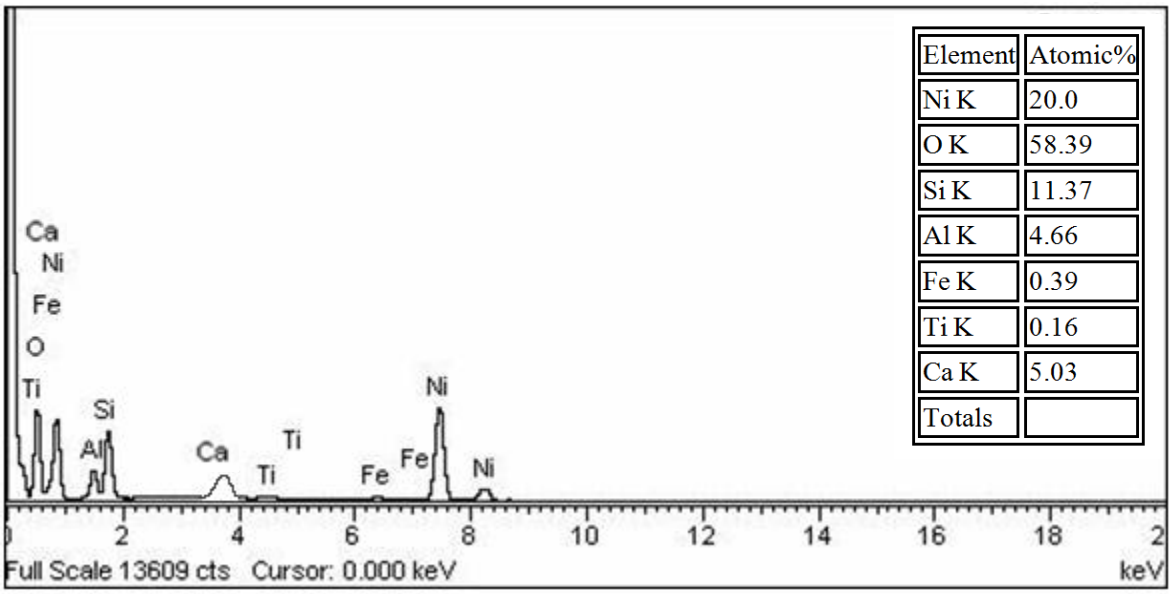

Figure 5. 6 EDS spectrum of $NiFA_k$ catalyst prepared using MWSCS, calcined at 400 ºC for 3h.

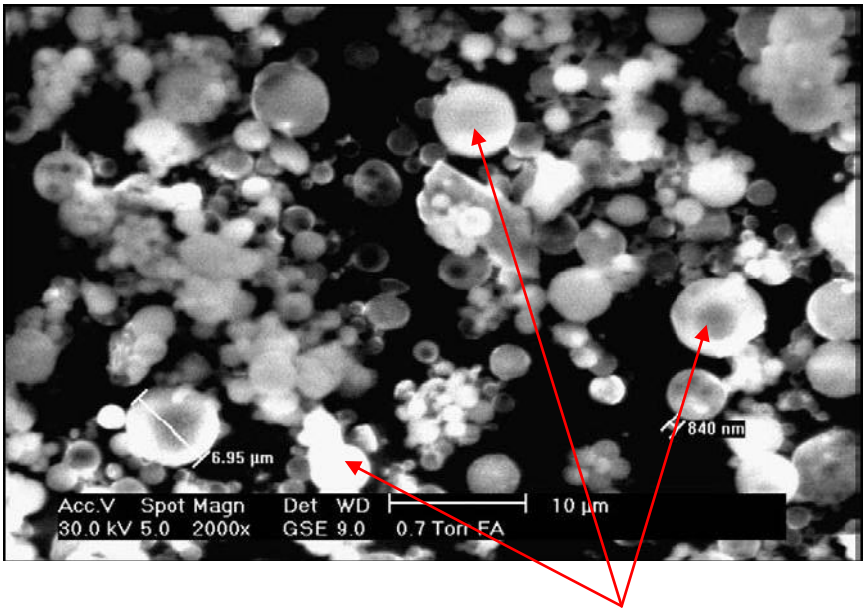

Figure 5. 7 SEM micrograph of FA_k.

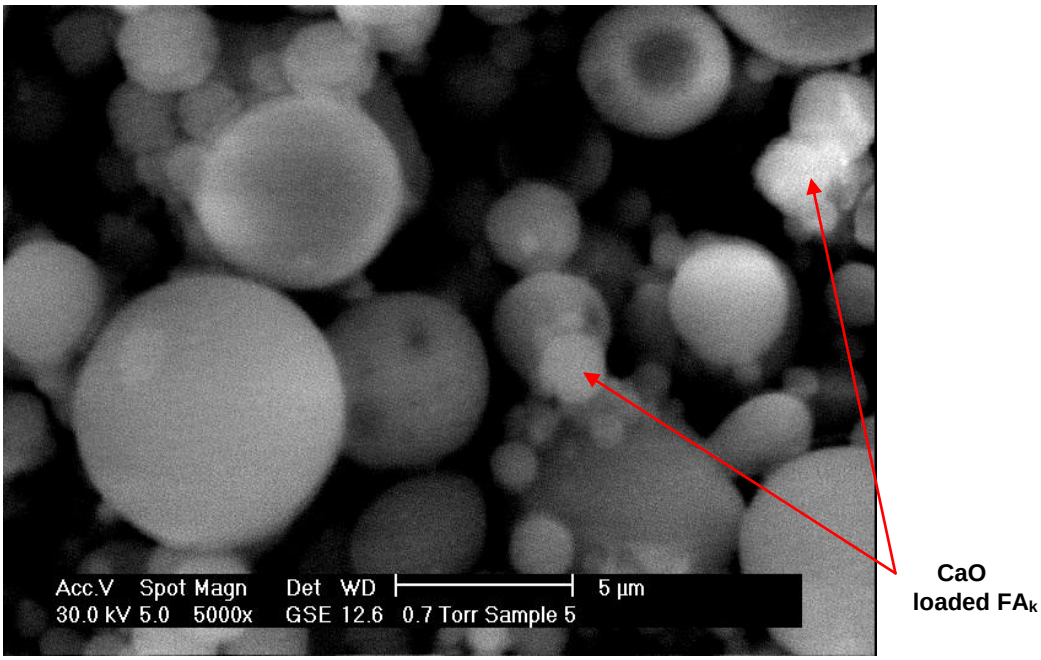

Figure 5. 8 SEM micrograph of CFA_k used as support for loading of NiO.

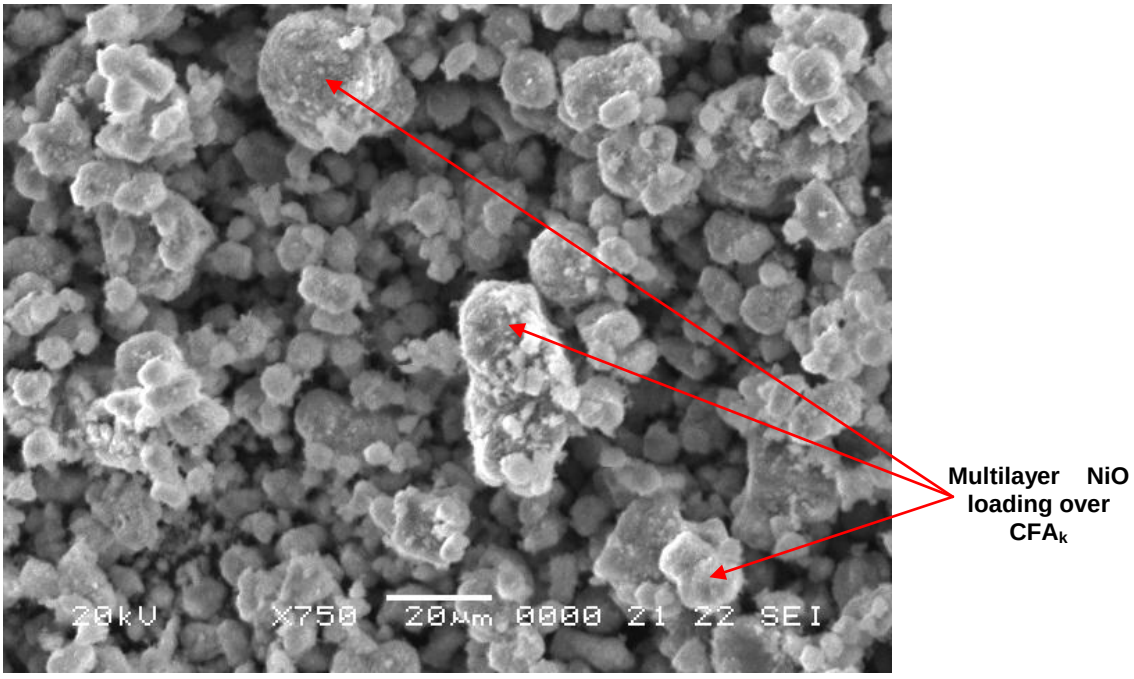

Figure 5. 9 SEM micrographs of NiFA$_k$ catalyst prepared using MWSCS, calcined at 400 ºC for 3h.

Microwave causes an increase in the molecular vibrations and thus the frequency factor of the reaction increases. Microwave irradiation can also decrease the activation energy Q of the reaction and thus cause the acceleration. Conventionally by combustion route using urea, metal oxide formation takes approximately 24h but using microwave assisted route the $NiFA_k$ catalyst was produced within 2h as mentioned in experimental section. These findings are consistent with those of previous studies [49]**.**

5.4 Catalytic Performance

In order to test the catalytic properties of the $NiFA_k$, an attempt has been made to study the decomposition of hydrogen peroxide in aqueous solution in the presence of prepared catalyst under different experimental conditions, described below.

5.4.1 Effect of Catalyst

To evaluate the factual catalytic activity of the prepared catalysts calcined at 400 °C for 3h, four H_2O_2 decomposition processes were compared, namely, blank, FA_k, CFA_k, $NiFA_k$, by corresponding experiments to evaluate the effect of catalyst on the overall decomposition of H_2O_2 as shown in **Figure 5.10**. Experimental results depict that under blank condition the H_2O_2 could be decomposed to a certain degree (**Figure 5.10 (a)**). The adsorption of H_2O_2 on FA_k, CFA_k were saturated after 6 min, the decomposition of H_2O_2 did not increase any further with time. This indicated that FA_k, and CFA_k do not have sufficient catalytic activity (**Figure 5.10 (b, c)**). The H_2O_2 decomposition rates increased for $NiFA_k$ catalyst which shows highest decomposition rate (99%) among the others. Results indicate that microwave irradiation as well as calcium activation of support reduces the mean crystallite size of the synthesized powder hence increases the surface area of catalyst. The higher surface area provides more active sites for catalytic decomposition.

5.4.2 Effect of Calcination Temperature

Effect of calcination temperature on catalytic activity of $NiFA_k$ catalyst is shown in **Figure 5.11.** It can be seen that the calcination temperature significantly

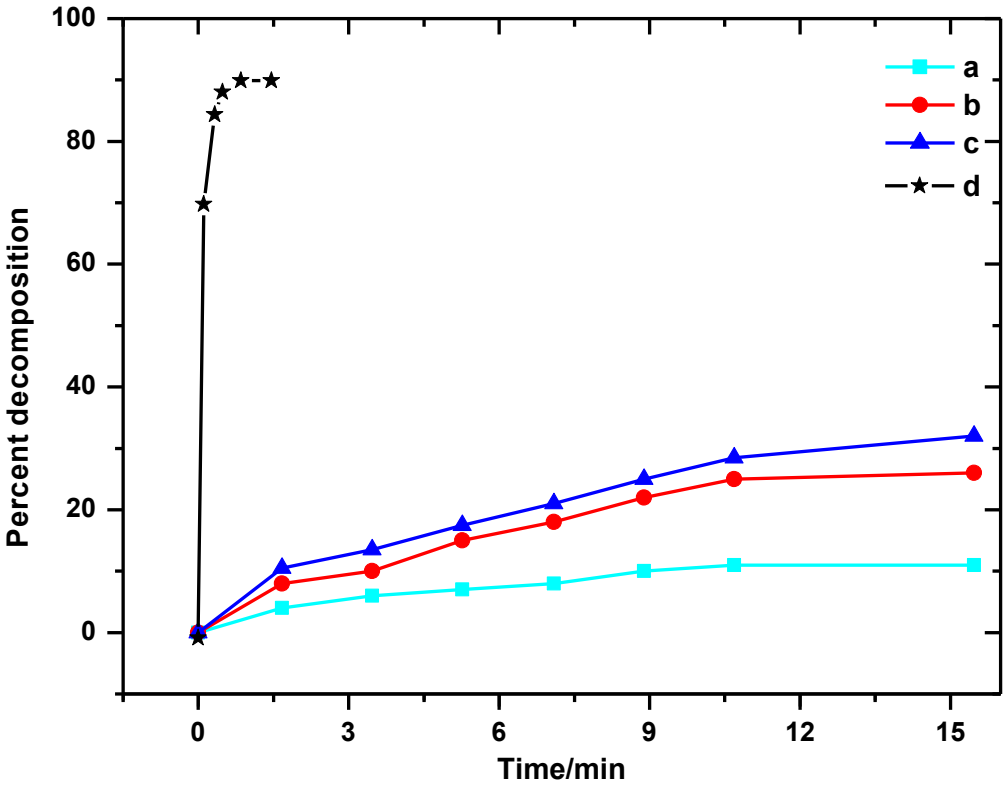

Figure 5. 10 **Effect of catalysts on decomposition of H_2O_2 (a) Blank condition, (b) FA_k, (c) CFA_k, (d) $NiFA_k$. Initial conditions: H_2O_2 concentration = 0.002 M catalyst dose = 0.02 g, pH = 10, reaction temp = 55 ºC, calcination temp = 400 ºC for 3h.**

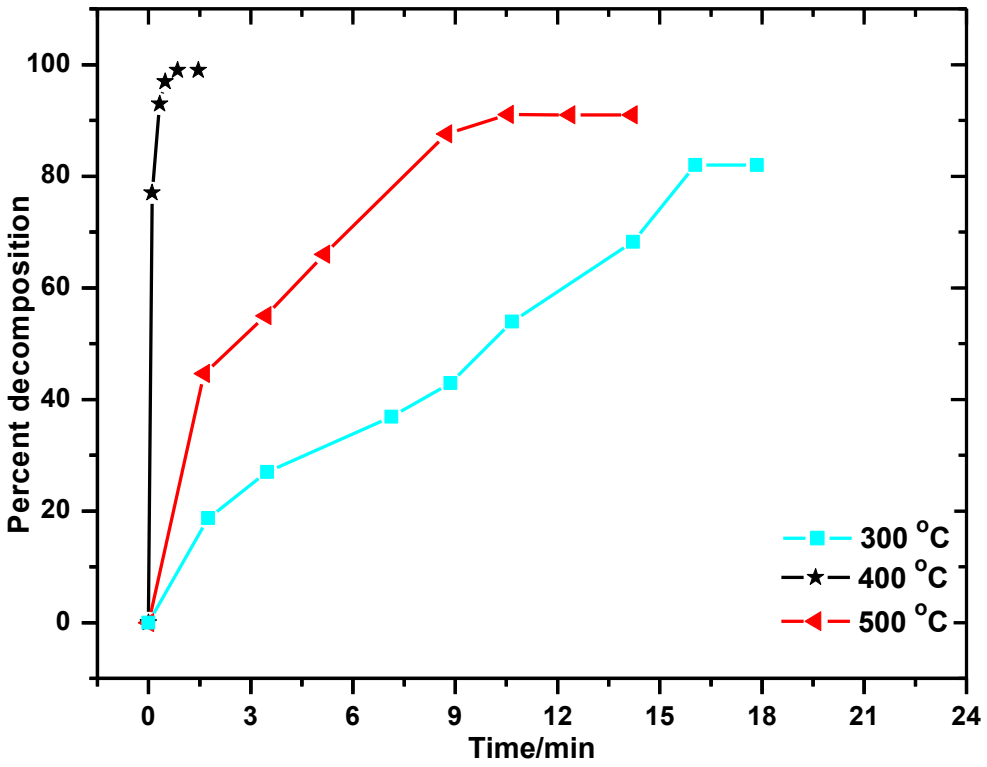

Figure 5. 11 Effect of calcination temperature on the decomposition of H_2O_2 over $NiFA_k$ catalyst. Initial conditions: H_2O_2 concentration = 0.002 M catalyst dose = 0.02 g, pH = 10, reaction temp = 55 °C.

affects the catalytic activity of $NiFA_k$ catalyst. The catalyst displays some differences in H_2O_2 degradation rate, degradation rate increases notably with increasing calcination temperature from 300 to 400 °C, but decreases when temperature is further raised to 500 °C, much in accordance with a previous report [50]. This phenomenon can be attributed to the improvement in crystallinity of the FCC structure of NiO phases of $NiFA_k$ as calcination temperature increases. However, when the calcination temperature increases to 500 °C, the crystallite size is increased with decrease in surface area, hence active sites are also decreased which resulted in a decrease in catalytic activity [51].

5.4.3 Effect of Reaction Temperature (35-60°C)

To evaluate the effect of catalytic reaction temperature, catalytic decomposition of H_2O_2 were performed at different temperatures ranging from 35 to 60 ºC. The rate of decomposition increases from 35 to 60 ºC [4].

5.4.4 Effect of pH

The decomposition of hydrogen peroxide was studied at pH values of 10, 7, 5, and 3 in the presence and absence of $NiFA_k$ catalyst, at 55 °C using HCl, HNO_3, KOH, NaOH, and NH_4OH solutions for adjusting pH of the reaction mixtures. It was observed that NaOH and KOH have a significant effect on the decomposition reaction of hydrogen peroxide in the absence of catalyst. **Figure 5.12** shows the percent decomposition versus time curves for hydrogen peroxide at different pH values in the presence of $NiFA_k$ catalyst. It is clear from this figure that at the pH values, in basic range, decomposition of hydrogen peroxide is measurable and increases with the increase in pH, whereas at the pH values in acidic the decomposition is negligible. This suggests the fact that the positive surface sites are passive and only the negative surface sites are catalytically active for the decomposition of hydrogen peroxide. At the high pH values the surface carries high negative charge which causes enhance decomposition.

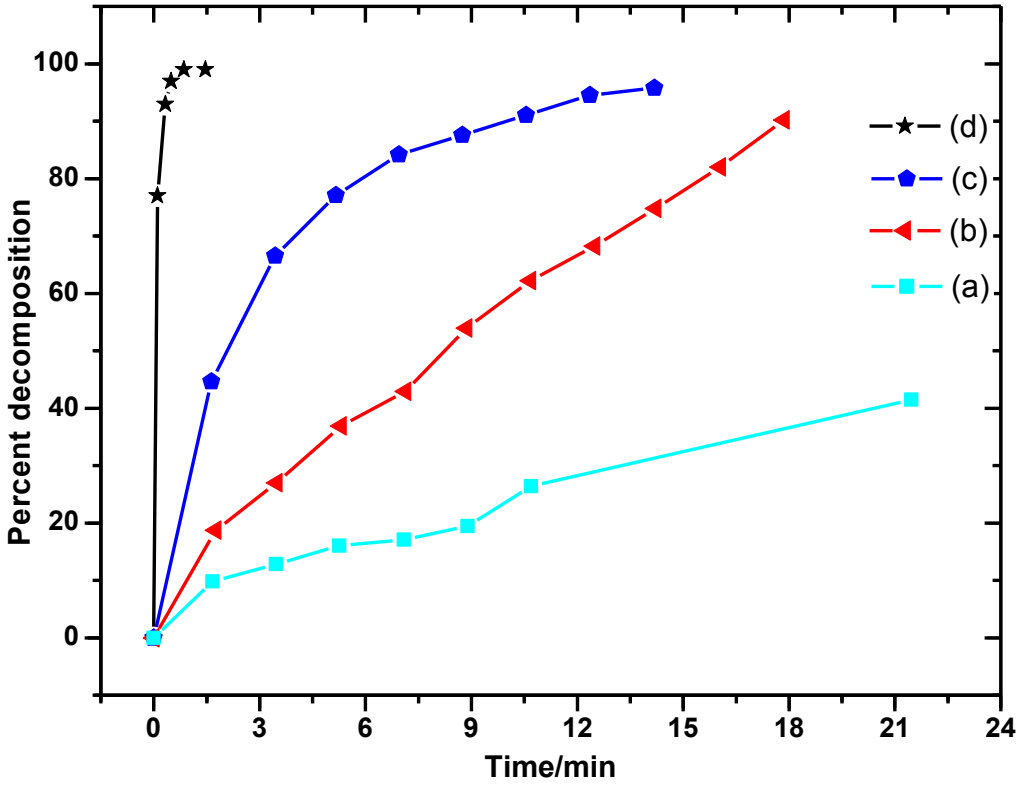

Figure 5. 12 **Decomposition of hydrogen peroxide on $NiFA_k$ catalyst as a function of time at different pH values: (a) 4.00, (b) 6.00, (c) 8.00, (d) 10.00. Initial conditions: H_2O_2 concentration = 0.002 M catalyst dose = 0.02 g, reaction temp = 55 °C, calcination temp = 400 °C for 3h.**

5.4.5 Proposed Mechanism

On the basis of H_2O_2 decomposition results, it has been assumed that the decomposition of hydrogen peroxide on the negative sites proceeded through the following mechanism (**eq. 5.2** to **5.4**) [52,53]:

$$SO^{-} + H_2O_2 \longrightarrow SO + HO^{-} + HO^{\cdot} \quad \textbf{(eq. 5.2)}$$

$$HO^{\cdot} + H_2O_2 \longrightarrow HO_2^{\cdot} + H_2O \quad \textbf{(eq. 5.3)}$$

$$HO_2^{\cdot} + SO \longrightarrow SO^{-} + O_2 + H^{+} \quad \textbf{(eq. 5.4)}$$

Where SO^{-} represents the surface negative sites appeared at higher pH over $NiFA_k$ catalyst.

The net result of these reactions is the generation of oxygen, which was observed experimentally in the form of bubbles formation during the decomposition reaction. Furthermore, no change in the pH of the medium was observed during and after the decomposition reaction, which agreed well with the above mentioned proposed mechanism. Moreover, to see the activity of the regenerated negative sites i.e. SO^{-}, the same catalyst was re-dispersed in hydrogen peroxide solution and the decomposition reaction was monitored under the same experimental conditions. It was observed that the catalyst was equally active and decomposed hydrogen peroxide to the same extent. These observations support the mechanism of decomposition reaction of H_2O_2 over $NiFA_k$ catalyst, described above and in **Scheme 5.1**. $HO^{\cdot}$ radicals, OH^{-} ions and O_2 obtained by the catalytic decomposition of H_2O_2 are very reactive oxidizing agents for complete oxidation of organic pollutants present in waste water. In this way catalyst is very useful in waste water treatment of advanced oxidation processes (AOP) in presence of H_2O_2 as source of reactive oxygen species.

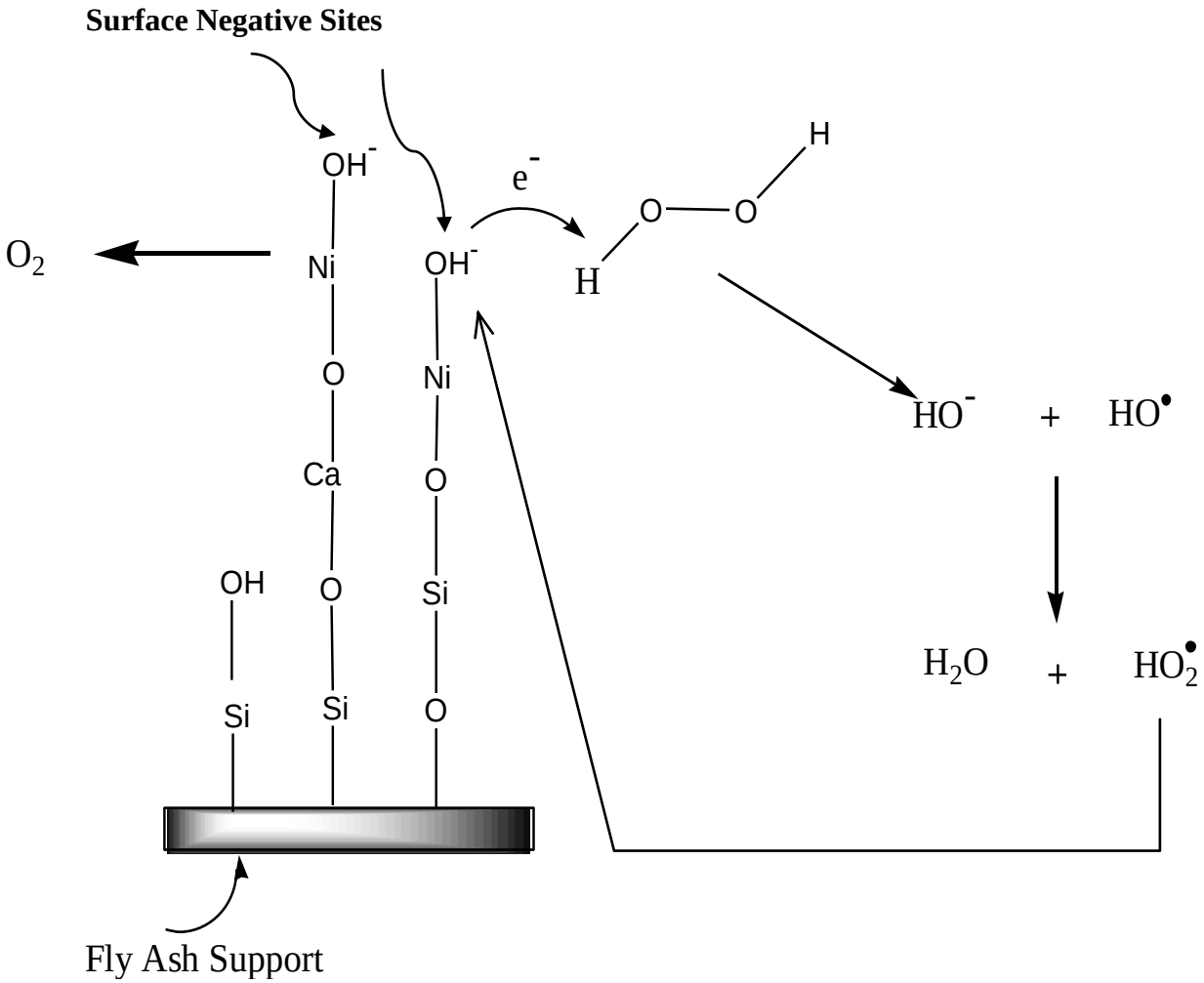

Scheme 5. 1 Proposed mechanism of H_2O_2 decomposition over $NiFA_k$ catalyst.

5.5 Conclusion

The following conclusions can be drawn from the results described in the present Chapter.

1. A novel process involving MWSCS has been developed for preparing fly ash supported nickel oxide ($NiFA_k$) catalyst.
2. The novelty of the process lies in the fact that conventionally in microwave assisted route effect of microwave irradiation on drying or calcination of prepared materials have been seen. Whereas in the present developed novel process preparation of $NiFA_k$ catalyst has been carried out under microwave environment using CEM discover microwave synthesizer.
3. The chemical activation of fly ash (CFA_k) increases loading of NiO over fly ash surface due to increase in –OH content and formation of C–S–H phase.
4. The X-ray diffraction pattern confirms that NiO loaded over CFA_k in nano range with NiO crystallite size 6.4 nm.
5. The SEM images, XRD diffraction patters, FT-IR studies confirm the loading of nanosized NiO over support.
6. MWSCS using urea as fuel for the synthesis of $NiFA_k$ catalyst has been found suitable, eco-friendly and efficient process.
7. Color alteration has been recognized during nickel oxide formation. This phenomenon has been attributed to the non-stoichiometric character of the nanoparticles.
8. An attempt has been made in this investigation to evaluate the catalytic properties of $NiFA_k$ by using decomposition reaction of hydrogen peroxide.
9. Effect on nature of catalyst on catalytic activity for decomposition of H_2O_2 has been evaluated. $NiFA_k$ catalyst shows best catalytic activity among others.
10. Effect of different reaction parameters on decomposition of H_2O_2 shows that higher pH range is favorable for the used reaction, 50-55 ºC reaction

temperature is suitable for the decomposition and 400 ºC for 3h calcination temperature of $NiFA_k$ catalyst has been found the best suitable for the enhanced catalytic activity.

11. Prepared catalyst can be applicable at industrial scale for removal of organic pollutants present in industrial waste water using AOP in presence of H_2O_2 as source of reactive oxygen species.

5.6 References

[1] C. Farr, G. Josephs, W.C. Douglass, W.O. Grotz, D. Edward, Supplement to The Art of Getting Well Hydrogen Peroxide Therapy, 1992.

[2] R. Eloirdi, S. Rossignol, C. Kappenstein, D. Duprez, N. Pillet, J. Propuls. Power 19 (2003) 213.

[3] C. Kappenstein, L. Pirault-Roy, M. Guerin, T. Wahdan, A. Ali, F. Al-Sagheer, M. Zaki, Appl. Catal. A-GENERAL 234 (2002) 145.

[4] V.S. Shivankar, N. V Thakkar, J. Sci. Ind. Res. (India). 64 (2005) 496.

[5] S. Perathoner, G. Centi, Top. Catal. 33 (2005) 207.

[6] W.H. Glaze, J.W. Kang, Ind. Eng. Chem. Res. 28 (1989) 1573.

[7] C. Walling, Acc. Chem. Res. 8 (1975) 125.

[8] A.H. Abdullah, W.W. Yuan, M.I. Yaziz, J. Phys. Sci. 21 (2010) 29.

[9] X. Hu, L. Lei, H.P. Chu, P.L. Yue, Carbon N. Y. 37 (1999) 631.

[10] N. Al-Hayek, M. Doré, Water Res. 24 (1990) 973.

[11] G.A. El-Shobaky, T. El-Nabarawy, G.A. Fagal, A.S. Ahmad, Mater. Lett. 17 (1993) 297.

[12] S. Wang, G.Q. (Max) Lu, Ind. Eng. Chem. Res. 36 (1997) 5103.

[13] Z.H. Zhu, L.R. Radovic, G.Q. Lu, Carbon N. Y. 38 (2000) 451.

[14] Z. Zhu, Z. Liu, S. Liu, H. Niu, T. Hu, T. Liu, Y. Xie, Appl. Catal. B Environ. 26 (2000) 25.

[15] F. L. Y. Lam, X. Hu, Chem. Eng. Sci. 58 (2003) 687.

[16] T. Tsoncheva, S. Vankova, D. Mehandjiev, Fuel 82 (2003) 755.

[17] J. Zhao, Z. Liu, D. Sun, J. Catal. 227 (2004) 297.

[18] H.H. Tseng, M.Y. Wey, Carbon N. Y. 42 (2004) 2269.

[19] N. Barrabes, J. Just, A. Dafinov, F. Medina, J. Fierro, J. Sueiras, P. Salagre, Y. Cesteros, Appl. Catal. B Environ. 62 (2006) 77.

[20] S.J. Park, B.J. Kim, J. Colloid Interface Sci. 292 (2005) 493.

[21] R.-S. Chen, Y.-S. Chen, Y.-S. Huang, Y.-L. Chen, Y. Chi, C.-S. Liu, K.-K. Tiong, A.J. Carty, Chem. Vap. Depos. 9 (2003) 301.

[22] L. Omiciuolo, E.R. Hernández, E. Miniussi, F. Orlando, P. Lacovig, S. Lizzit, T.O. Menteş, A. Locatelli, R. Larciprete, M. Bianchi, S. Ulstrup, P. Hofmann, D. Alfè, A. Baraldi, Nat. Commun. 5 (2014) 5062.

[23] D. V Ahire, S.D. Shinde, G.E. Patil, K.K. Thakur, V.B. Gaikwad, V.G. Wagh, G.H. Jain, V.N.N. Arts, 5 (2012) 592.

[24] C. Li, B. Wang, H. Cui, J. Zhai, Q. Li, J. Mater. Sci. Technol. 29 (2013) 835.

[25] A. Sharma, O.P. Modi, G.K. Gupta, Adv. Appl. Sci. Res. 3 (2012) 2151.

[26] T. Mimani, K.C. Patil, Mater. Phys. Mech. 4 (2001) 134.

[27] A.S. Prakash, A.M.A. Khadar, K.C. Patil, M.S. Hegde, J. Mater. Synth. Process. 10 (2002) 135.

[28] R.K. Jha, R. Pasricha, V. Ravi, Ceram. Int. 31 (2005) 495.

[29] T. Yamauchi, Y. Tsukahara, K. Yamada, T. Sakata, Y. Wada, Chem. Mater. 23 (2011) 75.

[30] J.A. Gerbec, D. Magana, A. Washington, G.F. Strouse, J. Am. Chem. Soc. 127 (2005) 15791.

[31] A. Lagashetty, V. Havanoor, S. Basavaraja, S.D. Balaji, A. Venkataraman, Sci. Technol. Adv. Mater. 8 (2007) 484.

[32] M. Harada, T. Sada, Y. Takahashi, Phot. Fact. Act. Rep. 30 (2013) 15791.

[33] P. Lidström, J. Tierney, B. Wathey, J. Westman, Tetrahedron 57 (2001) 9225.

[34] H.H. Huang, M.C. Lu, J.N. Chen, Water Res. 35 (2001) 2291.

[35] M. Hermanek, R. Zboril, I. Medrik, J. Pechousek, C. Gregor, J. Am. Chem. Soc. 129 (2007) 10929.

[36] W.P. Kwan, Decomposition of Hydrogen Peroxide and Organic Compounds in The Presence of Iron and Iron Oxides, Massachusetts Institute of Technology May 2003 D, 2003.

[37] H.H. Huang, M.C. Lu, J.N. Chen, C. Te Lee, Chemosphere 51 (2003) 935.

[38] M.C.G. Albuquerque, I. Jiménez-Urbistondo, J. Santamaría-González, J.M. Mérida-Robles, R. Moreno-Tost, E. Rodríguez-Castellón, A. Jiménez-López, D.C.S. Azevedo, C.L. Cavalcante Jr., P. Maireles-Torres, Appl. Catal. A Gen. 334 (2008) 35.

[39] J.-I.C. for D. Data, Mineral Powder Diffraction File, Swarthmore, Pa. : JCPDS International Centre for Diffraction Data, 1980.

[40] D. Jain, R. Hada, A. Rani, J. Catal. 2013 (2013) 1.

[41] S.C. Mojumdar, L. Raki, J. Therm. Anal. Calorim. 85 (2006) 99.

[42] G.S. Pappas, P. Liatsi, I.A. Kartsonakis, I. Danilidis, G. Kordas, J. Non. Cryst. Solids 354 (2008) 755.

[43] I.G. Richardson, Cem. Concr. Res. 38 (2008) 137.

[44] F. Chen, I. Lin, H. Li, G.J. Gan, K. Toh, L. Tham, Catal. Commun. 8 (2007) 2053.

[45] N.B. Singh, N.P. Singh, J. Therm. Anal. Calorim. 89 (2007) 159.

[46] O.S. Ayanda, O.S. Fatoki, F.A. Adekola, B.J. Ximba, S. Africa, 1 (2012) 95.

[47] X. Liu, C. Chun, I.A. Aksay, W. Shih, 3 (2000) 684.

[48] S. Ramesh, Y. Koltypin, R. Prozorov, A. Gedanken, Chem. Mater. 4756 (1997) 546.

[49] D. Mohammadyani, S. a. A. Hosseini, S.K.K. Sadrnezhaad, Int. J. Mod. Phys. Conf. Ser. 05 (2012) 270.

[50] M.T. Makhlouf, B.M. Abu-Zied, T.H. Mansoure, Appl. Surf. Sci. 274 (2013) 45.

[51] M. Ohta, Y. Ikeda, A. Igarashi, Appl. Catal. A Gen. 258 (2004) 153.

[52] K. Akhtar, J. Chem. Soc. Pakisthan 31 (2009).

[53] A. Quintanilla, J.A. Casas, J.J. Rodríguez, in:, Proc. Eur. Congr. Chem. Eng., Copenhagen, 2007, pp. 16–20.

Annexure-I and II

Characterization Techniques

Physicochemical properties of all catalytic materials were studied by XRD, FT-IR and SEM, SEM-EDX, TEM, TGA, UV-Vis DRS, N_2 adsorption-desorption techniques. The reaction products are analyzed by gas chromatography.

1. X-ray Diffraction Analysis (XRD)

The structural features of samples are analyzed by X-ray diffraction studies. X-ray diffraction patterns are recorded by Bruker D8 Advance diffractometer, using Ni-filter and Cu K_α radiation (E = 8047.8 eV, λ = 1.5406A˚). The samples are scanned at different 2θ range and a scanning rate of $0.04^\circ s^{-1}$. XRD analysis has been done at AMPRI, CSIR, Bhopal and UGC-DAE CSR, Indore.

2. Fourier Transform Infra-Red Analysis (FT-IR)

FT-IR study is executed on Bruker FT-IR Spectrophotometer (TENSOR 27) in DRS (Diffuse Reflectance System) mode by mixing samples with KBr in 1:20 weight ratio. The acidity of the catalysts is measured by pyridine adsorbed FT-IR. The samples (0.2 g) were activated at 450 °C for 2 h and exposed to pyridine (25 ml) for 24 h. The spectra were recorded in the range of 550-4000 cm^{-1} with a resolution of 4 cm^{-1}. FT-IR analysis is conducted at Department of Pure and Applied Chemistry, University of Kota, Kota.

3. Scanning Electron Microscopy (SEM and SEM-EDX Analysis)

The detailed imaging information about the morphology and surface topography is studied by Scanning electron microscope (SEM, Model-JEOL-JSM 5600). SEM analysis is done at AMPRI, CSIR, Bhopal and UGC-DAE CSR, Indore.

4. Transmission Electron Microscopy (TEM Analysis)

The surface morphology and texture of samples is further confirmed by TEM analysis With lattice resolution of 0.14 nm and a point to point resolution of 0.12 nm and Gatan digital camera. Model: JEOL 3010. TEM analysis is done at IIT Madras, Chennai.

5. Thermo-Gravimmetric Analysis (TGA)

Thermo gravimetric analysis (TGA) of the samples is carried out using Mettler Toledo analyzer Model: TGA/DSC 1, STAR^e system, SW 9.20, USA, by heating the samples in the range of 50–1000 °C with a heating rate of 10°C/min under nitrogen flow (50 cm^3/min). TGA analysis of samples is done at AMPRI, CSIR, Bhopal.

6. Ultra Violet-Visible Diffuse Reflectance Spectroscopy (UV-Vis Analysis)

UV–Vis spectra in the range of 200–800 nm were measured with UV–Vis spectrophotometer at ambient temperature. UV-Vis DRS analysis is done at University of Delhi, New Delhi.

7. BET Analysis

Specific surface area and average pore diameter of samples are determined from N_2 adsorption-desorption, done by using Thermo Scientific^{TM} Surfer surface area analyzer. The samples are degassed under vacuum at 120°C for 4 h, prior to adsorption in order to evacuate the physisorbed moisture. BET analysis is done at University of Pune, Pune.

8. Gas Chromatography

The products are analyzed by Gas Chromatograph (Agilent Technologies 7820A) having FID and Agilent J&W Advanced Capillary HP 5 GC Columns of 30 m length and 0.320 mm diameter, programmed oven temperature of 60–325ºC and N_2 (1.5 ml/min) as a carrier gas. GC analysis is conducted at Department of Pure and Applied Chemistry, University of Kota, Kota.

List of publications

In International Journals

1. A Novel Synthesis Process for Making Nickel Oxide Nanoparticles, **Renu Hada**, Ashu Rani, Vijay Devra, S.S. Amritphale, International Research Journal of Pure and Applied Chemistry, 2013, 3(2), 111-117.

2. Fly Ash Supported Scandium Triflate as an Active Recyclable Solid Acid Catalyst for Friedel-Crafts Acylation Reaction, Ashu Rani, Chitralekha Khatri, **Renu Hada,** Fuel Processing Technology 116 (2013) 366–373**.**

3. Surface Modification of Fly Ash for Active Catalysis, Deepti Jain, **Renu Hada**, and Ashu Rani, Journal of Catalysts, 2013, Article ID 723957, pg 9.

4. Surface Modification of Fly Ash by Thermal Activation: A DR/FTIR Study, Stuti Katara, Sakshi Kabra, Anita Sharma, **Renu Hada** and Ashu Rani, International Research Journal of Pure and Applied Chemistry, 2013, 3(4), 299-307.

In National Journals

5. Synthesis of Nanosized Titania by Sol Gel Route, **Renu Hada**, Sakshi Kabra, Stuti Katara, Ashu Rani, Vijay Devra, S. S. Amritphale, Indian Journal of Applied Research, 2013, 3(4), 49-50.

6. DRIFT- Spectroscopic Study of Modification of Surface Morphology of Perlite During Thermal Activation, Sakshi Kabra, Anita Sharma, Stuti Katara, **Renu Hada**, Ashu Rani, Indian Journal of Applied Research, 2013, 3(4), 40-42.

In International Conferences/Workshop/Symposium

7. Synthesis of Fly Ash Supported Nanosized Titania, **Renu Hada**, Ashu Rani, Vijay Devra, International Workshop on Green Initiatives in Energy, Environment and Health, in New Delhi, December 2-3, 2013.

8. Synthesis of fly ash supported TiO_2 Photo-Catalyst from Coal Generated Fly Ash, **Renu Hada**, Ashu Rani, Vijay Devra, Waste, Wealth and Health (ICWWH), in Bhopal, February 15-17, 2013.

9. Participated in Indo-Swedish Symposium on Strategic Knowledge on Climate Changes, in Kota, October 09, 2012.

In National Conferences/Workshop/Symposium

10. Participated in Workshop on Question Bank Repository (Chemistry), School of Science and Technology, VMOU, Kota, (Raj.), February 08-10, 2014.

11. Presented Research Work in Annual Research Seminar, J.D.B. Government, Girls College, Kota (Raj.), January 23, 2014.

12. Participated in Symposium on E-Resources, Department of Library and Information Science, University of Kota, Kota, (Raj.), December 16-17, 2013.

13. Actively Participated in 5^{th} National Academic Workshop on "Organic Reaction Mechanisms & Analytical Techniques Used in Chemical Sciences", Department of Pure and Applied Chemistry, University of Kota, Kota, (Raj.), October 21-25, 2013.

14. Participated in National Seminar on "Socio-Legal Issues and Challenges of Female Foeticide and Infanticide in India", Women Cell, Univ. of Kota, Kota, (Raj.) October 4-5, 2013.

15. Participated in Workshop on Open Educational Resources, VMOU, Kota, (Raj.), May 17-19, 2013.

16. Presented Research Work in Annual Research Seminar, J.D.B. Government, Girls College, Kota, (Raj.), March 2, 2013.

17. Presented Research Work in Annual Research Seminar, J.D.B. Government, Girls College, Kota, (Raj.), March 2, 2012.

18. Oral-Presentation, National Seminar on Chemistry: A modern & Innovative Tool, Government, Madhav Science P.G. College, Ujjain, (M.P.), March 4-5 2011.

19. Synthesis of TiO_2 Nanoparticles by Alcoholic Sol-gel Route, **Renu Hada**, Ashu Rani, Vijay Devra, National Symposium on Recent Advances in Chemical Sciences (NSRACS-2011), Kota, (Raj.), 07-08 January 2011.

School Participation

20. Participated and received Best Performer Award in **BRNS-AEACI** Ninth School on Analytical Chemistry (**SAC-9**) at North Eastern Region, Atomic Minerals Directorate, Shillong during October 27 to November 03, 2014.

Communicated Papers

1. Non Aqueous Synthesis of Fly Ash Supported TiO_2 Nanoparticles for Enhanced Photo-Oxidation of Congo Red Dye, **Renu Hada**, Sakshi Kabra, Stuti Katara, Vijay Devra, Ashu Rani, Fuel Processing Technology.

2. Microwave Assisted Solution Combustion Synthesis of Activated Fly Ash Supported NiO Nanoparticles for Hydrogen Peroxide Decomposition, **Renu Hada**, Stuti Katara, Sakshi Kabra, Vijay Devra, Ashu Rani, Fuel.

3. Perlite Supported Nickel Catalyst: Synthesis, Characterization and Catalytic Activity in Claisen-Schmidt Condensation Reactions, Sakshi Kabra, Stuti Katara, **Renu Hada** and Ashu Rani, Catalysis Communications.

4. Fly Ash Supported Phosphomolybdic Acid as A Highly Efficient Solid Lewis Acid Catalyst for Microwave Assisted Friedel- Crafts Acylation Reactions, Sakshi Kabra, **Renu Hada**, Stuti Katara and Ashu Rani, Fuel.

5. An Efficient and Cost-Effective Solid Base Catalyst for Cross-Aldol Condensation of Ketones with Aromatic Aldehydes under Solvent Free Condition. Stuti Katara, Sakshi Kabra, **Renu Hada**, Ashu Rani, Catalysis Communications.

6. Fly ash supported solid base catalyst for microwave assisted Michael addition reaction. Stuti Katara, **Renu Hada,** Sakshi Kabra, Ashu Rani, Catalysis Communications.

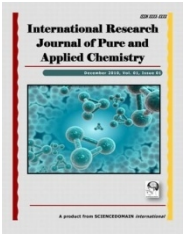

International Research Journal of Pure & Applied Chemistry
3(2): 111-117, 2013

SCIENCEDOMAIN *international*
www.sciencedomain.org

A Novel Synthesis Process for Making Nickel Oxide Nanoparticles

Renu Hada[1], Ashu Rani[1], Vijay Devra[2] and S. S. Amritphale[3*]

[1]Department of Pure and applied Chemistry, University of Kota, Kota (Raj), India.
[2]Jankidevi Bajaj Government Girls College, Kota (Raj), India.
[3]Advanced Materials & Processes Research Institute (CSIR), Hoshangabad Road, Bhopal (M.P), India.

Authors' contributions

This work was carried out in collaboration between all authors. Senior authors SSA and AR supervised and designed the study, author RH performed the experimental and analytical study, wrote the protocol, and first draft of the manuscript, author VD managed the literature search and some experimental part. All authors read and approved the final manuscript.

Research Article

Received 28th December 2012
Accepted 25th February 2013
Published 22nd March 2013

ABSTRACT

The main aim of this research was to prepare nanoparticles of nickel oxide through a new mixed reverse microemulsion route. Quaternary microemulsion (water/surfactant/co-surfactant/oil-phase) was used to synthesize nickel oxide nanoparticles. The microemulsion was prepared by Tween-80, Aerosol-OT, n-Propanol, Cyclohexane, and Nickel Chloride. Previously nickel oxide nanoparticles were synthesized by reverse microemulsion method but the novelty of the process lies in the fact that conventionally either cationic or anionic or non ionic surfactants are used for the synthesis of nickel oxide nanoparticles.Whereas in the present developed novel process preparation of nickel oxide nanoparticles has been carried out using a unique blend system consisting of Tween-80 and AOT. The average particle size of as synthesized nickel oxide powder, calculated by Scherrer equation, is observed to be 14 nm. The X-ray diffraction pattern confirms the presence of pure bunsenite phase with FCC Scanning Electron Microscopy (SEM) shows that particles have spherical morphology.

**Corresponding author: Email: ssamritphalerrl@yahoo.co.in;*

Keywords: Nickel oxide; nanoparticles; synthesis; mixed reverse microemulsion.

1. INTRODUCTION

Nanoparticles show novel properties that are significantly differ from their corresponding bulk solid state materials. This difference in properties is due to the different effects like as small size effect, surface effect, quantum size effect, and macroscopic quantum tunnel effect as discussed elsewhere [1,2]. In recent years, nickel oxide nanoparticles has attracted much interests due to its novel optical [3], electronic [4], magnetic [5], thermal, mechanical properties, potential application in catalyst, battery electrodes [6,7], gas sensors [8], electrochemical films, photo electronic devices, and so on as discussed elsewhere [9].

The uses and performance for a given property and application are, however, strongly influenced by the crystalline structure, the morphology, and the size of the particles Therefore, it is very important to develop methods for the synthesis of nickel oxide nanoparticles in which the particle size and the crystal structure of the products can be controlled.

There are many different methods used for the synthesis of nickel oxide nanoparticles, such as ultrasonic radiation, hydrothermal synthesis, carbonyl method [10], laser chemical method, pyrolysis by microwave [11], sol-gel method, precipitation-calcinations, microemulsion method [12], anodic arch plasma method [13], thermal deposition method [14] and so on as discussed elsewhere [15]. However, to the best of our knowledge, most of the used experimental techniques for the synthesis of nanopowders are still have some unresolved problems, such as special conditions, tedious procedures, and complex apparatus.

In the last few years reverse micelle method was successfully applied to synthesize nickel oxide nanoparticles in reverse micelles or water/oil (W/O) microemulsion systems using different nickel salts as starting materials as discussed by [16,17,12].Reverse micelles are small aggregates (60-800 Å) formed by surfactant molecules that surround a well defined nanometre-sized water core as discussed by Nassos [18]. This unique formation of water droplets in a microemulsion may be considered as a small reactor used for the synthesis of nanoparticles. The reactants are confined within such dispersed droplets when water-soluble precursors are used. The synthesis of the metal nanoparticles may be carried out in two different manners as discussed by Pham and Herranz [19,20]. The first manner includes the addition of a reducing agent, such as hydrazine directly into the microemulsion containing the metal precursor. The second manner involves the mixing of two reverse-micelle microemulsion solutions, one containing the metal precursor and the other one containing the reducing (or precipitating) agent as discussed by Pileni [21].

In the present work we prepared nickel oxide nanoparticles using the single microemulsion system in which mixed reverse microemulsion of aqueous nickel salt solution, blend of anionic and non-ionic surfactant, and oil phase was used. Liquid ammonia was directly added to the above microemulsion system. The synthesis involves hydrolysis of nickel salt in the mixed reverse micelle system leading to the formation of phase pure bunsenite nickel oxide nanoparticles at room temperature.

In the present work a unique blend of anionic and non-ionic surfactant was used, this blend is more rigid than single moiety of ionic surfactant due to polymer nature of non-ionic surfactant, rigidity of the surfactant layer is essential factor for controlling the size of the

nanoparticles in single microemulsion approach [22]. Intermediate values of occupancy the number and surfactant layer rigidity, both intramicellar and intermicellar nucleation and growth contribute to the final particle size and polydispersity [22].

2. EXPERIMENTAL DETAILS

2.1 Materials and Reagents

The materials used for making phase pure nanoparticles of nickel oxide included cyclohexane as oil phase (AR grade, Merck LTD., assay 99.5%), distilled water, Tween 80 as surfactant (AR grade, Merck LTD., 99.98%), AOT as surfactant (AR grade, HiMedia Laboratories Pvt. Ltd., assay 98.0%), n-propanol as co-surfactant (AR grade, RANBAXY, assay 99.0%), Nickel Chloride hexahydrate as nickel precursor (AR grade, Merck LTD), Liquid Ammonia (AR grade, RANKEM, assay 25%).

2.2 Synthesis of Phase Pure Nanoparticles of Nickel Oxide

The flow chart for the preparation of nanoparticles of nickel oxide powder in mixed reverse microemulsion is given in Fig. 1 and the detailed discussion of the same is as mentioned below.

First of all a mixed reverse microemulsion was prepared using 400 ml Cyclohexane, 6 ml of 0.1 M Nickel Chloride Hexahydrate aqueous solution, 8.89 g AOT, 49.4 ml Tween 80, and 20 ml n-Propanol and this microemulsion mixture was stirred vigorously using a magnetic stirrer at 1500 RPM at room temperature to obtain transparent green solution revealing the formation of micron size water droplets homogenously dispersed in continuous oil phase. Further the solution of liquid Ammonia was taken in a burette and was added drop wise at the rate of 0.2 ml/min to the mixed reverse microemulsion system using a magnetic stirrer at 1500 RPM at room temperature till the precipitate of the nickel hydroxide was appeared. Then the precipitate of the nickel hydroxide so obtained was filtered using whatman 42 filter paper, and was washed repeatedly with 15 ml water deionised water in each washing cycle and followed by washing with 15 ml solution of methanol and chloroform in 1:1 volume ratio in each washing cycle, in order to remove the organic residues and surfactant. The washed material was then dried in an air oven at 80ºC for 10 h. The dried material was powdered with mortar and pestle and was then calcined at 450ºC for 3 h in muffle furnace. The fired powder was again slightly crushed with mortar and pestle.

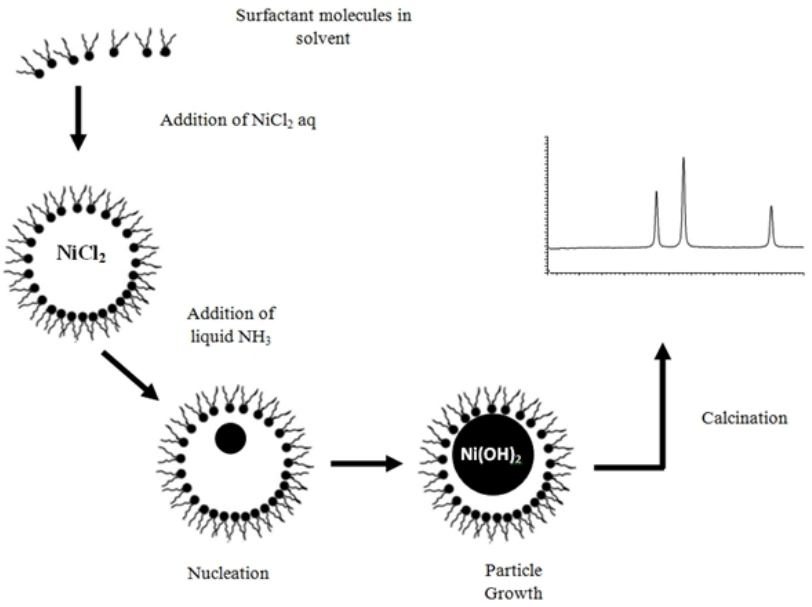

Fig. 1. Overall process for synthesizing nickel oxide nanopartices

3. RESULTS AND DISCUSSION

3.1 X-Ray Diffraction Study

The purity and crystallinity of the as-synthesized nickel oxide nanoparticles were examined using powder X-ray diffraction (PXRD) as shown in Fig. 2. It can be seen from Fig. 2 that the diffraction peaks are low and broad due to the small size effect and incomplete inner structure of the particles. The peaks appearing at 2θ = 37.185º, 43.223º, and 62.828º are indexed as (111), (200), and (220) respectively and represents face-centered cubic (FCC) crystalline structure of nickel oxide. All these diffraction peaks, not only in peak position but also in their relative intensity, are absolutely matched with the standard spectrum (JCPDS, No. 04-0835) [23]. The PXRD pattern shows that the sample is single phase and no any other impurities diffraction peak except the characteristic peaks of FCC phase nickel oxide was detected. The average crystallite size is calculated by X-ray diffraction line broadening using the Scherrer formula-

$$d = K\lambda/B \cos\theta$$

where d represents the grain size; K = 0.9 is Scherrer constant related to the spherical shape; λ represents the wavelength of the X- ray (Cu Kα, 1.54 Å); θ is the diffraction angle of the peak; B represents the full width of half maximum of the peak (in radian) The crystallite size of nickel oxide sample is 14 nm which was calculated from measured values for the spacing of the (200) plane. In comparison with other microemulsion systems formed in presence of single surfactant, the mixed reverse microemulsion process produced small,

less aggregated, and phase pure nickel oxide nanoparticles, due to intermediate effect of both surfactants which causes both inter and intramiceller nucleation and growth [24,25].

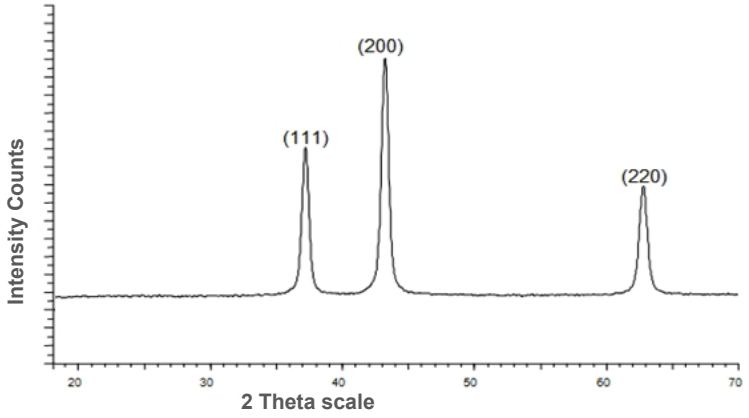

Fig. 2. XRD pattern of nickel oxide nanoparticles calcined at 450ºC for 3h

3.2 SEM Study

For microstructural studies samples are prepared for SEM analysis as given in experimental paragraph Fig. 3 presents the SEM image of nickel oxide powder obtained by mixed reverse microemulsion route, using Tween 80 and AOT as surfactants. As can be seen from the figure that the particles are spherical in shape and the particle size was estimated to be 14 - 50 nm by SEM image.

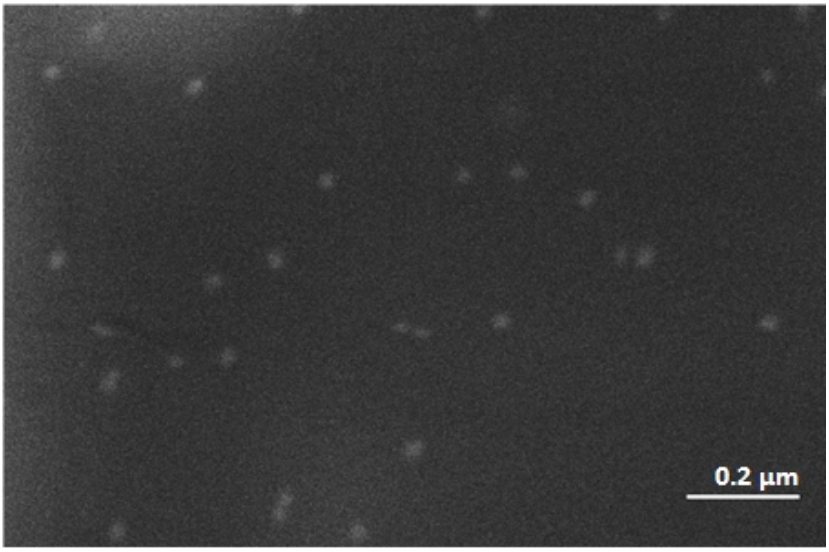

Fig. 3. The SEM photograph of nickel oxide nanoparticles

4. CONCLUSION

The following conclusions can be drawn from the results described in the present paper.

1. A novel process involving mixed reverse microemulsion route has been developed for preparing nickel oxide nanoparticles.
2. The novelty of the process lies in the fact that conventionally either cationic or anionic or non ionic surfactants are used for the synthesis of nickel oxide nanoparticles whereas in the present developed novel process preparation of nickel oxide nanoparticles has been carried out using a unique blend system consisting of Tween-80 and AOT.
3. The X-ray diffraction pattern confirms the presence of pure bunsenite phase with FCC crystal structure.
4. The SEM image exhibits the particle size of 14 to 50 nm, spherical shape and narrow size distribution of the nickel oxide nanoparticles.

ACKNOWLEDGEMENTS

The authors are grateful to the Director, AMPRI, CSIR, Bhopal for encouragement of the present research work. The financial support was provided by Fly Ash Mission, Department of Science and Technology, New Delhi, India.

COMPETING INTERESTS

Authors have declared that no competing interests exist.

REFERENCES

1. Gleiter H. Nanocrystalline materials. Prog Mater Sci. 1989;33:223-315.
2. Sessoli R, Gatteschi D, Caneschi A, Novak MA. Magnetic bistability in a metal-ion cluster Nature. 1993;365:141-3. doi:10.1038/365141a0.
3. Wang G, Zhang L, Mou J. Preparation and optical absorption of nanometer-sized NiO powder. Acta Phys Chim Sin. 1997;13(5):445-8.
4. Fukui T, Ohara S, Okawa H, Hotta T, Naito M. Properties of NiO cathode coated with lithiated Co and Ni solid solution oxide for MCFCs. J Power Sources. 2000;86(1-2):340–6.
5. Bi H, Li S, Zhang Y, Du Y. Ferromagnetic-like behavior of ultrafine NiO nanocrystallites. J Magn Magn Mater. 2004;277:363-7.
6. Izaki Y, Mugikura Y, Watanabe T, Kawase M, Selman JR. Direct observation of the oxidation nickel in molten carbonate. J Power Sources. 1998;75(2):236–43.
7. Ichiyanagi Y, Wakabayashi N, Yamazaki J, Yamada S, Kimishima Y, Komatsu E, et al. Magnetic properties of NiO nanoparticles. Phys. B. 2003;329–333:862-3.
8. Hotovy I, Huran J, Spiess L, Hascik S, Rehacek V. Preparation of nickel oxide thin films for gas sensors applications. Sens Actuators. B. 1999;57(1-3):147-52.
9. Biju V, Khadar MA. Fourier transform infrared spectroscopy study of nanostructured nickel oxide. Spectrochim Acta Part A. 2003;59(1):121-34.
10. Katz JL, Miquel PF. Syntheses and applications of oxides and mixed oxides produced by a flame process.Nanostruct Mater. 1994;4(5):551-7.

11. Yan W, Ke JJ. Preparation of nickel oxide powder by decomposition of basic nickel carbonate in microwave field with nickel oxide seed as a microwave absorbing additive. Mater Res Bull. 1996;31(1):55-61.
12. Wu Y, He Y, Wu T, Weng W, Wan H. Effect of synthesis method on the physical and catalytic property of nanosized NiO. Mater Lett. 2007;61(13):2679–82.
13. Qiao H, Wei Z, Yang H, Zhu L, Yan X. Preparation and Characterization of NiO Nanoparticles by Anodic Arc Plasma Method. J Nanomater. 2009(2009); doi: 10.1155/795928.
14. Wang W, Liu Y, Xu C, Zheng C, Wang G. Synthesis of NiO nanorods by a novel simple precursor thermal decomposition approach. Chem Phys Lett. 2002;362:119-22.
15. Xing L, Deng XY, Jin Y. Experimental study on synthesis of NiO nano-particles. Scr Mater. 2002;47:219-24.
16. Ahmada T, Ramanujachary KV, Loflandb SE, Ganguli AK. Magnetic and electrochemical properties of nickel oxide nanoparticles obtained by the reverse-micellar route. Solid State Sci. 2006;8(5):425-30.
17. Han DY, Yang HY, Shen CB, Zhou X, Wang FH. Synthesis and size control of NiO nanoparticles by water-in-oil microemulsion. Powder Technol. 2004;147(1-3):113-16.
18. Nassos S. Ph.D thesis Development of catalytic nanomaterials for three industrial processes. Chalmers Univ Technol Göteborg, Sweden 2007; ISBN 978-91-7291-949-5.
19. Pham HN, Nowicki L, Xu J, Datye AK, Bukur DB, Bartholomew CH. Attrition Resistance of Supports for Iron Fischer-Tropsch Catalysts. Ind Eng Chem Res. 2003;42:4001-8.
20. Herranz T, Rojas S, Pérez-Alonso FJ, Ojeda M, Terreros P, Fierro JLG. Carbon oxide hydrogenation over silica-supported iron-based catalysts: Influence of the preparation route. Appl Catal A Gen. 2006;308:19-30 DOI:10.1016/j.apcata.2006.04.007.
21. Pileni MP. Reverse micelles as microreactors. J Phys Chem. 1993;97:6961-73.
22. Zielińska-Jurek A, Reszczyńska J, Grabowska E, Zaleska . NanoparticlesPreparation Using Microemulsion Systems, Microemulsions - An Introduction to Properties and Applications,Dr. Reza Najjar (Ed.), ISBN: 978-953-51-0247-2, 2012. InTech. Available: http://www.intechopen.com/books/microemulsions-an-introduction-to-properties-and applications/nanoparticles-preparation-using-microemulsion-systems.
23. Mineral power diffraction file search manual JCPDS international centre for diffraction data, Swarthmore, USA; 1980.
24. Du Y, Wang W, Li X, Zhao J, Ma J, Liu Y, Lu G. Preparation of NiO nanoparticles in microemulsion and its gas sensing performance. Mater Lett. 2012;68:168–170.
25. Palanisamy P, Raichur AM. Synthesis of spherical NiO nanoparticles through a novel biosurfactant mediated emulsion technique. Mater Sci Eng C. 2009;29:199–204.

Peer-review history:
The peer review history for this paper can be accessed here:
http://www.sciencedomain.org/review-history.php?iid=212&id=7&aid=1148

Fuel Processing Technology 116 (2013) 366–373

Contents lists available at ScienceDirect

Fuel Processing Technology

journal homepage: www.elsevier.com/locate/fuproc

Fly ash supported scandium triflate as an active recyclable solid acid catalyst for Friedel–Crafts acylation reaction

Ashu Rani *, Chitralekha Khatri, Renu Hada

Department of Pure and Applied Chemistry, University of Kota, Kota-324005, Rajasthan, India

ARTICLE INFO

Article history:
Received 12 April 2012
Received in revised form 3 August 2013
Accepted 5 August 2013
Available online 3 September 2013

Keywords:
Fly ash
Solid Lewis acid
Scandium triflate
Acylation

ABSTRACT

Coal generated fly ash is converted into an efficient solid Lewis acid catalyst by loading scandium triflate on thermally and chemically activated fly ash. The activation of fly ash increased the surface silanol groups responsible for loading of scandium triflate species on fly ash surface. The physico-chemical properties of prepared fly ash supported scandium triflate (FST) catalyst were examined by XRD, FTIR, TEM and TGA analysis. The proposed model structure of FST shows that the triflate species withdraws the electron density from the scandium resulting in generating electron deficient Lewis acid sites on fly ash surface as confirmed by NH_3 adsorbed FT-IR spectrum of FST catalyst. The catalyst showed higher activity for solvent free single pot Friedel–Crafts acylation of 2-methoxynaphthalene (2-MN) using acetic anhydride as an acylating agent achieving conversion up to 84% and selectivity of the desired product, 2-acetyle-6-methoxynaphthalene (6-AMN) up to 73%. 6-AMN is a precursor for anti-inflammatory drug, (S)-(+)-6-mathoxy-α-methyl-2-naphthaleneacetic acid, known as Naproxen. The stability of the catalyst was confirmed by hot filtration test. The catalyst could be easily regenerated and reused giving similar conversion up to three reaction cycles under similar experimental conditions. The work reports an alternative pathway for utilization of waste fly ash by using it in developing novel and cost effective, recyclable catalyst system for industrially important acylation reactions.

1. Introduction

Fly ash is a waste material, accumulating at staggering rates as it is generated in very large volume, from the coal based thermal power plants. The disposal of waste is now becoming difficult which is not only occupying valuable land resources but also causing a threat to surface and ground water bodies. Development of innovative methodologies for utilization of this industrial waste in various value added materials has become an essential objective of the present research and development work related with fly ash management and utilization.

Every year, more than 300 billion tons of fly ash is generated all over the world [1,2]. It is a chemical ensemble of silica, alumina, iron oxide, lime, magnesia and alkali in varying amounts with some unburnt activated carbon, with a specific surface area typically between 250 and 600 m^2/kg. Till today, fly ash is mainly consumed in the production of building materials [3], agriculture [4], metal recovery [5], water and atmospheric pollution control [6], dye removal [7] etc. These applications could succeed up to some extent to utilize the huge volume of fly ash. Nevertheless, the search of new applications of the fly ash as catalytic material is still ongoing. Our interest in the catalytic applications of solid waste fly ash was generated by finding some preliminary reports on application of activated fly ash in catalyzing oxidation [8], chlorination [9], condensation of short chain olefins [10], Knoevenagel condensation [11], Beckmann rearrangement [12], etc. These investigations reported SiO_2 and Al_2O_3 as the main fly ash components for catalyzing the organic reactions although the yield of reaction products was quite low. Recently we started the utilization of fly ash in synthesis of several solid acid and base catalysts by developing techniques for activation and loading of sulfated Zirconia [13], Ce triflate [14], sulfuric acid [15], sodium hydroxide [16], magnesium oxide [17], calcium oxide [18], and 3-amminopropyltrimethoxysilane [19] over silica enriched fly ash surface. Fly ash supported catalytic materials can be highly significant as they are highly cost effective due to use of solid waste fly ash as solid support in place of costly commercial silica materials. All fly ash supported catalysts synthesized in our laboratory [13–21] are recyclable, atom efficient and have effectively catalyzed several industrially important organic transformations under solvent free conditions giving higher conversion and selectivity of the desired product. Suitable thermal and chemical activation of fly ash has resulted in increased silica percentage and nano crystalline nature with higher surface silanols groups thus increasing surface active sites suitable for stabilizing chemical moieties.

Synthesis of fly ash supported strong Lewis acid catalyst for Friedel–Crafts acylation is our current interest as this reaction is an extremely important and widely accepted method for synthesis of aromatic ketones, used largely as intermediates in the fine chemicals and pharmaceutical industries [22]. Among acylation of aromatic ethers the selective acylation of 2-methoxynaphthalene (2-MN) is of particular interest as this

* Corresponding author at: 2-m-1, Rangbari scheme, Kota-324005, Rajasthan, India. Tel.: +91 9352619059.
E-mail addresses: ashu.uok@gmail.com (A. Rani), chitra_cool81@yahoo.com (C. Khatri), rosenrenu@gmail.com (R. Hada).

0378-3820/$ – see front matter © 2013 Elsevier B.V. All rights reserved.
http://dx.doi.org/10.1016/j.fuproc.2013.08.003

reaction leads to the synthesis of 2-acetyl-6-methoxynaphthalene (6-AMN), which is recognized as an important intermediate for the production of a non steroidal anti-inflammatory drug Naproxen [23]. The other product 1-acetyl-2-methoxynaphthalene (1-AMN) is an intermediate in phenylation reactions [24]. The conventional homogeneous Lewis acids for Friedel–Crafts acylation are metal halides ($AlCl_3$, $FeCl_3$, $TiCl_4$, etc.) and mineral acids (polyphosphoric acid, HF etc.) [25], which are harmful, corrosive, not regenerable, used in more than stoichiometric amounts and generate hazardous corrosive waste products. Owing to these problems, many research groups have tried to develop environmentally benign acylation processes using solid acid catalysts [26–29]. Most of the earlier reported solid acid catalysts for acylation of 2-MN are different forms of zeolites [26], ion exchanged beta zeolite [28], MCM-41 [29] etc. Among these solid acid catalysts zeolite beta was the most effective catalyst for acylation of 2-MN giving higher selectivity of desired product 6-AMN. These solid acids in previous studies have several drawbacks of low catalyst stability, use of solvents [26] and coke formation in catalysts [23].

Metal triflates are identified as strong Lewis acid catalysts for Friedel–Crafts acylation reactions [30,31]. For reducing the amount of catalyst, used in the catalytic reaction, supported triflates are preferred over pure triflates. Literature reports silica supported Cu triflate [32], La triflate [33], and Zn triflate [34] as solid Lewis acid catalyst for various organic transformations.

In this series, we have introduced an innovative, highly efficient, cost effective, re-generable solid Lewis acid catalyst (FST) by supporting scandium triflate (7%) over thermally and chemically activated solid waste fly ash. The activation of fly ash enhanced the surface silanol groups to alter fly ash as an active support for loading of Sc triflate. The structural, morphological, thermal and surficial properties of FST catalyst are presented in this work. Acylation reaction of 2-MN using acetic anhydride as an acylating agent under solvent free condition evaluated the catalytic performance and reusability of FST under optimized conditions. The reaction conditions such as temperature, time, substrate to catalyst weight ratio, reactants molar ratio etc., were optimized for maximum conversion (84%) and higher selectivity (73%) of the desired product 6-AMN. Thus, the work reports an alternative pathway for utilization of solid waste fly ash by using it for developing novel catalyst system for industrially important organic reactions.

2. Experimental

2.1. Reagents

Fly ash (SiO_2 (58%), Al_2O_3 (21%), Fe_2O_3 (9%), CaO (1.6%), MgO (0.8%), TiO_2 (1.3%), Na_2O (4.8%), K_2O (3.2%) and trace elements (4.0%)) was collected from Kota Thermal Power Plant (Rajasthan, India). The L.O.I. (loss on ignition) was 3 wt.% at 900 °C for 4 h. scandium triflate (Sc $(OTf)_3$) (Sigma Aldrich, 98%), concentrated sulfuric acid (H_2SO_4) (98%), methanol (99.99%), 2-methoxynaphthalene (98%) and acetic anhydride (96%) were purchased from S.D. Fine Chem. Ltd., India.

2.2. Catalyst preparation

Fly ash supported scandium triflate catalyst (FST) was prepared by loading Sc $(OTf)_3$ (7%) on thermally and chemically activated fly ash. The activation of fly ash was carried out by following procedures: —As received fly ash was preheated at 900 °C for 4 h at the rate 18 °C/min to remove C, S and other impurities [19]. The chemical activation was carried out in a stirred reactor taking thermally activated fly ash and concentrated H_2SO_4 in 1:2 weight ratios by heating at 110 °C for one day followed by washing and drying at 110 °C for 24 h and calcinations at 450 °C for 4 h. The activated fly ash (6 g) was heated at 400 °C for 4 h prior to being introduced in a 100-ml 2-necked round bottom flask containing solution of 0.42 g-Sc$(OTf)_3$ (7%) dissolved in 100 ml methanol. The flask was equipped with a reflux condenser and a magnetic stirrer. The slurry was refluxed at 110 °C for 24 h, filtered and washed with cold methanol to remove unloaded triflate on the fly ash surface. The resulting solid product (FST) was further dried in an oven at 110 °C for 24 h followed by calcination at 150 °C for 4 h in a muffle furnace under static condition.

2.3. Catalyst characterization

Powder X-ray diffraction studies were carried out by using Philips X'pert analytical diffractometer with monochromatic CuK_α radiation ($\lambda = 1.54056$ Å) in 2θ range of 5–80°. The FT-IR spectrum of the synthesized material was recorded using FT-IR spectrophotometer (Tensor 27, Bruker) in DRS (Diffuse Reflectance System) by mixing the sample with KBr in 1:20 weight ratio in the range 400–4000 cm^{-1} with a resolution of 4 cm^{-1}. The loading of scandium triflate on fly ash particles was confirmed by TEM analysis, Model: Tecnai 20 G2 (FEI make). Thermogravimetric analysis (TGA) was performed using simultaneous TGA (TA instrument, model SDT2960).

2.4. Catalytic activity of FST: acylation of 2-methoxynaphthalene with acetic anhydride

Acylation reaction of 2-methoxynaphthalene (2-MN) with acetic anhydride (Scheme 1) for synthesis of 6-AMN as major product, precursor for Naproxen (Scheme 2), was carried out in a liquid phase batch reactor consisting of 50 ml round-bottom flask with condenser in a temperature constant oil bath on magnetic stirrer. The freshly activated (150 °C, 2 h) 0.1 g of FST catalyst was added quickly into the flask containing mixture of 0.01 mol (1.58 g) 2-methoxynaphthalene (2-MN) and 0.02 mol (2.04 g) acylating reagent acetic anhydride. The reaction was carried out at different temperatures ranging from 90 to 150 °C, at different time ranging from 1 to 24 h and at different molar ratios of substrate and acetic anhydride. After completion of the reaction, catalyst was filtered and the product was analyzed by gas chromatography (Dani Master GC) having a flame ionization detector and HP-5 capillary column of 30 m length and 0.25 mm diameter, programmed oven temperature of 50–280 °C and N_2 (1.5 ml/min) as a carrier gas.

The conversion was calculated as follows:

$$\text{Conversion(wt.\%)} = 100 \times [\text{Initial wt.\%} - \text{Final wt.\%}]/\text{Initial wt.\%}.$$

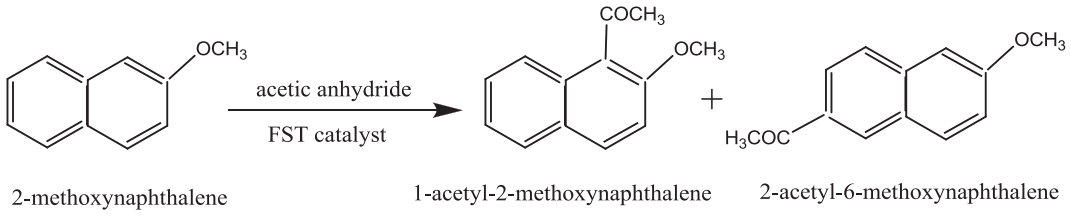

Scheme 1. Acylation of 2-methoxynaphthalene (2-MN) with acetic anhydride over FST catalyst.

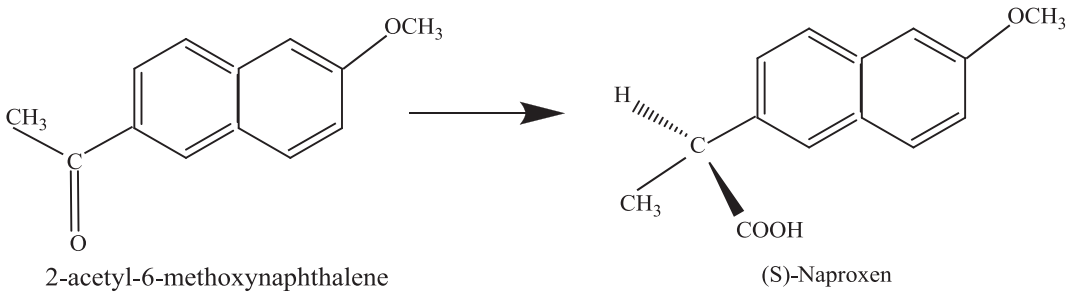

Scheme 2. Synthesis of naproxen from 6-AMN.

2.5. Catalyst regeneration

The spent catalyst was washed with acetone dried in oven at 110 °C for 12 h followed by calcination at 150 °C for 2 h and reused for next reaction cycle under similar reaction conditions as earlier.

3. Results and discussions

3.1. Catalyst characterization

After chemical activation, the silica content in fly ash sample was greatly increased from 58% to 81%, which is analyzed by AAS.

The XRD patterns of pure fly ash (FA, Fig. 1a), chemically activated fly ash (AFA, Fig. 1b), and fly ash supported scandium triflate catalyst (FST, Fig. 1c) show the presence of crystalline and amorphous phases. The amorphous phases of fly ash were increased by chemical activation, which resulted in decreased crystallite size from 33 nm to 12 nm [20]. The chemical activation removes some of the crystalline components present in the fly ash, lowering the crystallinity and increases the amorphous content [15]. In FST (Fig. 1c) the loading of scandium triflate on previously activated fly ash has increased the crystallinity and crystallite size from 12 to 35 nm due to presence of scandium having high crystallinity and crystallite size between 20 and 25 nm [25].

The FT-IR spectra of pure fly ash (FA) and activated fly ash (AFA) evidence a broad band in –OH region (3800–2700 cm^{-1}), which is attributed to surface–OH groups, particularly of silica and the water molecules adsorbed on the surface (Fig. 2a and b). The broadness of the band reflects strong hydrogen bonding between the hydroxyl

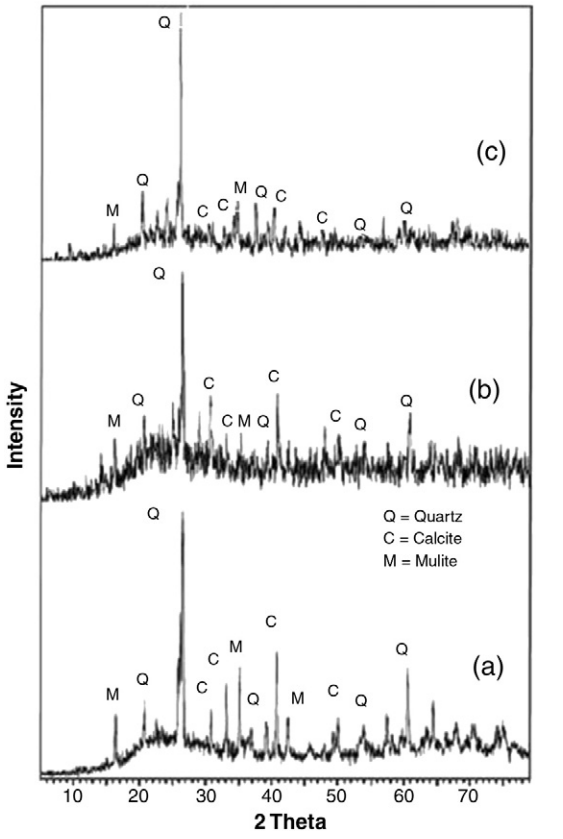

Fig. 1. X-ray diffraction pattern of (a) FA, (b) AFA, and (c) FST catalyst.

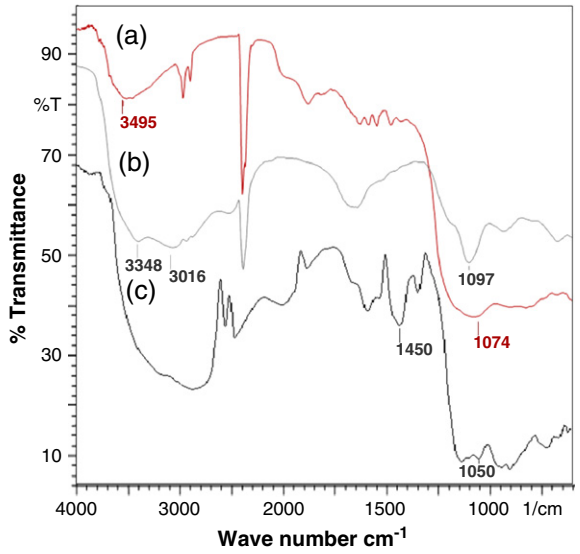

Fig. 2. FT-IR spectra of (a) FA, (b) AFA, and (c) FST catalyst.

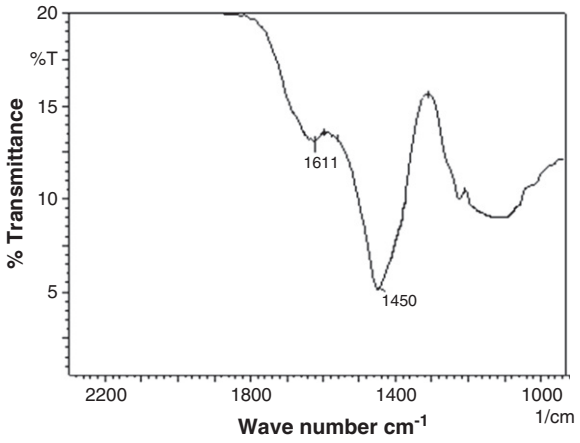

Fig. 3. FT-IR spectra of ammonia adsorbed FST catalyst after evacuation at 150 °C.

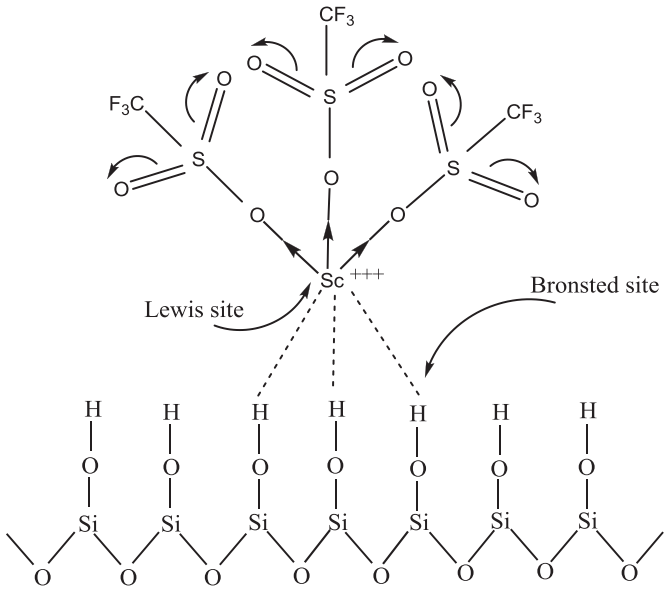

Scheme 3. The proposed structure for active site of the catalyst FST.

groups reported earlier [13,15]. The increased amorphous silica in the activated fly ash can be characterized by an intense band in the range 1000 – 1300 cm^{-1}, corresponding to the valence vibrations of the silicate oxygen skeleton. The main absorption band of the valence oscillations of the groups Si-O-Si in quartz appears with a main absorption maximum at 1100 cm^{-1} [15]. The chemical activation increases the silica content in the AFA, significantly increasing surface hydroxyl groups, which helps in loading of the triflate species. The interaction of triflates with surface –OH groups of silica present in fly ash binds triflates on the fly ash surface without diminishing the Lewis acidity of the scandium. The FT-IR spectrum of scandium triflate loaded fly ash catalyst FST in Fig. 2c shows a very intense peak at 1450 cm^{-1} (asymmetric stretching frequency of S═O bond i.e., $\nu_{S=O}$), which is attributed to the sulfonate group [35] of scandium triflate loaded on the activated fly ash. A small peak at ~1050 cm^{-1} is stretching frequency (ν_{as}) of C-F bond of triflate.

FT-IR spectra of the ammonia adsorbed sample in Fig. 3 indicates the presence of significant amount of Lewis acid sites, as inferred from the bands at 1608 cm^{-1} (δ_{asy} of NH_3 adsorbed on Lewis sites) and 1195 cm^{-1} (δ_{sym} of NH_3 adsorbed on Lewis sites). The Lewis acid centers are the Sc^{3+} ion present on the fly ash surface (Scheme 3) [14]. Thus, the study reveals that the synthesized FST catalyst possesses significant amount of Lewis acidity.

Thermogravimetric analysis of the prepared catalyst shows weight loss of 1% from 50 to 100 °C corresponds to the loss of water and solvent (methanol). The curve presented in Fig. 4, shows major weight loss of 5 wt.% between 200 and 350 °C at lower temperature (below 400 °C) which may be ascribed to the decomposition of triflate species, loaded on the surface as in case of silica supported copper and zinc triflate [32,34]. In the present case, the reaction of highly dispersed Lewis acid with silica surface silanol groups, hydrolyze the Sc-(OTf) bond to form ScO and triflic acid, which causes the thermal decomposition of triflate groups. After 450 °C, weight loss is attributed to decomposition of sulfur species present in the catalyst.

The TEM images of unloaded fly ash (FA) and scandium triflate loaded fly ash (FST) are given in Fig. 5. The images were used to identify the morphology of unloaded and Scandium triflate loaded fly ash. From Fig. 5 (b, c and d), we can see layers of scandium triflates on the surface of the fly ash.

3.2. Catalytic activity

FST shows high catalytic activity for acylation of 2-MN with acetic anhydride resulting 84% conversion of 2-MN, where as FA

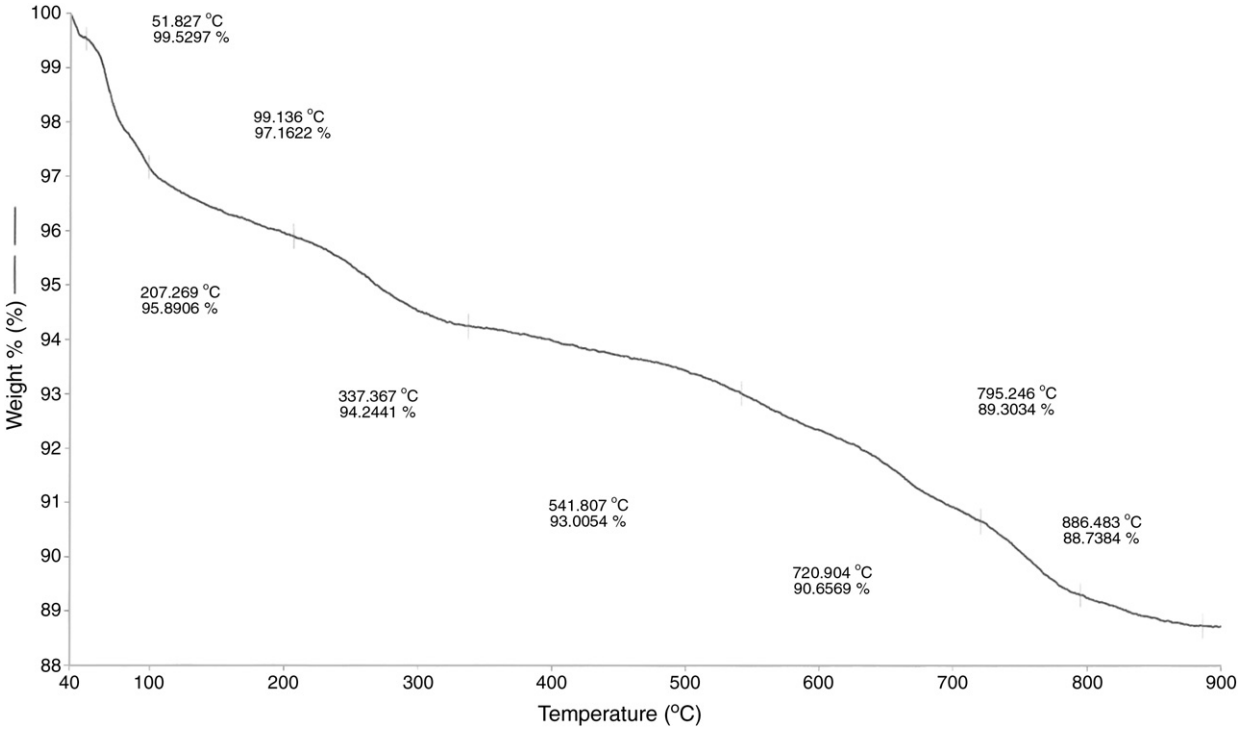

Fig. 4. TGA profile of FST catalyst.

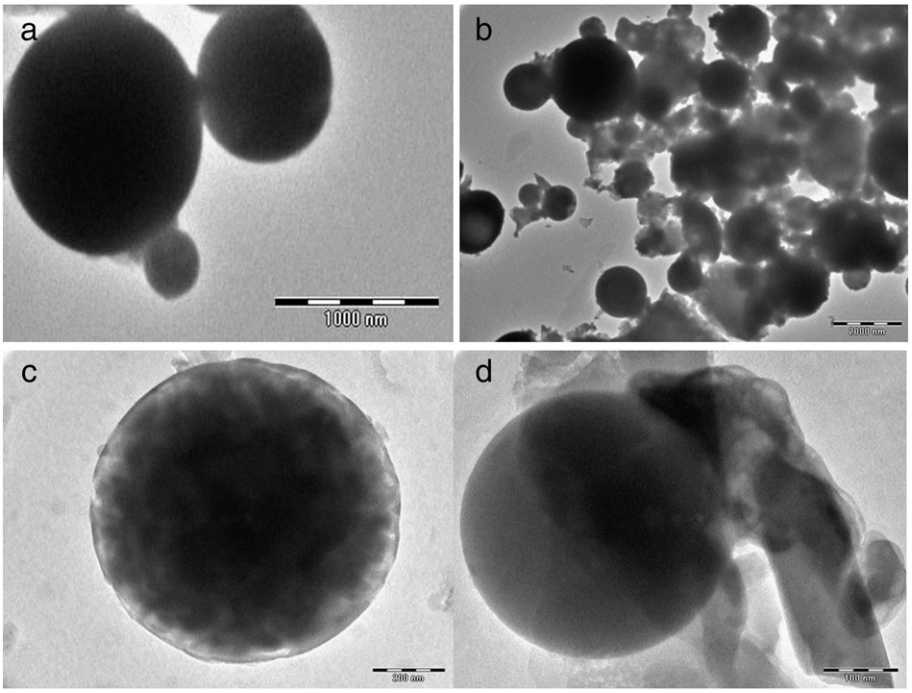

Fig. 5. TEM images of (a) FA, (b–d) FST catalyst.

and AFA due to absence of Lewis acidity on the surface do not catalyze the acylation reaction. The reaction conditions such as reaction temperature, time, molar ratios of reactants, substrate to catalyst ratio were optimized in order to achieve maximum conversion of 2-MN.

Optimization of reaction temperature to give maximum conversion of 2-MN was studied at temperature ranging from 90 to 150 °C for 4 h, The results show that the conversion of 2-MN with selectivity toward 6-AMN increases significantly with increase in temperature from 90 to 140 °C and vice versa for the selectivity of 1-AMN. The maximum conversion (84%) and selectivity (73%) of desired product was obtained at 140 °C, at temperatures above the boiling temperature of acetic anhydride (140 °C), conversion was decreased due to decrease in the contact time of acetic anhydride with 2-MN, as former mostly remained in the vapor phase during the reaction as shown in Table 1.

In acylation of 2-MN, the presence of the electron withdrawing groups activates the 1-, 6-, and 8-positions of the naphthalene ring. The 1-position is more active than the other two positions and the 6-position is more stable than the other two positions, so acylation of 2-MN generally occurs at this kinetically favored 1-position at low temperatures and at the thermodynamically favored 6-position at high temperatures [26].

The optimization of reaction time required to achieve maximum conversion was carried out at 140 °C for different reaction times ranging from 1 h to 24 h as shown in Table 2. It was found that in the first 4 h of the reaction period the conversion increases linearly up to 84%, which remained constant up to 24 h.

The effect of 2-MN to acetic anhydride molar ratio on conversion was also monitored at different molar ratios ranging from 1:1 to 1:5 at a temperature of 140 °C, for 4 h. The conversion was found maximum at 1:2 molar ratios with 84% conversion, which further decreases up to 71% on increasing the molar ratio up to 1:5 as given in Table 3.

The substrate to catalyst weight ratio was varied from 5 to 20. The maximum 84% conversion was obtained at weight ratio 10.

Table 1
Effect of temperature on conversion and product distribution of acylation of 2-MN and acetic anhydride over FST catalyst.

Temperature (°C)	Conversion(%) of 2-MN	Selectivity(%) of 6-AMN	Selectivity (%)1-AMN	Selectivity (%) of other acylated isomers
90	28	3	95	2
100	47	11	87	2
120	79	35	63	2
140	84	73	25	2
150	82	69	17	14

Reaction conditions: - acetic anhydride:2-MN = 2; substrate/catalyst = 10; time = 4 h.

Table 2
Effect of time on conversion and product distribution of acylation of 2-MN and acetic anhydride over FST catalyst.

Time (hour)	Conversion (%) of 2-MN	Selectivity(%) of 6-AMN	Selectivity (%)1-AMN	Selectivity (%) of other acylated isomers
1	28	73	25	2
2	47	73	25	2
4	84	73	25	2
6	84	73	25	2
8	83	72	23	5
24	83	61	21	18

Reaction conditions: acetic anhydride:2-MN = 2; substrate/catalyst = 10; temperature = 140 °C.

Table 3
Effect of molar ratio of 2-methoxynaphthalene (2-MN) to acetic anhydride (AA) on conversion of 2-MN.

2-MN:AA	Conversion (%) of 2-MN	Selectivity (%) of 6-AMN	Selectivity (%) 1-AMN	Selectivity (%) of other acylated isomers
1:1	12	73	25	2
1:2	84	73	25	2
1:5	71	39	21	40

Reaction conditions: substrate/catalyst = 10; temperature = 140 °C; time = 4 h.

Table 4
A comparison of Friedel–Craft acylation reaction over different types of solid acid catalysts.

Catalyst	Conversion (%) of 2-MN	Selectivity (%) of 6-AMN	Selectivity (%) 1-AMN	Reference
Zeolite beta[a]	57.6	60.5	31.7	[27]
Ion exchanged zeolite beta(La^{3+})[b]	34	75	19	[29]
FST[c]	84	73	25	Our study

[a] Reaction conditions: —acetic anhydride:2-MN = 2; temperature = 120 °C; time = 14 h; solvent = 50 ml of 1,2-dichloroethane.
[b] Acetic anhydride:2-MN = 2; temperature = 130 °C; time = 2 h; solvent =, tetradacane in 20 ml of nitrobenzene.
[c] Acetic anhydride:2-MN = 2; substrate/catalyst = 10; temperature = 140 °C; time = 4 h; solvent free condition.

FST gave higher conversion of 2-MN than some previously reported industrially viable catalysts, along with comparable selectivity, for 6-AMN, (Table 4).

The proposed model (Scheme 3) of the FST catalyst shows Lewis acid sites on scandium metal attached to activated surface of fly ash. The triflate species withdraws the electron density from the surficial metal atom making it electron deficit and generate Lewis acidity. The Lewis sites on FST catalyst are able to generate acylium ion intermediate from acetic anhydride, which attack on the π-electron system of 2-MN. The possible pathway for the production of 6-AMN in the acylation of 2-MN with acetic anhydride catalyzed by FST is shown in Scheme 4.

4. Catalyst regeneration

The used FST catalyst from the reaction mixture was filtered, washed with acetone and re-generated by heating at 150 °C for 2 h. The regenerated catalyst was used for the next reaction cycles under similar reaction conditions as first cycle. The catalyst was found efficient up to four cycles giving conversion in the range of 84–77%. The stability of FST catalyst toward leaching of triflate moiety during the reaction was also confirmed by hot filtration leaching test [34], which reveals no further reaction occurs if the catalyst was filtered off midway through a reaction. The results are confirmed by FT-IR studies of the fresh and regenerated catalyst (Fig. 6).

The FT-IR spectra of regenerated catalyst after second cycle in Fig. 6 show similarity with the fresh catalyst indicating the presence of triflate species and no change in chemical composition of catalyst surface. The significant decrease in conversion after fourth cycle is due to the deposition of carbonaceous material on the external surface of the used catalyst that may block the active sites present on the catalyst surface [23].

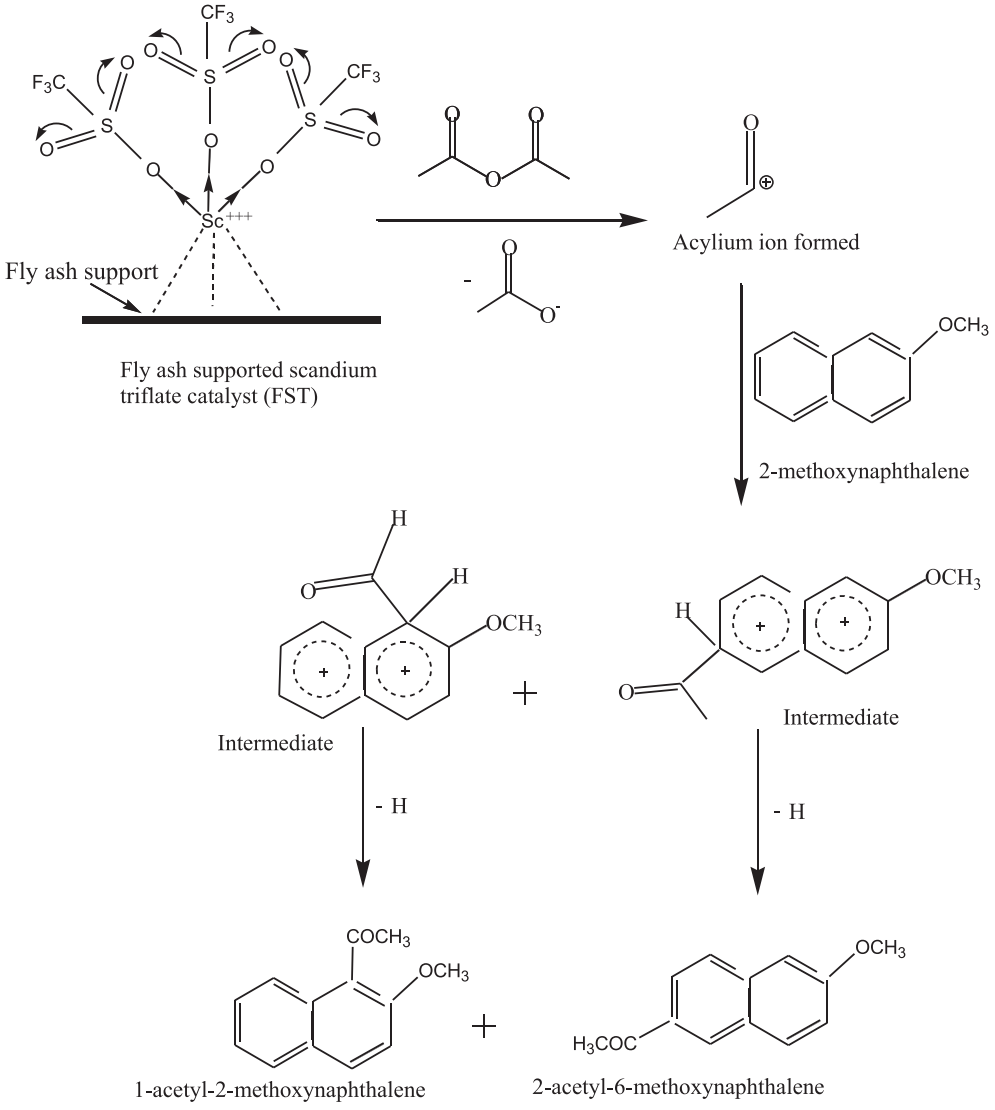

Scheme 4. Mechanistic pathway of acylation of 2-methoxynaphthalene over fly ash supported scandium triflate catalyst (FST).

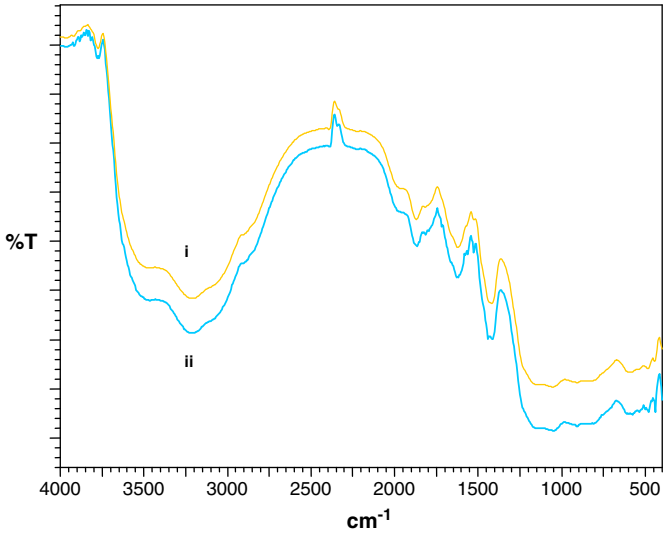

Fig. 6. FTIR spectra of (i) fresh and (ii) regenerated fly ash supported scandium triflate (FST).

5. Conclusion

In the present study, an efficient, recyclable and cost effective solid acid catalyst is synthesized by loading scandium triflate on thermally and chemically activated fly ash. The chemical activation of fly ash increases the silica content and surface hydroxyl contents. The characterization of the catalyst confirmed the loading of scandium triflate on activated fly ash surface. The prepared FST catalyst possesses significant amount of Lewis acidity responsible for high conversion values (84%) for acylation of 2-MN giving predominantly 6-AMN (73%) as product, which is an important precursor for synthesis of Naproxen (anti-inflammatory drug). At high temperature (140 °C), 6-AMN isomer is formed in higher amounts while other isomer 1-AMN remains in traces.

Higher conversion and higher selectivity for desired product make the FST most suitable catalyst for industrial scale production of acylating product (6-AMN). FST can replace zeolite β and other similar industrially favored catalysts reducing cost of production.

The present work provides a pathway for utilization of abundantly available solid waste fly ash, as a support material for synthesis of highly selective solid Lewis acid catalyst (FST). This fly ash supported catalyst is a practical alternative to soluble analogs in view of high stability of reactive sites, high activity under solvent free conditions, easy separation of catalyst by simple filtration and reuse after activation without loss of activity. This study suggests that fly ash could be an economical source of silica and alumina for synthesizing novel solid Lewis acid catalysts for catalyzing industrially important reactions in cost effective manner.

Acknowledgment

The authors are thankful to Vice-Chancellor Prof. Madhusudan Sharma, University of Kota, Kota, for providing laboratory and analytical facilities. TGA support was provided by Dharmsinh Desai University, Nadiad, Gujarat. XRD and TEM were performed at UGC-DAE Consortium for Scientific Research, Indore. Dr N. P. Lalla and Dr. Mukul Gupta helped in discussing TEM and XRD results respectively. Fly ash Mission, Department of Science and Technology, New Delhi, India provided the financial support through research project (no. FAU/DST/600(23)/2009-10) sanctioned to corresponding author.

References

[1] S. Wang, L. Baxter, Comprehensive study of biomass fly ash in concrete: strength, microscopy, kinetics and durability, Fuel Processing Technology 88 (2007) 1165–1170.
[2] R. Ciccu, M. Ghiani, A. Muntoni, A. Serci, The Italian approach to the problem of fly ash, Proceedings of the International Ash Utilization Symposium, Lexington, Kentucky, USA, 18–20 October, 1999.
[3] S. Wang, E. Llamazos, F. Fonseca, L. Baxter, Durability of biomass fly ash concrete: freezing and thawing and rapid chloride permeability tests, Fuel 87 (2008) 359–364.
[4] W. Arnold, E.S. Schumann, Malcolm, chemical evaluation of nutrient supply from fly ash, bio solid mixtures, Soil Science Society of American Journal 64 (2000) 419–426.
[5] J. Marrero, G. Polla, R.J. Rebagliati, R. Pla, D. Gomez, P. Smichowski, Characterization and determination of 28 elements in fly ashes collected in a thermal power plant in Argentina using different instrumental techniques, Spectrochimica Acta Part B 62 (2007) 101–108.
[6] M. Ahmaruzzaman, Role of fly ash in the removal of organic pollutants from wastewater, Energy & Fuels 23 (2009) 1494–1511.
[7] D. Mohan, K.P. Singh, G. Singh, K. Kumar, Removal of dyes from wastewater using fly ash, a low-cost adsorbent, Industrial and Engineering Chemistry 41 (2002) 3688–3695.
[8] D. Mallik, S.K. Chaudhuri, Air oxidation of aqueous sodium sulfide solutions with coal fly ash, Water Resources 33 (1999) 585–590.
[9] W. Jarmohamed, P. Mulder, Oxychlorination and combustion of propene on fly-ash. Formation of chlorinated benzenes, dibenzodioxines and mono- and dibenzofurans, Chemosphere 29 (1994) 1911–1917.
[10] M.F. Bergstra, Catalytic Ethylene Polymerization Novel Reactors for Kinetics in Gas, Slurry and Solution Processes, Thesis , 2004, ISBN 90-365-2091-6.
[11] X. Zhang, E.S.M. Lai, R.M. Aranda, K.L. Yeung, An investigation of Knoevenagel condensation reaction in microreactors using a new zeolite catalyst, Applied Catalysis A: General 261 (2004) 109–118.
[12] M. Gopalakrishnan, P. Sureshkumar, V. Kanagarajan, J. Thanusu, R. Govindaraju, A simplified green chemistry approaches to organic synthesis in solid media. Activated fly ash, an industrial waste (pollutant) as an efficient and novel catalyst for some selected organic reactions in solvent-free conditions under microwave irradiation, general papers, ARKIVOC (2006) 130–141, (xiii).
[13] C. Khatri, M.K. Mishra, A. Rani, Synthesis and characterization of fly ash supported sulfated zirconia catalyst for benzylation reactions, Fuel Processing Technology 91 (2010) 1288–1295.
[14] C. Khatri, D. Jain, A. Rani, Fly ash-supported cerium triflate as an active recyclable solid acid catalyst for Friedel–Crafts acylation reaction, Fuel 89 (2010) 3853–3859.
[15] C. Khatri, A. Rani, Synthesis of a nano-crystalline solid acid catalyst from fly ash and its catalytic performance, Fuel 87 (2008) 2886–2892.
[16] D. Jain, C. Khatri, A. Rani, Synthesis and characterization of novel solid base catalyst from fly ash, Fuel 90 (2011) 2083–2088.
[17] D. Jain, A. Rani, MgO enriched coal fly ash as highly active heterogeneous base catalyst for Claisen–Schmidt condensation reaction, American Chemical Science Journal (2011) 37–49.
[18] D. Jain, C. Khatri, A. Rani, Fly ash supported calcium oxide as recyclable solid base catalyst for Knoevenagel condensation reaction, Fuel Processing Technology 91 (2010) 1015–1021.
[19] D. Jain, M.K. Mishra, A. Rani, Synthesis and characterization of novel aminopropylated fly-ash catalyst and its beneficial application in base catalyzed Knoevenagel condensation reaction, Fuel Processing Technology 95 (2012) 119–126.
[20] C. Khatri, A. Rani, Green catalytic process for aspirin synthesis using fly ash as hetero-geneous solid acid catalyst, Indian Patent No. - 1980/DEL/2007.
[21] C. Khatri, A. Rani, Fly ash as heterogeneous solid acid catalyst for organic synthesis. IndianPatent No 452/del/2008.
[22] G.A. Olah, Friedel Crafts Chemistry, Wiley Interscience, New York, 1973.
[23] A.N. Parvulescu, B.C. Gagea, V.I. Parvulescu, D.D. Vos, P.A. Jacobs, Acylation of 2-methoxynaphthalene with acetic anhydride over silica-embedded triflate catalysts, Applied Catalysis A: General 306 (2006) 159–164.
[24] F. Kakiichi, M. Usui, S. Ueno, N. Chatani, S. Muraj, Ruthenium-catalyzed functionalization of aryl carbon– oxygen bonds in aromatic ethers with organoboron compounds, Journal of the American Chemical Society 126 (2004) 2706.
[25] P.H. Gore, in: G.A. Olah (Ed.), Friedel Crafts and Related Reactions, III, Wiley Interscience, New York, 1964, p. 64.
[26] S.D. Kim, K.H. Lee, J.S. Lee, Y.G. Kim, K.E. Yoon, The regioselective acylation of 2-methoxynaphthalene to 2-acetyl-6-methoxynaphthalene over zeolite beta, Journal of Molecular Catalysis A: Chemical 152 (2000) 33–45.
[27] D. Das, S. Cheng, Friedel–Crafts acylation of 2-methoxynaphthalene over zeolite catalysts, Applied Catalysis A: General 201 (2000) 159–168.
[28] I.C. Kantarli, L. Artok, H. Bulut, S. Yilmaz, S. Ulku, Acylation of 2-methoxynaphthalene over ion-exchanged β-zeolite, Studies in Surface Science and Catalysis 142 (2002) 799–806.
[29] E.A. Gunnewegh, S.S. Gopie, H. Bekkum, MCM-41 type molecular sieves as catalysts for the Friedel–Crafts acylation of 2-methoxynaphthalene, Journal of Molecular Catalysis A: Chemical 106 (1996) 151–158.
[30] A. Kawada, S. Mitamura, S. Kobayashi, Scandium trifluoromethanesulfonate. A novel catalyst for Friedel–Crafts acylation, Synlett 1994 (1994) 545–546.
[31] S. Kobayashi, I. Komoto, Remarkable effect of lithium salts in Friedel Crafts acylation of methoxynaphthalene catalyzed by metal triflates, Tetrahedron Letters 56 (2000) 6463–6465.

[32] M.J. Gronnow, D.J. Macquarrie, J.H. Clark, P. Ravenscroft, A study into the use of microwaves and solid acid catalysts for Friedel–Crafts acylations, Journal of Molecular Catalysis A: Chemical 231 (2005) 47–51.
[33] A.N. Parvulescu, B.C. Gagea, G. Poncelet, V.I. Parvulescu, Acylation of alcohols and acylated aromatic compounds on silica embedded-triflate catalysts, Applied Catalysis A: General 301 (2006) 133–137.
[34] K. Wilson, A. Renson, J.H. Clark, Novel heterogeneous zinc triflate catalysts for the rearrangement of α-pinene oxide, Catalysis Letters 61 (1999) 51–55.
[35] J. Coates, Interpretation of Infrared spectra, a practical approach, in: R.A. Meyers (Ed.), Encyclopedia of Analytical Chemistry, John Wiley & Sons Ltd, New York/Chichester, 2000, pp. 10815–10837.

Hindawi Publishing Corporation
Journal of Catalysts
Volume 2013, Article ID 723957, 9 pages
http://dx.doi.org/10.1155/2013/723957

Research Article

Surface Modification of Fly Ash for Active Catalysis

Deepti Jain,[1] Renu Hada,[2] and Ashu Rani[2]

[1] *Department of Applied Chemistry, Gautam Buddha University, Greater Noida, Uttar Pradesh 201308, India*
[2] *Department of Pure and Applied Chemistry, University of Kota, Rajasthan 324005, India*

Correspondence should be addressed to Deepti Jain; deepti_skjain@yahoo.com

Received 29 January 2013; Revised 5 May 2013; Accepted 20 May 2013

Academic Editor: Vijay Bokade

Fly ash based effective solid base catalyst (KF/Al_2O_3/fly ash^{473}, KF/Al_2O_3/fly ash^{673}, and KF/Al_2O_3/fly ash^{873}) was synthesized by loading KF over chemically and thermally activated fly ash. The chemical activation was done by treating fly ash with aluminum nitrate via precipitation method followed by thermal activation at 650°C to increase the alumina content in fly ash. The increased alumina content was confirmed by SEM-EDX analysis. The alumina enriched fly ash was then loaded with KF (10 wt%) and calcined at three different temperatures 473 K, 673 K and 873 K. The amount of loaded KF was monitored by XRD, FTIR spectroscopy, SEM-EDX, TEM and Flame Atomic Absorption Spectrophotometer. The catalytic activities of the catalysts were tested in the Claisen-Schmidt condensation of benzaldehyde and 4-methoxybenzaldehyde with 2′-hydroxyacetophenone to produce 2′-hydroxychalcone and 4-methoxy-2′-hydroxychalcone respectively. Higher conversion (83%) of benzaldehyde and (89%) of 4-methoxybenzaldehyde reveals that among these heterogeneous catalysts KF/Al_2O_3/fly ash^{673} is very active.

1. Introduction

Fluoride ion is useful as weakly basic, nonnucleophilic in many organic chemical processes involving hydrogen abstraction or hydrogen bond formation [1]. Fluoride has been reported as effective basic catalyst in Cannizzaro reaction to replace classical methods employing hydroxide base which gave large amount of Cannizzaro side reactions [2]. Potassium fluoride is a well-known source of fluoride and possesses a number of advantages of both solution and solid phase chemistry. Among the supported fluoride systems, potassium fluoride on activated alumina has been found to be more reactive than nonsupported KF, KF-silica gel, KF-celite and KF-molecular sieves [3]. When KF is loaded on alumina, it shows high catalytic activity towards organic reactions namely. Michael addition [4], aldol condensation [5] and transesterification reactions [6]. The basic sites on KF/alumina may be related to a very hard anion F^-; the catalyst may show the characteristic performances which differentiate KF/alumina from the oxide-type solid base catalysts such as alkaline earth oxides [7]. In contrast to many applications of KF/alumina to organic synthesis as a base catalyst, mechanisms of the appearance of the basicity of KF/alumina are not clarified. Insufficient coordination of KF only with surface OH groups may result in the formation of active F^- ions [8]. This possibility was supported by ^{19}F MAS NMR [9]. Three basic species or mechanisms of the appearance of the basicity of KF/alumina reported previously [10] are (a) the presence of active fluoride, (b) the presence of [Al–O–] ion which generates OH^- when water is added, and (c) the cooperation of F^- and [Al–OH]. It has been reported in the literature (1) that the formation of potassium hexafluoroaluminate must be accompanied by the formation of hydroxide and/or aluminate, responsible for the high reactivity of KF/Al_2O_3. However, F^- ion has little or no direct role in the catalytic activity of KF/Al_2O_3 catalyst:

$$12KF + Al_2O_3 + 3H_2O \longrightarrow 2K_3AlF_6 + 6KOH \quad (1)$$

The strong basic nature of KF/Al_2O_3 allowed it to replace organic bases in a number of organic reactions.

The Claisen-Schmidt condensation between acetophenone and benzaldehyde derivatives is a valuable C–C bond-forming reaction which produces α,β-unsaturated ketones

called chalcones which display a wide spectrum of biological activities including antioxidant, antibacterial, antileishmanial, anticancer, antiangiogenic, anti-infective and anti-inflammatory activities [11–13]. Traditionally, the Claisen-Schmidt condensation is carried out, using alkaline hydroxides or sodium ethoxide [14]. The use of basic solids, such as zeolites [15], alkali metal and oxides supported on alkaline earth oxide [16], MgO [17], calcined hydrotalcites [18] and KF [19], has received much attention over the last years as potential catalysts for Claisen-Schmidt condensations. Using solid catalysts, instead of stoichiometric amounts of soluble strong bases, the overall atom efficiency of reactions is improved, processes are simplified, the turn overnumber of the catalyst is increased, the volume of waste is significantly reduced, and product workup becomes easier, if necessary at all. Typically organic bases immobilized on different supports have been used as catalytic materials. Progress has predominately been limited because of leaching of the active material from the various types of support used.

Fly ash (SiO_2, Al_2O_3, Fe_2O_3, CaO, and MgO) by appropriate activation has been converted into solid acids and solid bases. H_2SO_4 treated fly ash has been used as Bronsted acid catalyst for synthesis of aspirin and oil of wintergreen as solid support for loading of cerium triflate and sulphated zirconia [20–22] for synthesis of 3,4-dimethoxyacetophenone (antineoplastic) and diphenylmethane. In recent years, fly ash treated with CaO, NaOH, MgO and aminopropyl trimethoxysilane has also been used as solid base catalysts in various condensation reactions [23–26]. In the present work, we attempted to introduce a novel solid base catalyst from chemically activated fly ash by loading KF followed by thermal activation at different temperatures. As received fly ash (silica 58%) was chemically activated to increase alumina and was thought to be used for supporting potassium fluoride. The use of fly ash as support not only reduced the cost of the catalyst it also showed high basicity and catalytic activity for benzaldehyde and 4-methoxybenzaldehyde with 2′-hydroxyacetophenone to produce 2′-hydroxychalcone and 4-methoxy-2′-hydroxychalcone in a single step, liquid phase and solvent free reaction conditions with high yield (>90%) and purity. We also examined the changes in bulk and surface structures of KF/Al_2O_3-fly ash catalysts pretreated at different temperatures by XRD, FTIR, SEM-EDX and TEM to elucidate catalytically active sites formed by chemical and thermal treatment of fly ash.

2. Experimental

2.1. Material. Fly ash (Class F type with SiO_2 and Al_2O_3 > 70%) used as solid support for the solid base was collected from Kota Thermal Power Plant (Rajasthan, India). α-Alumina, potassium fluoride (KF), aluminium nitrate ($Al(NO_3)_3{\cdot}9H_2O$), $(NH_4)_2CO_3$, NH_4OH, benzaldehyde (99%), 4-methoxybenzaldehyde (98%) and 2′-hydroxyacetophenone (99%) were purchased from S. D. Fine Chem Ltd., India.

2.2. Catalyst Preparation. The three catalysts KF/fly ash, KF/Al_2O_3/fly ash and KF/Al_2O_3 were prepared by using aqueous solution of potassium fluoride for wet impregnation of fly ash, alumina enriched fly ash and α-alumina respectively. All three catalysts were calcined at different temperatures (473 K, 673 K, and 873 K) and prepared by the following method.

2.2.1. KF/Fly Ash Catalyst. As received fly ash was preheated for 3 h at 900°C under static conditions. 10 g of thermally activated fly ash was added into a glass reactor containing aqueous solution of 0.166 g potassium fluoride (10 wt %). The reactor was equipped with a reflux condenser and a magnetic stirrer bar. The slurry was refluxed at 110°C for 24 h then filtered and washed to eliminate excess KF on the fly ash surface.

2.2.2. KF/Al_2O_3/Fly Ash Catalyst

Step 1. An aqueous solution of 0.09 mol of $Al(NO_3)_3{\cdot}3H_2O$ was added into thermally activated fly ash with constant stirring. Solution of 0.16 mol of $(NH_4)_2CO_3$ was added dropwise in the above solution and the pH was maintained close to 8.0 by the addition of appropriate amounts of NH_4OH (35% aqueous ammonia solution). The resulting gel-like slurry was washed with deionized water until pH = 7. Then the precipitate was dried at 373 K in air for approximately 12 h. The resulting solid was calcined at 673 K for 4 h under static conditions.

Step 2. The chemically activated fly ash was heated at 400°C for 4 h prior to its introduction in a glass reactor containing aqueous solution of 0.166 g potassium fluoride (10 wt%). The reactor was equipped with a reflux condenser and a magnetic stirrer bar. The slurry was refluxed at 110°C for 24 h then filtered and washed to eliminate any excess KF on the fly ash surface.

2.2.3. KF/Al_2O_3 Catalyst. 10 g of alumina milled to a fine powder was added into deionized water containing desired amount of KF (0.166 g for 10 wt% loading). Thereafter the resulting solid products of all three catalysts were further dried at 110°C for 24 h and calcined at three different temperatures 473 K, 673 K and 873 K for 2 h.

2.3. Characterization. The samples were characterized by Fourier transform infrared spectroscopy (FTIR), powder X-ray diffraction study (XRD), BET surface area analysis, scanning electron microscopy (SEM) and transmission electron microscopy (TEM). The loading of KF on the chemically activated fly ash was confirmed by FTIR study using FTIR spectrophotometer (IRPrestige-21, Shimadzu) having a Diffuse Reflectance Scanning technique by mixing the sample with dried KBr (in 1/20 wt ratio) in the range of 400–4000 cm^{-1} with a resolution of 4 cm^{-1}. X-ray diffraction studies were carried out by using X-ray diffractometer (Philips X'pert) with monochromatic CuK_α radiation (λ = 1.54056 Å) in a 2θ range of 5 to 65°. The detailed imaging information about the morphology and surface texture of the sample was provided by SEM-EDX (Philips XL30 ESEM TMP). The loading of KF

on fly ash particles was confirmed by TEM analysis (Tecnai 20 G2 (FEI make), Resolution: Line-1.4 A, Point 2.04 A).

2.4. Reaction Procedure: Claisen-Schmidt Condensation. Catalytic activity of prepared catalysts was tested by Claisen-Schmidt condensation of benzaldehyde and 4-methoxybenzaldehyde with 2′-hydroxyacetophenone in solvent free liquid phase reaction shown in Scheme 1.

The condensation was performed in liquid phase batch reactor, which consists of 50 mL round bottom flask, magnetic stirrer and condenser. A mixture of benzaldehyde (0.106 g, 1 mmol) or 4-methoxybenzaldehyde (0.136 g, 1 mmol) and hydroxyacetophenone (0.136 g, 1 mmol) was taken in round bottom flask. The catalysts, activated at different temperatures for 2 h (substrate to catalyst ratio = 10), were added in the reaction mixture. At the end of the reaction, the catalyst was filtered and the reaction mixture was analyzed by Gas Chromatography (Dani Master GC) having a flame ionization detector and HP-5 capillary column of 30 m length and 0.25 mm diameter, programmed oven temperature of 50–280°C and N_2 (1.5 mL/min) as a carrier gas.

2.5. Catalyst Regeneration. The used catalyst (KF/Al_2O_3/fly ash^{673}) was washed with acetone and dried in oven at 110°C for 12 h followed by activation at 450°C for 2 h before reuse in next reaction cycle under similar reaction conditions as earlier.

3. Results and Discussion

3.1. Characterization. Elemental analysis of fly ash and all three catalysts (KF/fly ash, KF/Al_2O_3/fly ash and KF/Al_2O_3) was done by EDX, the results are summarized in Table 1. With increasing the pretreatment temperature, the contents of K and F increased to a small extent by pretreatment at 673 K and decreased by pretreatment at 873 K for all three samples.

The FTIR spectrum of fly ash Figure 1 shows a peak at 3600 cm^{-1}, which indicates the presence of surface –OH groups, –Si-OH and absorbed water molecules on the surface. The spectra also shows a broad range of bands from 1055 cm^{-1} to 1100 cm^{-1} which is attributed to modes of Si-O-Si asymmetric band stretching vibrations. The low frequency modes at 794 cm^{-1} are due to the symmetric Si-O-Si stretching vibrations. The FTIR spectrum of KF/Al_2O_3/fly ash catalyst calcined at different temperatures (43 K, 673 K, and 873 K) shown in Figures 1(d), 1(e) and 1(f). The FTIR spectrum of KF/Al_2O_3/fly ash^{673} catalyst, shown in Figure 1(e) has a strong band at about 3500 cm^{-1},which indicates the presence of –OH groups on the surface of KF/Al_2O_3/fly ash^{673} catalyst. Thus result shows that hydroxyl groups can be the active sites when KF is supported on fly ash [27]. The intensity of the –OH peak increases with increasing temperature from 473 K to 673 K, assigned due to increase in KF content. Upon investigating the nature of the catalyst via infrared spectroscopic studies of the catalyst surface, it became apparent that fluoride ion has little or no direct role in the enhanced reactivity of KF/Al_2O_3/fly ash catalyst. The reaction between aqueous KF and alumina results in the formation of potassium hexafluoroaluminate and a strongly basic surface consisting of potassium aluminates and potassium hydroxide [28]. The later agents are responsible for both the increased base activity and the variable activity, a consequence of carbonate formation. A peak is present at 1650 cm^{-1} in the spectra of the samples, which is attributed to bending mode (δ_{O-H}) of water molecule [5]. An intense band at 570 cm^{-1} is also observed which is due to the presence of substantial amount of hexafluoroaluminate ion. In addition to features due to alumina and water, bands at 1519 cm^{-1} and 1381 cm^{-1} indicate that both bidentate and monodentate type carbonate species exist on the surface of KF/Al2O3/fly ash^{673} catalyst [5, 29], which seems to be generated due to reaction of atmospheric CO2 with KOH during drying of the catalyst.

X-ray diffraction pattern of raw fly ash is shown in Figure 2(a). Structural changes caused by pretreatment at different temperatures were studied by XRD for KF/Al_2O_3/fly ash^{473}, KF/Al_2O_3/fly ash^{673}, and KF/Al_2O_3/fly ash^{873} catalysts illustrated in Figures 2(b), 2(c) and 2(d). These patterns confirmed that deposition of the alkaline fluoride followed by the thermal treatment led to the formation of K_3AlF_6 by the reaction between KF and Al_2O_3 which is observed at 2 theta = 33°, 38°, and 63°. The intensity of the peaks assigned to this species is in agreement with the loadings of the alkaline fluoride [30].

SEM micrograph of raw fly ash Figure 3(a) shows the presence of hollow cenospheres, irregularly shaped unburned carbon particles, mineral aggregates and agglomerated particles, while the typical SEM images of the fly ash supported KF catalyst in Figure 3(b) show dense particles with distribution of varying particle size. TEM images of raw fly ash Figure 4(a) show smooth spherical particles, while TEM image of KF/Al_2O_3/fly ash^{673} catalyst Figure 4(b) shows KF loaded spheres.

3.2. Basic Sites on KF/Al_2O_3/Fly Ash Catalyst. There are several controversies on possibilities of formation of basic sites on KF/Al_2O_3 catalytic system, yet all the previous investigations [27] evidently reported the formation of K_3AlF_6 by the reaction of aqueous KF and alumina (1). Most of the studies were of the opinion that F^- ion has no direct role in the catalytic activity of KF/Al_2O_3. The formation of carbonate on the catalyst surface is responsible for high reactivity of KF/Al_2O_3 [28]. The carbonate was supposed to be formed by the reaction of CO_2 and produced KOH (2) during the drying procedure:

$$4KOH + 2CO_2 \longrightarrow 2K_2CO_3 + 2H_2O \quad (2)$$

Duke et al. has reported the formation of K_2CO_3 by the following successive reactions:

$$12KF + Al_2O_3 \longrightarrow 2K_3AlF_6 + K_2O \quad (3)$$

$$3K_2O + 3CO_2 \longrightarrow 3K_2CO_3 \quad (4)$$

where K_2O is formed as the alumina lattice is destroyed. However in preparation of the KF/Al_2O_3/fly ash catalyst in

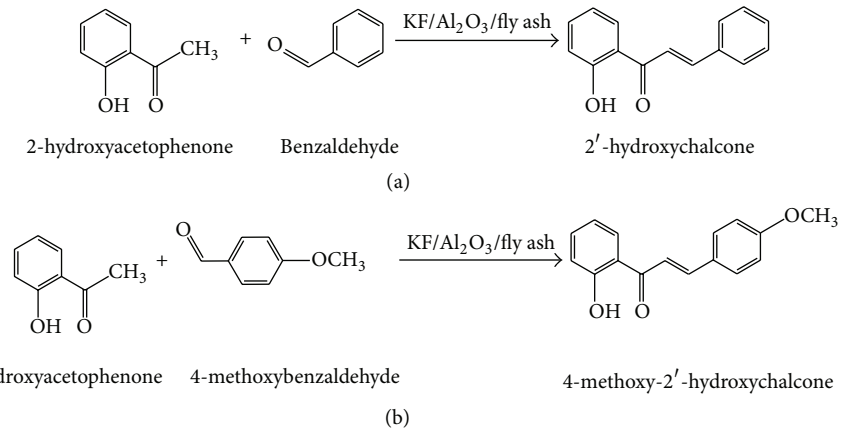

Scheme 1: Claisen-Schmidt condensation of (a) benzaldehyde and (b) 4-methoxybenzaldehyde with 2-hydroxyacetophenone over fly ash supported solid base catalysts.

Table 1: EDX analysis of prepared catalysts at different pre-treatment temperatures.

Catalyst	Pre-treatment temperature (K)	K (at.%)	F (at.%)	Al (at.%)	O (at.%)
Fly ash	NIL	0.09	NIL	4.10	50.2
Al_2O_3/fly ash	673 K	0.09	NIL	9.2	57.6
KF/fly ash	473 K	2.3	1.7	4.7	56.7
	673 K	2.7	1.8	4.8	56.9
	873 K	2.2	1.3	4.8	56.8
KF/Al_2O_3/fly ash	473 K	8.5	11.3	9.2	52.4
	673 K	9.1	12.1	9.4	51.9
	873 K	8.1	11.7	9.3	52.0
KF/Al_2O_3	473 K	20.8	19.6	12.7	46.9
	673 K	22.1	20.8	12.9	44.2
	873 K	18.8	17.7	17.2	46.3

[at.%: atomic percentage].

aqueous medium (2) seems to be more significant than (3) and (4).

In KF/Al_2O_3/fly ash catalyst, the formation of K_3AlF_6 is confirmed by XRD, while hydroxyl groups and carbonate ion are confirmed by intense peaks at 3500 $cm^{-1}$and 1550 cm^{-1} in FTIR spectrum Figure 1. Interestingly, the pretreatment temperature has significantly affected the catalytic activity of the system as reported previously for KF/Al_2O_3 catalyst. Both K_3AlF_6 and carbonate peaks are observed on increasing the pretreatment temperature from 473 K to 873 K as evident from Figure 1, whereas the catalytic activity of KF/Al_2O_3/fly ash catalyst was almost diminished at higher temperature 873 K Figure 5(a). These results have ruled out the possibility of carbonate or K_3AlF_6 being responsible for generating the active basic sites on the catalyst surface. KOH, an active base produced during reaction between KF and alumina generates hydroxyl groups on the catalyst surface, which become active basic sites for condensation reactions. At 873 K, surface hydroxyl groups are significantly decreased, resulting in decrease of active basic sites; thus catalytic activity of KF/Al_2O_3/fly ash catalyst was almost completely lost. Similar explanations on the surface properties of KF/Al_2O_3 system have been given in the literature [5] where the catalytic activity of KF/ Al_2O_3 was completely lost.

3.3. Catalytic Performance. The catalytic activity of KF/Al_2O_3/fly ash depends very much on drying condition of alumina after loading KF by impregnation. In this work we examined the dependence of catalytic activity for condensation on the heating temperature of the catalyst.

3.3.1. Effect of Pretreatment Temperature. The catalytic activity strongly depends on the evacuation temperature and reached around a maximum temperature of 673 K Figure 5(a). All catalysts showed significant activity for condensation reactions, whereas pure fly ash and chemically activated fly ash (Al_2O_3/fly ash) did not show any activity. Among remaining catalysts, the KF/Al_2O_3/fly ash^{673} showed

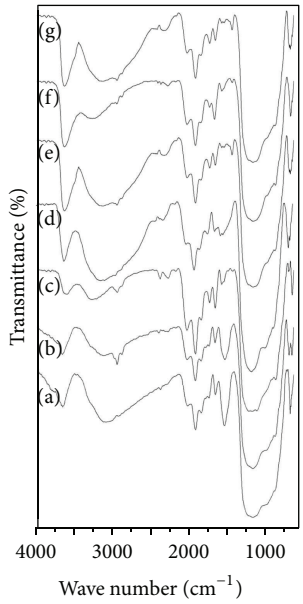

Figure 1: FTIR of (a) raw fly ash, (b) thermally activated fly ash, (c) KF/fly ash catalyst, (d) KF/Al_2O_3/fly ash^{873} catalyst, (e) KF/Al_2O_3/fly ash^{673} vatalyst, (f) KF/Al_2O_3/fly ash^{473} catalyst, and (g) regenerated KF/Al_2O_3/fly ash^{673} catalyst.

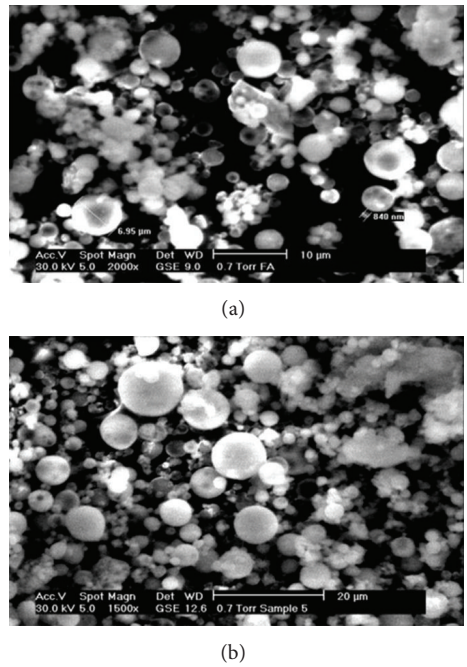

(a)

(b)

Figure 3: SEM micrograph of (a) Raw fly ash and (b) KF/Al_2O_3/fly ash^{673} catalyst.

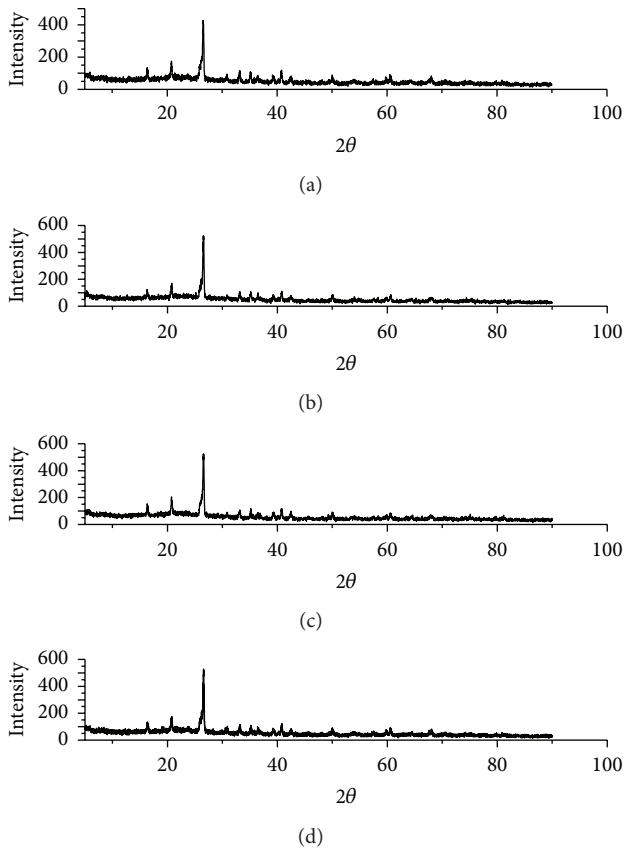

Figure 2: X-ray diffraction pattern of (a) raw fly ash (b) KF/Al_2O_3/fly ash^{473} catalyst (c) KF/Al_2O_3/fly ash^{873} and (d) KF/Al_2O_3/fly ash^{673} catalyst.

higher catalytic activity giving maximum conversion of benzaldehyde (83%) and 4-methoxybenzaldehyde (89%). For KF/Al_2O_3/fly ash^{473} and KF/Al_2O_3/fly ash^{873}, conversions of benzaldehyde and 4-methoxybenzaldehyde are comparatively low as shown in Figure 5(a). The activity of KF/Al_2O_3/fly ash catalyst appeared when the sample was pretreated at 473 K and reached its maximum at the temperature of 673 K. As the pretreatment temperature was raised higher than 673 K, the activity decreased sharply and finally disappeared at the temperature of 873 K. It is well reported that a high temperature treatment reveals active sites on catalyst either by removal of CO_2 and H_2O remaining on the surface in various forms or by formation of specific surface structure. The active sites are covered with H2O and/or CO2 when pretreated below 673 K [7].

In the light of the above inferences, the reaction conditions such as reaction temperature, reaction time, molar ratio of reactants and substrate to catalyst ratio for condensation of benzaldehyde and 4-methoxybenzaldehyde with 2′-hydroxyacetophenone were optimized using only KF/Al_2O_3/fly ash^{673} catalyst.

3.3.2. Effect of Temperature. The reaction for condensation of benzaldehyde and 4-methoxybenzaldehyde is carried out at temperatures ranging from 40°C to 140°C for 4 h. The effect of temperature on the condensation activity of KF/Al_2O_3/fly ash^{673} and kinetics is shown in Figure 5(b). It can be seen that at 80°C the conversion of benzaldehyde is 68% and increases to 83% at 120°C for a reaction time of 4 h, which remains constant till 140°C. Similarly, conversion of 4-methoxy benzaldehyde is maximum 89% at 140°C.

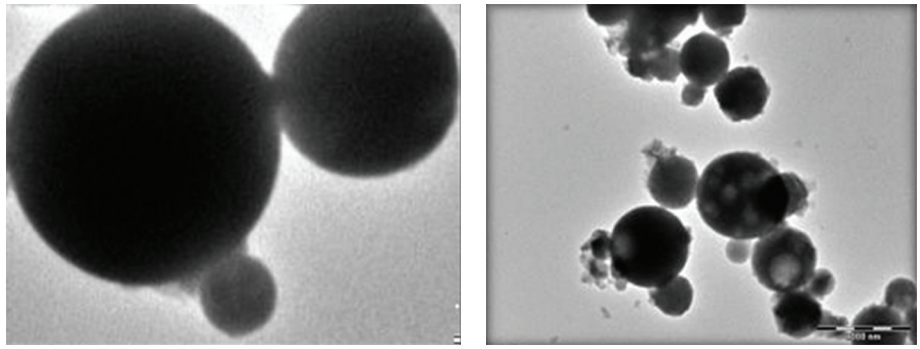

(a) (b)

Figure 4: TEM image of (a) Raw fly ash and (b) KF/Al_2O_3/fly ash^{673} catalyst.

3.3.3. Effect of Reaction Time. The optimum reaction time required, achieving maximum conversion of benzaldehyde and 4-methoxybenzaldehyde is carried out at 40 and 140°C for different time intervals from 30 min to 8 h. The conversion of benzaldehyde and 4-methoxybenzaldehyde gradually increases with time giving 83% and 89% after 4 h respectively as given in Figure 5(c) which remains constant till 8 h.

3.3.4. Effect of Molar Ratio (Substrate/2′-hydroxyacetophenone). The effect of the molar ratio of benzaldehyde to 2′-hydroxyacetophenone and 4-methoxybenzaldehyde to 2′-hydroxyacetophenone on conversion and yield of products is also studied at a reaction temperature of 120°C and 140°C and reaction time 4 h. At the molar ratio of 1 : 1, maximum conversion of benzaldehyde and 4-methoxybenzaldehyde with yield of their respective products was obtained (Figure 5(e)). With increasing the molar ratio, the conversion was observed to be decreased, which can be attributed to formation of benzoic acid as side product.

3.4. Comparison of Catalytic Activity of KF/Al_2O_3/Fly Ash with the Literature Data. The reaction between 2′-hydroxyacetophenone and benzaldehyde has been carried out over different catalysts as reported in the literature. The results obtained from the reported catalysts showed that when zeolite NaX and a sepiolite partially exchanged with Cs were used as catalysts, their activity was very low [31]. It is because of the fact that H atoms present in the methyl group of acetophenone has high pKa value (15.8) and it has been demonstrated previously that the basic sites of exchanged CsNaX and Cs sepiolite catalysts can only abstract proton with pKa = 10.7 and 13.3 respectively [31]. So it is evident from the above results that a catalyst with strong basic sites should be used to get the high conversion value. It is also reported when an excess of Cs is exchanged with zeolite, it can give completely high conversion, but the catalyst have to be use in the inert atmosphere, in order to avoid the formation of carbonates [32]. Mg-Al hydrotalcite derived catalyst has also been used in this reaction and a conversion of 78% was obtained [33]. The presence of water also affects the conversion value. Similarly reaction between 4-methoxybenzaldehyde and 2′-hydroxyacetophenone in the presence of MeOH/KOH at room temperature gives 65 % yield of 4-methoxy-2′-hydroxychalcone in 24 h [34].

In order to find the optimum for the studied reactions, we have synthesized highly basic KF/Al_2O_3/fly ash catalyst and it is found that with this catalyst the conversion value (83%) of benzaldehyde and (89%) of 4-methoxybenzaldehyde was increased. The prepared catalyst is also reused for up to three reaction cycles. The regenerated catalyst showed similar catalytic activity till 3rd reaction cycle giving approximately similar conversion of benzaldehyde (81%) and 4-methoxybenzaldehyde (86%), which indicates that the sites are not deactivated in the regenerated catalyst as confirmed by FTIR of regenerated catalyst (Figure 1(g)).

3.5. Characterization of Products. NMR of 2′-hydroxychalcone: H^1-NMR (200 MHz, CDCl3), δ ppm: 12.78 (s, 1H, 2′-OH), 7.91–7.96 (d, 1H, J = 7.6 Hz, and 1.8 Hz, H6′) 7.91–7.96 (dd, 1H, J = 14.4 Hz, H_β), 7.35–7.70 (m, 7H, H_α, H4′, H2, H3, H4, H5, and H6) and 7.02–7.09 (m, 2H, H3′, and H5′). NMR of 4-methoxy-2′-hydroxychalcone: H^1-NMR (200 MHz, $CDCl_3$), δ ppm: 12.95 (s, 1H, 2′-OH), 7.88–7.96 (d, 1H, J = 15.2 Hz, H_β), 7.87–7.91 (d, 1H, J = 7.4 Hz, H6′) 7.59–7.66 (d, 1H, J = 15.2 Hz, H_α) 7.62–7.66 (d, 2H, J = 8.8 Hz, H2 and H6) 7.45–7.49 (t, 1H, J = 8.8 Hz, and 7.6 Hz, H4′) 6.90–7.05 (m, 4H, H3, H5, H3′ and 5′ h) and 3.87 (s, 3H, OCH_3).

4. Conclusion

The study provides KF/Al_2O_3/fly ash as an efficient solid base catalyst possessing significant amount of basicity. The chemical activation of fly ash by alumina results in increased amorphous alumina content and thus surface hydroxyl contents produced due to the reaction of KF and alumina on fly ash support. Among all catalysts, KF/Al_2O_3/fly ash catalyst shows high catalytic activity towards condensation reaction. The experimental results indicate that the basicity of supported KF can be significantly increased by a proper choice of support. In KF/Al_2O_3/fly ash catalysts, KF reacts with alumina of fly ash and forms potassium hexafluoroaluminate

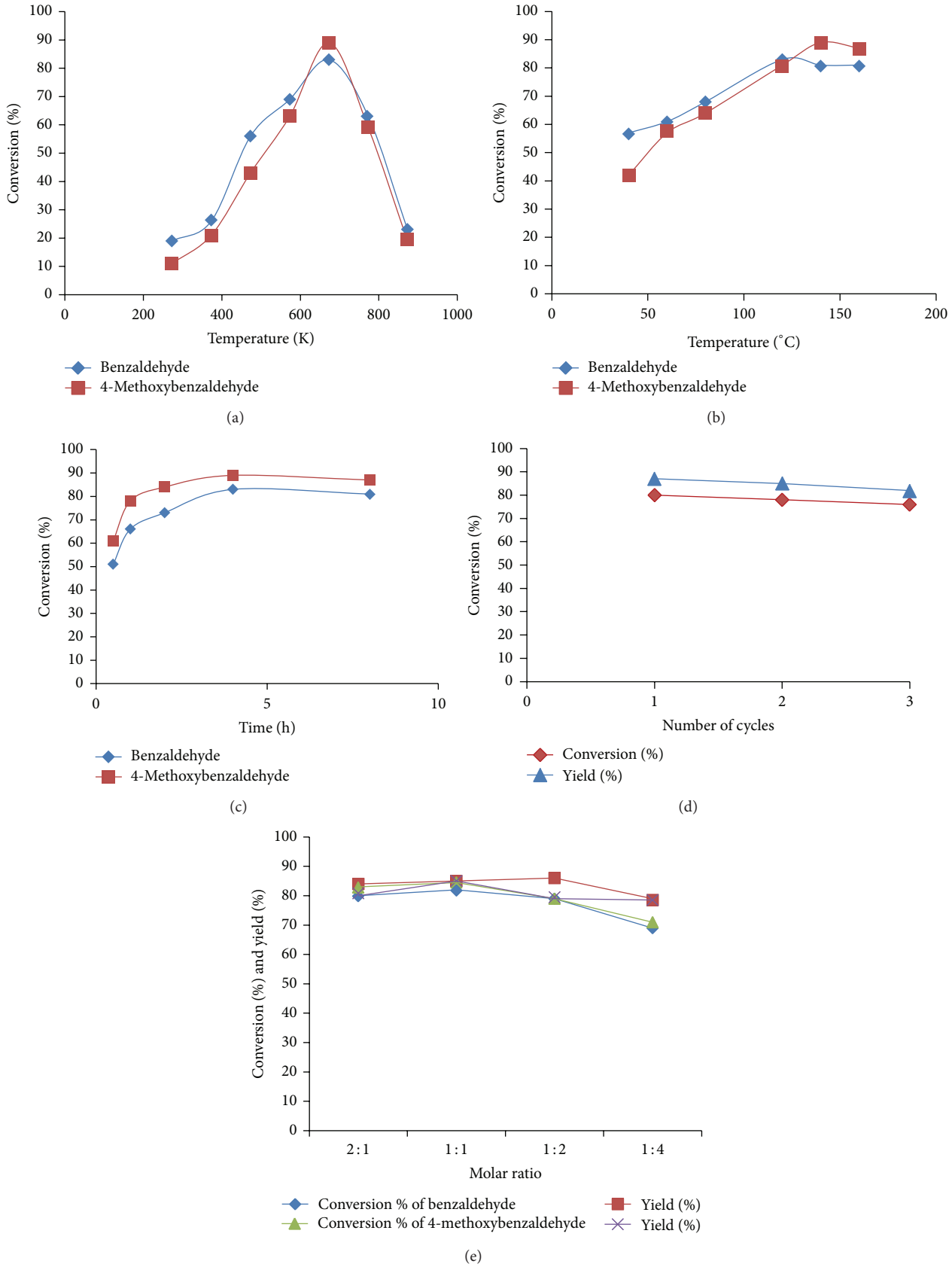

FIGURE 5: Conversion (%) of benzaldehyde and 4-methoxybenzaldehyde with KF/Al_2O_3/fly ash catalyst at (a) different pretreatment temperature (b) different reaction temperature (c) different time (d) different reaction cycles and (e) different molar ratios of benzaldehyde and 4-methoxybenzaldehyde.

and hydroxide, as the major phase which increases with increase in calcination temperature from 473 K to 673 K, responsible for enhancement of reactivity of catalyst. Along with these species, bidentate carbonate species exist on the surface of KF/Al_2O_3/fly ash^{673} catalyst which is formed by the formation of K_2CO_3. The KF/Al_2O_3/fly ash catalysts were found active for condensation of benzaldehyde and 4-methoxybenzaldehyde with 2′-hydroxyacetophenone, in which KF/Al_2O_3/fly ash pretreated at 673 K gave higher conversion of benzaldehyde (87%) with 91% yield of 2′-hydroxychalcone and 4-methoxybenzaldehyde (93%) with 93% yield of 4-methoxy-2′-hydroxychalcone. Experimental results also indicate that the basicity generated over only KF/fly ash catalyst was not sufficient to get higher yield of condensation products, but when fly ash was chemically activated by loading alumina through precipitation using aluminium nitrate as precursor, KF/Al_2O_3/fly ash catalyst has shown increased catalytic activity for the same reaction. The conversion (83% and 89%) of benzaldehyde and 4-methoxybenzaldehyde in KF/Al_2O_3/fly ash catalytic system was comparable to the only KF/Al_2O_3 system (conversion 61% and 59%) however, the cost of the KF/Al_2O_3/fly ash is lower than the KF/Al_2O_3, due to the replacement of α-alumina support by alumina/fly ash support. Fly ash already has 17 wt% alumina and by chemically activating it with aluminium nitrate, the alumina content was increased up to 37 wt%, which is found to be responsible for generating sufficient basic sites to catalyze the Claisen-Schmidt condensation. This catalyst may further be explored for several other organic transformations.

Recycling experiments showed that the catalyst is very stable up to three cycles. A composite material which can combine the advantages of fly ash, alumina and KF can expand the catalytic capabilities of the material especially in applications as strong base catalysts for industrially important reactions.

Conflict of Interests

The prepared KF/Al_2O_3/fly ash catalyst is novel and cost effective. The cost of the KF/Al_2O_3/fly ash is lower than the commercially available KF/Al_2O_3, due to the replacement α-alumina support by alumina/fly ash support. Fly ash already has 17 wt% alumina and by chemically activating it with aluminium nitrate (cheaper than pure alumina), the alumina content was increased up to 37 wt%, which is found to be responsible for generating sufficient basic sites to catalyze the Claisen-Schmidt condensation. So the prepared catalyst may further be used for several other organic transformations in cost effective way. We have used the α-alumina for comparing the catalytic activity of the prepared catalyst. There is no direct relationship with the commercial identity Chem Ltd.

Acknowledgments

XRD and TGA support was provided by Dharmsinh Desai University, Nadiad, Gujarat and TEM was performed at UGC-DAE Consortium for Scientific Research, Indore. Fly ash Mission, Department of Science and Technology, New Delhi, India provided the financial support through research Project no. FAU/DST/600(23)/2009-10 sanctioned to the corresponding author.

References

[1] N. Ohtani, Y. Inoue, A. Nomoto, and S. Ohta, "Polystyrene-supported ammonium fluoride as a catalyst for several base-catalyzed reactions," *Reactive Polymers*, vol. 24, no. 1, pp. 73–78, 1994.

[2] L. M. Weinstock, J. M. Stevenson, S. A. Tomellin et al., "Characterization of the actual catalytic agent in potassium fluoride on activated alumina systems," *Tetrahedron Letters*, vol. 27, no. 33, pp. 3845–3848, 1986.

[3] C. V. A. Duke, J. M. Miller, J. H. Clark, and A. P. Kybett, "A comparison of the adsorption of KF and NH4F onto silica gel," *Spectrochimica Acta A*, vol. 46, no. 9, pp. 1381–1389, 1990.

[4] H. Kabashima, H. Tsuji, T. Shibuya, and H. Hattori, "Michael addition of nitromethane to α,β-unsaturated carbonyl compounds over solid base catalysts," *Journal of Molecular Catalysis A*, vol. 155, no. 1-2, pp. 23–29, 2000.

[5] H. Handa, T. Baba, H. Sugisawa, and Y. Ono, "Highly efficient self-condensation of benzaldehyde to benzyl benzoate over KF-loaded alumina," *Journal of Molecular Catalysis A*, vol. 134, no. 1–3, pp. 171–177, 1998.

[6] M. Verziu, M. Florea, S. Simon et al., "Transesterification of vegetable oils on basic large mesoporous alumina supported alkaline fluorides-Evidences of the nature of the active site and catalytic performances," *Journal of Catalysis*, vol. 263, no. 1, pp. 56–66, 2009.

[7] K. Tanabe, M. Misono, Y. Ono, and H. Hattori, *New Solid Acids and Base*, Kodansha-Elsevier, Tokyo, Japan, 1989.

[8] H. Hattori, "Solid base catalysts: generation of basic sites and application to organic synthesis," *Applied Catalysis A*, vol. 222, no. 1-2, pp. 247–259, 2001.

[9] T. Baba, A. Kato, H. Takahashi et al., "Metathesis of silylalkynes and cross-metathesis of silylalkyne and 1-alkyne over solid-base catalysts," *Journal of Catalysis*, vol. 176, no. 2, pp. 488–494, 1998.

[10] H. Kabashima, H. Tsuji, S. Nakata, Y. Tanaka, and H. Hattori, "Activity for base-catalyzed reactions and characterizationof alumina-supported KF catalysts," *Applied Catalysis A*, vol. 194-195, pp. 227–240, 2000.

[11] S. J. Won, C. T. Liu, L. T. Tsao et al., "Synthetic chalcones as potential anti-inflammatory and cancer chemopreventive agents," *European Journal of Medicinal Chemistry*, vol. 40, no. 1, pp. 103–112, 2005.

[12] S. Alam and S. Mostahar, "Studies of antimicrobial activity of two synthetic 2′,4′,6′-trioxygenated flavones," *Journal of Applied Sciences*, vol. 5, no. 2, pp. 327–333, 2005.

[13] J. B. Daskiewicz, F. Depeint, L. Viornery et al., "Effects of flavonoids on cell proliferation and caspase activation in a human colonic cell line HT29: an SAR study," *Journal of Medicinal Chemistry*, vol. 48, no. 8, pp. 2790–2804, 2005.

[14] S. Abello, D. V. Shankar, and J. P. Ramırez, "Stability, reutilization, and scalability of activated hydrotalcites in aldol condensation," *Applied Catalysis A*, vol. 342, no. 1-2, pp. 119–125, 2008.

[15] A. Dhakshinamoorthy, M. Alvaro, and H. Garcia, "Claisen-schmidt condensation catalyzed by metal-organic frameworks,"

Advanced Synthesis and Catalysis, vol. 352, no. 4, pp. 711–717, 2010.

[16] A. Corma and S. Iborra, "Optimization of alkaline earth metal oxide and hydroxide catalysts for base-catalyzed reactions," *Advances in Catalysis*, vol. 49, pp. 239–302, 2006.

[17] B. M. Choudary, K. V. S. Ranganath, J. Yadav, and M. Lakshmi Kantam, "Synthesis of flavanones using nanocrystalline MgO," *Tetrahedron Letters*, vol. 46, no. 8, pp. 1369–1371, 2005.

[18] M. J. Climent, A. Corma, S. Iborra, K. Epping, and A. Velty, "Increasing the basicity and catalytic activity of hydrotalcites by different synthesis procedures," *Journal of Catalysis*, vol. 225, no. 2, pp. 316–326, 2004.

[19] D. J. Macquarrie, R. Nazih, and S. Sebti, "Kf/natural phosphate as an efficient catalyst for synthesis of 2′-hydroxychalcones and flavanones," *Green Chemistry*, vol. 4, no. 1, pp. 56–59, 2002.

[20] C. Khatri, D. Jain, and A. Rani, "Fly ash-supported cerium triflate as an active recyclable solid acid catalyst for Friedel-Crafts acylation reaction," *Fuel*, vol. 89, no. 12, pp. 3853–3859, 2010.

[21] C. Khatri, M. K. Mishra, and A. Rani, "Synthesis and characterization of fly ash supported sulfated zirconia catalyst for benzylation reactions," *Fuel Processing Technology*, vol. 91, no. 10, pp. 1288–1295, 2010.

[22] C. Khatri and A. Rani, "Synthesis of a nano-crystalline solid acid catalyst from fly ash and its catalytic performance," *Fuel*, vol. 87, no. 13-14, pp. 2886–2892, 2008.

[23] C. Khatri, D. Jain, and A. Rani, "Fly ash-supported cerium triflate as an active recyclable solid acid catalyst for Friedel-Crafts acylation reaction," *Fuel*, vol. 89, no. 12, pp. 3853–3859, 2010.

[24] D. Jain, C. Khatri, and A. Rani, "Synthesis and characterization of novel solid base catalyst from fly ash," *Fuel*, vol. 90, no. 6, pp. 2083–2088, 2011.

[25] D. Jain, C. Khatri, and A. Rani, "MgO enriched coal fly ash as highly active heterogeneous base catalyst for Claisen-Schmidt condensation reaction," *Journal of the American Chemical Society*, vol. 1, no. 2, pp. 37–49, 2011.

[26] D. Jain, M. Mishra, and A. Rani, "Synthesis and characterization of novel aminopropylated fly ash catalyst and its beneficial application in base catalyzed Knoevenagel condensation reaction," *Fuel Processing Technology*, vol. 95, pp. 119–126, 2012.

[27] J. M. Clacens, D. Genuit, L. Delmotte et al., "Effect of the support on the basic and catalytic properties of KF," *Journal of Catalysis*, vol. 221, no. 2, pp. 483–490, 2004.

[28] L. M. Weinstock, J. M. Stevenson, S. A. Tomellin et al., "Characterization of the actual catalytic agent in potassium fluoride on activated alumina systems," *Tetrahedron Letters*, vol. 27, no. 33, pp. 3845–3848, 1986.

[29] C. V. A. Duke and J. M. Miuer, "19F mas NMR and FTIR analysis of the adsorption of alkali metal fluorides onto alumina," *Journal of Molecular Catalysis*, vol. 62, no. 2, pp. 233–242, 1990.

[30] M. Verziu, M. Florea, S. Simon et al., "Transesterification of vegetable oils on basic large mesoporous alumina supported alkaline fluorides-Evidences of the nature of the active site and catalytic performances," *Journal of Catalysis*, vol. 263, no. 1, pp. 56–66, 2009.

[31] A. Corma, V. Fornes, R. M. Martin-Aranda, H. Garcia, and J. Primo, "Zeolites as base catalysts: condensation of aldehydes with derivatives of malonic esters," *Applied Catalysis*, vol. 59, no. 1, pp. 237–248, 1990.

[32] M. Larpess, A. Camboda, D. Bronel, J. Rodriguesz, and P. Geneste, "Characterization of basicity in alkaline cesium-exchanged X zeolites post-synthetically modified by impregnation: a TPD study using carbon dioxide as a probe molecule," *Microporous Materials*, vol. 1, no. 5, pp. 343–351, 1993.

[33] M. J. Climent, A. Corma, S. Iborra, and J. Primo, "Base catalysis for fine chemicals production: claisen-schmidt condensation on zeolites and hydrotalcites for the production of chalcones and flavanones of pharmaceutical interest," *Journal of Catalysis*, vol. 151, no. 1, pp. 60–66, 1995.

[34] T. D. Tran, H. Park, G. F. Ecker, and K. M. Thai, "2′-hydroxychalcone analogues: synthesis and structure-PGE2 inhibitory activity relationship," in *Proceedings of the 12th International Electronic Conference on Synthetic Organic Chemistry (ECSOC '08)*, November 2008.

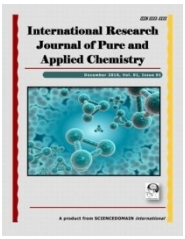

International Research Journal of Pure & Applied Chemistry
3(4): 299-307, 2013

SCIENCEDOMAIN *international*
www.sciencedomain.org

Surface Modification of Fly Ash by Thermal Activation: A DR/FTIR Study

Stuti Katara[1], Sakshi Kabra[1], Anita Sharma[1], Renu Hada[1] and Ashu Rani[1*]

[1]Department of Pure and Applied Chemistry, University of Kota, Kota, Rajasthan, India.

Authors' contributions

This work was carried out in collaboration between all authors. Authors SK and AR supervised and designed the study. Author SK (Stuti Katara) performed the experimental and analytical study, wrote the protocol, and wrote the first draft of the manuscript. Authors SK, AS and RH managed the literature searches and helped in analytical study. All authors read and approved the final manuscript.

Research Article

Received 31st March 2013
Accepted 12th July 2013
Published 24th July 2013

ABSTRACT

To acquire a deeper understanding of surface chemistry of fly ash along with thermal activation, the states of mineral phases, water and –OH groups on silica are studied in fly ash at different calcination temperatures by DR/FTIR spectroscopic technique. DR/FTIR spectroscopy allows differentiation of various types of bonds in a material on a molecular level. The spectroscopic results are also supported by XRF, XRD and SEM analysis. Studied fly ash was collected from Jamshedpur Thermal Power Station as an extremely fine ash, formed from the inorganic components of the coal, mainly silica and alumina which remain after combustion of the carbonaceous part of the coal. Distinguish changes were observed in fly ash IR bands regarding absorbed water, -OH group and Si-O-Si group with thermal activation. This investigation reveals that as the temperature increases, the physically adsorbed water begins to remove first, then silanol groups on surface is dehydrated. Increased temperature causes formation of different crystalline phases like quartz, mullite and hematite etc. and increased the crystallinity of the calcined samples.

**Corresponding author: Email: ashu.uok@gmail.com;*

Keywords: DR/FTIR; thermal activation; silanol groups; fly ash.

1. INTRODUCTION

The coal fired power plant which consumes pulverized solid fuels composed of combustible organic matter with varying amount of inorganic mineral parts produce large amount of solid waste fly ash. Every year a crude estimation of 600 million tons of fly ash generated worldwide [1] and about 110 million tons only in India [2]. The combustible gasification takes place in coal fired boiler at an operative temperature 1450ºC under reducing atmosphere. The mixture of effluent gases is cooled and fly ash gets solidify at temperature from 950ºC to 400ºC. In the form of spherical particles consisting of SiO_2 , Al_2O_3, Fe_2O_3, CaO, MgO and alkali in varying amounts with some unburned activated carbon [3]. As per the ASTM C618-12a guideline [4] the fly ash containing >70% SiO_2, Al_2O_3 and Fe_2O_3 is classified as Class F type fly ash and those consists mainly of silica, alumina and calcium containing SiO_2, Al_2O_3 and Fe_2O_3 minimum upto 50 % are referred to as Class C fly ash. Class F type fly ash is used in agriculture, metal recovery, water and atmospheric pollution control [5] while class C type fly ash is used in cement production [6], steam cured bricks manufacturing [7] etc. Calcination temperature of fly ash before using as source material for synthesis of concrete material and geopolymer etc. is reported to be crucial for the end product [8]. Fly ash has a complex microstructure comprising of mixture of amorphous and crystalline components. The chemical and mineralogical compositions of fly ash vary with coal source as well as calcination temperature [9]. Fly ash also contains different amount of unburned carbon which may reach upto 17% [10] responsible for high ignition loss and undesirable constituents for geopolymerisation and concrete formation. Fly ash is also being used as heterogeneous catalytic support material due to high silica, surface mineralogy, morphology and surface silanol groups [11, 12]. Both the adsorbed water and silanol groups on surface may affect the surface modification process thus play important roles in catalytic application on silica surface. It is difficult to distinguish between the adsorbed moisture and actual surface hydroxyl groups in a form of crystalline water or amorphous silanol (Si-OH) [13]. Literature reports that high temperature calcination forms new crystalline phases on fly ash surface modifying siloxane groups (Si-O-Si) and different forms of silanol groups [8]. Therefore it is of interest to understand the modification of fly ash mineralogy and morphology with thermal activation by using Diffuse Reflectance Fourier Transform Infrared (DR\FTIR) spectroscopic technique, which is one of the advance techniques to illustrate the chemical structure of the bonding materials. The results of the DR\FTIR study are supported by other characterization tools such as X-ray Fluorescence (XRF), X-ray Diffraction (XRD) and Scanning Electron Microscopy (SEM).

2. EXPERIMENTAL DETAILS

2.1 Materials

The coal fly ash (Class F type with SiO_2 and Al_2O_3 > 70%) used in this study was collected from Jamshedpur Thermal Power Station (Jamshedpur, Jharkhand, India). Fly ash (FA) was thermally activated by calcining in muffle furnace at 400, 600, 800 and 1000ºC for 3h and abbreviated as TFA-400, TFA-600, TFA-800 and TFA-1000 respectively (TFA –Thermally activated fly ash).

2.2 Sample Preparation and Characterization

DR/FTIR analysis of fly ash samples were carried out by diluting fly ash samples with KBr in 1:20 weight ratio and mixed gently with the help of mortar and pestle, being careful about atmospheric moisture absorption. In this study, FTIR spectra of the materials were recorded using FTIR Tensor 27 Brucker with DR (Diffuse Reflectance) accessory. The spectra were recorded in the range 550 – 4000 cm^{-1} with a resolution of 4 cm^{-1}. The chemical composition was determined by wavelength dispersive X-ray fluorescence (WD-XRF) model Bruker S8 Tiger. The detailed imaging information about the morphology and surface texture of the sample was provided by SEM (Philips XL30 ESEM TMP). The XRD measurements were carried out using Bruker D8 Advance X-ray diffractometer with monochromatic CuKα radiation (λ = 1.54056 Å) in a 2θ range of 5-70º.

3. RESULTS AND DISCUSSION

The chemical composition of FA and all TFA samples reveals that major components of fly ash are SiO_2 and Al_2O_3. Some minor components like Fe_2O_3, CaO, MgO, TiO_2, Na_2O, K_2O and trace elements around 1.5 wt% are also present in FA and all TFA samples (Table 1). The thermal activation of fly ash removes C, S, moisture and other adsorbed gases. The removal of moisture and co-existing unburned carbon increases with increasing temperature [14]. It can be concluded that all the compounds remained almost constant after thermal treatment, besides a reduction in Na_2O, K_2O and other elements in all TFA samples.

Table 1. Chemical composition of FA and all TFA samples

Sample	SiO_2 (wt%)	Al_2O_3 (wt%)	Fe_2O_3 (wt%)	CaO (wt%)	MgO (wt%)	TiO_2 (wt%)	Na_2O (wt%)	K_2O (wt%)	Other elements (wt%)
FA	62	30	3.0	0.4	0.3	1.4	0.4	0.8	1.7
TFA-400	62.3	30	3.2	0.4	0.3	1.4	0.3	0.5	1.6
TFA-600	62.5	30.1	3.2	0.3	0.3	1.4	0.3	0.3	1.6
TFA-800	62.8	30.3	3.2	0.3	0.2	1.3	0.2	0.2	1.5
TFA-1000	63	30.5	3.2	0.3	0.2	1.3	0.2	0.1	1.2

The FTIR spectra in Fig. 1 shows a broad band between 3400-3000 cm^{-1}, which is attributed to surface –OH groups of silanol groups (-Si-OH) and adsorbed water molecules on the surface. The broadness of band indicates the presence of strong hydrogen bonding [11]. The gradual decrement in the intensity and broadness in this band, as shown in Fig. 1 confirms loss of water in all TFA samples during thermal activation. Most of the molecular water gets removed from the sample by heating up to 250ºC, while crystalline –OH remains in the sample till 700ºC [15]. A peak around 1607 cm^{-1} (Fig. 1) is attributed to bending mode (δO-H) of water molecule [16] which is shown in all fly ash samples. A broad band ranging from 1070 cm^{-1} to 1170 cm^{-1} due to Si–O–Si asymmetric stretching vibrations [17] of silica is present in FA and all TFA samples. FA shows Si–O–Si asymmetric stretching vibration centered at 1100 cm^{-1} which get shifted towards higher wave number at 1162 cm^{-1} in case of TFA-1000. This high wave number shift is the result of loss of water thus transformation of Q^3 units [Si (OH) $(SiO_4)_3$] to Q^4 units [Si $(SiO_4)_4$] thus decrease in silanol groups (-Si-OH). This phenomenon shows reverse accordance with the statement that an increase in the hydroxide concentration shifts the position of the maximum absorbance of Si-O bands toward lower number, indicating the transformation of Q^4 units [Si $(SiO_4)_4$] to Q^3 units [Si(OH)

$(SiO_4)_3$] [18]. Peak at 2887 cm^{-1} could be assigned to C-H stretching vibration of organic contaminants which may be introduced during sample handling or some hydrocarbon present in fly ash [17.] This peak shows high intensity in FA while on thermal activation organic contaminants get removed from FA and show low intense peak in all TFA samples as compared to FA. Peaks appeared around 2343 cm^{-1} attributed to v O-H stretching [19], 2241 cm^{-1} responsible for H-SiO_3 [20], 1984 cm^{-1} due to =Si-H monohydride [21], 1872 cm^{-1} due to calcium carbonate [22] present in FA and all TFA samples (Table 2). Peaks centered at 1521 cm^{-1} [23] and 1681 cm^{-1} [17] are due to $(CO_3)^{2-}$ stretching vibration show highest intensity in FA, which is reduced on thermal activation in all TFA samples conferring that during thermal activation C and C associated impurities like CO_2 are removed with increased temperature. A peak related to Al-O-Si stretching vibration appears around 600 cm^{-1} [24] and is present in FA and all TFA samples (Table 2) conferring that Si and Al are present in silico aluminate phase not affected by thermal activation [25].

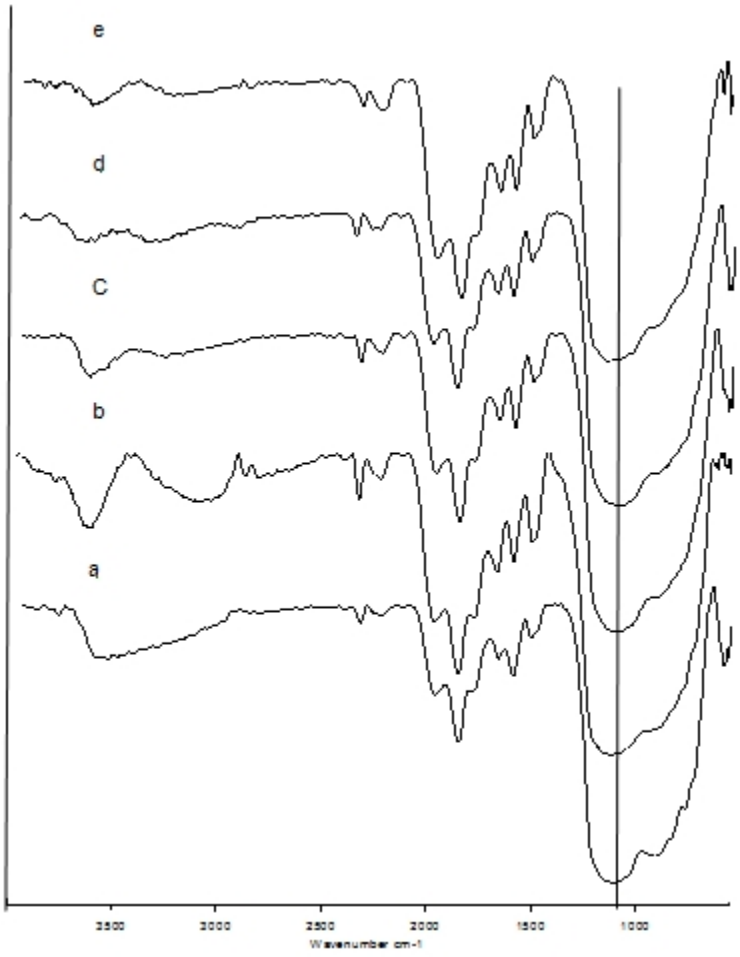

Fig. 1. DR/FTIR spectra of (a) FA (b) TFA-400 (c) TFA-600 (d) TFA-800 (e) TFA-1000

Table 2. Different DR/FTIR observed frequencies of (1.) FA (2.) TFA-400 (3.) TFA-600 (4.) TFA-800 (5.) TFA-1000 and their possible assignments

Assignments	FA	TFA-400	TFA-600	TFA-800	TFA-1000	Reference no.
Si-O-Al stretching vibration	600	611	589	592	603	24
Si-O-Si asymm. Stretching Vibration	1100	1102	1113	1148	1162	17
$(CO_3)^{2-}$ –stretching vibration	1521, 1679	1519, 1686	1519, 1680	1519, 1683	1521, 1681	23, 17
H-O-H bending Vibration	1608	1606	1606	1607	1607	16
Calcium Carbonate	1872	1872	1872	1872	1873	22
=Si-H (monohydride)	1984	1984	1986	1984	1987	21
H-SiO_3	2241	2240	2244	2236	2250	20
v -O-H stretching vibration	2343	2344	2341	2347	2345	19
-C–H stretching vibration	2827	2887	2886	2890	2895	17
-O-H stretching vibration	3553	3096	3276	3327	3260	11

The SEM image (Fig. 2) of FA demonstrates particles of different shapes and sizes, hollow cenospheres, irregularly shaped unburned carbon particles, miner aggregates and agglomerated particles whereas the typical SEM image of TFA-1000 shows different shape and size particles while irregular shaped unburned carbon is not seen. Some fused silica particles are showing which has been formed during thermal activation [11].

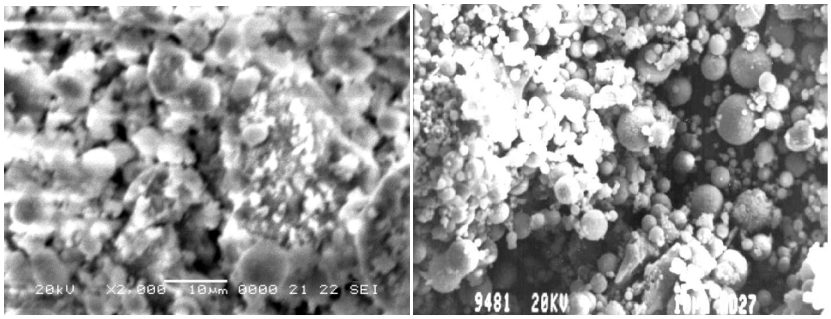

(a) **(b)**

Fig. 2. SEM images of (a) FA (b) TFA-1000

The XRD patterns of FA and TFA-1000 are shown in Fig. 3. In both FA and TFA-1000, peaks at 2θ values of 16.4º, 25.9º and 26.2º show presence of mullite (alumino-silicate)

phases and quartz (silica) exhibits strong peaks at 20.7º, 26.5º, 26.66º, 40.66º and 49.96º of 2θ values [26] while calcite shows peaks at 33.4º of 2θ values [11]. TFA-1000 shows number of crystalline phases like quartz, hematite, mullite, calcite in higher intensities than FA, due to high temperature calcination. With thermal activation magnetite peak tends to disappear while a peak responsible for hematite begins to appear (Table 3) [27].

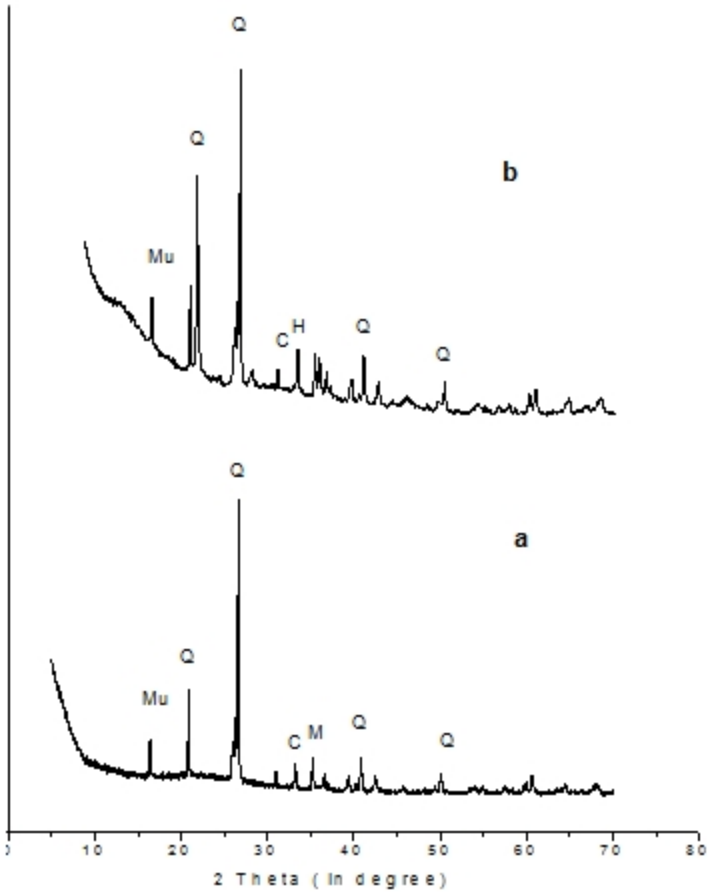

Fig. 3. XRD pattern of (a) FA (b) TFA-1000; (Q- Quartz, Mu- Mullite, M- Magnetite, H- Hematite, C- Calcite)

Table 3. Color and crystalline phases of FA and TFA samples

Sample	Color	Quartz	Magnetite	Hematite	Mullite	Calcite
FA	Grey	√	√	---	√	√
TFA-400	Light grey	√	√	---	√	√
TFA-600	Yellowish brown	√	√	---	√	√
TFA-800	Yellowish brown	√	---	√	√	---
TFA-1000	Reddish brown	√	---	√	√	---

(√ = Present, --- = Absent)

Variation of colors and crystalline phases of FA and TFA calcined at different temperatures is shown in Table 3. Initially fly ash was of grey color due to presence of unburned carbon content with increase in thermal activation temperature grey color of fly ash changes to yellowish brown and then finally red brown possibly due to hematite crystallization [8].

4. CONCLUSION

In each DR/FTIR spectrum broad band ranging from 3000-3400 cm^{-1} is showing a successive decrement in the intensity with increasing thermal activation temperature. It is thus revealed that as the temperature increases, physically adsorbed water is removed first, then silanol groups on surface is dehydrated resulting in transformation of Q^3 units [Si(OH) $(SiO_4)_3$] to Q^4 units [Si $(SiO_4)_4$]. Due to thermal activation of fly ash, SiO_2, Al_2O_3 are increased which is also evidenced by increased intensity of quartz and mullite phases, the magnetite phases are converted into hematite phase at higher temperature. It can be concluded that modification in properties of fly ash with reference to Si-OH, intensity and crystallinity of crystalline phases can be achieved by thermal activation method to generate a solid support material for catalytic applications.

ACKNOWLEDGEMENT

SEM and XRD characterizations were performed at UGC-DAE Consortium for Scientific Research, Indore. The authors are thankful to Dr. D.M. Phase and Er. V.K. Ahiray for SEM-EDX analysis and Dr. Mukul Gupta for XRD analysis. The authors are also thankful to SAIF, Punjab University for their XRF facility. Stuti katara is thankful to University Grants Commission, New Delhi, India for their financial support through Senior Research Fellowship scheme.

COMPETING INTERESTS

Authors have declared that no competing interests exist.

REFERENCES

1. Yao ZT, Xia MS, Ye Y, Zhang L. Synthesis of zeolite Li-ABW from fly ash by fusion method. J Hazard Mater. 2009;170(2):639-44. doi:10.1016/j.bbr.2011.03.031.
2. Senapati MR. Fly ash from thermal power plants - waste management and overview. Curr Sci. 2011;100(12).
3. Kutchko BG, Kim AG. Fly ash characterization by SEM–EDS. Fuel. 2006;85(17):2537-44. doi:10.1016/j.fuel.2006.05.016.
4. American Society for Testing and Materials (ASTM), ASTM C618 – 12a,"Standard specification for coal fly ash and raw or calcined natural pozzolan for use in concrete", Annual book of ASTM standards, Vol.04.02, Philadelphia, Pennsylvania,1994.
5. Blanco F, Garcia MP, Ayala J. The effect of mechanically and chemically activated fly ashes on mortar properties. Fuel. 2006;85(14):2018–26. doi:10.1016/j.fuel.2006.03.031.
6. Sahu S, Majling J. Preparation of sulphoaluminate belite cement from fly ash. Cem Concr Res. 1994;24(6):1065-72. doi:10.1016/0008-8846(94)90030-2.
7. Scheetz BE, Earle R. Utilization of fly ash. Curr Opin Solid State Mater Sci.1998;3(5):510-20. doi:10.1016/S1359-0286(98)80017-X.

8. Temuujin J, Riessen AV. Effect of fly ash preliminary calcination on the properties of geopolymer. J Hazard Mater. 2009;164:634–39. doi:10.1016/j.jhazmat.2008.08.065.
9. Van Jaarsveld JSG, Van Deventer JSJ, Lukey GC. The characterisation of source materials in fly ash-based geopolymers. Mater Lett. 2003;57(7):1272–80. doi: 10.1016/S0167-577X(02)00971-0.
10. Gray ML, Champagne KJ, Soong Y, Killmeyer RP, Maroto-Valer MM, Andresen JM et al. Physical cleaning of high carbon fly ash. Fuel Process Technol. 2002;76(1):11–21. doi:10.1016/S0378-3820(02)00006-1.
11. Khatri C, Rani A. Synthesis of a nano-crystalline solid acid catalyst from fly ash and its catalytic performance. Fuel. 2008;87(13):2886–92. doi:10.1016/j.fuel.2008.04.011.
12. Jain D, Rani A. MgO enriched coal fly ash as highly active heterogeneous base catalyst for Claisen-Schmidt condensation reaction. Am Chem Sci J. 2011;1(2):37-49.
13. Peng L, Qisui W, Xi L, Chaocan Z. Investigation of the states of water and OH groups on the surface of silica. Colloids and Surfaces A: Physicochem Eng Aspects. 2009;334:112–15. doi:10.1016/j.colsurfa.2008.10.028.
14. Kordatos K, Gavela S, Ntziouni A, Pistiolas KN, Kyritsi A, Rigopoulou VK. Synthesis of highly siliceous ZSM-5 zeolite using silica from rice husk ash. Micropor Mesopor Mater. 2008;115(1-2):189-96. doi:10.1016/S0167-577X(02)00971-0.
15. Richardson IG. The calcium silicate hydrates. Cem Concr Res. 2008;38:137–58.
16. Palomo A, Grutzeck MW, Blanco MT. Alkali-activated fly ashes a cement for the future. Cem Concr Res. 1999;29:1323-29.
17. Saikia BJ, Parthasarthy G, Sarmah NC, Baruah GD. Fourier-transform infrared spectroscopic characterization of naturally occurring glassy fulgurites. Bull Mater Sci. 2008;31(2):155–58.
18. Morten ES, Camilla S, Li Z, Sogaard EG. Xps and Ft-Ir Investigation of Silicate Polymers. J Mater Sci. 2009;44:2079–88. doi:10.1007/s10853-009-3270-9.
19. Zaki MI, Knozinger H, Tese B, Mekhemer GAH. Influence of phosphonation and phosphation on surface acid–base and morphological properties of CaO as investigated by in situ FTIR spectroscopy and electron microscopy. J colloid Interface Sci. 2006;303(1):9-17. doi: 10.1016/j.jcis.2006.07.011.
20. Sun XH, Wang SD, Wong NB, Ma DDD, Lee ST, Teo BK. FTIR spectroscopic studies of the stabilities and reactivities of hydrogen-terminated surfaces of silicon nanowires. Inorg Chem. 2003;42(7):2398-404. doi:10.1021/ic020723e.
21. Blanco F, Garcia MP, Ayala J. Variation in fly ash properties with milling and acid leaching. Fuel. 2005;84(1):89-96. doi:10.1016/j.fuel.2004.05.010.
22. Jacox EM. Vibrational and Electronic Energy Levels of Polyatomic Transient Molecules Supplement B. J Phys Chem Ref Data. 2003;32(1). doi: 10.1063/1.1497629.
23. Handa H, Baba T, Sugisawa H, Ono Y. Highly efficient self-condensation of benzaldehyde to benzyl benzoate over KF-loaded alumina. J Mol Catal A Chem. 1998;134(1):171-77. doi:10.1016/S1381-1169(98)00033-8.
24. Frances IH, Denisse VA, Meghan EG. High temperature aerogels in the Al_2O_3-SiO_2 system. Presented at the American chemical society 236th national meeting Philadelphia, Pa, August 20, 2008. Accessed 24 May 2013. Available: http://usrp.usra.edu/technicalPapers/glenn/arrandaAug08.pdf.
25. Temuujin J, Okada K, Kenneth JDM. Preparation and properties of potassium aluminosilicate prepared from the waste solution of selectively leached calcined kaolinite. Appl Clay Sci. 2002;21:125–31. doi:10.1016/S0169-1317(01)00082-5.
26. Sharma A, Srivastava K, Devra V, Rani A. Modification in Properties of Fly Ash through Mechanical and Chemical Activation. Am Chem Sci J. 2012;2(4):177-87.

27. Fox JM. Changes in fly ash with thermal treatment. Presented in 2005 World of Coal Ash (WOCA), April 11-15,2005, Lexington, Kentucky, USA. Accessed 24 May 2013. Available: http://www.flyash.info/2005/132fox.pdf.

Peer-review history:
The peer review history for this paper can be accessed here:
http://www.sciencedomain.org/review-history.php?iid=245&id=7&aid=1733

RESEARCH PAPER | Chemistry | Volume : 3 | Issue : 4 | April 2013 | ISSN - 2249-555X

Synthesis of Nanosized Titania by sol Gel Route

KEYWORDS: Titania; Sol gel; Ethylene glycol; Anatase

Renu Hada	Sakshi Kabra	Stuti Katara
Department of Pure and applied Chemistry, University of Kota, Kota (Raj), India	Department of Pure and applied Chemistry, University of Kota, Kota (Raj), India	Department of Pure and applied Chemistry, University of Kota, Kota (Raj), India

Ashu Rani	Vijay Devra	S. S. Amritphale
Department of Pure and applied Chemistry, University of Kota, Kota (Raj), India	Jankidevi Bajaj Government Girls College, Kota (Raj), India.	Advanced Materials & Processes Research Institute (CSIR), Hoshangabad Road, Bhopal (M.P), India.

ABSTRACT *The main objective of this work was to prepare anti-pollutant and photocatalyst Titanium dioxide nanoparticles by simple ethylene glycol route to synthesize titanium dioxide nanoparticles at industrial level. In this work TiO_2 was prepared by sol-gel route in presence of titanium n-butoxide (TNBT) as TiO_2 precursor, n-butanol as dilutant and EG as solvent and chelating agent. The X-ray diffraction and scanning electron microscopy studies show that the product has anatase crystal structure with average particle size 20-50 nm. The nanoparticles thus prepared can be used for gas sensing and biological applications, also as photo-electrodes for dye-sensitized solar cells and in removing the organic chemicals which occur as pollutants in wastewater effluents from industrial and domestic sources.*

Introduction

Nanosized titania has been the subject of a great deal of research because of their unique physicochemical properties and applications in the areas of pigments, catalysts and supports, cosmetics, gas sensors, inorganic membranes, environmental purification, and dielectric materials [1-9]. Much interest has been shown in photochemical reactions on nanosized titania particles due to their potential application in the conversion of solar energy into chemical energy [10-13] and electric energy [14, 15]. When titania powder is irradiated with photon energy larger than the band-gap energy, electrons (e^-) and holes (h^+) are generated in the conduction band and the valence band, respectively. These electrons and holes are thought to have the respective abilities to reduce and oxidize chemical species adsorbed on the surfaces of titania particles [16]. The uses and performance for a given application are, however, strongly influenced by the crystalline structure, the morphology, and the size of the particles. It is well known that titania exists in three kinds of crystal structures namely anatase, rutile and brookite. Anatase and brookite phases are thermodynamically metastable and can be transformed exothermally and irreversibly to the rutile phase at higher temperatures. The transition temperatures reported in the literature ranges from 450 to 1200 ^{0}C. The transformation temperature depends on the nature and structure of the precursor and the preparation conditions [17, 18]. Among the three kinds of crystal structures of Titania, anatase TiO^2 has been widely used as a well known catalyst, because of its various merits, such as electronic and optical properties, non-toxicity, high photocatalytic activity, low cost, and chemical stability [19-23]. A number of methods for the synthesis of TiO^2 nanoparticle have been reported, such as chemical precipitation [24], microemulsion [25], hydrothermal crystallization [26] and sol-gel [27]. The sol-gel process is the most successful for preparing nanosized metal oxide semiconductors. For example, sol-gel derived TiO^2 powders have been reported to show high catalytic activity due to their fine structure, wide surface area and high porosity. Thus in this research work we have prepared titania by sol gel route using ethylene glycol as gelling agent and titanium n-butoxide as titania precursor.

Experimental Work

Titanium (IV)-n-butoxide (TNBT) (20 g) was added to n-butanol (16 g) and the mixture was stirred for 5 min using a magnetic stirrer operating at 2000 rpm. After stirring, above mixture was added to Ethylene glycol (100 ml) and mixture was stirred with heating at 85 ^{0}C till sol converted to gel then gel was dried in oven at 50 ^{0}C. Dried sample was calcined at 500 ^{0}C for 3 h.

Results and discussion

The XRD pattern and SEM image of nanosized Titanium Oxide particles, prepared by EG route is shown in figure 1 and 2.

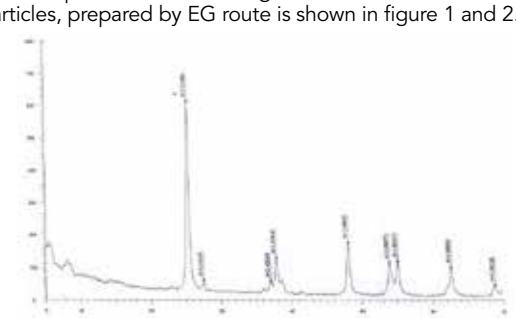

Figure 1. XRD patterns of nanosized titania obtained from sol gel route at 500 ^{0}C

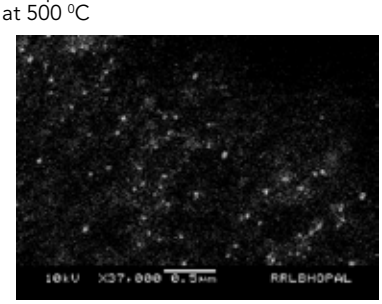

Figure 2. SEM photograph of nanosized titania obtained from sol gel route at 500 ^{0}C

Volume : 3 | Issue : 4 | April 2013 | ISSN - 2249-555X

The XRD patterns of the calcined sample of nanosized titania powder prepared using sol gel route is given in Figure 1. The presence of peaks of anatase titania at'd' values 3.49, 1.88, 2.35 have been observed in XRD pattern. The d-values of the pattern recorded were compared and matched with the standard d-values along with the intensity given in JCPDS manuals. The average crystalline size of nanosized titania has been calculated by applying Scherrer's equation ($d = k \lambda / \beta \cos \theta$) to the 100 % intensity peak and is found 19 nm. The prepared nanosized powder of TiO^2 was fired at 500 ^{0}C, leads to its conversion from amorphous phase to anatase phase.

The crystal size of the powder sample of TiO^2 is of 19 nm size as estimated by Scherrer equation. SEM photograph shows that particles are strongly aggregated which is typical for particles with a size less than 50 nm, so the particle size was estimated to be 20-50 nm.

Conclusion

We synthesized TiO^2 nanoparticles by sol gel route using ethylene glycol as gelling agent. The physical properties, such as crystallite size and crystallinity were investigated by XRD, and SEM. X-ray diffraction pattern shows that TiO^2 particles calcined at 500°C have a stable anatase phase with 19 nm average crystallite size, determined according to the Scherrer equation. The SEM image shows that particles have spherical shape. The yield of the prepared photocatalyst was comparatively higher than other methods used for nanoparticles preparation i.e. microemulsion route.

Acknowledgement

The authors are grateful to the Director, AMPRI, CSIR, Bhopal for encouragement of the present research work. The financial support was provided by Fly Ash Mission, Department of Science and Technology, New Delhi, India.

REFERENCE

1. T. Moritz, J. Reiss, K. Diesner, D. Su and A. Chemseddine, J. Phys. Chem. B, 1997 101, 8052-8053. | 2. J. Karch, R. Birriger and H. Gleiter, Nature, 1987, 330, 556-558. | 3. M. R. Hoffmann, S. T. Martin, W. Choi and D. W. Bahnemann, Chem. Rev., 1995, 95, 69-96. | 4. A. Fujishima and K. Honda, Nature, 1972, 238, 37-38. | 5. M. A. Fox and M. T. Dulay, Chem. Rev., 1993, 93, 341-357. | 6. R. J. Gonzalez, R. Zallen and H. Berger, Phys. Rev. B, 1997, 55, 7014-7017. | 7. K.-N. P. Kumar, K. Keizer and A. J. Burggraaf, J. Mater. Chem., 1993, 3, 1141 - 1149. | 8. R.Wang, K. Hashimoto, A. Fujishima, M. Chikuni, E. Kojima, A. Kitamura, M. Shimohigoshi and T. Watanabe, Nature, 1997, 388, 431-443. | 9. P. A.Mandelbaum, A. E. Regazzoni, M. A. Blesa and S. A. Bilmes, J. Phys. Chem. B, 1999, 103, 5505-5511. | 10. K. Fujiwara, T. Ohno, M. Matsumura, J. Chem. Soc., Faraday Trans., 1998, 94, 3705- 3709. | 11. T. Ohno, K. Fujihara, K. Sarukawa, F. Tanigawa, M. Matsumura, Z. Phys. Chem., 1999, 213, 165-174. | 12. Z.G. Zou, H. Arakawa, J. Photochem. Photobiol. A: Chem., 2003, 158, 145-162. | 13. R. Abe, K. Sayama, H. Arakawa, Chem. Phys. Lett., 2003, 371, 360-364. | 14. J. Ye, Z. Zou, H. Arakawa, M. Oshikiri, M. Shimoda, A. Matsushita, T. Shishido, J. Photochem. Photobiol. A: Chem., 2002, 148, 79-83. | 15. B. O'Regan, M. Gr¨atzel, Nature, 1991, 353, 737-740. | 16. S. Kambe, S. Nakade, T. Kitamura, Y. Wada, S. Yanagida, J. Phys. Chem. B, 2002, 106, 2967- 2972. | 17. H. Goto, Y. Hanada, T. Ohno, M. Matshmura, J. Catal., 2004, 225, 223-229. | 18. V. Chhabra, V. Pillai, B.K. Mishra, A. Morrone, D.O. Shah, Langmuir, 1995, 11, 3307- 3311. | 19. A. Rammal, F. Brisach and M. Henry, C. R. Chimie, 2002, 5, 59-66. | 20. P.V. Kamat, Chem. Rev., 1999, 93, 267-300. | 21. A. Mills, G. Hill, S. Bhopal, I.P.Parkin and S.A. O'Neill, J. Photochem. Photobiol. A: | Chemistry, 2003, 160, 185-194. | 22. P.S. Awati, S.V. Awate, P.P. Shah and V. Ramaswamy, Catal. Comm, 2003, 4, 393-400. | 23. R. Zhang, L. Gao and Q. Zhang, Chemosphere,2004, 54, 405-411. | 24. S. Jeon and P.V. Braun, Chem. Mater., 2003, 15, 1256-1263. | 25. Y. Bessekhouad, D. Robert and J.W. Veber, J. Photochem. Photobiol. A: Chemistry, 2003, 157, 47- 53. | 26. M.M. Yusuf, H. Imai and H. Hirashima, J. Sol-Gel Sci. Technol., 2002, 25, 65-74. | 27. Y. Diaoued, S. Badilescu, P.V. Ashirt, D. Bersani, P.P. Lottici and J. Robichaud, J. Sol- | Gel Sci.Technol., 2002, 24, 255-264.

RESEARCH PAPER | Chemistry | Volume : 3 | Issue : 4 | April 2013 | ISSN - 2249-555X

DRIFT- Spectroscopic Study of Modification of Surface Morphology of Perlite During Thermal Activation

KEYWORDS: perlite, DRIFT, thermal activation.

Sakshi Kabra
Department of Pure and Applied Chemistry, University of Kota, Kota 324005, Rajasthan, India

Anita Sharma
Department of Pure and Applied Chemistry, University of Kota, Kota 324005, Rajasthan, India

Stuti Katara
Department of Pure and Applied Chemistry, University of Kota, Kota 324005, Rajasthan, India

Renu Hada
Department of Pure and Applied Chemistry, University of Kota, Kota 324005, Rajasthan, India

Ashu Rani
Department of Pure and Applied Chemistry, University of Kota, Kota 324005, Rajasthan, India

ABSTRACT *This article presents the use of diffuse reflectance infrared Fourier transform (DRIFT) spectroscopic technique in investigation of the effect of thermal activation on morphology of perlite. Perlite, a naturally occurring waste siliceous material formed by rapid cooling of volcanic eruptions was thermally treated over a range of temperatures. This study focuses on changes in both structure and chemical bonding of perlite due to thermal activation at different temperatures viz., 400, 600, 800, 1000°C for certain time period. The results reveal that on increasing temperature of thermal activation, loss of water occurs which is confirmed by decrease in intensity and broadness of the band, appears between 3600-3300 cm^{-1}, attributing to surface –OH groups. Other bands present in the DRIFT spectra shows the presence of Si-O-Si network and amorphous nature of silica in perlite.*

Introduction
Infrared spectroscopy is a well established technique for the identification of chemical compounds and/or specific functional groups in compounds. An alternative is the use of Fourier Transform Infrared Spectroscopy (FTIR), which is both rapid, non-destructive and requires small, <1 mg, sized samples. Chemical bonds vibrate at a characteristic frequency representative of their structure, bond angle and length. Accordingly, individual molecules have the ability to interact with incident radiation by absorbing the radiation at specific wavelengths. FTIR spectroscopy takes advantage of this by recording the energy absorption of a sample over a range of frequencies. Diffuse reflectance infrared Fourier transform (DRIFT) spectroscopy in conjunction with other analytical techniques has been extensively applied over the years to explore the structure and bonding in amorphous siliceous materials [1]. This technique has proved to be a powerful method to identify the isolated and H-bonded hydroxyl groups on surface of silica [2,3].

R.L. Frost et al. [4] proposed that DRIFT spectroscopy is more applicable than transmission infrared spectroscopy for powdered samples because it provides a rapid technique for analyzing samples without any interference through sample preparation, suitable for the study on the hydroxyl stretching region of silicate minerals. DRIFT has several other advantages including ease of sample preparation, greater number of useful bands and the ability to detect both major and minor components from the same spectra.

Perlite is a hydrated, naturally occurring amorphous volcanic glass formed by cooling of volcanic eruptions, estimating about 700 million tonnes worldwide reserves. Its unique structure consists of numerous concentric layers having SiO_2, Al_2O_3, K_2O and Na_2O as major constituents while TiO_2, CaO, MgO, Fe_2O_3 and hydrated water as well as unburned carbon remain present in varying quantities [5]. On heating the perlite to its softening range, i.e., above 850°C, water molecules vaporize and escape resulting in unusual expansion of perlite up to 7-16 times of its original volume, creating inert, non-toxic, lightweight particles with specific surface area of about 1.22 m^2g^{-1} [6], density in the range of 0.6 - 2.30 gml^{-1} [7] and particle size in range of 0.2-4 mm. [8]. As far as applications of perlite are concerned, it is mainly consumed as fillers, filter aids, in producing building construction materials [9,10].

In the current work, perlite was thermally treated at different temperatures viz., 400, 600, 800 and 1000°C for 3 h and then analyzed by DRIFT spectroscopy. The purpose of this investigation is to use DRIFT spectroscopy to characterize the structure and determine the chemical bonding of silica with other species present in the perlite, so that it can be further utilized for various applications in future.

Material
Perlite sample was supplied by Indica Chem. Ind. Pvt. Ltd., India.

Experimental
Perlite sample was thermally treated in a muffle furnace under static conditions over a range of temperatures, 400, 600, 800 and 1000°C for 3h and abbreviated as TAP-400, TAP-600, TAP-800 and TAP-1000 respectively. The DRIFT spectroscopic study of the samples was done by Bruker FT-IR Spectrophotometer (TENSOR 27) in DRS (diffuse reflectance system) mode by homogenizing samples thoroughly with spectroscopic grade KBr in 1:20 weight ratio. The samples were crushed in an agate mortar. The spectra were recorded in the range 550-4000 cm^{-1} with a resolution of 4 cm^{-1}.

Results and discussion
The colour change is seen in perlite from light grey to white-light pink on thermal treatment at higher temperature. The chemical composition of perlite was determined by EDX analysis which is shown in Table 1. Loss on ignition (LOI) was determined by heating a certain weighed quantity of perlite in muffle furnace at 1000°C for 3 h. The LOI amount was 4.4 wt % which corresponds to the removal of moisture and coexisting unburned carbon from sample [11].

Volume : 3 | Issue : 4 | April 2013 | ISSN - 2249-555X

Table 1. EDX analysis of perlite.

Samples	O(wt%)	Si(wt%)	Al(wt%)	K(wt%)	Na(wt%)	Zn(wt%)	Fe(wt%)	Ti(wt%)	S(wt%)	LOI
Perlite	73.70	18.83	3.72	1.44	1.91	0.22	0.10	0.07	-	4.4

LOI- Loss on ignition

The FT-IR spectra of perlite and thermally activated perlite at different temperatures confirmed that the calcination at any conditions in this experiment produced dehydroxylation in the perlite samples i.e. elimination of the -OH stretching from Si-OH [12,13]. In this fig., a broad band between 3600-3300 cm^{-1} is shown, which is attributed to surface –OH groups of –Si-OH and water molecules adsorbed on the surface. The broadness of band indicates the existence of hydroxyl groups in higher degree of association with each other which results in extensive hydrogen bonding [14], while in FT-IR spectra of thermally activated perlite samples, the intensity and broadness of band is decreased, confirming the loss of water, which is highest in case of TAP-1000 (Fig. 1e). The strong band at 1030 cm^{-1} is due to the structural siloxane framework, which is the vibrational frequency of the Si-O-Si bond. The peak gets shifted to higher wave number, i.e., 1227 cm^{-1} after thermal treatment in TAP-1000 (fig. 1e), normally observed in amorphous silica samples [15]. An intense peak at 1632 cm^{-1} in the spectrum of perlite is attributed to bending mode (δ_{O-H}) of water molecule, which is again highly decreased in case of TAP-1000. The shoulder at about 3200 cm^{-1} (fig. 1a) could be assigned to the stretching vibrations of Si-OH groups in the structure of amorphous SiO_2 [16]. An intense band in the range of 1300-1100 cm^{-1}, corresponding to valence vibrations of the silicate oxygen skeleton is usually assigned to the amorphous silica content. The region around 805 cm^{-1} is characteristic of Si-O-Si symmetric stretching modes [17,18,19]. In the Si–O stretching vibration region (800–1195 cm^{-1}), the bands at 802, 808, 812, 942, 1050 cm^{-1} are identical to the bands at 800, 958, 1088 cm–1 due to amorphous silica [20]. Amorphous silica exhibited a relatively strong peak at about 800 cm^{-1} and it can be distinguished from the band of crystalline silicate [20]. The structure of most SiO_2 is polymorphous, both crystalline and amorphous, based on tetrahedral unit of silicon coordinated to four oxygen atoms. In the Si–O–Si bending vibration region (400–700 cm^{-1}) of quartz, the band at 695 cm^{-1} is determinative whether it is crystalline or amorphous [21]. The band at 695 cm^{-1} appears due to the vibrations in octahedral site symmetry [22]. In the amorphous state this band will be missing. In the perlite samples, we did not get this band which indicates that the silica mineral in this sample is in amorphous form. Another evidence of the presence of amorphous silica in perlite sample is the appearance of a peak at about 1100 cm^{-1}, which is normally assumed to be formed by continuous network of Q^4 species, characteristic in case of amorphous silica [23].

The major component of perlite is silica and untreated silica is totally hydroxylated and the hydroxyl layer is covered with physically adsorbed water. Thermal treatment of the support leads first to removal of water (dehydration) and then to combination of adjacent hydroxyl groups to form water (dehydroxylation) [24].

Fig. 2 shows the magnified FT-IR spectra of all studied samples in the range between 550-1750 cm^{-1}.

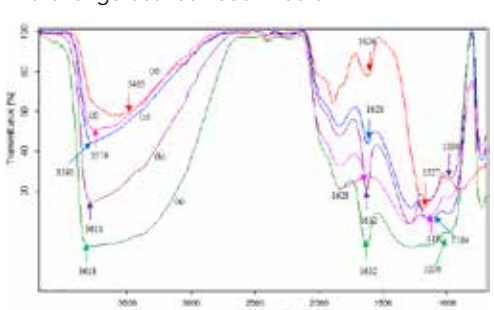

Fig 1. FT-IR spectrum of (a) perlite, (b) TAP-400, (c) TAP-600, (d) TAP-800 and (e) TAP-1000.

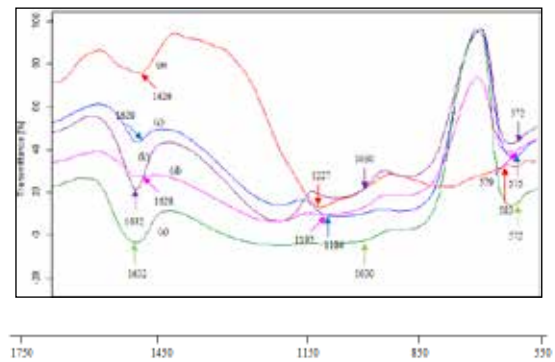

Fig 2. Magnified FT-IR spectrum of (a) perlite (b) TAP-400 (c) TAP-600 (d) TAP-800 and (e) TAP-1000

The observed frequencies of IR bands of all samples and their possible assignments are summarized in Table 2.

Table 2. The observed frequencies of IR Bands of all samples and their possible assignments

Assignments		Wave number (cm^{-1})			
	Perlite	TAP-400	TAP-600	TAP-800	TAP-1000
Si-O-Si symm. stretching vib.	802	802	808	812	942
Si-O-Si asymm. stretching vib.	1030	1030	1184	1192 1192	1227
Si-O-Si bending vib.	572	572	575	579	583
-O-H bending vib.	1632	1632	1628	1628	1626 1626
-O-H stretching vib.	3618	3611	3591	3579	3465

Conclusions

Results found in this paper showed that DRIFT can be successfully employed in investigation of the effect of thermal treatment on perlite morphology. After calcination, physically adsorbed water gets driven away from the surface, so intensity of –OH stretching and bending bands decreases. The present spectroscopic study could be useful in understanding characteristic features of perlite, changes occurred in its structure and chemical bonding because of thermal treatment. This knowledge may be employed in further utilization of perlite for several applications.

Acknowledgement

The authors are thankful to DST Lab, Deptt. Of Pure & Applied Chemistry, University of Kota, for providing DRIFT spectroscopic facility. The authors are also grateful to University Grants Commission, New Delhi, India for their Junior Research Fellowship scheme.

Volume : 3 | Issue : 4 | April 2013 | ISSN - 2249-555X

REFERENCE

1. A. Hamoudi, L. Khouchaf, C. Depecker, B. Revel, L. Montagne and P. Cordier, J. Non-crystalline Solids, 354 (2008) 5074–78. | 2. R K.Iller, The Chemistry of Silica, John Wiley & Sons, New York, 1979. | 3. H. E. Bergna. In the colloid chemistry of silica (ed. H.E. Bergna), American Chemical Society, 1994. | 4. R. L. Frost, U. Johansson, Clays and Clay Minerals 46 (1998) 466. | 5. M. Dogan, M. Alkan, U. Cakir, J. Colloid Interface Sci. 192 (1997)114-118. | 6. M. Dogan, M. Alkan, Chemosphere, 50 (2003) 517-528. | 7. M. Roulia, K. Chassapis, J. A. Kapoutsis, E. I. Kamitsos, T. Savvidis, J. Mater. Sci., 41 (2006) 5870-81. | 8. D. Bastani, A.A. Safekordi, A. Alihosseini, V. Taghikhani, Sep. Purif. Technol., 52 (2006) 295-300. | 9. M.S. Morsy , S.S. Shebl, M. Abd El Gawad Saif, Building Research Journal, 56 (2008) 49-58. | 10. H. Aglan , M. Morsy, A. Allie, F. Fouad, Construction and Building Materials, 23(1) (2009) 138-145. | 11. K. Kordatos, S. Gavela, A. Ntziouni, K.N. Pistiolas, A. Kyritsi, V. Kasselouri-Rigopoulou, Microporous Mesoporous Mater., 115(1-2) (2008) 189-196. | 12. C. Belver, M.A.B Munoz and M.A.Vicente. Chem. Mater., 14 (2002) 2,033-43. | 13. R.A. Shawabkeh and M.F. Tutunji. Clay. Sci., 24 (2003) 111-120. | 14. R.M. Silverstein, F.X. Webster, Spectrometric Identification of Organic Compounds, Sixth ed., John Wiley Pub., 2006, pp. 88. | 15. F. Adam, S. Balakrishnan, P.L. Wong, Journal of Physical Science, 17(2) (2006) 1–13. | 16. S. Music, N.F. Vincekovic, L. Sekovanic, Brazilian Journal of Chemical Engineering, 28(1) (2011) 89-94. | 17. S.H. Javed, S. Naveed, N. Feroze, M. Zafar, M. Shafaq, Journal of Quality and Technology Management, 6(1) (2010) 81-90. | 18. K. Amutha, R. Ravibaskar, G. Sivakumar, International Journal of Nanotechnology and Applications, 4(1) (2010) 61-66. | 19. J.P. Nayak, J. Bera, Trans. Indian Ceram. Soc., 68 (2) (2009) 1-4. | 20. J. Ojima, J. Occup. Health 45 (2003) 94-103. | 21. G. Parthasarathy, A.C. Kunwar and R. Srinivasan, Eur. J. Mineral. 13 (2001) 127. | 22. H. Schneider, Contrib. Miner. Petr. 43 (1974) 233. | 23. F.I. Hurwitz, D.V. Aranda and M.E. Gallagher, Presented at the 236th National Meeting, American Chemical Society, Philadelphia, PA (2008) | 24. B.M. Reddy, G.K. Reddy, K.N. Rao, A. Khan, I. Ganesh, J. Mol. Catal. A: Chem., 265 (2007) 276-82.